12-1-2017

Synthesis of Actinide Materials for the Study of Basic Actinide Science and Rapid Separation of Fission Products

Jacquelyn M. Dorhout
University of Nevada, Las Vegas, dorhoutj@lanl.gov

Repository Citation

SYNTHESIS OF ACTINIDE MATERIALS FOR THE STUDY OF BASIC ACTINIDE SCIENCE AND RAPID

SEPARATION OF FISSION PRODUCTS

By

Jacquelyn M. Dorhout

Bachelor of Science – Chemistry
University of Massachusetts Amherst
2012

A dissertation submitted in partial fulfillment

of the requirements for the

Doctor of Philosophy – Radiochemistry

Department of Chemistry and Biochemistry
College of Sciences
The Graduate College

University of Nevada, Las Vegas
December 2017

Dissertation Approval

The Graduate College
The University of Nevada, Las Vegas

September 29, 2017

This dissertation prepared by

Jacquelyn M. Dorhout

entitled

SYNTHESIS OF ACTINIDE MATERIALS FOR THE STUDY OF BASIC ACTINIDE
SCIENCE AND RAPID SEPARATION OF FISSION PRODUCTS

is approved in partial fulfillment of the requirements for the degree of

Doctor of Philosophy – Radiochemistry
Department of Chemistry and Biochemistry

Kenneth R. Czerwinski, Ph.D.
Examination Committee Chair

Ralf Sudowe, Ph.D.
Examination Committee Member

Paul Forster, Ph.D.
Examination Committee Member

Jaqueline L. Kiplinger, Ph.D.
Graduate College Faculty Representative

Kathryn Hausbeck Korgan, Ph.D.
Graduate College Interim Dean

ii

Abstract

This dissertation covers several distinct projects relating to the fields of nuclear forensics and basic actinide science. Post-detonation nuclear forensics, in particular, the study of fission products resulting from a nuclear device to determine device attributes and information, often depends on the comparison of fission products to a library of known ratios. The expansion of this library is imperative as technology advances. Rapid separation of fission products from a target material, without the need to dissolve the target, is an important technique to develop to improve the library and provide a means to develop samples and standards for testing separations. Several materials were studied as a proof-of-concept that fission products can be extracted from a solid target, including microparticulate (< 10 µm diameter) dUO_2, porous metal organic frameworks (MOFs) synthesized from depleted uranium (dU), and other organic-based frameworks containing dU. The targets were irradiated with fast neutrons from one of two different neutron sources, contacted with dilute acids to facilitate the separation of fission products, and analyzed via gamma spectroscopy for separation yields. The results indicate that smaller particle sizes of dUO_2 in contact with the secondary matrix KBr yield higher separation yields than particles without a secondary matrix. It was also discovered that using 0.1 M HNO_3 as a contact acid leads to the dissolution of the target material. Lower concentrations of acid were used for future experiments. In the case of the MOFs, a larger pore size in the framework leads to higher separation yields when contacted with 0.01 M HNO_3. Different types of frameworks also yield different results.

The second portion of this dissertation describes efforts to better understand electronic structure and bonding of the actinide metals in various environments. One project involved studying thorium and uranium bonding with the soft-donor chalcogenides, specifically sulfur. Results from these studies include the synthesis and characterization of the novel $(C_5Me_5)_2Th(SMe)_2$ complex; the synthesis of $(C_5Me_5)_2ThS_5$ by myriad routes, indicating the product is a thermodynamic sink; and evidence that sulfur is inserted

into the thorium-carbon bond of $(C_5Me_5)_2ThMe_2$ to form the pentasulfide. The second project involved unique activation of the strong carbon-halide bonds present in benzyl-halides mediated by a uranium-(2,2'-bipyridine) complex. The resultant products include a series of uranium-halide bonds from fluoride to iodide, and the addition of the benzyl group to the bipyridine ring. Studies of the mechanism indicate that the benzyl group is added first to the 6 position of the ring before migrating to its final place at the 4 position. The final project utilized a novel gold-tetrazolate complex that can be tailored to add high-nitrogen ligands to actinides in a facile and safe way. This transfer ligand was used to synthesize new uranium-tetrazolate species. A brief exploration into using the transfer ligand to add tetrazolates to lanthanides was also done. All resultant compounds from each of these projects was studied by NMR, IR, and UV-Vis-NIR spectroscopies, electrochemistry, and X-ray crystallography.

Acknowledgements

Department of Homeland Security Disclaimer

This work is dedicated to my parents Dr. Peter Dorhout and Carolyn Dorhout for their invaluable support

Table of Contents

List of Tables

List of Figures

List of Equations

Chapter 1: Background

1.1 Introduction

Separating fission product isotopes from one another in order to determine their concentrations, activities, and ratios has been a goal of nuclear forensics scientists for decades.[1,2] These isotopes and their ratios are signatures that are part of the desired outcome of nuclear forensic evaluation. Should a nuclear device be detonated, the identification of individual isotopes of elements in the fallout through effective separation can lead to answers on what type of device was detonated, how and when it was made, and the nature of the nuclear material production facility.[3]

In order to study the ratios of certain fission products that would be present after a device is detonated, actinide targets are irradiated in a neutron flux and the fission products are separated from the target.[4] The first step in processing these targets is to dissolve the actinide foil and remove the remaining actinide from the fission products.[4,5] The dissolution can be performed using a range of methods; it often involves a mixture of nitric acid and sulfuric acid, and it can take several hours for the target to completely dissolve.[4] Corrosive and radioactive waste is produced when separating the actinide target material from the fission products, and the process is time consuming.[6] Some effort has been made to reduce waste and reuse the target; this involves re-precipitating the actinide from the acid solution and processing it into a reusable form.[6] However, extra steps are added, which increases the time needed to work with these materials. The aim of this project is to create a target that doesn't need to be dissolved before separation of the fission product isotopes, and can potentially be re-used quickly.

Tangential to the nuclear forensic aspect of the project, there is also interest in isotope separation to support nuclear medicine. The United States government has goals to increase and sustain the reliable supply of radioisotopes that are used in medical procedures. There are few facilities around the world that can produce these isotopes, such as ^{99}Mo, and most are reaching the end of their lifespans.[4] Simplified

extraction methods could improve the production, distribution, and use of radioisotopes in nuclear medicine. The ability to rapidly separate fission products from a target could influence multiple fields of nuclear chemistry.

To create a target material that is robust to irradiation and dissolution of the fission products, the primary study of this project is focused on depleted uranium (dU) encased in a matrix material which can be easily removed in a liquid phase. Depleted uranium is comprised of over 99.3 atomic % of ^{238}U, with less than 0.7 atomic % ^{235}U.[7] In the initial studies performed in this thesis, KBr was selected as the matrix material. Solution conditions were selected in which the KBr dissolved and the uranium target remained in the solid phase. Explanations of these conditions can be found in Chapter 2. Fission of ^{238}U, the primary isotope of depleted uranium, can be achieved with fast neutrons, or those neutrons with energies over 1 MeV. In UO$_2$, fission products travel approximately 10 μm (based on recoil energy).[8] If the UO$_2$ material diameter is smaller than that distance, the fission products could potentially embed themselves on the surrounding matrix, thus using the recoil energies as a means of separation. Experiments based on this process are described in Chapter 2.

The uranium could also be coordinated within a mesoporous or nanoporous matrix comprising a Metal Organic Framework (MOF). The porosity of the MOF could serve as a means to increase the separation by allowing more of the material to be in contact with the liquid phase. However, the porosity increases the potential of the fission process destroying the backbone of the MOF through the impact of ionizing radiation or recoil particles on the bonds; however, high linear energy transfer will localize ionization and the bulk of the matrix will not experience a nuclear induced chemical reaction.[9] To find a robust but porous matrix, several different organic linker molecules based on prior MOF literature will be bound to uranium and then irradiated to serve as examples. Chapter 3 discusses MOF synthesis and irradiation experiments performed over the course of several years.

As part of this research, the targets are synthesized using depleted uranium as the matrix material. The material is characterized and irradiated, and the fission products are extracted and analyzed. The details for these experiments are listed in Chapters 2, 3, and 4. What follows are the background surveys on the literature, the results of synthetic strategies, and irradiation and extraction of fission products from the matrix materials.

1.2   Dissertation Overview

This chapter provides an introduction to the project and background information on the chemistry of thorium and uranium, synthetic methods, and analytical techniques used in the first half of this thesis work. Chapter 2 details the synthesis and irradiation of UO_2 targets and how a matrix material affects the separation potential of fission products from the target. Chapter 3 describes the synthesis and irradiation of UO_2-MOF (metal-organic framework) targets and the results from those separation experiments. This chapter also discusses the differences in results between the MOF targets and the UO_2 targets. Chapter 4 is the final chapter in the irradiation portion of this manuscript, and it details the less successful irradiation targets. The work in the remaining chapters was performed at Los Alamos National Laboratory and includes basic actinide syntheses designed to gain a better understanding of their bonding characteristics. The results from these studies may be useful to the radiochemical field for separating actinides from each other, or from lanthanides. Chapter 5 details chalcogenide studies, Chapter 6 explains experiments related to actinide mediated C-X activation, and Chapter 7 discusses high-nitrogen ligand addition to actinides using gold. Conclusions to both sections of the research, as well as future directions each project could take are described in Chapter 8.

1.3   Background of Methods and Materials

1.3.1   Chemistry of the Actinides

Both thorium and uranium are of interest throughout this thesis work; below is a historical description of the chemistry of both elements. The actinides are the first series to have a 5f subshell in their electronic structure.[10] In its ground state, thorium does not have any electrons in its 5f subshell, and can therefore be a useful tool for comparisons in the chemistry with elements, such as uranium, that do have occupied 5f orbitals. The ionic radius difference is also unlike that found for the majority of the periodic table; due to relativistic effects, the ionic radius of the actinides decreases from left to right. This is known as the actinide contraction, and may also give rise to differences in chemistry between thorium and uranium.

1.3.1.1   Thorium

Thorium (element 90) was discovered in 1828 by Swedish chemist Jöns Jacob Berzelius and was named after Thor, the Scandinavian god of thunder and weather. It was isolated from thorite, which is essentially thorium silicate. Thorite also contains a significant amount of uranium, and so the chemical formula is written as $(Th,U)SiO_4$.[11] For nearly 50 years, thorium had no application. It wasn't until the invention of the incandescent gas mantle by C. Auer von Welsbach that thorium was used commercially because of its heat-resistant properties.[11] It also has applications in the production of ceramics, as a coating for tungsten welding rods, as it provides a hotter arc, and strong alloys. More recently, thorium has been used in dating very old geological materials, such as mountain ranges, and as a nuclear fuel source.[11] Thorium is more abundant in the Earth's crust than uranium - nearly as abundant as lead and molybdenum - and ^{232}Th can be converted to fissile ^{233}U using thermal neutrons. As the isotope ^{233}U is fissile, it can be fissioned by thermal neutrons to produce neutrons and continue the cycle.[11]

Natural thorium is almost exclusively ^{232}Th with a very small amount of ^{228}Th (also known as radiothorium), which comes from the decay chain of ^{232}Th. Thorium occurs almost exclusively in the tetravalent state,

and is frequently found in ores mixed with uranium.[11] Thorium metal has the highest melting point among

the actinides (1750 °C) and the lowest density in the series apart from actinium (11.724 g/cm^3).[11] It is also

paramagnetic, with a ground state of 6d^{2}7s^2, and is quite reactive toward elements such as oxygen,

hydrogen, and the halogens. It does not contain any f-electrons in its ground state, and as such is

commonly used as a tool to study the effects of the f-electrons in bonding when compared to uranium.

Thorium is arguably one of the most well-studied of the actinides, given its lengthy half-life (1.4E10 years)

and low energy gamma emissions; there are several hundred known compounds involving thorium.

However, the organometallic chemistry of thorium (see Chapter 5) wasn't well studied until the 1970s

when Marks and co-workers became interested in the cyclopentadienyl-thorium system.[12]

1.3.1.2   Uranium

Uranium (element 92) was discovered in 1789 by Martin Heinrich Klaproth in the form of pitchblende, a

combination of UO_2 with U_3O_8.[7,13] Uranium dioxide was believed to be the pure elemental form until 1841

when Eugene-Melchior Peligot prepared metallic uranium from UO_2. He was also the first to describe the

yellow salts of uranium as "uranyl" compounds. Uranium was primarily used for colorants in ceramics and

glasses for the first century after its discovery, until Becquerel discovered in 1896 that it emitted

penetrating rays. Until the discovery of nuclear fission in 1938 by Strassman, Hahn, and Meitner, uranium

was not regarded as an especially important element. Now, however, uranium is used in multiple

applications from energy to weapons.[7,13]

Natural uranium contains three isotopes of uranium in varying concentrations atom percentage: ^{235}U

(0.005%), ^{235}U (0.720%), and ^{238}U (99.275%). Depleted uranium consists of more than 99.3 atomic percent

^{238}U and less than 0.7 atomic percent ^{235}U, whereas enriched uranium has levels of both ^{234}U and ^{235}U

above their natural abundances. The isotopes can be separated through gaseous diffusion – where UF_6

vapor diffuses through a series of barriers – or gas centrifuge – where the isotopes are physically

separated via centripetal force.[14] It is found in ore bodies mainly in Australia (31%), Kazakhstan (12%), Russia (9%), and Canada (9%). The United States has uranium ores that contain about 4% of the world's uranium supply.[15]

Uranium metal is strongly electropositive, similar to aluminum and magnesium, and it is highly reactive. The oxidation states of uranium range from +3 to +6, with +4 and +6 the most stable in aqueous conditions.[13,14] Figure 1 shows the Eh-pH diagram of U-O-H. The species of uranium in aqueous conditions at any given pH or potential can be found by using this diagram. For example, it can be seen that trivalent uranium is easily oxidized due to its high negative potential. Pentavalent uranium in the form of UO_2^+ will disproportionate into U(4+) and UO_2^{2+} under aqueous conditions.[13,14] Tetravalent uranium is insoluble in mildly acidic (pH = 4.2) to alkaline conditions (pH = 9.8). Hexavalent uranium is highly soluble, especially in aqueous solutions, and is very mobile. These properties are part of what makes storing used fuel so difficult.[7,13,14]

U (FACT/FACTSAGE)

$UO_2[2+]$

$H_7O_{13}U_3[-]$

$UO_2[+]$

$UOH[3+]$

$H_5O_5U[-]$

$UO_2(s)$

$U[3+]$

Eh(V)

pH
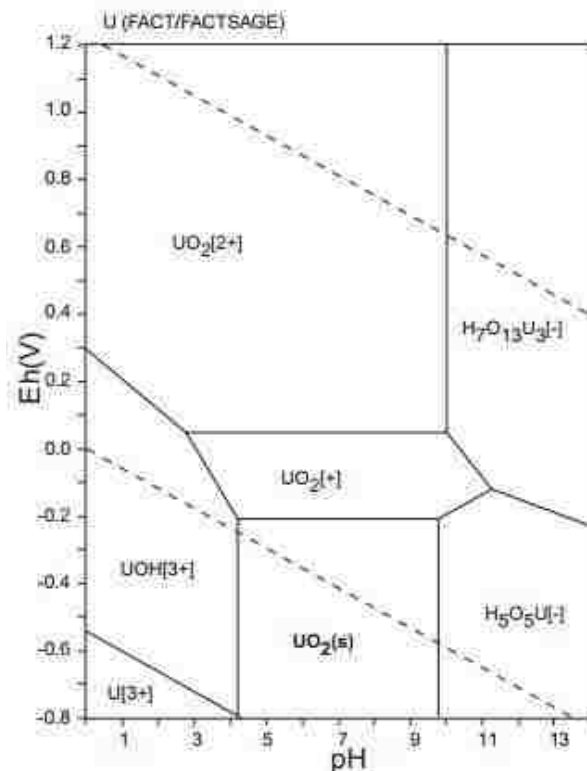
Figure 1. Eh-pH diagram of the U-O-H system [U]=10⁻¹⁰, 25°C, 1 bar.[16]

The majority of hexavalent uranium compounds contain the uranyl (UO_2^{2+}) cation. Uranyl is a linear molecule with the oxygen atoms double bonded to the uranium metal 180° apart. Other groups can bond to the uranium in its equatorial plane. For example, uranyl nitrate has two bidentate nitrate (NO_3^-) groups bound equatorially around the uranyl moiety (Figure 2).[17] The resulting geometries of coordination with UO_2^{2+} are square-, pentagonal-, and hexagonal-bipyramidal. A variety of ligands have been shown to coordinate to the uranyl molecule, especially those with O donor functional groups, such as carboxylic acids, enolates, and Schiff bases.[18] This means that a range of organic linker molecules can be explored, which allows novel compounds to be synthesized fairly easily.[17]
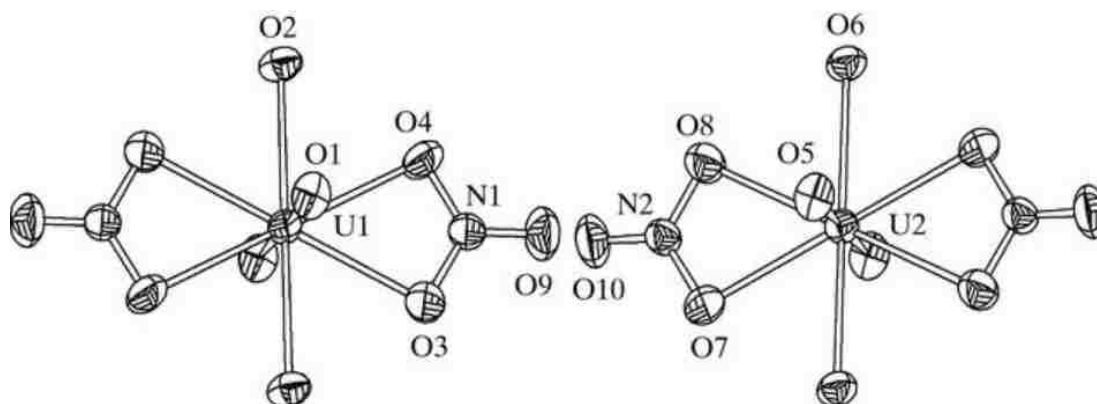
Figure 2. Crystal structure of uranyl nitrate trihydrate. Water molecules omitted for clarity.[17]

Absorption of uranyl in aqueous solution occurs around 400 nm (Figure 3),[19] giving uranyl compounds a distinctive yellow color. The absorption band in UV-Visible spectroscopy often exhibits fine structures due to progressions in symmetric O=U=O vibrations in the excited state.[14] For the synthetic procedures described in the first four chapters of this manuscript, the uranium starting material is in the form of uranyl nitrate hexahydrate, which is very similar to the trihydrate shown in Figure 2.
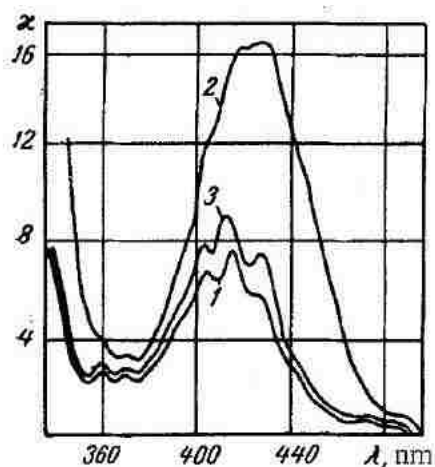
Figure 3. Absorption spectra in water of: 1) UO_2^{2+}, 2) $UO_2NO_3^+$, and 3) $UO_2(NO_3)_2$.[19]

1.4   Metal-Organic Frameworks

Porous organic coordination networks have been studied with respect to various applications for decades.[20] The first organic coordination network was discovered in 1897 by Hofmann and Küspert, but

8

the structure was not confirmed until 1954.[21] This discovery was important because the possibility existed

to control the pore size and overall structure of the framework by selecting ligands with determined

shapes and functionalizations. In this way, both the size and environment of the pore could be engineered

for a specific application. Prior to the discovery of organic coordination networks, inorganic frameworks,

such as zeolites or sieves, were the only type of structures used for their porosity. Their uses included the

removal of solvents (e.g. water) from an environment.[21] Other applications such as petroleum refinement,

ion exchange, and molecular adsorption depend on zeolites, but because of the restricted pore size, they

can only be used with small molecules.[21] Zeolites are purely inorganic, and while they are the most

prominently used group of porous materials, they are highly limited by their pore sizes. These pore sizes

often range from 4 to 9 Å in diameter, and can be round or elongated in shape.[22] This restriction lead to

the development of metal-organic materials.
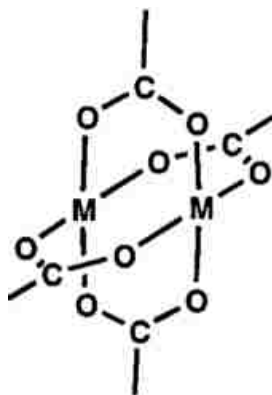
Figure 4. Generic example of a MOF with carboxylate organic linker molecules.[23]

A metal-organic framework (Figure 4) is composed of a metal center linked with organic ligands, which

allows for the potential of exploiting properties of both the organic and inorganic components within a

single material.[20,21] The organic molecule can be used to control the size, shape, and functionality of the

pore in the material, while the inorganic metal offers thermal and mechanical stability. Optical and

electronic properties of interest may also be changed based on the metal center. The components of

MOFs are connected via coordination bonds such as H-bonds, π-electron stacking, and van der Waals

interactions. These interactions lead to a structural flexibility in the crystalline state, which promotes the unique character of MOFs.[20] Late transition metals such as copper, silver, zinc, and cadmium tend to provide a multi-dimensional framework. Theoretically, MOFs can be constructed from multiple organic ligands or metal ions; however there are very few reports on frameworks that have more than two kinds of either ligand or metal.[20]

The MOFs are a relatively new topic in synthetic chemistry, having only been studied in depth since the late 1980s. Permanent porosity was discovered in the 1990s, which lead to even more interest in MOFs as a way to store gases; however, carboxylate based ligands (on which this thesis work is based) were not well explored until the mid-1990s.[20] Carboxylates are useful linking ligands because they can be deprotonated for charge balances, and they can bind the metal in a variety of ways. The carboxylate group also allows for the formation of multiple bonds to the metal, which adds to stability of the framework. The pore sizes used in this thesis work are relatively small – between 5 and 9 Å in diameter – but the possibility for pore sizes in excess of 30 Å exists.[24]

Metal-organic frameworks have traditionally been made with transition metals, and in a few cases the lanthanides, but there are far fewer records of MOFs made with actinides. Progress is continuing with researchers looking into the potential of actinides as the metal center.[18,25-32] For example, the Cahill group has been studying uranium MOFs for over a decade; they are interested in using dicarboxylate[18,33-35] and mixed aliphatic[28,29] ligands to create the 3-dimensional structures. The Thuéry group has also studied uranium MOFs using dicarboxylate linkers,[31,32] as well as flexible aromatic groups.[30]

This thesis work uses uranium as the metal center for the production of irradiation targets. The porosity of the MOF may allow for easy, rapid separation of the fission products that are formed in the irradiation. Chapter 3 details the results of irradiations on uranium MOFs.

1.5   Hydrothermal Chemistry

Hydrothermal chemistry is a solid-state chemistry technique used to grow single crystals of a material from water, and is often used for synthesis of MOFs. It is typically performed in a stainless steel autoclave (Figure 5) at temperatures up to 250 °C and pressures up to 1800 psig (pounds per square inch gauge). The temperature limitation is due to the use of a Teflon liner. Glass tubes can also be used in place of the autoclave, although that method has fallen out of favor due to pressure limitations.
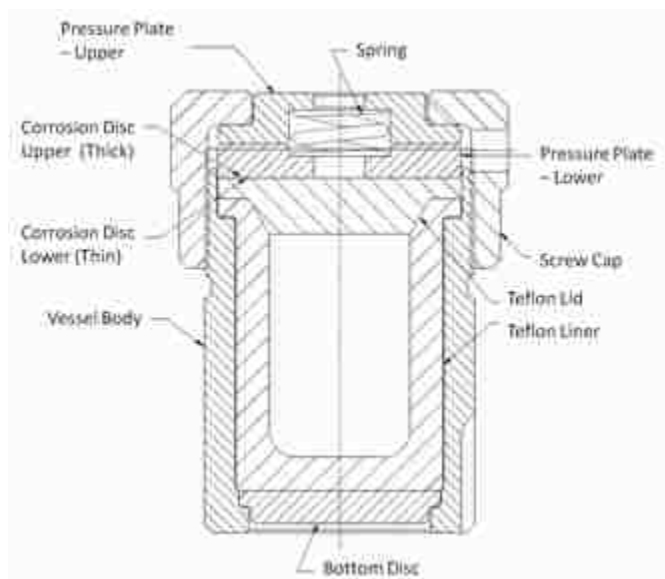
Figure 5. Parr acid digestion vessel model 4749.[36]

The autoclave is comprised of two major parts – the inner Teflon liner, and the outer steel body. The materials and solvents are placed in the Teflon liner and capped with a Teflon lid. The liner is place in the steel outer body on top of a removable steel disk. Two corrosion disks are placed on top of the Teflon lid to prevent the corrosion of the steel body in the event of a leak. Two pressure plates are placed on top of the corrosion disks with a spring between them. These plates allow for pressure release should the autoclave become over pressurized. However, the plates only prevent the autoclave from exploding radially because they are purposefully the weakest point in the design. Over pressurization still results in an explosive force that expands axially and could potentially blow the top off of the autoclave. This situation is not ideal, and great care is taken to ensure that the final pressure of the reaction is far below

the limit of the autoclave. Finally, a steel cap is screwed on to hold everything together. The autoclave is then placed in a furnace at a certain temperature, depending on the solvent used, for a specific period of time. Typical time scales are on the order of hours to days. Once the autoclave has been allowed to cool, it is opened and the material is harvested. In general, the slower the rate of cooling of the autoclave, the greater the probability of getting an X-ray quality crystal. This method was used throughout this thesis research to create targets for irradiation, which are described in more detail in Chapters 2 and 3.

1.6   Neutron Sources from Fusion and Fission

Nuclear fusion is the process by which two or more nuclei collide at very high velocity and join to form a new nucleus.[37] Some energy is given off in the process, which makes the mass of the new nucleus slightly less than the sum of the constituents. Fusion requires high energy and high density in order to occur, and the larger the mass of the nuclei, the more energy is required. Therefore, only lighter elements, such as hydrogen, helium, and boron, are fusible. There are some events, such as a supernova in a star, in which elements up to ^{56}Fe can be fused together.[38] If the elements are any larger, there is not enough energy in the system to force them to stick together.[37] Figure 6 depicts the average binding energy per nucleon as the number of nucleons increases. Simply put, the greater the binding energy, the more stable the isotope. Isotopes smaller than ^{56}Fe can undergo fusion, and isotopes larger than ^{56}Fe can undergo fission.[39] Those isotopes with full nuclear shells, such as ^{4}He, ^{12}C, and ^{16}O, have higher binding energies and thus are more likely to be stable.
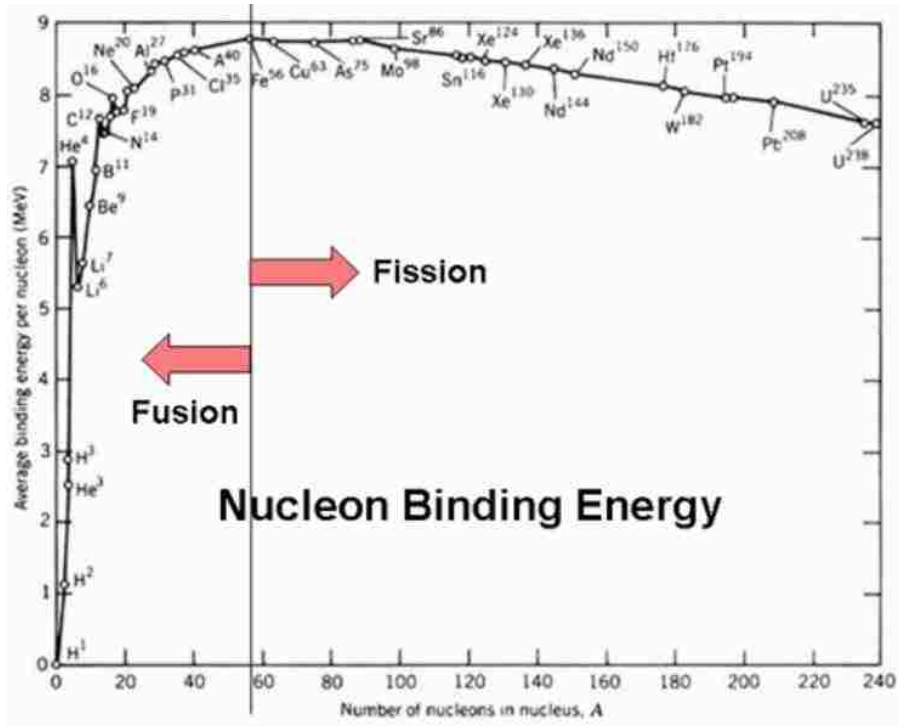
Figure 6. Binding energy curve[39]

The process of fission can occurs when a fissile isotope is bombarded with a thermal neutron. Fertile isotopes, such as ^{238}U, require a higher energy neutron to induce fission. Fissile isotopes require less energy to fission due to the pairing of nucleons, and can be fissioned by thermal neutrons (< 0.025 eV). For example, when ^{235}U captures a neutron, it becomes ^{236}U. The Q value from this reaction can be found from the mass excess of ^{235}U and a neutron minus the ^{236}U mass excess value. The resulting Q value of 6.5 MeV is sufficient to overcome the fission barrier of 6.2 MeV. The energy needed to excite ^{236}U into a fissionable state is exceeded by even thermal energy neutrons (< 0.025 eV).[40] A similar calculation for thermal neutron capture on ^{238}U to produce ^{239}U yields a Q value of 4.8 MeV, which is not sufficient to overcome the fission barrier of 6.6 MeV.[40] Thus higher energy neutrons are necessary to overcome the fission barrier and induce fission of ^{238}U.

The result of fission is generally two products ranging in mass from Z = 23 to Z = 72, with A values anywhere from A = 66 to A = 172 (in the case of ^{235}U, see Figure 7).[38] A couple of neutrons are also released in the

13

process, and they can cause fission in nearby fissile atoms. Breakup of the atom into three products (ternary fission) is less likely than binary fission, but does occur. The third particle is most likely a light particle, such as ^{3}H (0.01% yield).[41] For the purposes of this discussion, binary fission is assumed to be the only mode.

A nucleus can fission into two equal fragments, but it is not the most probable mode. It is far more likely the fragments will be asymmetric – that is to say they are not of equal mass. The thermal fission yields for uranium isotopes are often shown in what is colloquially referred to as the "double-hump curve" (Figure 7). Generally, the two humps are centered near A = 95 and A = 140, although the lower mass curve shifts depending on the starting material. The centering of the two humps is mainly driven by what are known as "magic numbers" – representations of filled nuclear shells.[40] These magic numbers are Z or N = 2, 8, 20, 28, 50, 82, and 126, and are derived from the potential of the nuclear shell structure.[40] Nucleons with two full shells are referred to as "doubly magic" and are particularly stable. For example, ^{132}Sn is a doubly magic isotope (A = 50, Z = 82) and is found near the apex of the second "hump".

The shape of the curve changes as a function of both the starting isotope and incident neutron energy. For ^{239}Pu, the lower mass curve becomes centered near A = 103 and the upper mass curve shifts slightly to around A = 135. This is mainly due to the increase in nucleons in the system. The incident neutron energy shapes the valley of the graph. As shown in Figure 7, the greater the neutron energy, the higher the valley that appears between the two peaks. This translates to more symmetry in the fission products.[38] There are some isotopes that are heavy enough to undergo spontaneous fission; fission that occurs without additional energy from neutrons. Some isotopes with high spontaneous fission yields include ^{248}Cm, ^{252}Cf, and ^{254}Cf.[38] This type of fission is not relevant to this thesis work and will not be discussed further.
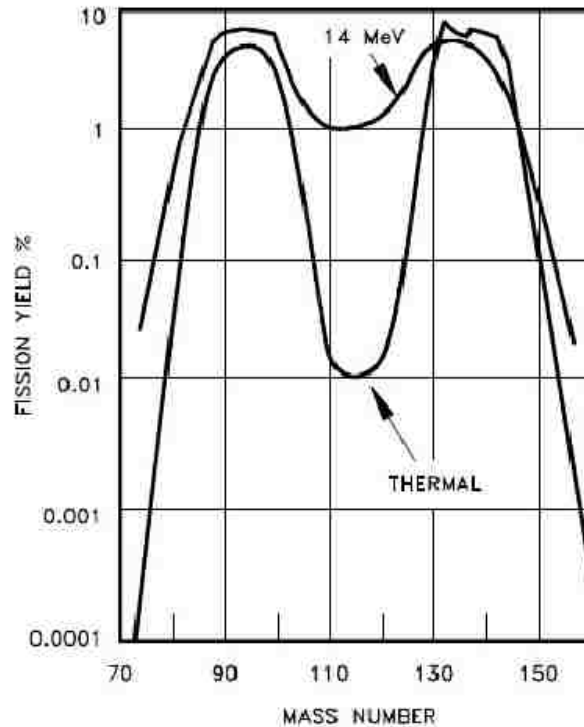
Figure 7. Fission yields for 235U at different neutron energies.[42]

There are a number of neutron generating sources that can induce fission in fertile or fissile material, but this discussion will only include two neutron sources: a dense plasma focus and a criticality device known as Flattop. The two devices were chosen for their convenience, availability, and cost.

1.6.1 Fusion - Dense Plasma Focus

The dense plasma focus (DPF) is a neutron sources located at the National Security Technology (NSTec) North Las Vegas site. Dense plasma focus technology has existed for several decades; it was independently discovered by two groups in the early 1960s.[43] Essentially, it consists of a short-lived plasma that is hot and dense enough to cause nuclear fusion, and therefore the emission of neutrons.[43,44] This plasma can be made up of deuterium atoms, or a combination of deuterium and tritium atoms. The energy released during fusion is dependent upon the make-up of the plasma. The D-D reactions release neutrons on the order of 3 MeV, and D-T reactions release neutrons on the order of 14 MeV.[37,43,44] The DPF used within

15

this work contains a D-D plasma, and therefore emits lower energy neutrons. These neutrons are still fast enough to induce fission in depleted uranium.

An electric current is applied to the deuterium gas, which breaks down into an ionized plasma. The plasma flows in the direction of the current and is accelerated along an anode. Eventually, the plasma slides off of the anode and comes into contact with itself, forming a "pinch" (Figure 8). The plasma is highly unstable and quickly breaks up. This break-up causes particle bursts, along with electromagnetic radiation, and these particles are what interact with a target material. The bursts are only nanoseconds to microseconds long, depending on the size of the machine, so an irradiation requires several hundreds of bursts over a period of time.[43,44] Figure 9 shows images of the radial motion of the plasma taken in 1977 by Bernard et.al.[45] One sample was sent to be irradiated at the DPF. The experiment and its results are discussed in Chapter 2.5.2.
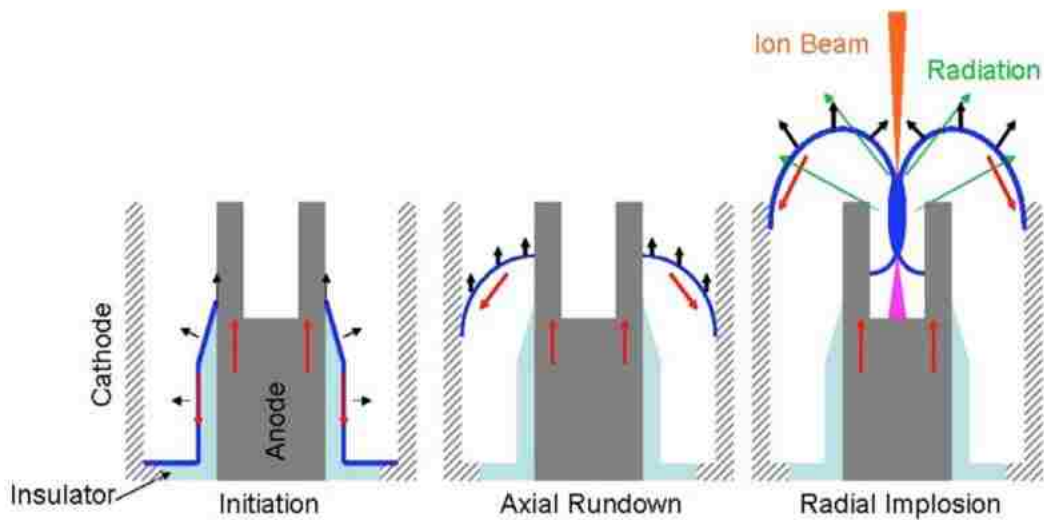
Figure 8. The three phases of a typical DPF current pulse: initiation via flashover of the insulator, axial run-down phase, and radial implosion to form beams and dense pinch.[43]
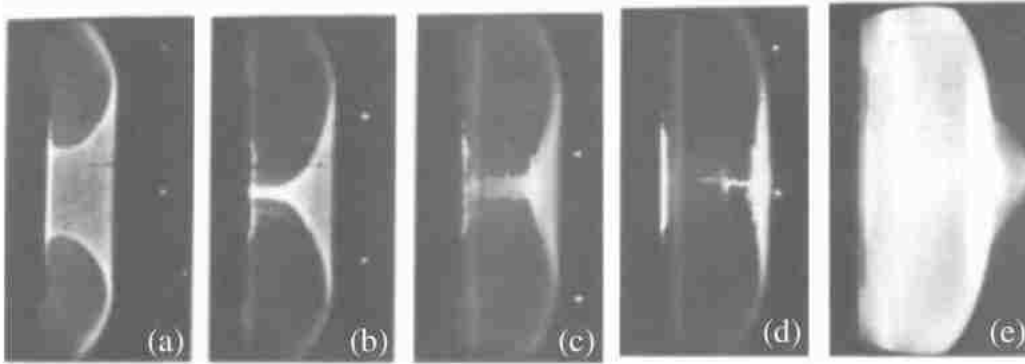
Figure 9. (a) Radial compression, (b)-(d) Pinch formation, (e) Bubble ionization and axial shock wave into cold gas.[43]

1.6.2 Fission – Flattop Critical Assembly Device

Flattop (Figure 10) is one of several critical assembly devices originally built and housed at Los Alamos National Laboratory (LANL). It was built in the 1950s and has been used for neutron activation studies, reactivity measurements, and calibrations of a variety of elements.[46] In 2004, it was relocated to the National Criticality Experiments Research Center (NCERC) at the DAF in Nevada. The Device Assembly Facility (DAF) is an underground facility which was constructed in the mid-1980s to be used with underground nuclear testing. Since the implementation of the Comprehensive Nuclear Test-Ban Treaty in 1996, the facility serves as a support for several experiments, including Stockpile Stewardship Science. It includes weapon assembly cells, irradiation assemblies (e.g. Flattop), plasma physics capabilities, laboratory space, and bunker areas.[47]

Flattop received several safety system upgrades and came back online in 2011.[48] It is essentially a highly enriched uranium (HEU, >90% ^{235}U) core surrounded by a reflector of natural uranium. The core is comprised of two hemispheres of HEU joined by HEU screws. Both the reflector and the core have a 1.27 cm inner diameter "glory hole" into which small samples may be placed.[49] The reflector has three parts to it – one hemisphere is completely stationary, and the other is broken up into two moveable parts. These movable parts are on hydraulic tracks and can be moved quickly to control the criticality of the device.

There are also three control rods of natural uranium that can be inserted into the stationary hemisphere of the reflector. Combined with the two movable sections of the reflector, these rods act as scrams for the device.[46] There are two other cores that can be used with Flattop – one consists of ^{240}Pu, and the other of ^{233}U. The latter has been in storage for several years, as its gamma levels are too high to be safely operated.[49]

Figure 10. Flattop critical assembly device[48,49]

The device is assembled by moving the core along its track into place within the stationary reflector section, and then moving the remaining parts of the reflector into place (Figure 11).[49] The diagram in Figure 11 shows the placement of the control rods as well as the glory hole for sample loading. The glory hole can hold small samples (see Chapter 2) as well as filler pieces (Figure 12, number 31). These filler pieces are generally made of natural uranium or HEU metal, and can be used to adjust the reactivity of the devices, as well as hold samples in place.
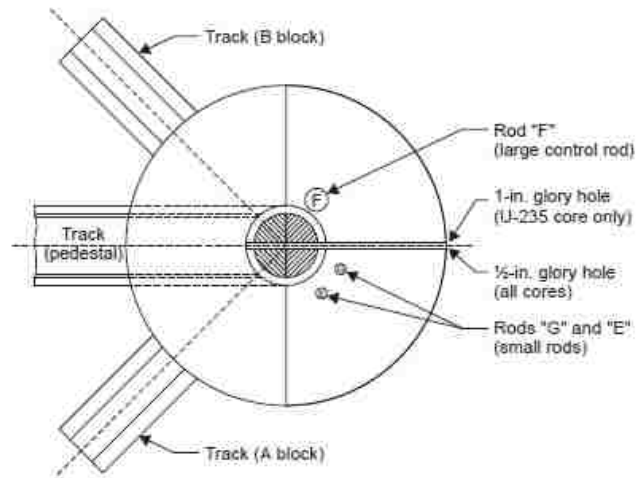
Figure 11. Diagram of Flattop from above[49]

HEU Core with Glory Hole Filler Pieces in Place
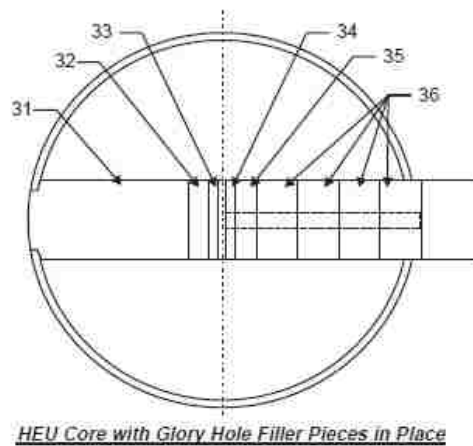
Figure 12. Diagram of the Flattop core with fillers (labeled as 31) in the glory hole[49]

Flattop differs from other criticality devices in that it is characterized by a fast-neutron spectrum in the core, and a decreased neutron spectrum in the reflector. The neutronic properties (e.g. energy) and other characteristics are well known from studies over the past several decades.[48] A number of depleted uranium samples have been sent to Flattop for this thesis research. The experimental details and results of these irradiations are discussed in Chapter 2.

19

1.7   Gamma Spectroscopy

One of the major types of ionizing radiation is the photon – also known as a gamma-ray at certain energies. Gamma rays are not charged, and often behave more like waves than particles. There are three main types of interaction mechanisms that gamma rays undergo when they interact with matter: photoelectric absorption, Compton scattering, and pair production.[50]

In the photoelectric absorption process, a photon interacts with an absorber atom. This leads to the partial or complete transfer of the photon's energy to the absorber atom, which releases a photoelectron – an electron from one of the bound shells of the atom. The photoelectron has the energy of the photon minus the binding energy of the electron. The absorber atom becomes ionized, and can either capture a free electron from the environment, or rearrange its already bound electrons to fill the hole. The latter case causes the release of an X-ray whose energy is equal to that of the difference in energy between electronic shells.[50]

Compton scattering occurs between the incident gamma-ray photon and an electron in the absorber. The incident photon is deflected at an angle with respect to the original direction. The photon transfers a portion of its energy to the electron. All angles of scattering are possible, so the energy transferred from the photon to the electron can vary between zero and a large fraction of the gamma-ray energy.[50]

 The final interaction mechanism is pair production, which only occurs if the incident photon has an energy greater than twice the rest mass of an electron (1.022 MeV). The higher the incident energy above that threshold, the higher the probability that pair production will occur. If the photon enters the coulomb field of a nucleus, it can spontaneously become an electron-positron pair. Any excess energy (energy from the photon above 1.022 MeV) becomes kinetic energy for the electron and positron. Once the positron has slowed down in the absorbing medium, it will interact with an electron and annihilate, producing two photons at 511 keV.[50]

The probability (σ) that each interaction mechanism will occur is dependent upon both the energy of the

incident photon energy as well as the density (and atomic number) of the absorber material (Figure 13).

As the energy of the photon increases, the dominant interaction mechanism changes. At energies above

several MeV, pair production is the most dominant interaction. Notice that as the atomic number of the

absorber material increases, the probability of the photoelectric effect being the dominant mechanism

increases. It is important to note that in any given area, the probability of other interactions is not

necessarily zero. Along the lines in the plot, the probabilities of dominance are equal between two

mechanisms.[50] Although this chart encompasses energies up to 50 MeV, for most isotopes, the gamma

decay energy does not extend much beyond 2 MeV.
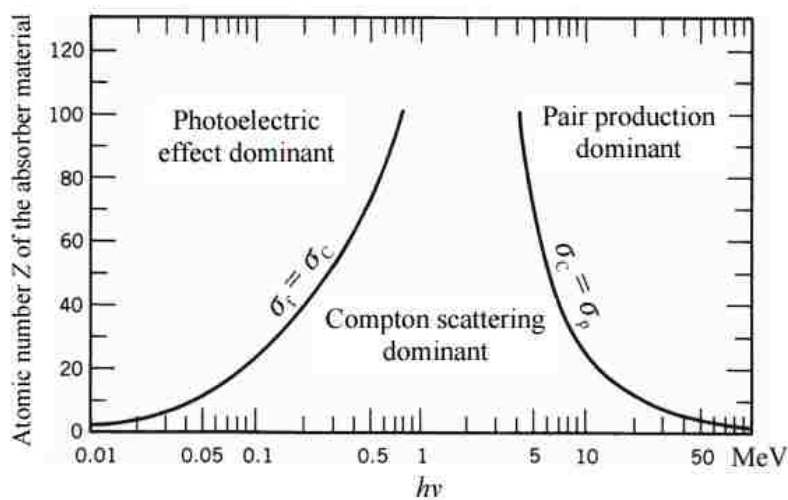
Figure 13. The probability of an interaction mechanism occurring based on the energy of the incident photon and the atomic number of the absorber.[51]

All three types of interactions can be seen in gamma detectors. There are several types of instruments

that can be used to identify gamma radiation, such as NaI scintillation detectors and HPGE detectors. High

Purity Germanium (HPGe) detectors are a type of semiconductor detector used to identify gamma-rays

whose energies are on the order of keV – MeV. Because gamma rays are not charged, the likelihood of

their interaction with material is decreased. To circumvent this problem, a higher volume of germanium

crystal is used. A coaxial geometry, where the crystal is long in the axial direction, allows for a higher

detector volume and is generally the chosen geometry for modern HPGe detectors.[50] One electrode is placed along the outside surface of the crystal, and the other electrode is situated in the core of the crystal (Figure 14). When an electric field is applied, a steady-state charge distribution is established in an area of the crystal.[50] This area is referred to as the depletion region, and it is where the interactions of gamma rays with the crystal are detected.
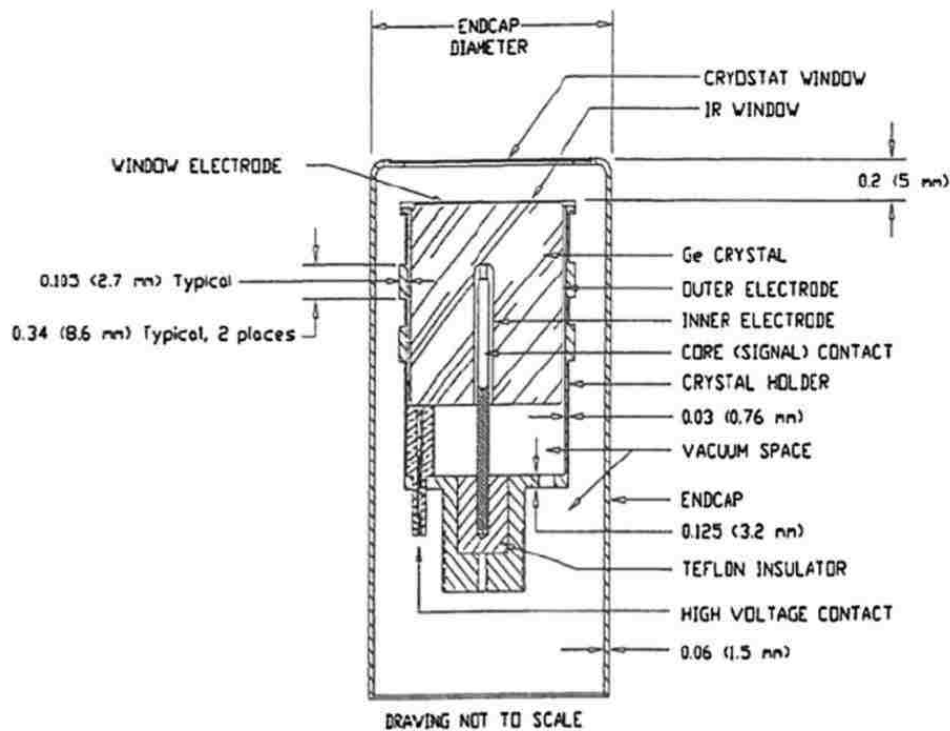
Figure 14. Technical drawing of an HPGe detector crystal.[52]

However, because the bandgap in germanium is so small (0.7 eV), the detector cannot be used at room temperature. Thermal excitation of electrons within the crystal is enough to cause a leakage current resulting in the recording of false events. For this reason, the detector must be cooled down to 77 K using liquid nitrogen.[50] Figure 15 shows a generic diagram of an HPGe detector from Canberra. The sample being counted is placed on top of the detector holder and surrounded by thick lead shielding to prevent contamination of the data from the environment.
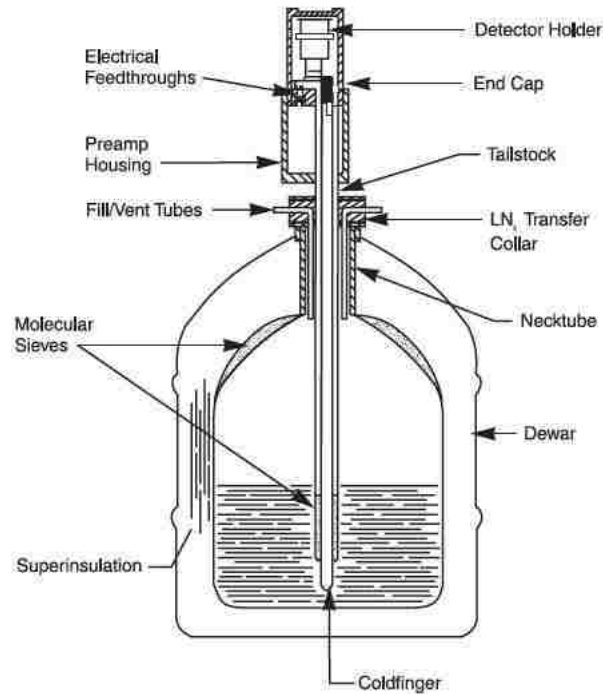
Figure 15. Generic example of an HPGe detector and liquid nitrogen dewar from Canberra.[53]

As the name implies, HPGe detectors are highly pure germanium crystals, which allows for high energy resolution compared to NaI detectors.[50] This is advantageous when the samples being analyzed have several isotopes with closely spaced energies, or when the sources are weak because it allows for the spectroscopic peaks to rise above the background, or statistical noise of a continuum.[50] Figure 16 depicts a general example of the features common to a gamma spectrum. The full energy peak (E_γ) appears when the full amount of energy from an incident gamma ray is deposited within the detector area. The broad plateau is from the Compton scattering; the range of energies from Compton interactions causes this continuum.[50] Likewise, the annihilation peak is a result of positron emission or pair production occurring in the surrounding material. The double and single escape peaks occur in the spectrum when the photons from pair production are not captured in the detector medium and "escape". Their energies are equal to the full energy peak minus either 511 keV (one annihilation peak escaped) or the full energy minus 1.022 MeV (both annihilation peaks escaped). X-ray escape peaks occur when the X-rays formed from photoelectric interactions escape the detector without depositing their energy.
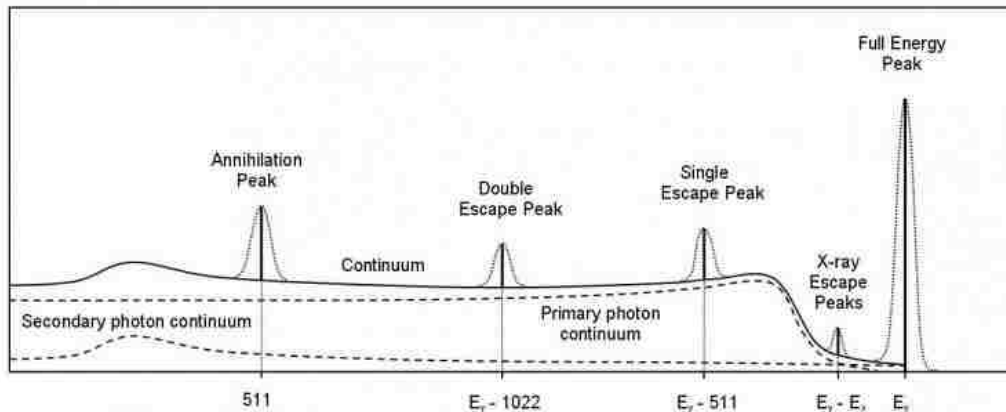
Figure 16. Generic example of gamma spectrum features

Gamma spectroscopy is a useful tool to identify the presence and energy of certain radionuclides. It was the major means of identifying the fission products produced and separated during the irradiation of samples (see Chapters 2-4). It is not a perfect method, due to efficiency and the presence of non-gamma emitting nuclides, but it is a relatively rapid, non-destructive one that does not require the separation of fission products from each other prior to analysis as in ICP-MS or alpha spectroscopy. The relative efficiency of the detector used in the analyses presented herein was 60%.

1.7.1 BEGe detectors

A specific type of HPGe detector used in this research is a Broad Energy Germanium (BEGe) detector. The BEGe can cover a full range between 3 keV and 3 MeV, but due to their short, fat shape, there is enhanced efficiency and resolution at lower energies (<1 MeV).[54] However, it also has comparable resolution at high energies to a standard HPGe detector, which makes it a useful diagnostic tool. Several samples in this work were counted on a BEGe detector rather than a standard co-axial HPGe. The detector used in these experiments had an active diameter of 69.5 mm, an active area of 3800 mm^2, and a thickness of 30 mm.[55]

1.8   Inductively Coupled Plasma Mass Spectrometry

Inductively Coupled Plasma Mass Spectrometry (ICPMS) is a technique used to detect low limits of elements in a sample.[56] In the case of the experiments presented herein, an ELAN DRC II ICPMS from Perkin Elmer was used to detect the concentration of ^{238}U dissolved in liquid samples. Liquid samples are sent through a nebulizer and then the ICP torch atomizes and ionizes the sample. The hot plasma gas is cooled by rapidly expanding it, and then a fraction of the gas is sampled. The gas is positively ionized and is separated from electrons using a negative voltage. The ions are then accelerated and focused based on their mass to charge ratio using magnets. Typically, ICPMS instruments can measure mass ranges from 30 to 300 amu, and can resolve ions differing in their mass to charge ratio by 1.[56]

1.9   Autoradiography

Autoradiography is a non-destructive method used to determine the location of radioactive material within a sample. It has been widely used in monitoring radioactive fallout from weapons tests or incidents at nuclear power plants.[57] A sample is placed on photo-phosphor imaging film within a light-proof box. The material decays and emits particles that interact with the film, producing a black spot. The size of the spot is related to the number of radioactive events in that area during the film exposure, which can be used to identify the activity of the particle in question.[57-58] For experiments herein, this technique was used to identify the distribution of radioactive particles (i.e. UO_2) within a sample, and the imaging occurred over 24 hours. The plates were developed and digitized using specialized software to show images of the intensity of the radioactivity.

1.10 NMR Spectroscopy

The use of nuclear magnetic resonance (NMR) spectroscopy to identify and characterize synthesized compounds has been in place for decades.[59] The spectrometers generally have powerful magnets on the order of several tesla (T), and radiofrequencies ranging from 60 to 700 megahertz (MHz).[60] The frequency

most commonly used in the following chapters is 400 MHz. Nuclei with nonzero spin (e.g. ^{1}H, ^{13}C, ^{31}P) are

placed in the strong magnetic field and perturbed with radio waves at a given frequency. As they relax

from the perturbation, they emit nonradiative signals which can provide specific information on the

nucleon's environment.[59,61] In an atom, the electrons orbit the nucleus and generate a small induced

magnetic field. This magnetic field opposes the field applied externally by the NMR spectrometer.[60] If the

magnetic field surrounding a particular nucleus is weaker than the external field, the nucleus is shielded.

The more shielded a nucleus, the farther upfield (to the right) its resonance will appear in a spectrum.[60]

As an example, if a proton is bound to an atom that is more electronegative, such as oxygen, the electron

density is withdrawn and the proton is said to be less shielded. Its resonance will appear more downfield

(to the left) in a spectrum.[60] The position of the resonance is indicative of the amount of shielding, and

therefore the chemical environment surrounding the proton. The structure and functional groups of a

molecule can be determined using the position of a resonance in the spectrum as well as the number of

resonances – indicating how many different types of protons are present; the intensity of the resonance

– which implies how many protons of each type are present; and the splitting of the resonance signals –

which give information related to the nearby protons.[60,61] In the following chapters, NMR spectra are

generally referenced to a deuterated solvent such as tetrahydrofuran-d_8 (THF-d_8) or benzene-d_6 (C_6D_6),

which allows for consistency in analyzing the data.

1.11 UV-Visible-Near IR Spectroscopy

Ultraviolet (UV) spectroscopy detects the electronic transitions of systems and can provide information

on the conjugation of the ligand, and/or the oxidation state of the metal center.[62] However, it does not

necessarily give structural information. The UV-visible region corresponds to wavelengths of light

between 200 and 800 nm. The Near-IR region is generally between 800 and 2500 nm.[61]

In this work, the samples are dissolved in 1 mL of a solvent such as toluene or tetrahydrofuran (THF), and placed in an air-tight quartz cell. The light beam passes through the sample at varying wavelengths and then hits a detector.[62] The amount of light absorbed by the sample is calculated as an intensity ratio between the intensity of light from the beam (I_0) and the intensity of light that reaches the detector (I). The wavelengths of light absorbed by the molecule in question are determined by the differences in electronic energy between orbitals.[62] The absorption wavelengths can therefore give certain information about the molecule, and is generally measured by molar absorptivity (ε). Molar absorptivity ($M^{-1}cm^{-1}$) is calculated using Beer's Law from the concentration of the solution and the cell path length (Equation 1), where A is absorbance (unit less, taken from the spectrum), c is the sample concentration (mol/L), and l is the path length of the cell (cm).[62]

$$A = \varepsilon cl$$

Equation 1. Calculation of the absorbance of a molecule at a given wavelength.

Samples in this discussion were collected in 0.1 cm path length quartz cuvettes loaded in the drybox using a PerkinElmer model Lambda 1050 UV-visible-near-infrared spectrophotometer. Samples were typically run at two dilutions to optimize absorbance in the UV-visible and near-IR, respectively. Sample spectra were obtained versus air and corrected for solvent absorption subsequent to data acquisition.

1.12 Infrared Spectroscopy

Infrared (IR) spectroscopy observes the vibrations (e.g. stretches, bends) of bonds and uses those observations to give details about the structure of the molecule. The IR region of the electromagnetic spectrum 800 – 100,000 nm, but is generally reported in wavenumbers (cm^{-1}), so the region becomes 12500 – 100 cm^{-1}. The most commonly used region of the infrared is 4000 to 670 cm^{-1}.[61]

The IR spectrum is a depiction of the energy absorbed by a molecule as a function of the frequency of light.[63] The radiation is not energetic enough to cause the type of electronic transitions seen in UV-Visible spectroscopy; the absorption of the radiation instead results in the stretching and/or bending of the bonds between atoms, and depends on the masses of the atoms and the stiffness of the bonds.[61] For example, heavier atoms vibrate more slowly, thus the frequency of the vibration is decreased. Similarly, the weaker a bond between two atoms, the less frequent the vibrations.[63]. Because bonds can often stretch, bend, and twist in different directions, there are several absorptions in an IR spectrum that can result from the same bond.[63]

For the purposes of this discussion, all of the IR spectra were taken using a Thermo Scientific Nicolet iS5 FT-IR spectrometer, and a Golden Gate Diamond ATR (ZnSe lenses) with a reaction anvil (neat solid samples). The infrared light goes from the source to a diamond beamsplitter. Some of the light reflects at a right angle and strikes a stationary mirror, while the rest of it passes through the diamond, through the sample, and hits a mirror moving at a constant velocity. Both beams are reflected back into a detector. FT-IR spectrometers have a better signal-to-noise ratio than other types of IR spectrometers, and therefore are more sensitive.[61]

1.13 Electrochemistry

For the purposes of this discussion, the electrochemistry was performed in an inert-atmosphere drybox using either THF or trifluorotoluene (TFT). Unless otherwise noted, the electrolyte for these analyses is ~ 0.1 M $[NPr_4][BAr^F_4]$. There are three electrodes involved in the potentiometry; the reference electrode, which is a Ag pseudo reference that maintains constant potential through the experiment; the counter electrode – a platinum wire that helps balance the flow of current through the reaction; and the working electrode – a platinum disk electrode at which the reaction takes place.[64] The cyclic voltammogram is given in potential (volts) vs. current (amps) and can be used to determine the oxidation state of the

actinide, as well as the influence of the ligand on the electrochemical potential of the molecule.[64] This information is particularly useful when comparing the chemistry of thorium, which has no 5f-electrons, to that of uranium.

The data described herein were collected with a PerkinElmer Princeton Applied Research Corporation (PARC) model 263 potentiostat under computer control with PARC model 270 software. All data were collected with positive-feedback IR compensation activated to ensure minimal contribution to the voltammetric waves from uncompensated solution resistance. Scan rates from $50 - 5000$ mV/s were employed to assess the chemical reversibility of the observed redox transformations. Half-wave potentials were determined from the peak values in the square-wave voltammograms or from the average of the cathodic and anodic peak potentials in a reversible cyclic voltammogram. Potential calibrations were performed at the end of each data collection cycle using the ferrocenium/ferrocene couple as an internal standard.

1.14 X-ray Diffraction

When X-rays pass through a sample, such as a single crystal, the radiation interacts with the electrons in the matter to product scattering.[56] When these X-rays are scattered by an ordered crystal, interferences occur between the scattered rays because the distances between the scattering centers (i.e. atoms in the crystal structure) are the same order of magnitude as the wavelength of radiation.[56] As the X-ray strikes a crystal surface, only part of the beam is scattered. The remainder of the wave penetrates to the next layer of atoms in the crystal, and so on. The accumulation of these scatterings from the regularly spaced layers of crystal gives rise to information on the order of the crystal, the types of atoms present, as well as their distances and connectivity.[56]

Data for the following experiments were collected on a Bruker D8 Quest diffractometer, with a CMOS detector in shutterless mode. The crystals were cooled to 100 K employing an Oxford Cryostream liquid

nitrogen cryostat. The data collection employed graphite-monochromatized Mo Kα (λ = 0.71073 Å) radiation. A hemisphere of data was collected using ω scans, with 10 s frame exposures and 0.5° frame widths. Data collection and initial cell refinement were handled using APEX 2 software.[65] Frame integration, including Lorentz-polarization corrections, and final cell parameter calculations were carried out using SAINT software.[66] The data were corrected for absorbance using redundant reflections and the SADABS program.[67] Decay of reflection intensity was monitored through analysis of redundant frames. The structure was solved using direct methods and difference Fourier techniques. Unless otherwise noted, non-hydrogen atoms were refined anisotropically and hydrogen atoms were treated as idealized contributions. Structure solutions, refinement, and creation of publication materials were performed using SHELXTL.[68]

1.15 Summary

The presented research covers both fission product separation from a variety of targets and exploration of organoactinide synthetic chemistry. The first few chapters will describe the synthesis, preparation, irradiation, and analysis of both UO_2 and uranium-based metal-organic framework targets. The results will describe the effectiveness of both target materials and certain acid solutions at separating fission products from the uranium, and will detail potential steps forward with the project. The remaining chapters detail the synthetic achievements of several projects involving uranium and thorium organometallic reactions as a means to better understand the basic chemistry of the actinides. Exploration of organoactinides with chalcogenides, halides, and high-nitrogen ligands will be documented, and the results will be tied in with nuclear forensics.

Chapter 2: Irradiation of UO_2

This chapter details the synthesis of UO_2 target material, the creation of target materials, and the irradiation of several targets using two different methods. These methods were described in Chapter 1, Section 1.6. An overview of the separation method is presented here, and analysis of the irradiated targets using gamma spectroscopy is reported for each target material. A comparison between several targets contacted with different extractants is given.

2.1. UO_2 Synthesis

2.1.1 Experimental

The investigation of UO_2 particles as potential target materials that support the goal of simple separations is not a novel idea; UO_2 has been used as a nuclear fuel, which results in the creation of fission products, for decades.[69-72] However, a serendipitous discovery lead to the formation of microparticles (e.g. <10 μm diameter) of UO_2, which could prove useful for a target material. The microparticles of UO_2 were created using depleted uranium via hydrothermal synthesis of $UO_2(NO_3)_2$ with either glutamic or aspartic acid as the reducing ligand at 180 °C for several days. A stoichiometric ratio of 3:1 ligand:$UO_2(NO_3)_2$ generated the highest percent yield (56%). The resulting solid product was a fine black powder with an average particle size of 2.66 ± 0.76 μm, which is ideal for a target because the fission particle recoil distance is 10 μm in UO_2.[8,73] A solid UO_2 product did not appear when the reaction was performed at temperatures below 160 °C and was present only in small amounts below 170 °C.

The UO_2 was removed from the reaction vessel by decanting the solution into a centrifuge tube and centrifuging at 3500 rpm for 3 minutes. The liquid solution above the solid phase was removed by pipetting. The powder was washed with fresh DI water and centrifuged again. The powder was then moved to a scintillation vial and dried in the furnace at 120 °C.

Optical analysis of the particles was done using a Leica DM 2500 P microscope and the results are presented below. Powder XRD analysis establishing the identity of the crystalline sample is also presented.

The UO_2 produced via this synthetic strategy has been used as a target material to determine if it is a viable candidate for fission product removal, along with addition of a secondary matrix material. This matrix provides a backdrop onto which the fission products may embed themselves, and should therefore be easily soluble in aqueous solutions to increase the rapidity of the separation. It should also not interfere with the irradiation or data collection processes. The procedures for target synthesis, irradiation, and data collection and analysis are described in the sections below.

2.1.2 Results

As discussed previously, fine black UO_2 is the product of the hydrothermal reaction of $UO_2(NO_3)_2$ with either aspartic or glutamic acids above 160 °C. The result is easily reproducible, and an average yield of 56% is obtained at a scale of 100 mg. The reaction has been scaled up to the 500 mg scale with an average 79.2% yield. Several grams of material were successfully synthesized.

Figure 17 is a microscope image of the UO_2 particles. It shows that, while many of the particles have clumped together, there are particles smaller than the 10 μm scale bar. This is important for a target material as stated above.
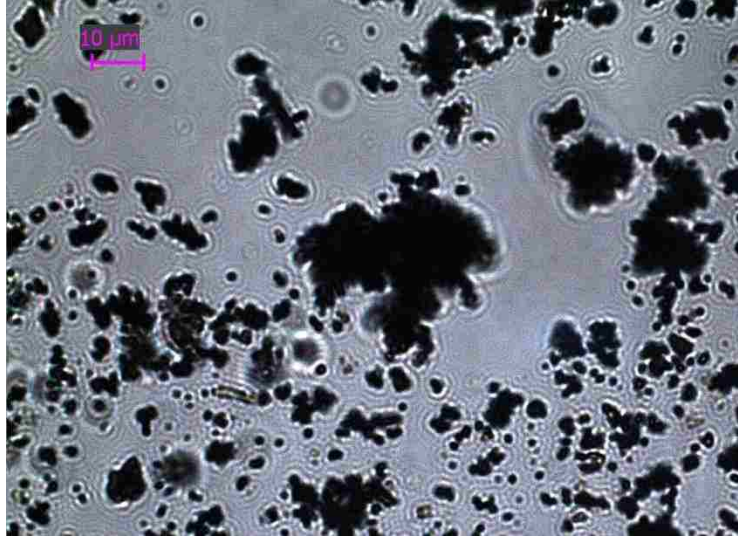
Figure 17. Microscope image of UO_2 particles

Figure 18 is a powder XRD data set comparing a sample of the UO_2 particles (red line) to a known uraninite compound (blue line). The Rietveld refinement of the XRD pattern was performed, showing the sample was 100% uraninite. This is evident by the evaluation in the top right corner.
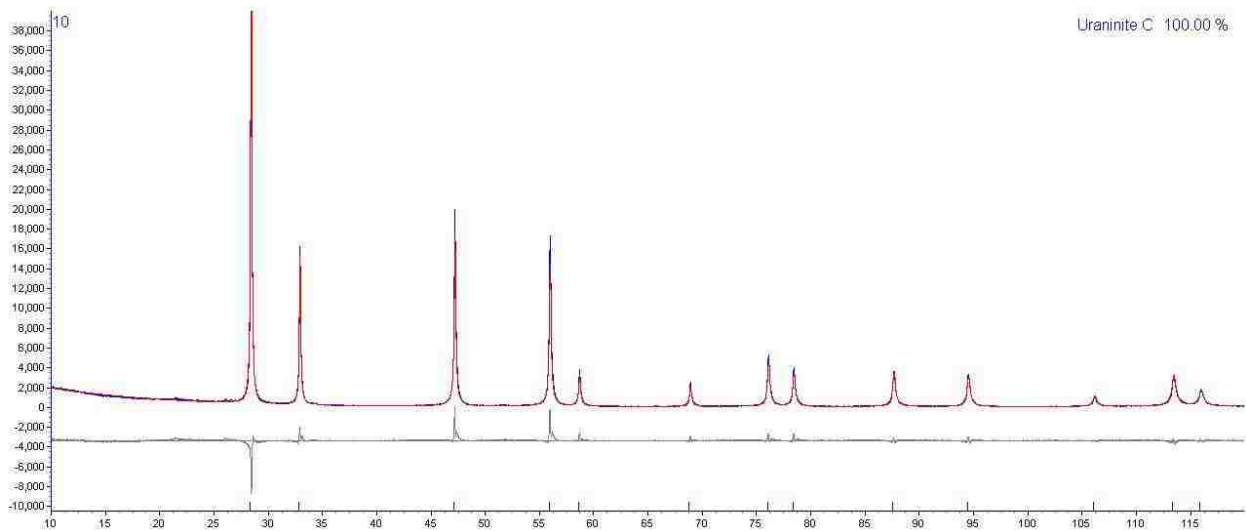
Figure 18. Powder XRD data of the UO_2 sample compared to known uraninite

2.2   UO$_2$ Dissolution

2.2.2   Experimental

The main goal of this experiment was to determine how much solid UO$_2$ is present in target extraction solutions as a function of time using solvent mixtures designed to remove the fission products after samples are irradiated. It is critical to establish the ideal solvent conditions for fission product extraction, while simultaneously minimizing the dissolution of the target UO$_2$. Both HNO$_3$ and HCl were chosen as extractants because those acids have been used historically to extract fission products from actinide materials.[4] In these previous studies, 3M HNO$_3$ and 2M H$_2$SO$_4$ were combined for the dissolution procedure of uranium metal, which has a higher density than UO$_2$ (19.1 g/cm^3 and 10.97 g/cm^3, respectively).[7] The authors report a concentration of the uranium metal dissolved in this acid mixture of 6.30 mmol/L in under 30 minutes.[4] In the experiments described herein, because the goal was not to fully dissolve the UO$_2$, significantly more dilute acid solutions were tested.

An initial study was performed using 1 M HCl. Roughly 200 mg of UO$_2$ was added to 10 mL of 1 M HCl and placed on a rocking table. The solution was centrifuged and samples were collected at specified time intervals between 10 and 1440 minutes. Each sample was diluted and concentrations of dissolved UO$_2$ were determined with an ELAN DRC II ICP-MS from Perkin Elmer. A second study was performed using 100 mg of UO$_2$ in 10 mL 0.01 M HCl. The experiment was done exactly as described above, but with two additional time points of 7200 minutes and 8640 minutes to determine if the solution arrived at equilibrium within a week of initial contact with the acid. A third solvation study was performed with roughly 50 mg of UO$_2$ in 10 mL of 0.01 M HNO$_3$ to determine if there was a substantial difference between the two acids. Apart from the amount of UO$_2$ in the system and the acid used, the experimental conditions were identical to the second experiment.

2.2.3 Results

The initial study was done with 234.4 mg of UO_2 particles and 10 mL of 1 M HCl. As stated above, the solution was contacted with the particles for a specific amount of time before an aliquot of solution was collected. This aliquot was then diluted and examined with the ICP-MS (Figure 19). After 24 hours of contact with the particles, the solution measured a concentration of ^{238}U at 8.19 mmol/L. The data suggests that with more time, the dissolution of UO_2 would increase.
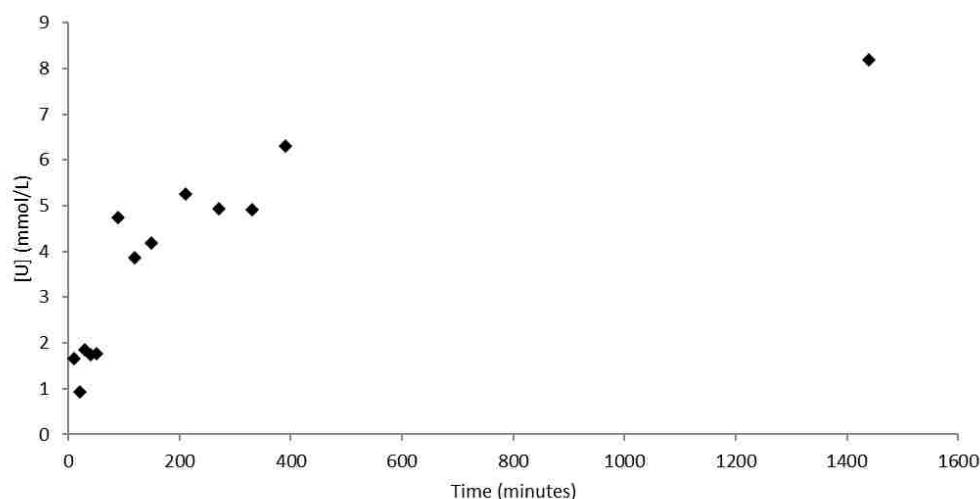
Figure 19. ICP-MS data for UO_2 contacted with 1 M HCl

The same process was then repeated with 0.01 M HCl to see if less UO_2 dissolved in a weaker acid solution (Figure 20). In this experiment, 99.7 mg of UO_2 was contacted with 10 mL of 0.01 M HCl. This time aliquots were taken up to 8640 minutes (6 days) to determine if equilibrium was reached. The maximum concentration of ^{238}U in the solution was 6.53 mmol/L, which occurred after 6 days. After 24 hours, the concentration was 6.19 mmol/L. This suggests that, while some uranium is still dissolving in this weaker acid solution, there is less dissolution than in a 1 M HCl solution, and that after an additional 5 days of contact the concentration does not increase very significantly.
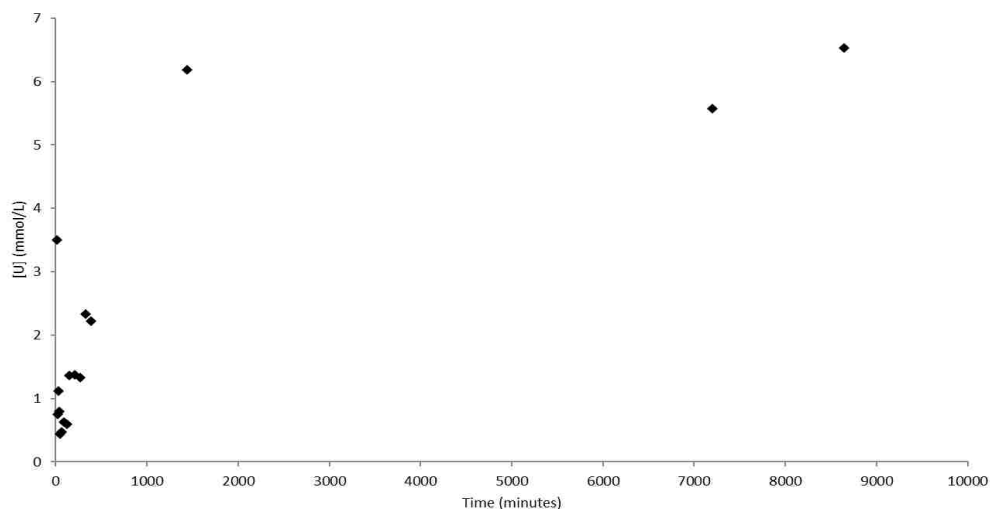
Figure 20. ICP-MS data of UO_2 contacted with 0.01 M HCl

A third experiment was done using 0.01 M HNO_3 to see if the acid type affected the dissolution rates of UO_2. This time 52.3 mg of UO_2 were contacted with 10 mL of 0.01 M HNO_3 for 8640 minutes (6 days). The solution appeared slightly darker in color than the HCl, perhaps due to better suspension of the UO_2 particles. The maximum concentration was found to be 7.00 mmol/L after 7200 minutes (5 days) (Figure 21). However, after 6 days the concentration was slightly less. This is more likely due to error in dilution rather than UO_2 re-precipitating into the solution. Due to the slight decrease of dissolution rate, 0.01 M HCl and 0.01 M HNO_3 were chosen as extraction solvents in the separation experiments.
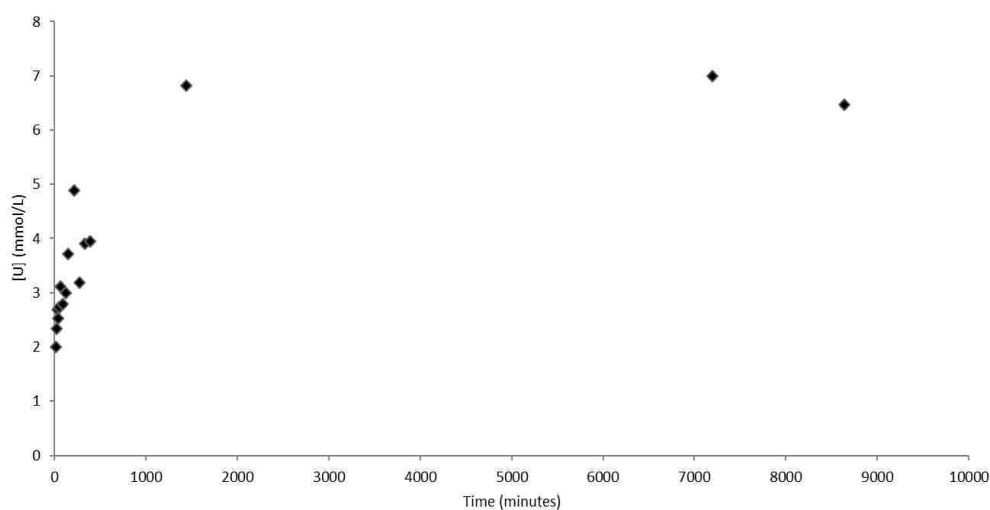
Figure 21. ICP-MS data of UO_2 contacted with 0.01 M HNO_3

2.3   KBr Ratio Determination

2.3.2   Experimental

As previously mentioned, a matrix material was mixed with the target material to capture the fission products and facilitate removal. Potassium bromide was chosen as the secondary target material because of its low water content, its availability, and its high solubility in aqueous media. However, the neutron activation of KBr produces ^{82}Br ($t_{1/2}$ = 1.5 days), which has several gamma lines associated with its decay over a range of energies. This can cause problems when analyzing data because smaller gamma signatures can be masked by the larger peaks from the ^{82}Br. Too much KBr could also act as a poison in the neutron flux, preventing the UO_2 from interacting with enough high-energy neutrons to induce fission. The isotope ^{39}K has a neutron capture cross-section of 2.1 barns at neutron energies less than 0.025 eV, and 1 barn at neutron energies above 0.025 ev; ^{81}Br has neutron capture cross sections of 2.4 and 51 barns, respectively.[38] Though relatively low, these neutron capture cross sections could inhibit the neutron flux. However, if there is not enough KBr, the fission products may not embed themselves in the matrix and instead interact with neighboring UO_2 particles, which may prevent their extraction. To determine the appropriate ratio of KBr to UO_2 in a target, several pellets with varying ratios were prepared and then analyzed using both optical microscopy and SEM imaging.

The ratios of KBr:UO_2 investigated were 5:1, 4:1, 3:1, 2:1, and 1:1. Each mixture was vortexed to achieve homogeneity and then pressed into a 6mm pellet using 4 tons of pressure for 10 minutes. Each pellet was then analyzed using optical microscopy for a visual approximation of homogeneity. The same pellets were subsequently coated in carbon and imaged using scanning electron microscopy (SEM) to compare the ratios.

2.3.3 Results

Below are the optical and SEM images of each pellet (Figure 22-26). The SEM image for the 5:1 ratio (Figure 26) shows large pockets of KBr present. Though it is unclear if this was due to the pellet preparation or an excess of KBr, this ratio was disregarded as ideal. Due to homogeneity and the concerns with excess KBr, a ratio of 3:1 KBr:UO_2 was chosen for each target irradiated at Flattop.
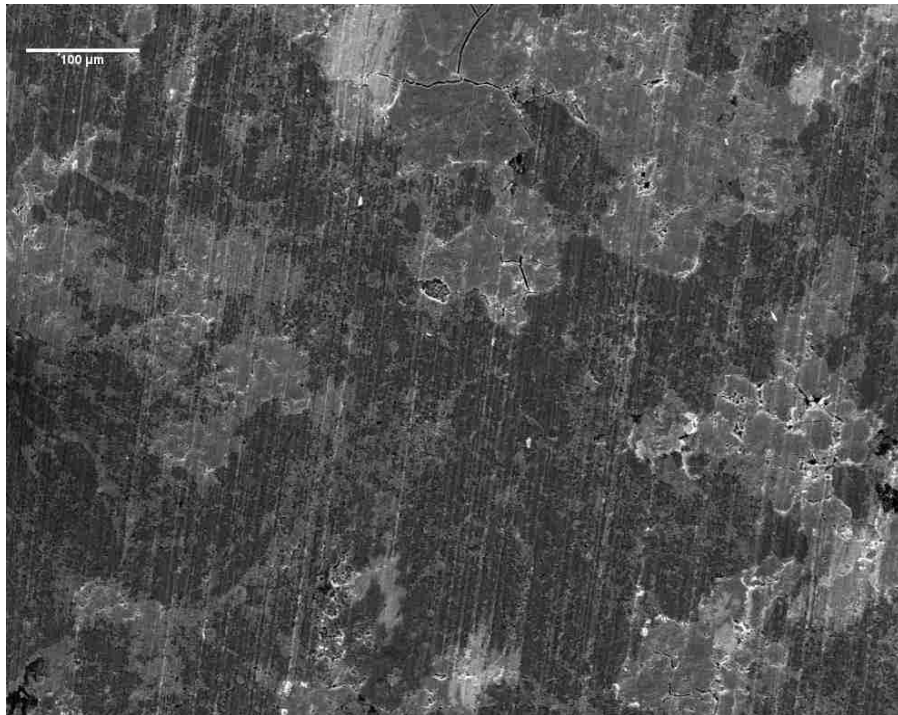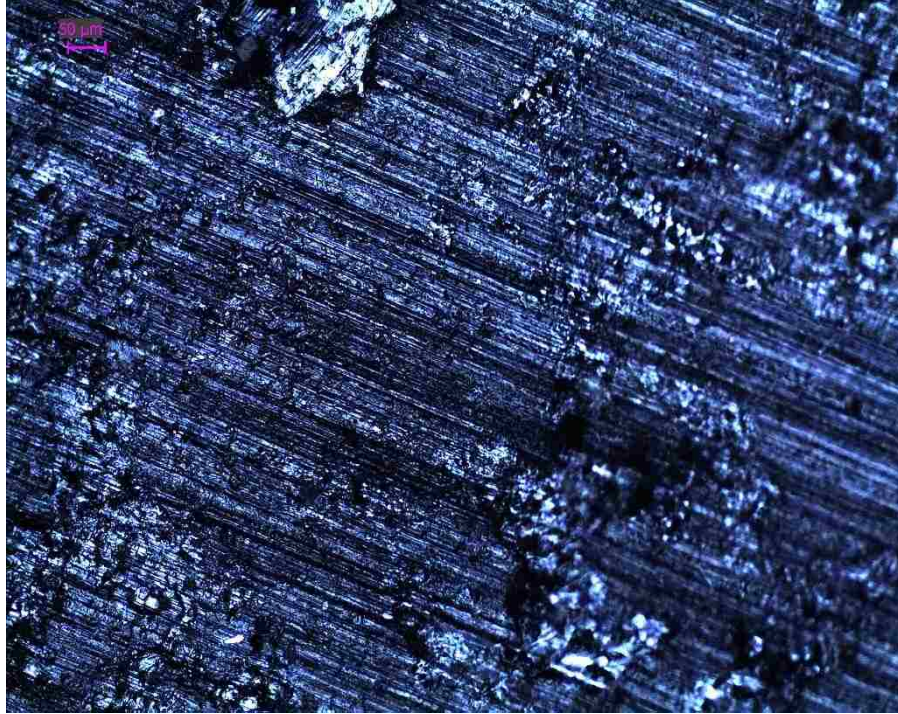
Figure 22. Optical image (top) and SEM image (bottom) of the 1:1 KBr:UO$_2$ pellet with scale bars. In the SEM image, a lighter color represents a more dense material (e.g. uranium).

Figure 23. Optical image (top) and SEM image (bottom) of the 2:1 KBr:UO$_2$ pellet with scale bars.
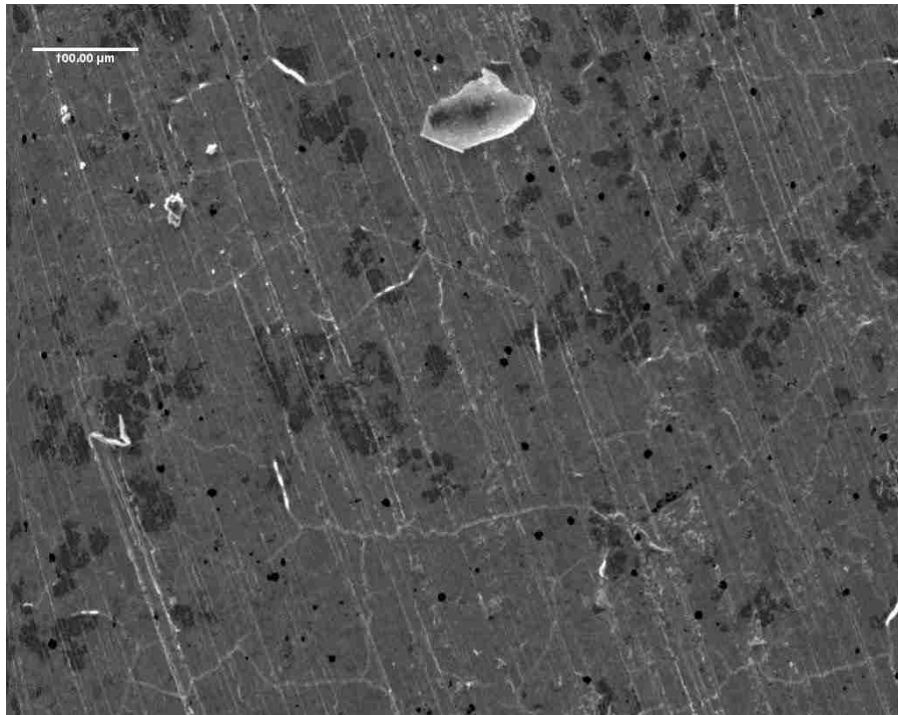
Figure 24. Optical image (top) and SEM image (bottom) of 3:1 KBr:UO$_2$ pellet with scale bars.
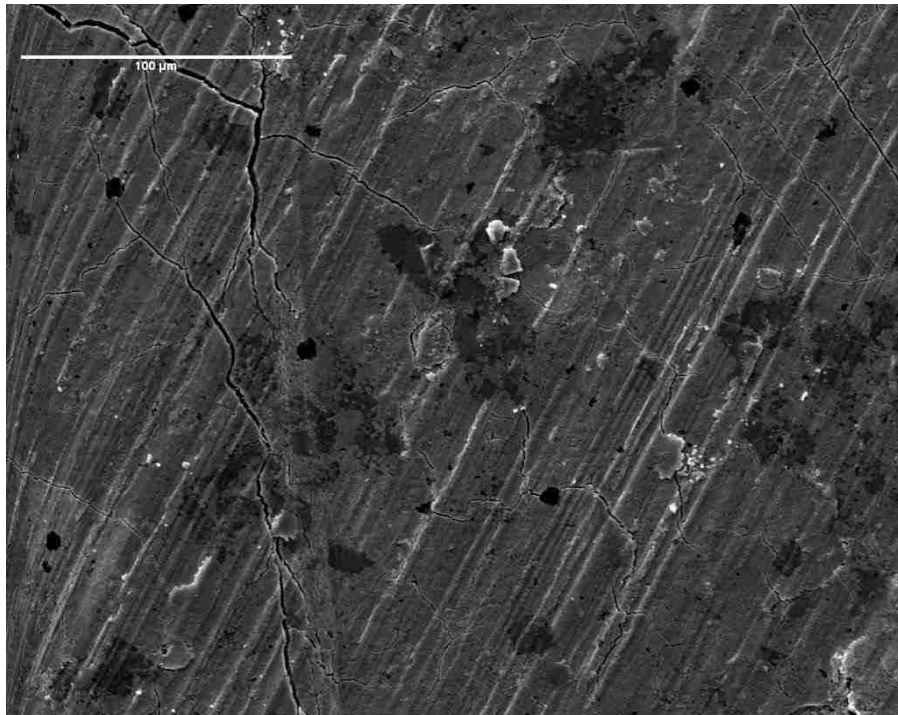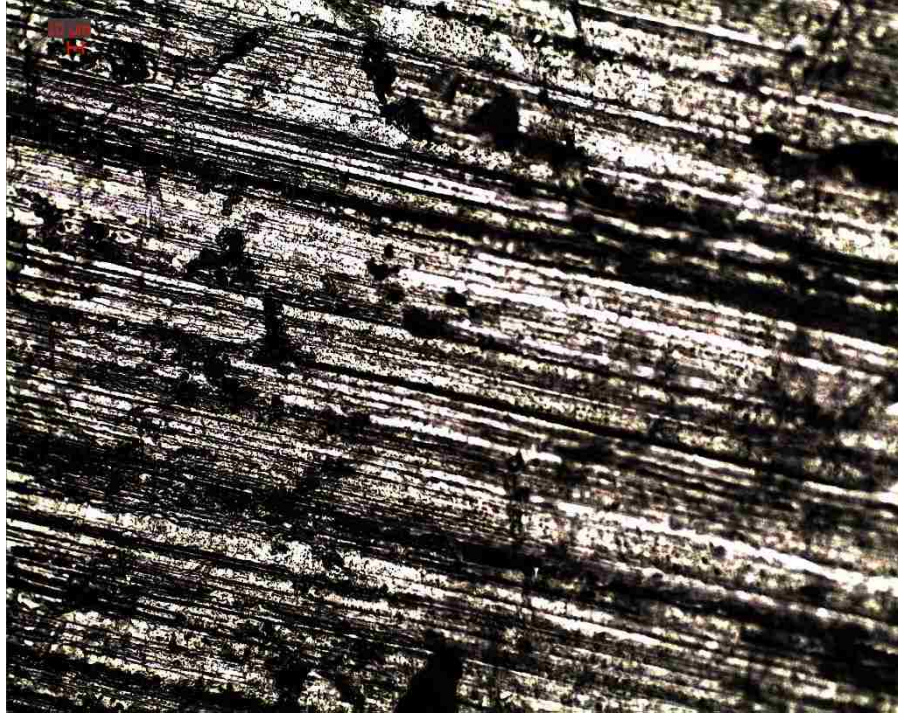
Figure 25. Optical image (top) and SEM image (bottom) of 4:1 KBr:UO$_2$ pellet with scale bars.
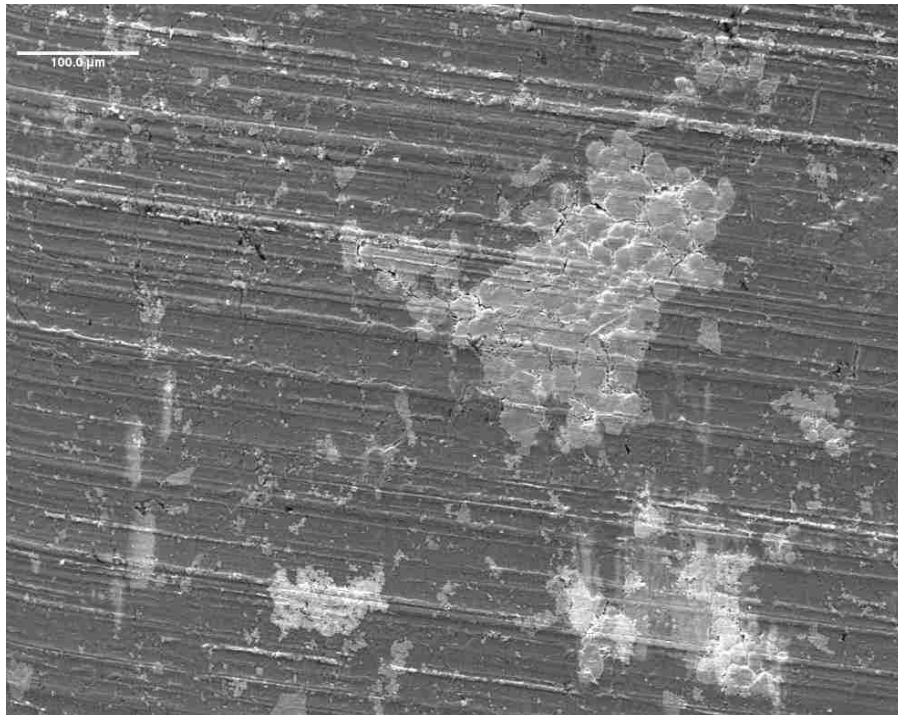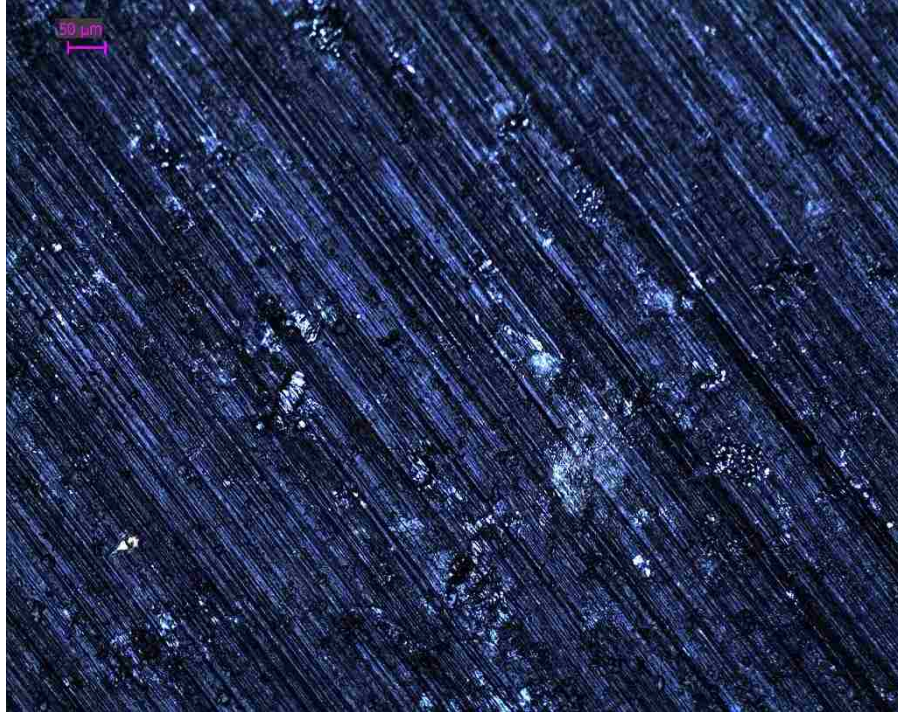
Figure 26. Optical image (top) and SEM image (bottom) of 5:1 KBr:UO$_2$ pellet with scale bars.

2.4 Target Creation and Fission Product Extraction

Unless otherwise noted, all targets were treated identically, and all target material used was depleted uranium. Table 1 lists the targets discussed in this chapter, as well as their composition, amount of UO_2, and the acid with which it was contacted to remove the fission products. With the exception of Target 1, all of the targets were created in the same manner. The description of the preparation of Target 1 can be found in Section 2.5.2. In total, there were eight targets, seven of which were irradiated using fast neutrons from Flattop. Target 7 did not contain KBr in order to determine whether the secondary matrix is necessary for extraction. A more detailed description of Target 8 can be found in Section 2.1.2.1.

The KBr (99% Sigma Aldrich) was used as a matrix to suspend the target and to facilitate the collection of fission products from the UO_2. It is possible that some fission products may become embedded in neighboring UO_2 particles, but the mild acid treatment used to dissolve the KBr post-irradiation should remove those products as well as fission products trapped in the KBr matrix. The KBr was dried in a furnace at 180 °C for several days prior to use to remove excess moisture. The UO_2 and KBr (unless otherwise noted) were vortexted together in a 20 mL scintillation vial until the mixture appeared homogenous. The target material was placed in a 6 mm KBr pellet die (Figure 27) and pressed into a pellet under 2 tons of pressure for ten minutes (Figure 28). The resulting pellet was wrapped in aluminum foil to prevent the spread of contamination and placed into aluminum sample holders (Figure 29).

Table 1. Description of all targets discussed in this chapter

Target	Composition (mass ratio)	UO$_2$ (mg)	Neutron Source	Extractant
1	UO$_2$:5KBr	227.9	DPF	0.01 M HCl
2	UO$_2$:3KBr	23.8	Flattop	0.01 M HCl
3	UO$_2$:3KBr	23.1	Flattop	0.01 M HCl
4	UO$_2$:3KBr	23.4	Flattop	0.1 M HNO$_3$
5	UO$_2$:3KBr	24.2	Flattop	0.1 M HCl
6	UO$_2$:3KBr	23.1	Flattop	0.01 M HNO$_3$
7	UO$_2$	21.3	Flattop	0.01 M HNO$_3$
8	UO$_2$ foam	31.7	Flattop	0.01 M HCl

Figure 27. KBr pellet die (6 mm)

Figure 28. Pellet press with die

Figure 29. Example of a target prepared to irradiation at Flattop (ruler is in cm).

Figure 30. Examples of sample holders labeled for an irradiation. The foil-wrapped targets at the bottom of the image were placed into their respective sample holders.

Each target (Figure 30) was irradiated and returned to UNLV within 36 hours. After removal from its sample holder, the target was placed in a 15 mL plastic centrifuge tube containing 5 mL of its respective acid extractant (Table 1). It was vortexed for 2 minutes to facilitate the dissolution of the KBr (where applicable), placed on a rocking table for 6 minutes, and then centrifuged at 1500 rpm for 2 minutes. The liquid and the solid were then separated and placed into individual 5 mL plastic scintillation vials. Each vial was counted on a closed-end coaxial Canberra HPGe gamma counter (relative efficiency of 60%) for 1 hour. The solid material was then returned to the 15 mL centrifuge tube and contacted with 5 mL of fresh acid. Aliquots (2 mL) were removed at 30 minutes, 60 minutes, and 13 hours, unless otherwise noted. Each aliquot was counted separately on an HPGe detector for 1 hour. Prior to each experiment, a calibration of the detector and a background measurement of the pure acid blank were done.

Extraction percentages were calculated according to Equation 2. The numerator is the total counts for a nuclide in all liquid samples (e.g. the original contact and all aliquots). This indicates how many counts were extracted from the solid over the course of the experiment. The denominator is the total counts in

the original two samples (e.g. the target). The error in extraction is calculated according to Equation 3. An example of these calculations is given in Scheme 1.

$$\% \, Extracted = \frac{total \; counts \; in \; all \; liquid \; samples}{total \; counts \; in \; original \; liquid + original \; solid \; samples} * 100$$

Equation 2. Calculating the extraction percentage of fission products

$$sqrt \left(\frac{(counts \; extracted)}{(counts \; extracted)^2} + \frac{(counts \; total)}{(counts \; total)^2} \right) = error$$

Equation 3. Calculation of error

$$\% \, Extracted = \frac{6869 \; counts}{9949 \; counts} * 100 = 69.04 \, \%$$

$$Error = sqrt \left(\frac{(6869)}{(6869)^2} + \frac{(9949)}{(9949)^2} \right) = 0.016$$

$$69.04\% * 0.016 = 1.08 \, \% \; error$$

Scheme 1. An example of calculations of percent extraction and error for ^{131}I.

Any targets that had KBr present showed peaks from the activation product ^{82}Br at several different energies in the gamma spectra. This can lead to problems with obscuring fission products by either appearing at similar energies, or obscuring small peaks. The solids and the original liquids for any target with KBr were recounted for 24 hours each after two weeks to allow for the decay of ^{82}Br. More than 99.8 % of the ^{82}Br, which has a half-life of 1.47 days,[38] had decayed to stable ^{82}Kr and was no longer visible in the spectrum. Table 2 lists the half-lives of isotopes present in the separation, as well as their respective daughters and daughter half-lives. Short lived, stable, and gamma stable daughters are not seen in the gamma spectrum. Those that are measured using gamma spectroscopy can be used to confirm the presence of their parent in the original spectra.

Table 2. Data for daughters of fission products.[38] vw = very weak

Fission Product	$T_{1/2}$	Daughter Product	$T_{1/2}$	Daughter Energy (keV)
^{143}Ce	1.38 d	^{143}Pr	13.57 d	vw
^{239}Np	2.36 d	^{239}Pu	2.41E4 y	vw
^{147}Nd	10.98 d	^{147}Pm	2.62 y	vw
$^{99m}Tc/^{99}Mo$	6 h/66 h	^{99}Tc	2.13E5 y	vw
^{141}Ce	32.5 d	^{141}Pr	stable	N/A
^{132}Te	3.2 d	$^{132}I --> ^{132}Xe$	1.3 h -> stable	N/A
^{135}Xe	9.14 h	^{135}Cs	2.3E6 y	no γ
^{97}Zr	16.75 h	$^{97}Nb --> ^{97}Mo$	1.23 h -> stable	N/A
^{93}Y	10 h	^{93}Zr	1.5E6 y	vw
^{135}I	6.6 h	$^{135}Xe --> ^{135}Cs$	9.14 h -> 2.3E6 y	no γ
^{149}Pm	53 h	^{149}Sm	stable	N/A
^{133}I	20.8 h	^{133}Xe	5.24 d	80.99
^{105}Rh	35 h	^{105}Pd	stable	N/A
^{151}Pm	28 h	^{151}Sm	90 y	vw
^{103}Ru	39 d	^{103}Rh	stable	N/A
^{140}Ba	12.7 d	^{140}La	1.68 d	1596.2, 487.0, 815.8, 328.8
^{95}Zr	64.02 d	^{95}Nb	34.99 d	765.8
^{91}Sr	9.5 h	^{91}Y	58.5 d	vw
^{82}Br	1.47 d	^{82}Kr	stable	N/A

2.5 UO$_2$ Irradiation

Each irradiation on Flattop was carried out during a previously scheduled run by colleagues at Los Alamos National Laboratory, Lawrence Livermore National Laboratory, or Pacific Northwest National Laboratory, who graciously allowed additional samples to be added to their experiments. Due to the non-central location of the samples, exact data regarding the fluence (flux per unit time) and positioning of the samples within the core were not available. To negate the differences in these variables between irradiations, the experiments described below use percent extraction from the solid material as a means to describe the effectiveness of a separation (Equation 2).

2.5.2 Dense Plasma Focus

2.5.2.1 Experimental

Only Target 1 was sent to the Dense Plasma Focus (DPF) at the NSTec North Las Vegas site. For the creation of the UO_2 neutron irradiation target, KBr was mixed with microparticulate UO_2 powder in a 5:1 KBr:UO_2 weight ratio (891.9 mg KBr : 227.9 mg UO_2 total) and two pellets were pressed with this mixture. This ratio of KBr to UO_2 was chosen in order to increase the amount of material contained within the target without adding more UO_2. The two pellets were sealed in a glass ampoule using a flame, creating a sealed target for the samples of approximately 2.3 cm in length (Figure 31).
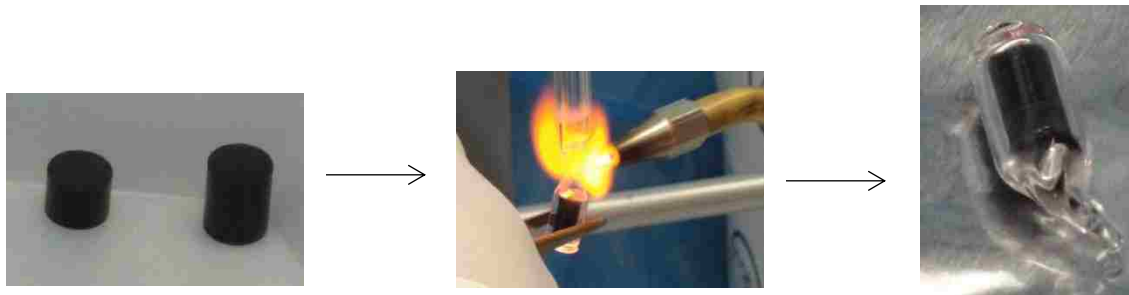
Figure 31. A series of images showing the creation of the UO2/KBr target

The target was irradiated for three days with a total fluence of 10^{13} neutrons. Once the irradiated target was returned, the glass tube was broken and both pellets were removed. The separation was performed as described in Section 2.4, although aliquots were removed at 5, 10, and 15 minutes. The gamma activity of the UO_2 microparticles, the acid solution, and each aliquot were obtained by counting the samples for three days using an HPGe detector (relative efficiency of 60%.

2.5.2.2 Results

Based on the gamma data from this experiment, the fluence and/or energy of the neutrons were not high enough to induce many fission events. There are, however, many signatures stemming from ^{82}Br in the solution spectrum due to the neutron activation of the KBr. In addition, ^{40}K is evident from the neutron activation of the glass ampoule, as well as the KBr.
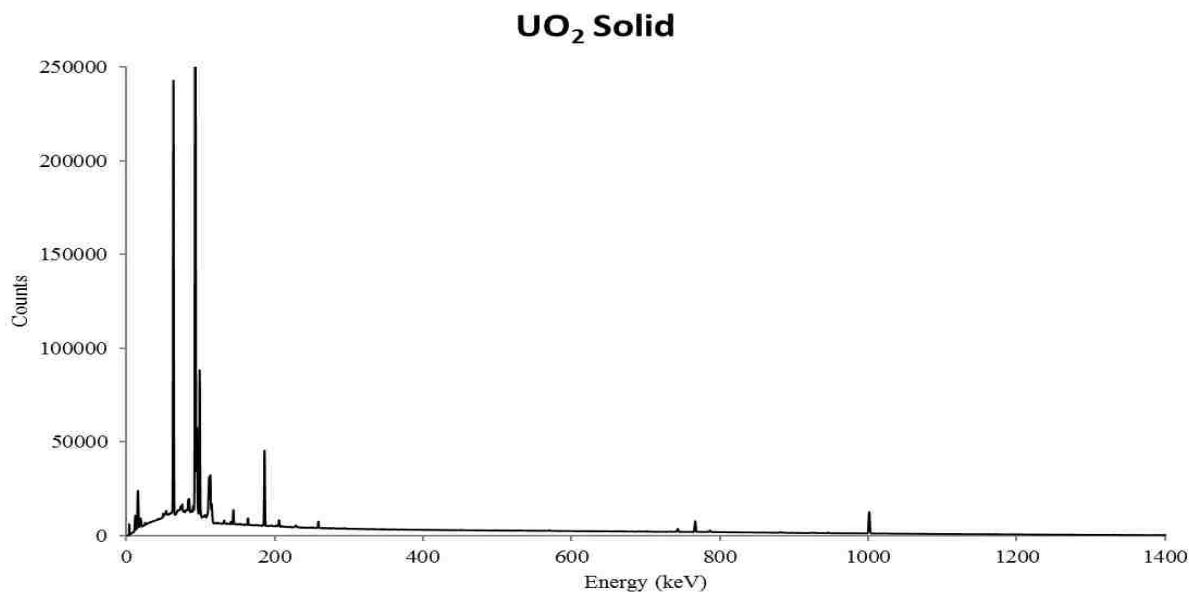
Figure 32. Gamma spectrum of UO2 solid target from DPF irradiation

The spectrum in Figure 32 shows the data from the UO_2 solid after it had been contacted with 0.01 M HCl. Very few lines are seen in the spectrum, indicating a lack of fission products. A small amount of [82]Br and [40]K are present. The high counts in the lower energy region are likely due to X-rays, as the detector was not shielded from external X-rays.

The data for the 0.01 M HCl solution post-separation (Figure 33) mainly shows [82]Br, but almost no fission products. Table 3 lists the gamma ray energies and their intensities for [82]Br; these energies match with the major peaks present in Figure 33. Because the results show a lack of fission events, and therefore a negligible separation of fission products, future samples were not irradiated at the DPF. It was determined that either higher energy neutrons or a higher fluence of neutrons would be necessary to get better results. The remainder of the irradiation experiments were therefore carried out using the criticality device "Flattop".
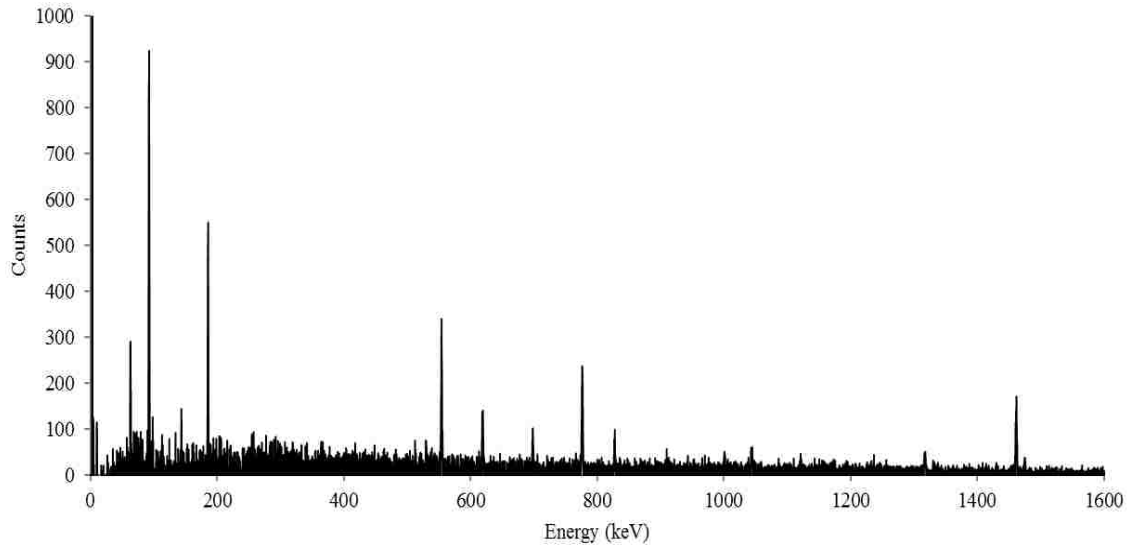
Figure 33. Gamma spectrum of 0.01 M HCl solution after contact with the target for 10 minutes.

Table 3. Gamma energies from [82]Br and their intensities.[74]

Energy (keV)	Intensity (%)
221.48	2.26
554.35	71.1
619.11	43.5
698.37	28.3
776.52	83.4
827.83	24.0
1044.00	28.3
1317.47	26.8
1474.88	16.6

2.5.3   Flattop

The remainder of the targets were irradiated using Flattop at the National Criticality Experiments Research Center (NCERC) at the Nevada National Security Site (NNSS). Flattop is a criticality device (see Chapter 1, Section 1.6.2) that produces high-energy neutrons with a constant fluence. The majority of the targets described below were irradiated during different experiments.

2.5.3.1   Target 2

The target was prepared as described in Table 1, with 23.8 mg of dUO_2 and a 3:1 ratio of KBr to UO_2. The separation was done with 0.01 M HCl and proceeded as described in Section 2.4, with aliquots removed at 10, 15, 30, and 60 minutes. This irradiation produced significantly more fission and activation products than the irradiation using the DPF (Figure 34). There was also a large amount of ^{82}Br present from neutron activation of KBr (not shown). The isotopes ^{147}Nd, ^{149}Pm, and ^{105}Rh were all extracted with yields greater than 50% in this experiment. The data for these isotopes and select others are shown in Table 4. The isotopes presented in Table 4 were chosen because of their presence in all of the targets studied, with the exception of ^{99}Mo. Some of the isotopes are also of interest to the medical field (i.e. ^{131}I) or because of their inclusion in the epsilon phase of irradiated material (i.e. ^{105}Rh).[38] The target was only contacted with extractant for 1 h; perhaps a longer contact time will lead to a better yield of fission products extracted.

Table 4. Select fission products and their percent extraction from Target 2 in 60 minutes.

Nuclide	Energy (keV)	Percent Extraction
^{143}Ce	293.8	25.87 ± 0.59
^{239}Np	104	26.75 ± 0.18
^{147}Nd	91.04	52.69 ± 1.00
^{99}Mo	181	0.00 ± 0.00
^{93}Y	267.22	0.00 ± 0.00
^{149}Pm	285.7	65.86 ± 1.70
^{105}Rh	319.57	92.01 ± 1.86
^{131}I	364.63	30.64 ± 0.85
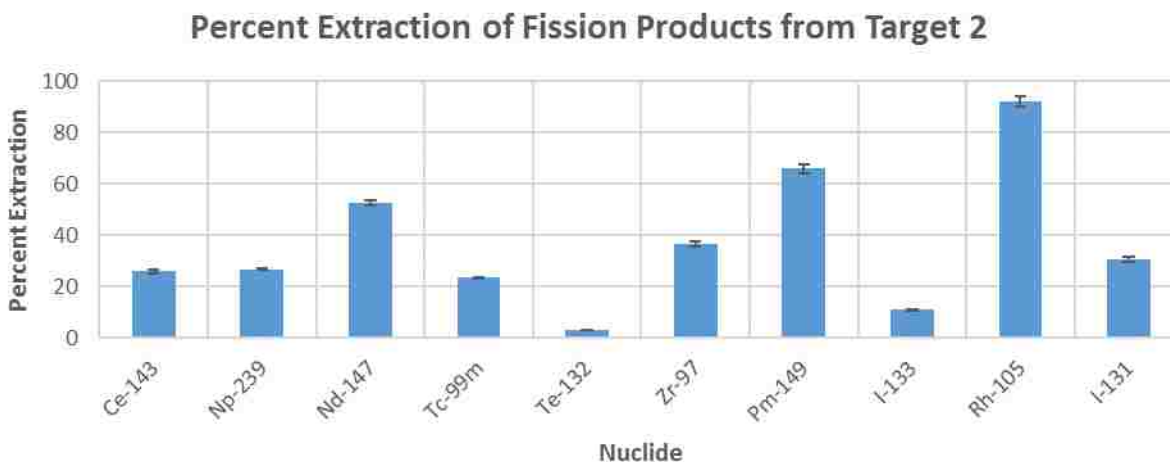
Figure 34. Bar chart describing the percent extraction of certain fission products from the target using 0.01 M HCl over 1 hour. Error bars are present, but may be too small to see in some cases.

2.5.3.2   Target 3

Target 3 contained 23.1 mg of dUO_2 and 71.9 mg of KBr and was stored in an inert atmosphere dry box between preparation and shipment. The irradiation and separation were completed as detailed above using 0.01 M HCl. Figure 35 shows a graphical representation of the fission products extracted from the target. Error was calculate according to Equation 3 (page 48). The 0.01 M HCl was reasonably effective at removing several fission products, including ^{93}Y and ^{131}I (Table 5). The particular isotopes listed in Table 5 are the same as in Table 4; however, they were extracted over 13 hours. Also listed in Table 5 are the major gamma decay branching energy for each isotope, the raw counts in the target material prior to extraction, as well as the raw counts extracted into the liquid phase. Some fission products, such as ^{99}Mo were not extracted at all. There are a number of counts due to ^{99}Mo present in the solid material, but not in the 0.01 M HCl extractant. This was the only acid that did not extract ^{99}Mo, perhaps because it wasn't concentrated enough.

Table 5. Percent extraction data for specific isotopes from Target 3 using 0.01 M HCl over 13 hours.

Nuclide	Energy (keV)	Raw Counts from Target	Raw Counts Extracted	Percent Extraction
^{143}Ce	293.8	16763	9752	53.58 ± 0.74
^{239}Np	106.27	103449	13365	12.92 ± 0.12
^{147}Nd	91.04	15303	8317	54.25 ± 0.74
^{99}Mo	181	4488	0	0.00 ± 0.00
^{93}Y	267.22	8260	6655	77.20 ± 1.26
^{149}Pm	285.7	3184	189	5.94 ± 0.44
^{105}Rh	319.57	10443	6993	66.96 ± 1.03
^{131}I	364.63	9474	6988	73.76 ± 1.16
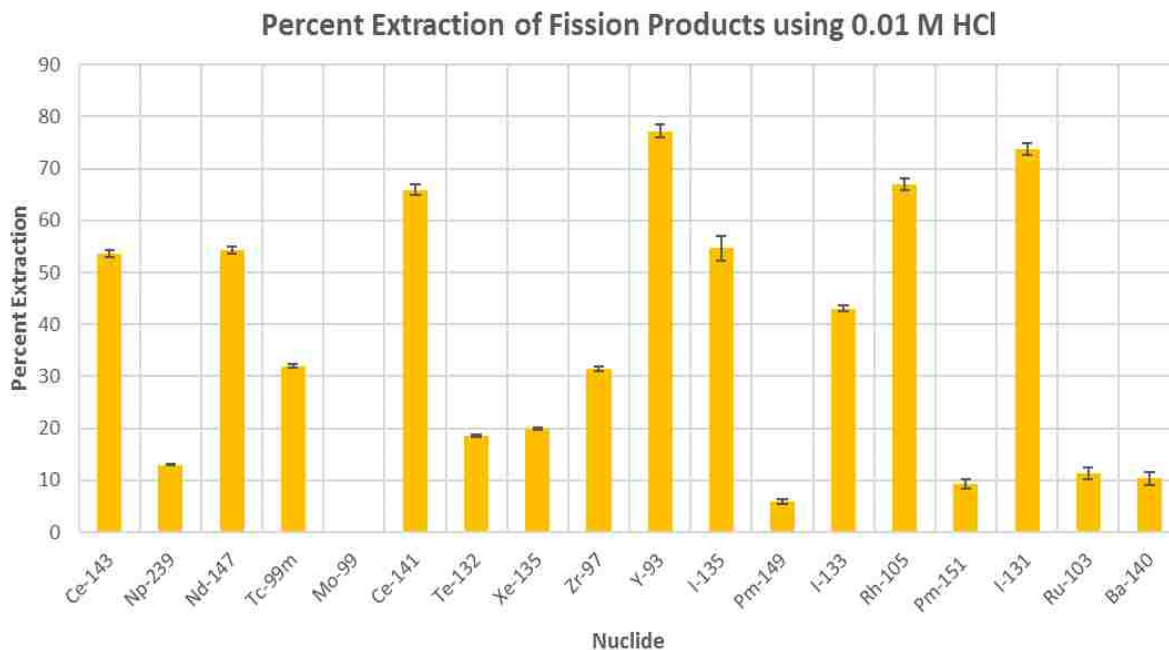
Figure 35. Bar chart describing the percent extraction of certain fission products from Target 3 using 0.01 M HCl. Error bars are present, but may not be visible on all data.

2.5.3.3   Target 4

Target 4 was prepared similarly to the previous targets using 23.4 mg UO_2 and 72.3 mg KBr, and contacted

with 0.1 M HNO_3 after irradiation. After a period of 13 hours in contact with 0.1 M HNO_3, most of the

remaining solid material had completely dissolved. Any results were therefore artificially high (Figure 36).

Several isotopes, including ^{143}Ce, were extracted with high yields (Table 6), which is unsurprising given

that the target material entirely dissolved. Table 6 lists the raw counts in the original target material for

each isotope, along with the raw counts that were extracted from the target. The energies for each nuclide

can be found in Table 5.

Table 6. Percent extraction of certain fission products from Target 4 using 0.1 M HNO$_3$ over 13 hours.

Nuclide	Raw Counts from Target	Raw Counts Extracted	Percent Extraction
^{143}Ce	9646	7392	76.63 ± 1.18
^{239}Np	63586	16976	26.70 ± 0.23
^{147}Nd	12664	7702	60.82 ± 0.88
^{99}Mo	7259	5457	75.18 ± 1.35
^{93}Y	5766	4936	85.61 ± 1.66
^{149}Pm	1326	151	11.39 ± 0.98
^{105}Rh	6470	5328	82.35 ± 1.52
^{131}I	6206	5438	87.62 ± 1.63
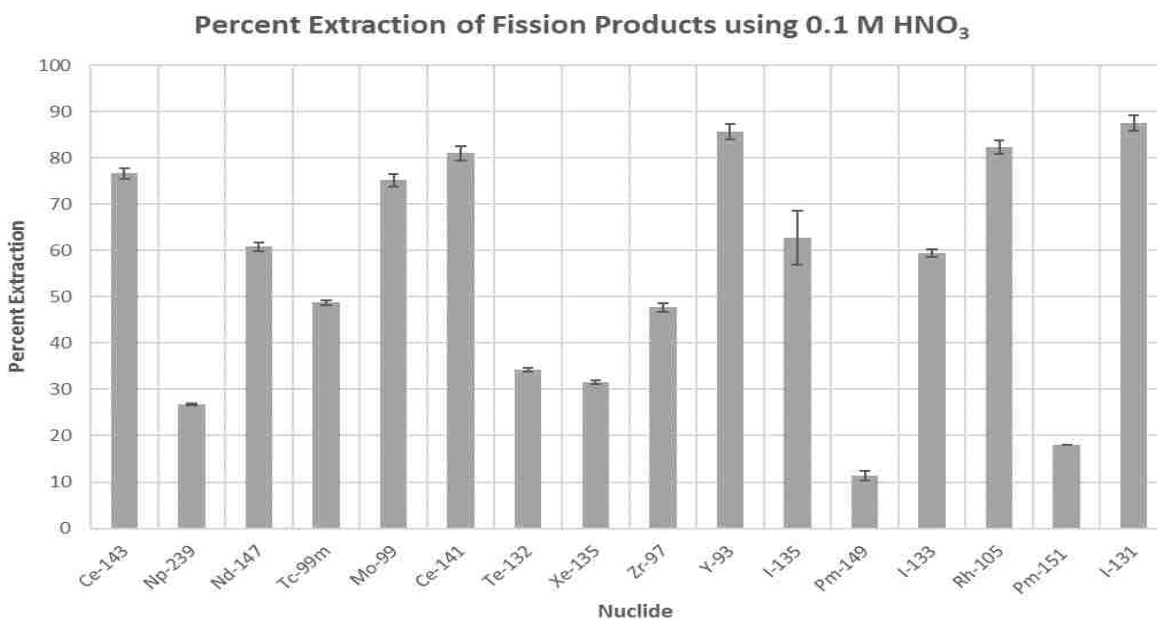
Figure 36. Bar chart describing the percent extraction of fission products from Target 4. Error bars are present, but may be too small to see.

2.5.3.4   Target 5

Target 5 was a UO_2:3KBr target composed of 24.2 mg UO_2 and 72.8 mg KBr. It was stored in an inert atmosphere dry box for three months prior to usage. Target 5 remained intact throughout the irradiation and transport. It was treated identically to previous targets using 0.1 M HCl as the extractant.

Table 7 lists some of the fission products extracted using 0.1 M HCl, their raw counts present in the target material, their raw counts extracted, and the percent extraction from the target material. The more concentrated HCl extracted ^{99}Mo better than the 0.01 M concentration, though the yield is still not good. High amounts of ^{131}I and ^{105}Rh were also extracted, but the yield of ^{93}Y decreased significantly compared to previous targets. Figure 37 depicts the percent extraction of certain fission products from Target 5.

Table 7. Extraction percentages of certain fission products from Target 5 using 0.1 M HCl over 13 hours.

Nuclide	Raw Counts from Target	Raw Counts Extracted	Percent Extraction
^{143}Ce	22714	10974	48.31 ± 0.56
^{239}Np	202180	25583	12.65 ± 0.08
^{147}Nd	27572	11431	41.46 ± 0.46
^{99}Mo	6220	141	2.27 ± 0.19
^{93}Y	2765	196	7.09 ± 0.52
^{149}Pm	4558	330	7.24 ± 0.41
^{105}Rh	12368	7105	57.45 ± 0.86
^{131}I	11723	7996	68.21 ± 0.99

Only ^{105}Rh and ^{131}I were extracted with greater than 50% yield using 0.1 M HCl. More than 40% of the isotopes ^{143}Ce and ^{147}Nd were extracted, and all other fission products were extracted with less than 40% yields (Table 7). This shows that 0.1 M HCl is not the acid concentration to use to extract the highest percentage of fission products. However, many types of fission products were present in the extractant, including fission products of interest to the medical community, such as ^{99}Mo, ^{99m}Tc, and ^{131}I.
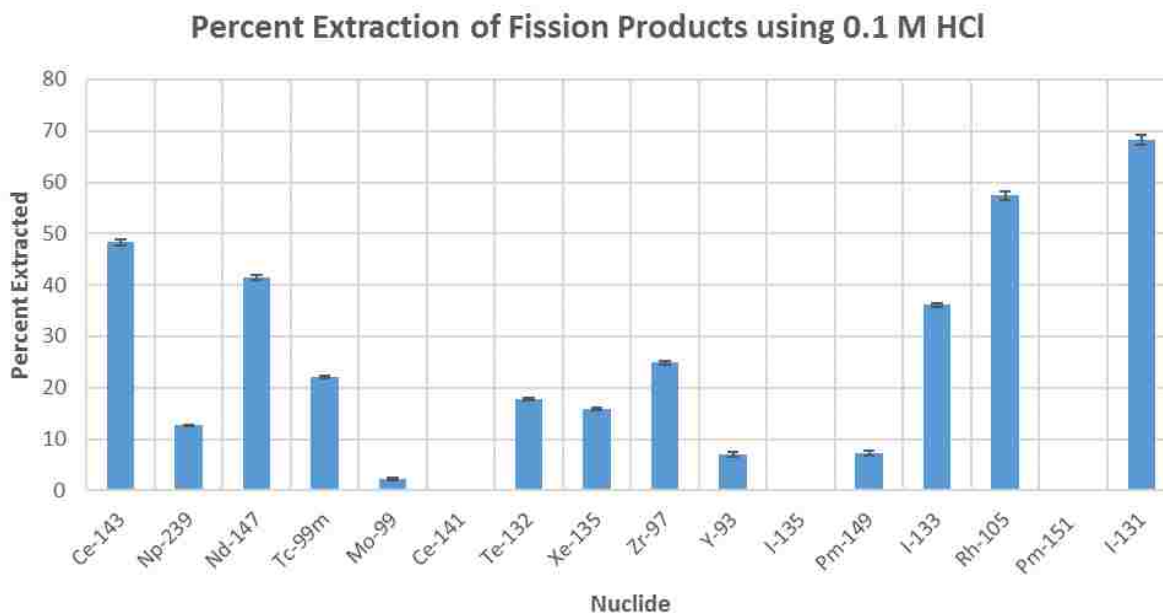
Figure 37. Bar chart describing the percent extraction of certain fission products from Target 5. Error bars are present, but may be too small to see.

2.5.3.5   Target 6

Target 6 was prepared similarly, but it was composed of 23.1 mg UO_2 and 73.6 mg of KBr. It was broken into several large pieces when the sample holder was opened after the irradiation. The target did not dissolve in this case, but did have higher yields of extraction than either target contacted with HCl (Table 8). Table 8 lists the raw counts from the target material as well as the raw counts extracted using 0.01 M HNO_3. Figure 38 shows the extraction percentage of fission products using 0.01 M HNO_3 as the extractant. This acid was also the one to remove the most ^{99}Mo – an important fission product in medical imaging. Because of its ability to remove ^{99}Mo, and the fact that it did not dissolve the target material, 0.01 M HNO_3 was chosen as the extractant to use for future target separations.

58

Table 8. Extraction of certain fission products from Target 6 using 0.01 M HNO_3 over 13 hours.

Nuclide	Raw Counts from Target	Raw Counts Extracted	Percent Extraction
^{143}Ce	16132	7952	49.29 ± 0.68
^{239}Np	96242	15238	15.83 ± 0.14
^{147}Nd	14977	8425	56.25 ± 0.77
^{99}Mo	5224	569	10.89 ± 0.48
^{93}Y	3161	196	6.20 ± 0.46
^{149}Pm	4061	1053	25.93 ± 0.90
^{105}Rh	9958	5837	58.62 ± 0.97
^{131}I	9949	6869	69.04 ± 1.08
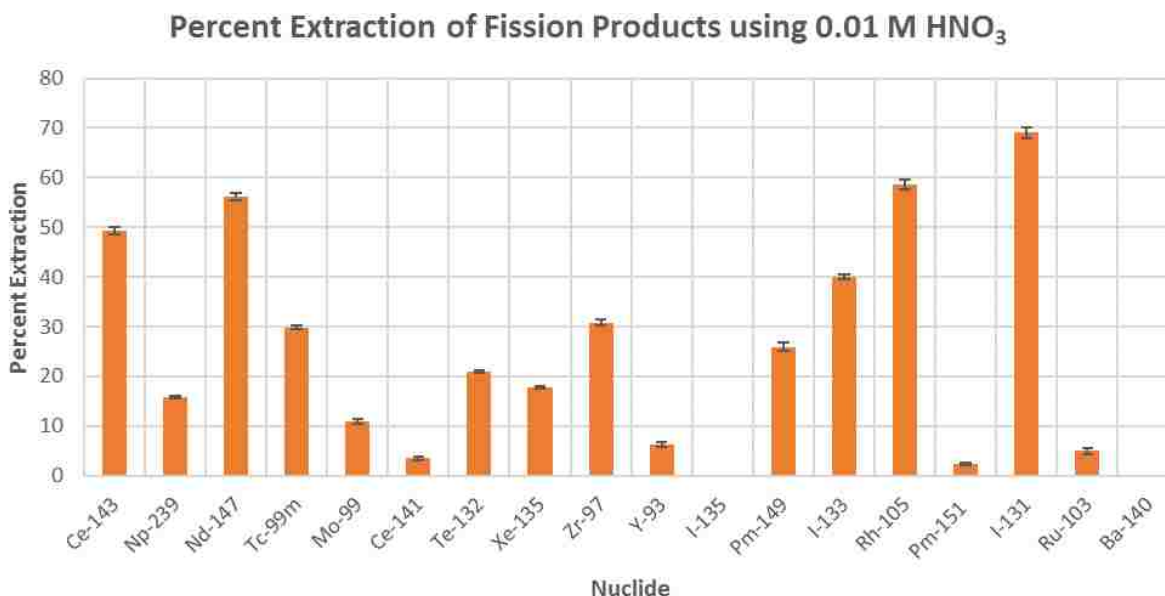
Figure 38. Bar chart describing the fission products extracted from Target 6. Error bars are present in the figure.

2.5.3.6　　　Target 7

Target 7 was comprised of only UO_2 (21.3 mg) without the KBr in order to ascertain the necessity for a matrix in these separations. The target was prepared, irradiated, and analyzed via the standard route described using 0.01 M HNO_3.

A BEGe detector (Figure 39) was set up for use, and the samples were measured 10 days after the irradiation. The samples were counted for 3 hours, but otherwise were treated identically to the

experiments previously described. The data for the UO$_2$ target (Figure 40) shows that an absence of some form of secondary matrix decreases the extraction potential of the target. In some cases, the fission products could not be extracted as well from this UO$_2$ target compared to its matrix-containing counterpart. Table 9 describes certain fission products and their extraction yields from Target 7, including their raw count extractions from the target material. These data show clearly that fission products are extracted in much smaller yields when no secondary matrix is present.

Figure 39. BEGe detector
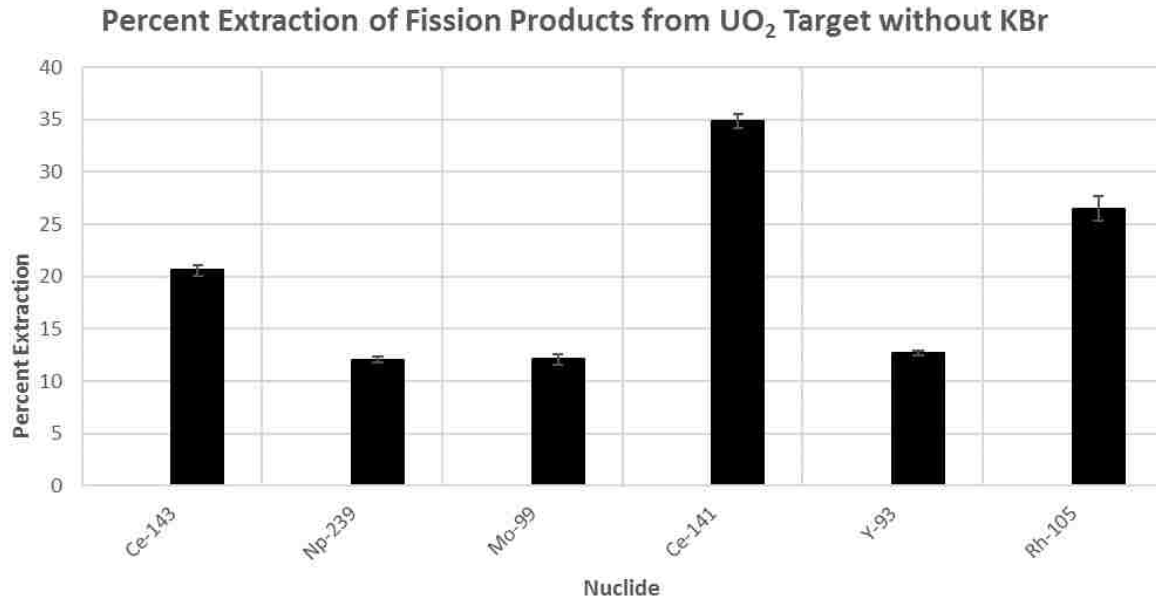
Figure 40. Bar chart describing the percent extraction of fission products from Target 7 - the UO_2 target that did not have any KBr matrix. Error bars are present, but may be too small to see.

Table 9. Extraction of certain fission products from Target 7 using 0.01 M HNO_3 over 13 hours.

Nuclide	Raw Counts from Target	Raw Counts Extracted	Percent Extraction
^{143}Ce	0	0	0.00 ± 0.00
^{239}Np	17442	2102	12.05 ± 0.28
^{147}Nd	0	0	0.00 ± 0.00
^{99}Mo	611	74	12.11 ± 1.49
^{93}Y	3634	460	12.65 ± 0.21
^{149}Pm	0	0	0.00 ± 0.00
^{105}Rh	528	140	26.52 ± 2.52
^{131}I	176	0	0.00 ± 0.00

61

2.5.3.7 Comparison of Targets 3-7

Target 3-7 can be compared because they were contacted with their respective acids for 13 hours, with aliquots extracted at the same times during the experiments. All of the samples were counted in 5 mL clear plastic scintillation vials, placed approximately the same distance away from the detector, so they have similar geometries.

Table 10 lists the raw counts and the percent extractions of certain nuclides for Targets 3-7. There are nuclides that were only extracted with the HNO_3, such as ^{141}Ce, ^{151}Pm, and ^{103}Ru, and others, such as ^{140}Ba that were only extracted with HCl. This indicates that different extractants could be used depending on the fission products of interest. Figure 41 is a graph showing the extraction percentages for certain isotopes based on the extractant (e.g. concentration and type of acid) compared to the target with no KBr matrix material (black bars). These data clearly show that the hypothesis was correct: the presence of a matrix material increases the percentage, and number, of isotopes extracted into solution. In most cases, it is obvious that HNO_3, though more dilute, is a better extractant than HCl. This is not surprising, as the ICP-MS results discussed earlier in this chapter show that HNO_3 is slightly better than HCl at dissolving the UO_2 particles over time. A slight dissolution of the particles, perhaps only of the outermost layers, could easily result in a better extraction of fission products. It is entirely possible that the fission products escaped from one particle and embedded themselves in another, rather than in the KBr. For future targets, 0.01 M HNO_3 was used as the extractant due to its ability to extract a general range of fission products in good yields without dissolving the target material.

Table 10. Comparison of raw counts extracted and percent extraction yield of targets 3-7.

Nuclide	0.01 M HCl Counts	0.01 M HCl % Extd.	0.1 M HNO₃ Counts	0.1 M HNO₃ % Extd.	0.1 M HCl Counts	0.1 M HCl % Extd.	0.01 M HNO₃ Counts	0.01 M HNO₃ % Extd.	No KBr Counts	No KBr % Extd.
^{143}Ce	9752	53.58 ± 0.74	7392	76.63 ± 1.18	10974	48.31 ± 0.56	7952	49.29 ± 0.68	0	0.00 ± 0.00
^{239}Np	13365	12.92 ± 0.12	16976	26.70 ± 0.23	25583	12.65 ± 0.08	15238	15.83 ± 0.14	2102	12.05 ± 0.28
^{147}Nd	8317	54.25 ± 0.74	7702	60.82 ± 0.88	11431	41.46 ± 0.46	8425	56.83 ± 0.77	0	0.00 ± 0.00
^{99}Mo	0	0.00 ± 0.00	5457	75.18 ± 1.35	141	2.27 ± 0.19	569	10.89 ± 0.48	74	12.11 ± 1.49
^{93}Y	6655	77.20 ± 1.26	4936	85.61 ± 1.66	196	7.09 ± 0.52	196	6.20 ± 0.46	460	12.66 ± 0.63
^{143}Pm	189	5.94 ± 0.44	151	11.39 ± 0.98	330	7.24 ± 0.41	1053	25.93 ± 0.90	0	0.00 ± 0.00
^{105}Rh	6993	66.96 ± 1.03	5328	82.35 ± 1.52	7105	57.45 ± 0.86	5837	58.62 ± 0.97	140	26.52 ± 2.52
^{131}I	6988	73.76 ± 1.16	5438	87.62 ± 1.63	7996	68.21 ± 0.99	6869	69.04 ± 1.08	0	0.00 ± 0.00
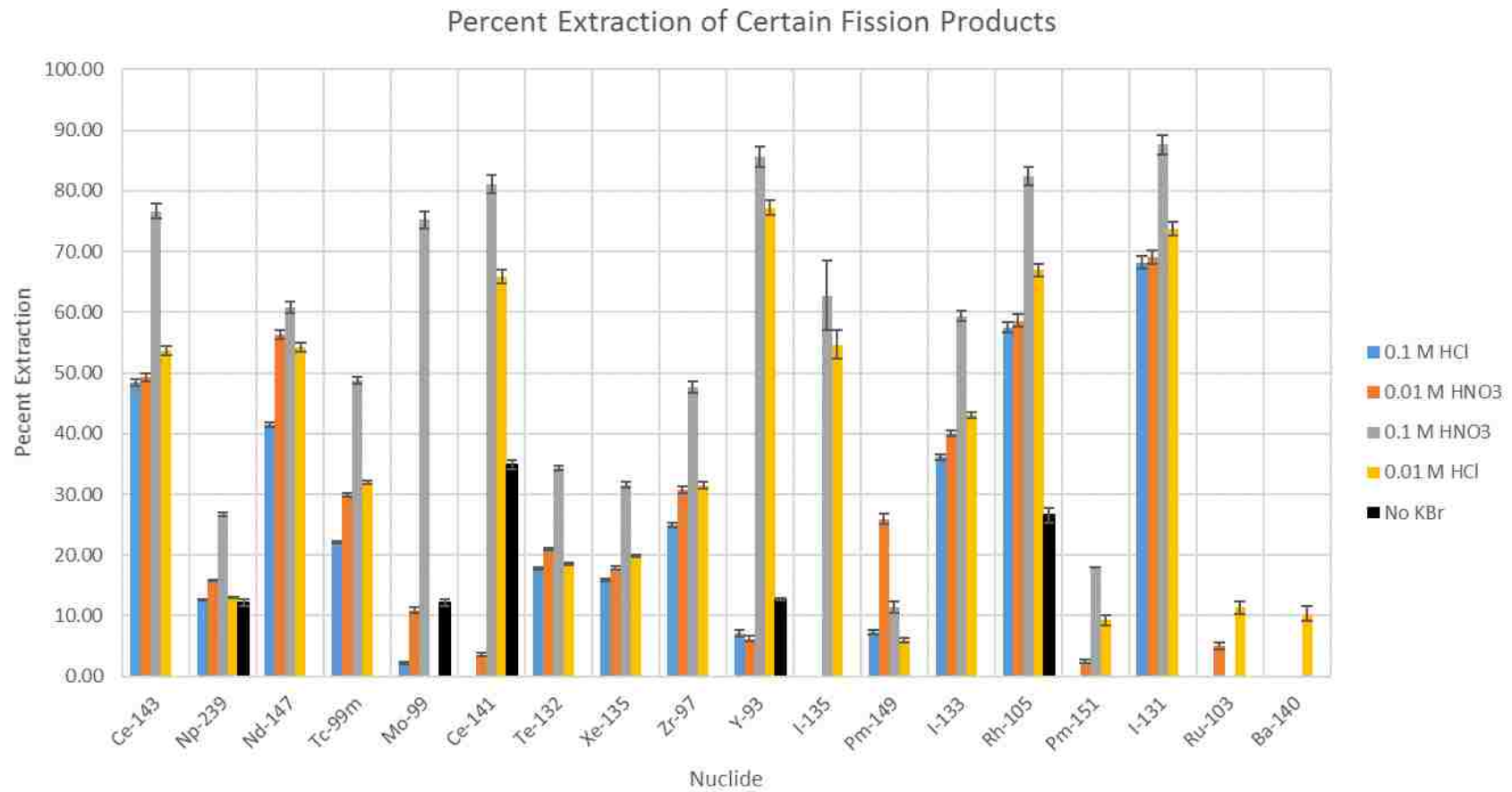
Figure 41. Graph comparing the four different acid extractants and the UO₂ pellet without a matrix (black bars). The bottom axis shows both the isotope and its respective gamma energies. Error bars are present, but may not be visible on all columns.

2.5.3.8   Target 8

Target 8 was comprised of a microporous UO_2 "foam" sent from colleagues at LANL. It was synthesized by laser-induced reduction of the high-nitrogen uranyl complex UO_2(BTA) (BTA = bistetrazoleamine). The material was sent to UNLV in sealed ampoules and stored in an inert atmosphere dry box until the preparation of the target began. No KBr was used in this target as the foam was porous and could have been able to trap the fission products in the pores. The final pellet weight was 31.7 mg. Though microscope analysis of the pellet did not show pores on the surface, it was assumed that the foam retained its porosity. The pellet was wrapped in premium aluminum foil to prevent the spread of contamination should the pellet break upon opening, and then placed in an aluminum sample holder like those described above.

The target itself was broken into several large pieces post-irradiation; whether it was destroyed due to irradiation damage, transport damage, or damage when the sample holder was opened is unclear. All of the pieces were transferred to a 15 mL plastic centrifuge tube with 5 mL of 0.01 M HCl and the separation was completed as normal. Each gamma spectrum was background corrected and analyzed for fission products. The extraction results from the UO_2 foam sample were less than 8% for most of the fission products (Figure 42). This lack of extraction could be due to a structural change in the foam when it was pressed into a pellet, or the pores could have been too small to allow for the release of fission products. The percent extraction of specific nuclides, as seen for previous targets, along with the raw counts found in both the target material and the extractants, are shown in Table 11. Nuclides such as ^{99}Mo and ^{149}Pm are not seen at all in the extractant, and the extraction of ^{239}Np is negligible. Clearly, the nanoporous foam material is not a good example of a target material in terms of extraction of fission products.

Table 11. Extraction of certain fission products from Target 8.

Nuclide	Energy (keV)	Raw Counts from Target	Raw Counts Extracted	Percent Extraction
^{143}Ce	293.8	37978	3618	9.53 ± 0.17
^{239}Np	106.27	234120	2003	0.86 ± 0.02
^{147}Nd	91.04	22378	850	3.80 ± 0.13
^{99}Mo	181	0	0	0.00 ± 0.00
^{93}Y	267.22	10996	699	6.36 ± 0.25
^{149}Pm	285.7	0	0	0.00 ± 0.00
^{105}Rh	319.57	17741	856	4.82 ± 0.17
^{131}I	364.63	13635	1043	6.43 ± 0.22
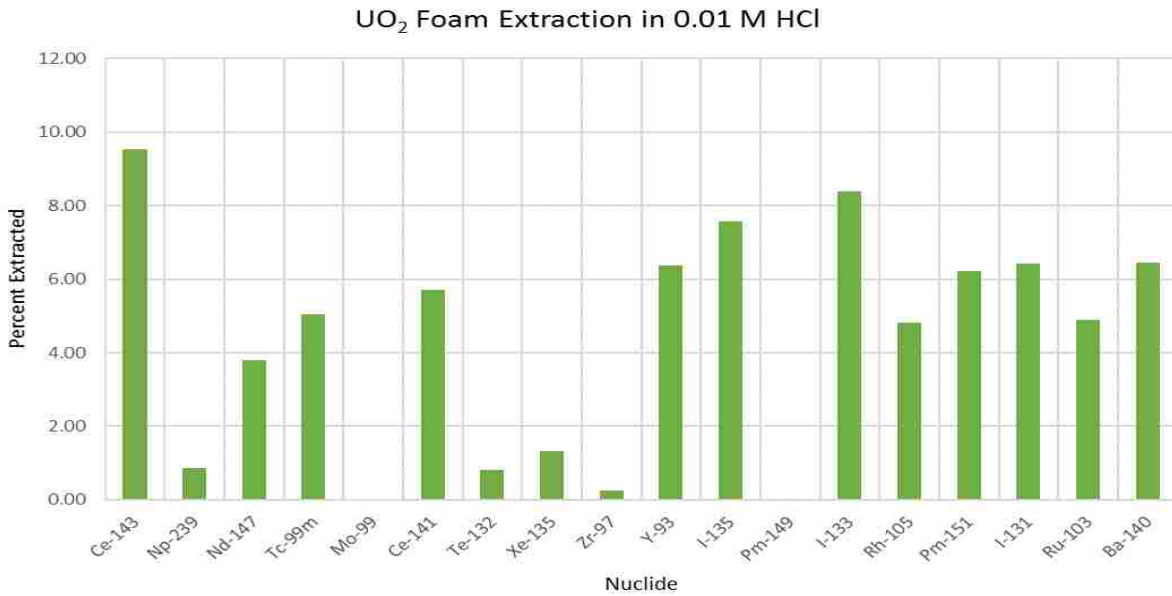
Figure 42. Extraction percentages of the dUO$_2$ foam sample. Error bars are present, but may be too small to be visible on some bars.

The poor extraction potential of the nanoporous foam target could also be due to a lack of secondary matrix. Because there was no matrix, such as KBr, onto which the fission products could embed, they may have travelled too deep within the UO$_2$ to be removed by the dilute HCl. The nanoporous foam UO$_2$ sample can be compared to the UO$_2$ microparticle target without KBr present (Target 7). Though the extractant used differed between the two samples, the differences in extraction capability between 0.01 M HCl and

0.01 M HNO_3 is not drastic. Table 12 describes the comparison between the extraction of certain fission products from Target 7 (0.01 M HNO_3) and Target 8 (0.01 M HCl). While the results show that more products were extracted from Target 8, the yields were much lower than for Target 7, the UO_2 target without KBr present, particularly in the case of ^{105}Rh.

Table 12. Comparison of the extraction of certain fission products from Target 7 and Target 8

Nuclide	Target 7 Results	Target 8 Results
^{143}Ce	0.00 ± 0.00	9.53 ± 0.17
^{239}Np	12.05 ± 0.28	0.86 ± 0.02
^{147}Nd	0.00 ± 0.00	3.80 ± 0.13
^{99}Mo	12.11 ± 1.49	0.00 ± 0.00
^{93}Y	12.65 ± 0.21	6.36 ± 0.25
^{149}Pm	0.00 ± 0.00	0.00 ± 0.00
^{105}Rh	26.52 ± 2.52	4.82 ± 0.17
^{131}I	0.0 0.00	6.43 ± 0.22

2.6   Conclusions

The data presented in this chapter show that the use of a secondary matrix, such as KBr, can increase the amount and yield of fission products extracted from the target. In most cases, the UO_2 was not dissolved during the course of the experiment, and so it can be concluded that it is possible to extract a reasonable percentage of fission products using this rapid method. Though the method needs to be optimized, it does show a proof-of-principle that can be changed based on the target material, or fission products of interest.

The use of a secondary matrix other than KBr should be looked at in the future. In the neutron flux, the bromine is activated to give ^{82}Br, which is a short-lived isotope with many gamma signatures. These extra signatures in the gamma spectrum often complicate the data and make it difficult to extract data for nuclides of importance. Some form of salt that does not activate to give a gamma-emitting isotope would be beneficial. An example is potassium iodide (KI). The iodine would activate to give the short-lived isotope ^{128}I ($t_{1/2}$ = 25 min),[38] which decays to stable ^{128}Xe. The gamma signatures from ^{128}I would not be

visible in the spectrum by the time the material is being counted because the target materials do not return to UNLV until roughly 24-36 hours after irradiation.

Some fission products were extracted into certain acid solutions more effectively than others. For example, ^{99}Mo was extracted into 0.01 M HNO_3 and 0.1 M HCl in yields high enough to be measured. However, it was not extracted into 0.01 M HCl. This acid solution may be too dilute to effectively dissolve ^{99}Mo and remove it from the target. Other fission products were extracted well into any solution. Examples include ^{105}Rh, ^{131}I, and ^{131}I. Iodine, particularly in the form of potassium iodide, is quite soluble in aqueous solutions. If the iodine ions are interacting with the KBr matrix, its extraction potential may increase.[75] The interaction with a variety of ions present may also increase the solubility of rhodium. Similarly, ^{97}Zr could interact with the KBr to form $ZrBr_4$, which reacts with aqueous solutions and may increase the extraction potential in all of the tested acid solutions. Other fission products may react with the KBr matrix, the acid, or oxygen to form insoluble compounds. These insoluble compounds would remain with the solid UO_2 target material rather than being extracted into the aqueous solutions, and would not appear by gamma spectroscopy to have been extracted from the target. The addition of such a small amount of precipitated solid in the UO_2 sample would be negligible.

Chapter 3: Irradiation of MOFs

3.1   Introduction

As stated in Chapter 1 Section 1.4 metal-organic frameworks (MOFs) are composed of metal centers linked with organic ligands. The organic linkers control the size, shape, and functionality of the pore in the material. In the case of this work the pores can be used to allow the removal of fission products via a solvent rinse. The nature of the linker molecules was confined to dicarboxylic acids to simplify the project and allow for easier comparisons between samples. A number of examples of uranium-carboxylic acid frameworks can be found in the literature.[18,25-35,76,77] The Cahill group at The George Washington University has been exploring uranyl-containing MOFs since 2006,[18,28,29,33-35] including several pyridinedicarboxylic acid-based frameworks discussed in this chapter.[34,35] The Thuéry group at the Université Paris-Saclay in France has had several publications in the past decade on uranyl-organic frameworks using carboxylic acid linker molecules, such as phenyl- and cyclohexyl-based acetates.[30-32] The Loiseau group at the Université de Lille Nord de France has been studying polycarboxylate molecules as linker groups for uranyl-based MOFs for several years, including a structure described in Section 3.3.2.4.[78] The work in this chapter includes irradiations of previously published materials by these and other groups.

Table 13 describes each of the MOF targets discussed in this chapter, its corresponding organic ligand, the amount of material present in the target, and the extractant used to remove the fission products. Each MOF was synthesized using depleted uranium. The four ligands are 2,6-pyridinedicarboxylic acid (2,6-pydc), 2,5-pyridinedicarboxylic acid (2,5-pydc), 2,4-pyridinedicarboxylic acid (2,4-pydc), and pyromellitic acid (prma). They are described in detail in Section 3.2.

Table 13. Description of all targets discussed in this chapter, the organic ligand present in the framework, and the extractant used.

Target	Ligand	Target Mass (mg)	Extractant
1	2,6-pydc	36.0	0.01 M HCl
2	2,6-pydc	24.4	0.01 M HNO$_3$
3	2,5-pydc	24.6	0.01 M HNO$_3$
4	2,4-pydc	26.5	0.01 M HNO$_3$
5	prma	26.5	0.01 M HNO$_3$

3.2   Synthesis of MOFs

The general synthetic route was similar for all of the targets discussed in this chapter. Approximately 100 mg of UO$_2$(NO$_3$)$_2$, one equivalent of the respective ligand (2,6-pydc, 2,5-pydc, 2,4-pydc, or prma), 5 µL of NH$_4$OH, and 2 mL of DI H$_2$O were added to a hydrothermal cell. An explanation of hydrothermal chemistry is given in Chapter 1, Section 1.5. The reaction proceeded at 150 °C for 24-48 hours before the cell was cooled to room temperature and opened. The yellow product material was harvested, washed with DI H$_2$O and dried in a furnace at 100 °C. The ligands and the MOF frameworks are described in Sections 2.1-2.4.

3.2.1   2,6-pyridinedicarboxylic acid

One ligand used was 2,6-pyridinedicarboxylic acid (2,6-pydc, Figure 43). Examples of UO$_2$-2,6-pydc frameworks exist in literature;[34,35] however, the majority of the structures show linear geometry. The UO$_2$-2,6-pydc material produced in this work exhibits helical geometry, which has not been well represented in previous literature. In fact, as of this writing, few examples of helical uranium compounds have been published,[76,79] although many transition-metal helical MOFs exist.[80-82]

Figure 43. 2,6-pyridindicarboxylic acid molecule.

This unique uranium framework crystallizes in 1D chiral spirals, or helices, in the space group $P6_5$ (or $P6_1$; both left- and right-handed versions of the helix exist) and was first published in 1975 by Immirzi et.al.[76] A second, non-helical structure was discovered and published by Cahill et.al. in 2006.[35] The material in this work was isolated as a mixture of yellow crystalline clumps and yellow rod-shaped crystals (Figure 44). X-ray diffraction analysis shows the clumps are the same material that was reported by Cahill.[35] The fragile rod-shaped crystals are helical, with a pore size of 8 Å (Figure 45).[76] Targets 1 and 2 were comprised of UO_2-2,6-pydc helical crystals, which were chosen in lieu of the clumps due to their more consistent porosity.

Figure 44. Microscope image of the material showing both crystalline clumps and rod-shaped crystals.
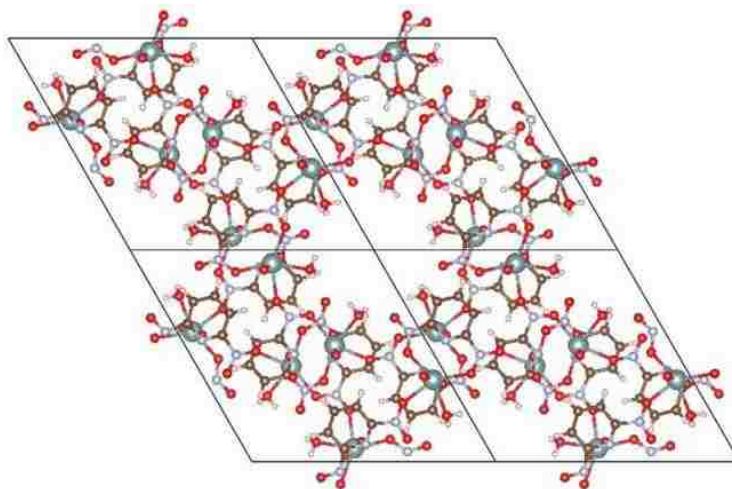
Figure 45. Structure of UO_2-2,6-pydc rod-shaped helical crystals

3.2.2 2,5-pyridinedicarboxylic acid

This framework uses a 2,5-pydc ligand (Figure 46), which is very similar to the 2,6-pydc ligand described above, however it does not have a helical crystal structure. Its structure has also been previously reported by Cahill et.al.[29] The framework published by Cahill has a pore size of 9.5 x 6.1 Å and a monoclinic crystal structure in the $P2_1/n$ spacegroup (Figure 47).[34] The pores are larger in one dimension than the 2,6-pydc framework, but they are less symmetrical. Target 3 was a pressed pellet of yellow, microcrystalline UO_2-2,5-pydc material.
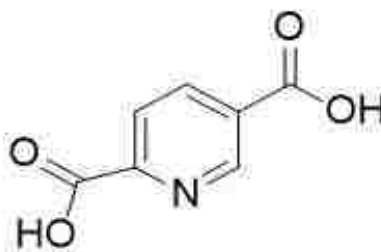
Figure 46. 2,5-pyridinedicarboxylic acid molecule
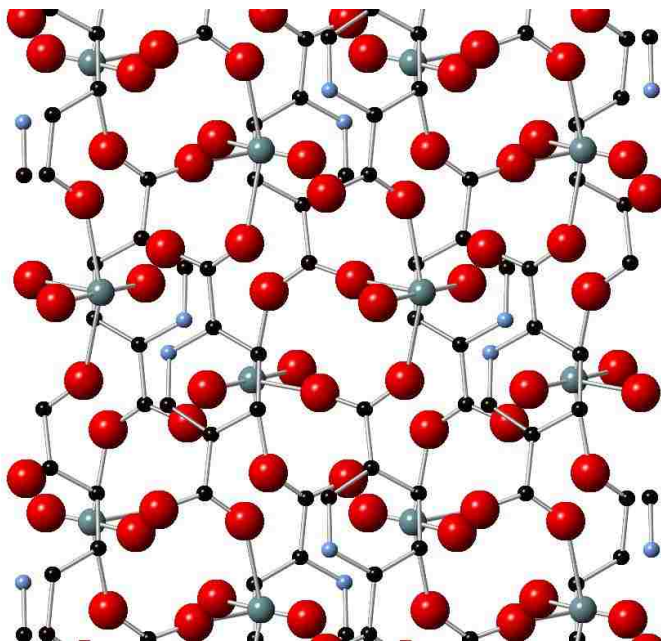
Figure 47. Crystal structure of UO_2-2,5-pydc as viewed down the x-axis. Red atoms are oxygen, light blue atoms are nitrogen, grey atoms are uranium, and black atoms are carbon.

3.2.3 2,4-pyridinedicarboxylic acid

In order to complete the series, the UO_2-2,4-pydc MOF was also irradiated. As with the previous MOFs,

this framework uses 2,4-pydc linker molecules (Figure 48), and its synthesis and structure were previously

published by Cahill with a pore size of 6.8 Å (Figure 49).[29] The crystal structure is also different from the

previous MOFs; this material crystallizes in the orthorhombic space group $Pca2_1$. The pore size is

significantly smaller than that of the the previous two frameworks. Target 4 was comprised of

microcrystalline UO_2-2,4-pydc material.
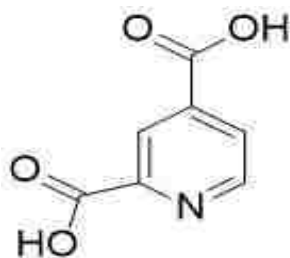
Figure 48. 2,4-pyridindedicarboxylic acid linker
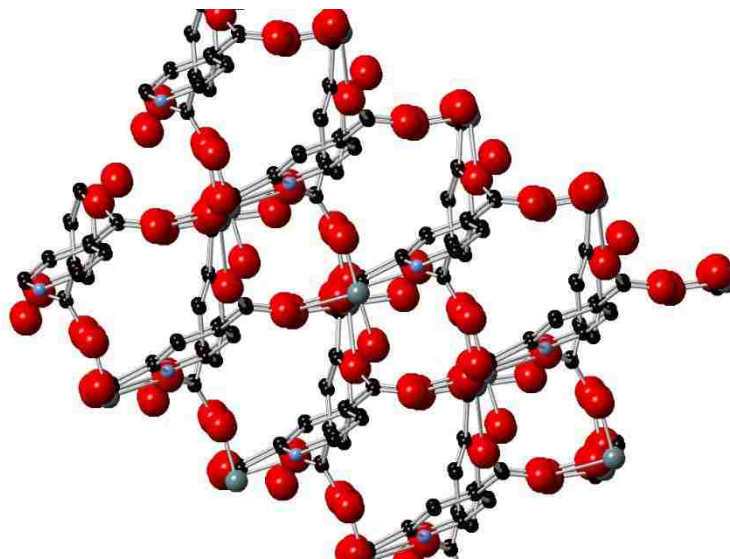
Figure 49. Crystal structure of UO_2-2,4-pydc viewed down the x-axis. Red atoms are oxygen, blue atoms are nitrogen, grey atoms are uranium, and black atoms are carbon.

3.2.4 Pyromellitic Acid

Pyromellitic acid (prma, also called 1,2,4,5-benzenetetracarboxylic acid, Figure 50), has a history of use in

metal-organic frameworks; its four coordination sites give rise to more flexibility in the system, leading to

multi-dimensional frameworks with large channels.[83-85] Louiseau et.al. reported the 3D crystal structure

of $(UO_2)_2(H_2O)_2$(btec)·H_2O in 2012;[78] the yellow rod-shaped crystals are orthorhombic in the Pbcn space

group. The framework is created through the four carboxylate arms of the pyromellitic acid linkers.
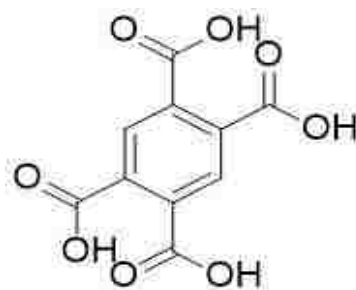
Figure 50. Structure of prma

The resulting material could be isolated as a clump of yellow rod-shaped crystals (Figure 51), or as yellow

semi-crystalline powder. Single crystal XRD analysis shows the crystals match the structure reported by

74

Loiseau et.al., with a pore size of 7.3 Å (Figure 52).[78] Target 5 was microcrystalline UO_2-prma MOF material.

Figure 51. Microscope image of UO_2-prma.
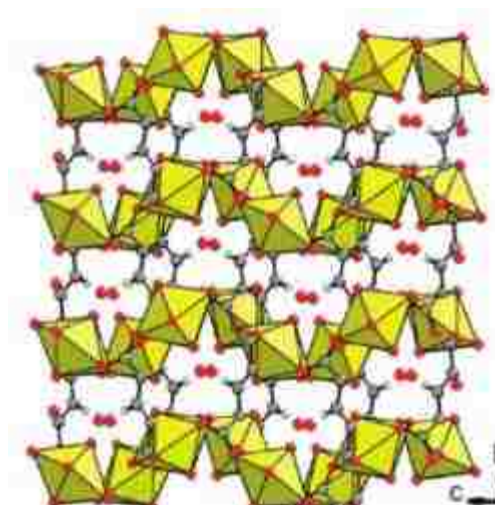
Figure 52. Structure of UO_2-prma with water in the channels as reported by Loiseau et.al.[78]

3.3　Target Production

3.3.1　Target 1 – UO$_2$-2,6-pydc

To produce Target 1, the small rod-shaped crystals of UO$_2$-2,6-pydc were separated by hand from the

larger yellow crystalline clumps (Figure 44). The isolated rods were then suspended in DI H$_2$O, and

transferred to a pre-cut piece of premium aluminum foil. The target material (36.0 mg of UO$_2$-(2,6-pydc)

helices) was adhered to the foil by evaporation of the water in a furnace at 60 °C, and then wrapped in an

aluminum sample holder (

 Figure **53**).

Figure 53. UO$_2$-(2,6-pydc) target after being dried on the aluminum foil

3.3.2　Targets 2-5

Table 14 lists the ligand framework and the total mass of each target. All four targets were created the

same way: by pressing the semi-crystalline material into 6 mm pellet at 2 tons for 10 minutes. The pellets

were thin and fragile (Figure 54), and occasionally broke into a few pieces during the process of wrapping

in aluminum foil. Each foil-wrapped target was sealed in an aluminum sample holder like those described

in Chapter 2 Section 2.4.

Table 14. List of targets 2-5

Target	Ligand	Target Mass (mg)
2	2,6-pydc	24.4
3	2,5-pydc	24.6
4	2,4-pydc	26.5
5	prma	26.5

Figure 54. Target 3 – UO_2-2,5-pydc

3.4   Irradiation and Target Treatment

Prior to irradiation, a sample of each MOF material was contacted with acid (0.01 M HCl or 0.01 M HNO_3)

to confirm that the target material would not be soluble in it. This ensures that any dissolution of the

irradiated sample is due to weakening of the framework backbone from irradiation events. None of the

MOF materials were soluble in their respective acids prior to irradiation (Figure 55).

Figure 55. MOF material was contacted with acid for a 24 hour period to ensure insolubility prior to irradiation.

All targets were irradiated using fast neutrons from Flattop (Chapter 1, Section 1.6.2). The targets were not irradiated at the same time, and thus have different irradiation variables such as fluence, duration of irradiation, and position in the core. The only difference in treatment of the irradiated targets is that Target 1 was treated with 0.01 M HCl and Targets 2-5 were treated with 0.01 M HNO_3. The target was removed from its sample holder and contacted with 5 mL of acid in a 15 mL plastic centrifuge tube for a total of 10 minutes. For 8 minutes, the centrifuge tube was placed on a table rocker (Figure 56) to evenly contact the solution with the material. For the remaining two minutes, the tube was centrifuged at 1500 rpm in order to facilitate separation of the liquid from the solid. The solid and liquid were placed in separate 5 mL plastic scintillation vials (Figure 57).
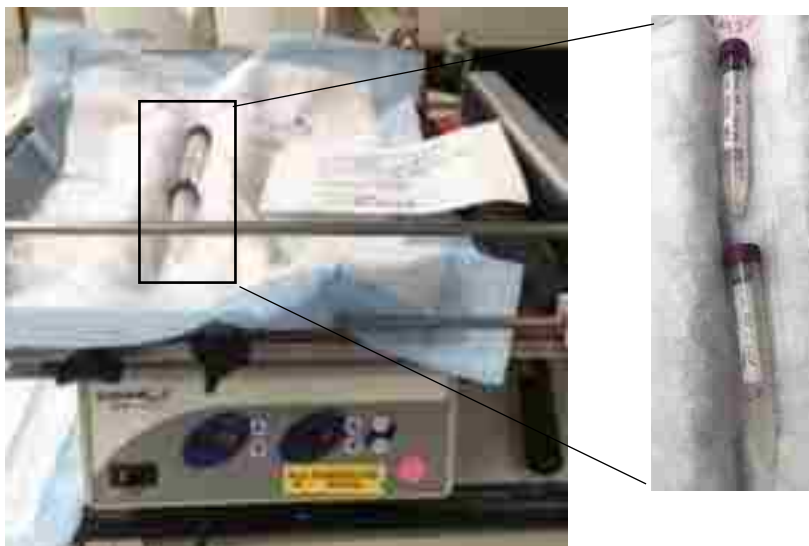
Figure 56. Rocking table used to contact the solid targets with acid solutions.

Figure 57. 5 mL plastic scintillation vials like these were used to hold the samples as they were counted.

Each vial was counted for 1 hour of live time on an HPGe or BEGe detector. The solid material was then returned to the plastic centrifuge tube and contacted with 6 mL of fresh acid. A 2 mL aliquot was removed after 30 minutes, 60 minutes, and 13 hours, respectively. Each of these aliquots was counted for 1 hour on the BEGe detector.

Activities were calculated for each nuclide extracted and specific activities were compared within one sample; the activities cannot be compared between each target due to the differences in irradiation

79

conditions. Observed activity for a particular nuclide in Becquerel (decays/second) was calculated as shown in Equation 4. Observed counts were divided by the amount of live time that the sample was counted, in seconds. The relative detector efficiency is an inherent property of the detector, and is 34% for the BEGe BE3830 used in these experiments.[86] The gamma yield describes what percentage of gammas released during a decay occur at a particular energy.

$$Activity\ (Bq) = \frac{\left(\frac{observed\ counts}{time(s)}\right)}{(relative\ detector\ efficiency) * (gamma\ yield)}$$

Equation 4. Calculation of activity for an isotope in Becquerel

3.5   Results

3.5.1   Target 1 – UO$_2$-2,6-pydc

The target was treated as described previously using 0.01 M HCl; however, the solid completely dissolved overnight. This ease of dissolution may be due to radiation damage along the backbone of the polymer structure; an un-irradiated sample of UO$_2$-2,6-pydc does not dissolve in 0.01 M HCl, even after 24 hours (Section 3.4). This target may only be suitable for irradiation in an attenuated neutron flux (see Section 3.5.2), or extraction with a milder solution, such as DI H$_2$O.

Because the target completely dissolved in the 0.01 M HCl solution over the course of the experiment, the results show a much greater extraction percentage than other targets. This result, while accurate, was not the goal of the project, and therefore shows that the material may be unsuitable for target reuse. Figure 58 shows the extraction percentages for selected fission products from the target. The majority of the products are extracted with yields greater than 80%. The value for ^{99m}Tc exceeds 100% because the ^{99}Mo present in the solution is decaying to ^{99m}Tc over the course of the experiment. By using Equation 5 to calculate the time correction for the decay of ^{99}Mo to ^{99m}Tc over the course of the experiment, the actual percent extraction for ^{99m}Tc is 86.3 %.

$$A_2 = N_0 \frac{\lambda_2 \lambda_1}{\lambda_2 - \lambda_1} (e^{-\lambda_1 t} - e^{-\lambda_2 t})$$

Equation 5. Calculation of the activity of a radioactive daughter nuclide after time t.

Some isotopes, such as ^{93}Y, have short half-lives– the half-life for ^{93}Y is 10.2 hours,[38] which is less time than the course of the experiment. Between counting the initial solid target material and counting the final extracted aliquot, approximately 15 hours had passed. During that time, slightly more than half of the ^{93}Y had decayed, reducing the activity in the sample. However, this will have no effect on the percent extraction calculations, as the ^{93}Y still present in the target material decays at the same rate as that found in the extracted aliquots. The same can be said for ^{91}Sr and ^{97}Zr, which have half-lives of 9.5 hours and 16.75 hours, respectively.[38]
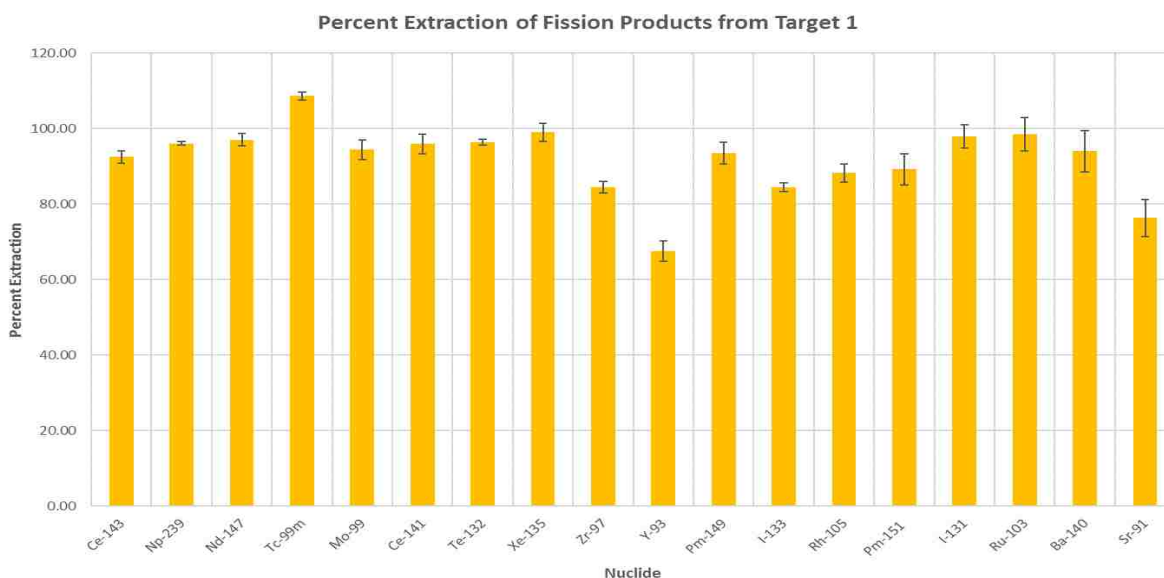
Figure 58. Bar graph depicting the percent extraction of certain fission products from the first UO_2-2,6-pydc target.

3.5.2 Target 2 – UO_2-2,6-pydc

Another UO_2-2,6-pydc target was prepared and irradiated to determine if the material would dissolve in a different extractant post-irradiation. The aluminum foil was removed and the powdered material was treated as previously described using 0.01 M HNO_3. After 13 hours, the yellow MOF material had not

dissolved. The difference in dissolution between this sample and the previous UO_2-2,6-pydc sample could be due to differences in the irradiation variables. For example, a decrease in the neutron flux could elicit less damage on the framework and reduce the possibility of dissolution. Assuming that the flux of neutrons decreases relative to the distance of the sample from the core, changes in the positioning of the sample between the two experiments could lead to less neutron exposure.

Though the separation was done immediately following the irradiation, this sample was not counted using the BEGe until 10 days after the irradiation occurred. Each sample (the solid, and four liquid aliquots, as explained at the end of Section 3.4) was counted for 3 hours on the BEGe detector. A background vial containing 0.01 M HNO_3 was also counted for 3 hours. Unlike the UO_2 salt targets, the UO_2-2,6-pydc MOF target was only able to allow for extraction of certain isotopes, albeit in relatively good yields (Figure 59). There are several possible reasons for this result: because the samples were not counted until 10 days after the irradiation, some fission products will have decayed and will not appear to have been extracted from the MOF; the fission products could have been unable to escape from the framework due to size exclusion or embedding themselves too far into the framework to escape.
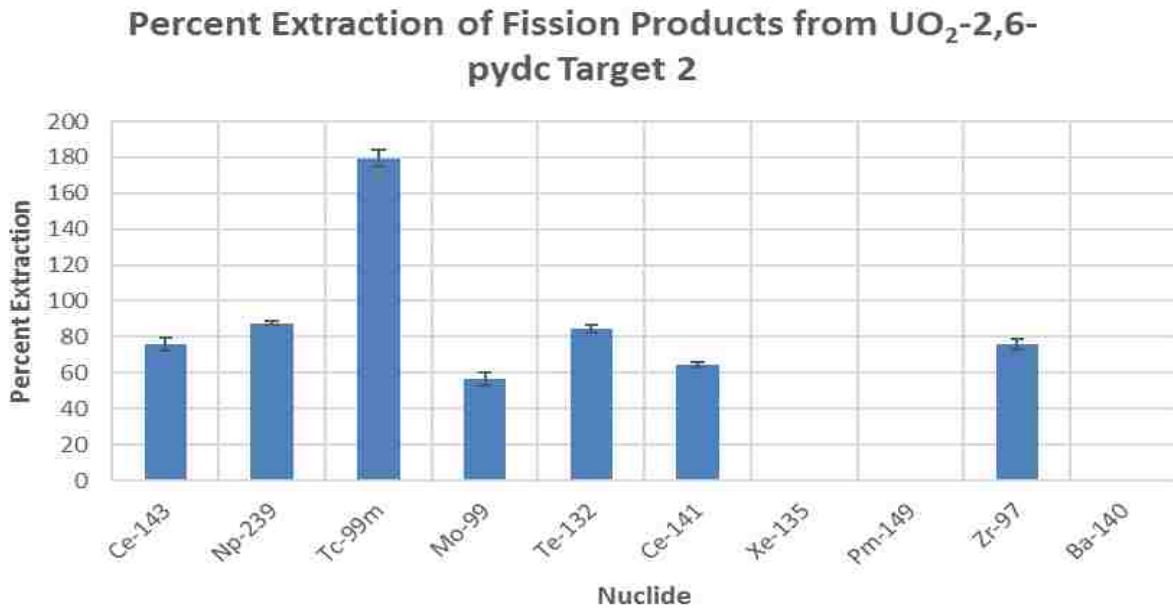
Figure 59. Bar chart depicting the percent extraction of certain fission products from the second UO_2-2,6-pydc target material. Error bars are present.

No other isotopes were seen in the extractant. It could be that these nuclides are the only ones that are able to escape from the framework, or that this target was not located in a position with high enough fluence to produce the same number of low-yield fission products seen in previous experiments. Due to the delay in gamma analysis, certain isotopes with short half-lives such as ^{135}Xe (9 hours), and ^{149}Pm (2 days) had decayed sufficiently and were no longer present in the samples.[38] This explains the lack of these isotopes in the data in Figure 59. The extraction percentage for ^{99m}Tc ($t_{1/2}$ = 6 hours) is above 100% due to the ingrowth of the nuclide from the decay of ^{99}Mo ($t_{1/2}$ = 66 hours), which had undergone more than 3 half-lives before the samples could be counted on the BEGe detector. The amount of ^{99}Mo still remaining in the solid target sample post-separation represents only 44% of the ^{99}Mo created during the irradiation. The liquid aliquots contain the other 56%, which will result in the formation of 56% more ^{99m}Tc over 10 days in the liquid samples compared to the solid material. Thus it will appear that the separation of ^{99m}Tc resulted in a yield above 100%, when in actuality, the amount of ^{99m}Tc separated is 95.1%. For the solid material, time is 327 hours post-separation, and the time for the liquid aliquots is 360 hours. By using

83

Equation 5 to calculate the decay corrected ^{99m}Tc activity from the ^{99}Mo parent activity in the aliquots, and taking into account the difference in counts of ^{99}Mo material between the solid and liquid samples, the corrected percent yield of ^{99m}Tc is 95.1 %.

Table 15 lists the counts originally in the target for a given nuclide. The low count numbers observed for these nuclides suggest that the target was placed in a relatively low neutron flux.

Table 15. Counts in original target for nuclides extracted from the UO_2-2,6-pydc MOF

Nuclide	Energy (keV)	Gamma Yield	Counts in Target
^{143}Ce	57.32	0.117	1128
^{239}Np	106.27	0.2534	13045
^{99m}Tc	140.8	0.89	2154
^{99}Mo	181.32	0.0614	651
^{132}Te	228.64	0.88	3301
^{141}Ce	145.98	0.48	3400
^{97}Zr	355.72	0.021	1603

When compared with the isotopes extracted from the UO_2 target without KBr using 0.01 M HNO_3 (Table 16), the UO_2-2,6-pydc MOF allows for the extraction of fewer isotopes, but it has a more efficient extraction potential. The isotopes described in Table 16 were chosen in particular because of their presence in most of the MOF materials discussed in this chapter, and the UO_2 target. The same isotopes are shown in comparison to the UO_2 target for each MOF material in Sections 3.5.3 – 3.5.5.

Table 16. Comparison of extraction percentages for selected isotopes from the UO_2-2,6-pydc MOF to the UO_2 target without KBr, both contacted with 0.01 M HNO_3 for 13 hours.

Nuclide	% Extracted from MOF	% Extracted from UO_2
^{143}Ce	75.80 ± 3.43	20.59 ± 0.48
^{239}Np	87.57 ± 2.18	12.11 ± 0.52
^{99}Mo	56.68 ± 3.69	12.11 ± 0.52
^{141}Ce	64.50 ± 1.77	34.85 ± 0.69

3.5.3 Target 3 – UO$_2$-2,5-pydc

The solid and all four liquid aliquots were counted on the BEGe detector for one hour each within 48 hours of the irradiation. At the end of the experiment, yellow powder remained. A comparison between this target and the UO$_2$ microparticle target is shown in Table 18. With the exception of [141]Ce, Target 3 extracts better than the UO$_2$ target. Figure 60 shows the percent extractions for certain nuclides from the UO$_2$-2,5-pydc target. Based on the gamma spectra, no other nuclides appeared to have been extracted. Some nuclides, such as [140]Ba – whose fission yield is roughly 6.0 %,[87] were not extracted at all from this target. Barium has a relatively large ionic radius of 1.35 Å,[88] and could potentially become trapped within the framework rather than escaping through the pores, which for this MOF are 9 x 6.5 Å.[34] Barium also has an oxidation state of 2+, which could theoretically allow it to bind with the oxygen molecules of the carboxylic acid molecules within the framework. Other fission products have lower fission yields, such as [149]Pm, whose yield is approximately 2%,[87] and may not have been produced in high enough concentrations to be present in the gamma spectrum. For example, the calculated minimum detectable activity for [149]Pm is 2591.6 counts/hour (see Equation 6). If the amount of [149]Pm in the sample is below that limit, the detector will not be able to detect it.

$$MDA = \frac{2.71 + 4.65\sqrt{N_B}}{\varepsilon a_\gamma t}$$

Equation 6. Calculating the minimum detectable activity for any given isotope. N$_B$ represents the background counts at a given energy, ε is the relative efficiency of the detector, a$_\gamma$ is the decay branching ratio for the given decay energy, and t is the time that the sample was counted.

The position of the target in the core could have been such that the flux was not high enough to produce the low-yielding fission products. The discrepancy in results between the two cerium isotopes, [141]Ce and [143]Ce, may be due to the increase in specific activity of [143]Ce. The half-life of [143]Ce is significantly shorter than that of [141]Ce – 1.377 days and 32.50 days respectively – which causes the specific activity of [143]Ce to

be higher. Table 17 lists the number of counts in the original target material for the nuclides extracted from the UO_2-2,5-pydc target. These values are higher than those listed in Table 15, indicating that this target was placed in a greater neutron flux than the UO_2-2,6-pydc target. Nuclides with shorter half-lives, such as [239]Np and [99]Mo, have higher counts due to their increased activities.

Table 17. Counts in original target for nuclides extracted from the UO_2-2,5-pydc MOF

Nuclide	Energy (keV)	Gamma Yield	Counts in Target
[143]Ce	57.32	0.117	10123
[239]Np	106.27	0.2534	119400
[99m]Tc	140.8	0.89	26884
[99]Mo	181.32	0.0614	5040
[132]Te	228.64	0.88	31129
[135]Xe	250.2	0.90	25972

Table 18. Comparison of extraction percentages for certain isotopes from the UO_2-(2,5-pydc)MOF to the UO_2 target without KBr, both contacted with 0.01 M HNO_3 for 13 hours.

Nuclide	% Extracted from MOF	% Extracted from UO_2
[143]Ce	35.15 ± 0.69	20.59 ± 0.48
[239]Np	40.57 ± 0.22	12.11 ± 0.52
[99]Mo	32.82 ± 0.93	12.11 ± 0.52
[141]Ce	0.00 ± 0.00	34.85 ± 0.69
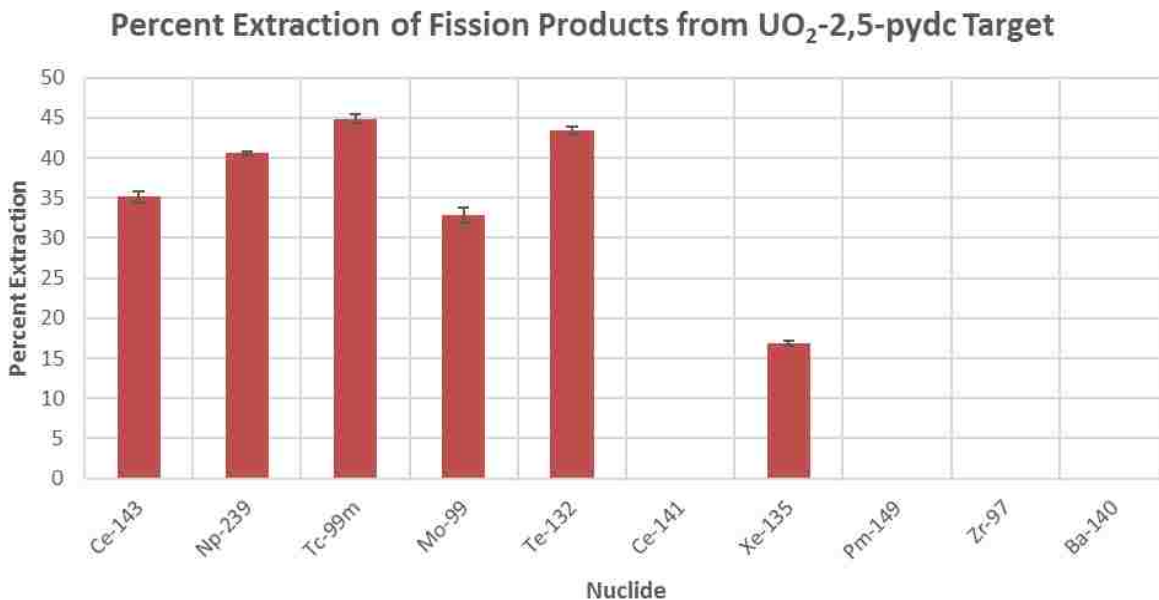
Figure 60. Bar graph showing the percent extraction of certain fission products from the UO_2-2.5-pydc target material.

3.5.4   Target 4 – UO_2-2,4-pydc

The solid target material, and all four liquid aliquots were counted on the BEGe detector within 48 hours of the irradiation. The target had been reduced to a fine powder during irradiation, shipping, and handling, but it did not dissolve in the 0.01 M HNO_3 contact solution. Figure 61 depicts the nuclides extracted from the target, as well as their yields. The framework of this MOF does not appear to allow for easy extraction of many nuclides, which may be due to its tighter structure and smaller pore size than that of the previous pydc MOFs (6 Å compared to 9 x 6.5 or 8 Å).
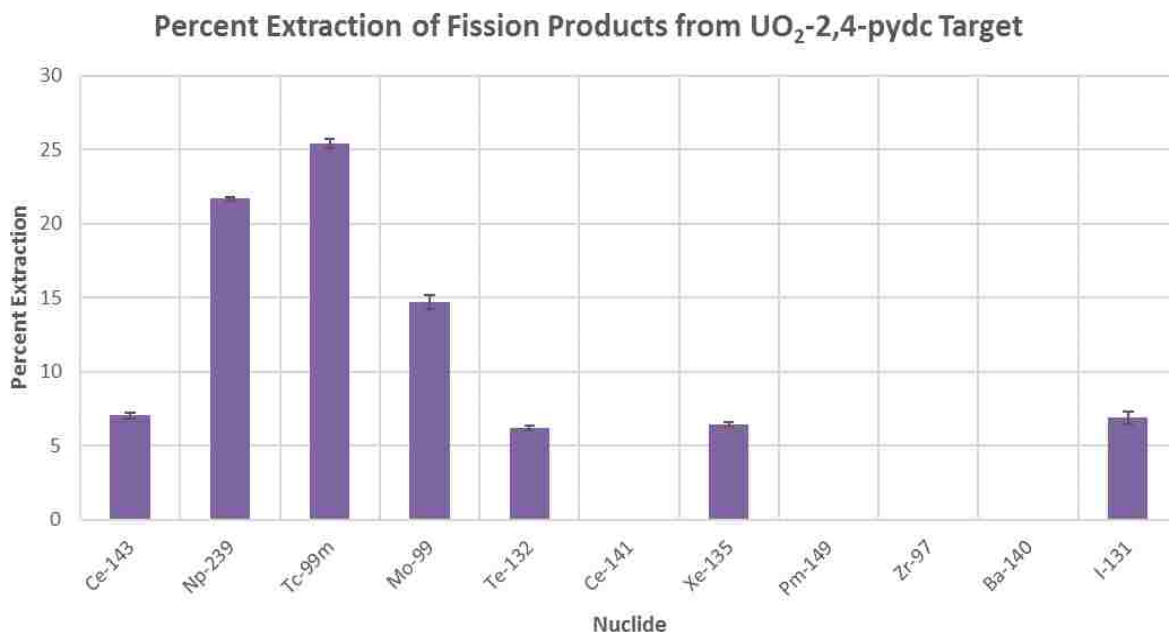
Figure 61. Bar graph showing the percent extraction of certain fission products from the UO_2-2.4-pydc target material. Error bars are present but may be too small to observe.

Table 19 lists the counts observed in the original target material for the nuclides extracted. Nuclides with moderately short half-lives, defined between 12 and 72 hours, have higher count rates; examples include ^{239}Np and ^{99}Mo. These data were obtained 25–36 hours after irradiation, which reduces the amount of short-lived ($t_{1/2}$< 12 hours) nuclides.

Table 19. Counts in original target for nuclides extracted from the UO_2-2,4-pydc MOF

Nuclide	Energy (keV)	Gamma Yield	Counts in Target
^{239}Np	106.27	0.2534	162772
^{99m}Tc	140.8	0.89	34161
^{99}Mo	181.32	0.0614	8013
^{132}Te	228.64	0.88	39022
^{135}Xe	250.2	0.90	32611
^{131}I	364.64	0.815	8147

When compared to UO_2 target material (Chapter 2 Section 2.5.3.6), cerium is extracted at a lower yield in the MOF. This framework has the smallest pore size of all the MOFs irradiated, which may affect the

extraction potential of the material. Certain fission products, such as ^{97}Zr, may be able to interact chemically with the framework rather than being extracted from it. As the pores decrease in size from 8 to 6 Å, this interaction is more likely.

Table 20. Comparison of extraction percentages for certain isotopes from the UO$_2$-(2,4-pydc)MOF to the UO$_2$ target without KBr, both contacted with 0.01 M HNO$_3$ for 13 hours.

Nuclide	% Extracted from MOF	% Extracted from UO$_2$
^{143}Ce	7.04 ± 0.20	20.59 ± 0.48
^{239}Np	21.68 ± 0.13	12.11 ± 0.52
^{99}Mo	14.70 ± 0.46	12.11 ± 0.52
^{141}Ce	0.00 ± 0.00	34.85 ± 0.69

3.5.5   Target 5 – UO$_2$-prma

The solid material and all four liquid aliquots were counted on the BEGe detector within 48 hours of irradiation. Though the target material turned pale-yellow in the solution of 0.01 M HNO$_3$, it did not dissolve. Figure 62 shows the percent extraction of nuclides from the pyromellitic acid target. No other gamma-active nuclides were extracted from this target, although ^{97}Zr was present in the solid material. Table 21 lists the counts observed in the original target material for each nuclide extracted. The counts extracted from the UO$_2$-prma target are significantly higher than for any other UO$_2$-MOF target. This is most likely a reflection of where the target was placed during the irradiation. This target was probably located within a higher neutron flux than previous target materials; more fission events occurred and more fission products were created.

Table 21. Counts in the original target for nuclides extracted from the UO$_2$-prma MOF

Nuclide	Energy (keV)	Gamma Yield	Counts in Target
^{239}Np	106.27	0.2534	203298
^{99m}Tc	140.8	0.89	40746
^{99}Mo	181.32	0.0614	7532
^{132}Te	228.64	0.88	50277
^{135}Xe	250.2	0.90	7677
^{149}Pm	285.7	0.872	10204
^{140}Ba	537.74	0.24	2087

The extraction yields for this target were not high, but the majority were above 50%. Neither cerium isotope was extracted from this material, which could be related to size exclusion or chemical interactions within the framework. Cerium can adopt a 4+ oxidation state, and could therefore chemically interact with the framework after it was produced. This possibility may, in part, explain why no cerium was extracted from the UO_2-prma target. It may also explain the lack of ^{97}Zr extraction. Though ^{239}Np could conceivably replace ^{238}U in the framework, as the ionic radius of ^{239}Np is reasonably similar to ^{238}U (0.87 and 0.89 Å, respectively),[88] neptunium can adopt many oxidation states, the most likely of which under atmospheric conditions is the 5+ oxidation state.[14] The ^{239}Np(V) isotope will be less likely to coordinate to the framework than atoms in 4+ or 6+ oxidation states. Molybdenum, which is most often in the 6+ oxidation state, has a much smaller ionic radius than other 6+ ions (0.65 Å, compared to 0.72 Å for zirconium or 0.87 Å for cerium),[88] and could be less likely to interact with the framework.
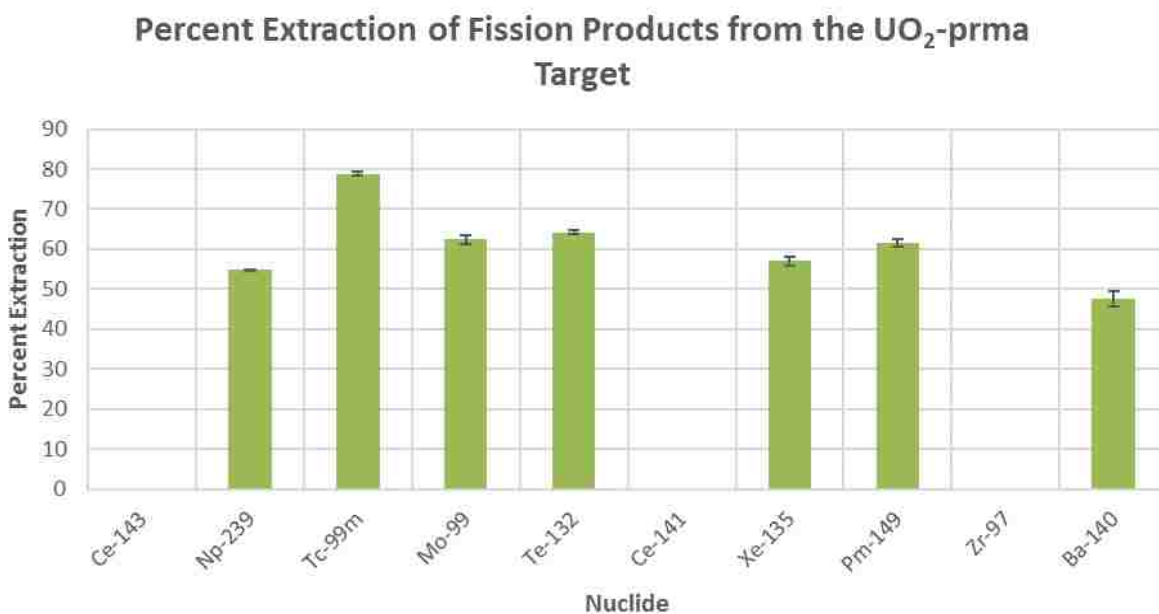
Figure 62. Bar chart describing the percent extraction of certain fission products from the UO_2-prma target. Error bars are present but may be too small to observe.

Table 22 describes the extraction of certain nuclides from Target 5 versus the UO$_2$ target from Chapter 2. Though no cerium was extracted from Target 5, more ^{239}Np and ^{99}Mo were extracted compared to the UO$_2$ target.

Table 22. Comparison of extraction percentages for certain isotopes from the UO$_2$-(prma)MOF to the UO$_2$ target without KBr, both contacted with 0.01 M HNO$_3$ for 13 hours.

Nuclide	% Extracted from MOF	% Extracted from UO$_2$
^{143}Ce	0.00 ± 0.00	20.59 ± 0.48
^{239}Np	54.80 ± 0.20	12.11 ± 0.52
^{99}Mo	62.45 ± 1.16	12.11 ± 0.52
^{141}Ce	0.00 ± 0.00	34.85 ± 0.69

3.6   Comparison of MOF targets

Because Targets 2-5 were treated with 0.01 M HNO$_3$, their results can be compared. Due to differences in irradiation parameters, such as fluence, duration, and position of the target in the core, the results will be discussed in terms of percent of each fission product extracted from the solid target. This method was explained in more detail in Chapter 2 Section 2.4. Table 23 lists each nuclide extracted from the UO$_2$-MOFs, its gamma ray yield and energy, and the raw counts extracted. Certain gamma signatures are low yielding, such as the one from ^{143}Ce. Lower yielding gamma rays will produce fewer counts in a detector, and therefore fewer counts will appear to have been extracted from the target. For example, ^{239}Np and ^{99}Mo have half-lives on the same order of magnitude, but ^{239}Np has a higher gamma yield (25.34 %) than ^{99}Mo (6.14 %). There are far more counts extracted for ^{239}Np than for ^{99}Mo. Though there are many explanations for this data, the higher gamma yield may contribute to the difference in number of counts extracted. Nuclides that have shorter half-lives, such as ^{99m}Tc or ^{135}Xe, will have higher specific activities, and more counts seen by the detector. The data in Table 23 for ^{99m}Tc generally shows a higher count rate than longer lived nuclides with comparative gamma yields, such as ^{132}Te.

Table 23. Raw counts of nuclides extracted from each UO_2-MOF

Nuclide	Gamma Yield (%)[89]	Gamma energy (keV)[89]	$T_{1/2}$ (hours)[38]	Counts from UO_2-2,6-pydc	Counts from UO_2-2,5-pydc	Counts from UO_2-2,4-pydc	Counts from UO_2-prma
^{143}Ce	11.70	57.32	33.05	855 ± 29.2	3558 ± 59.6	0.00 ± 0.00	0.00 ± 0.00
^{239}Np	25.34	106.27	56.54	11424 ± 106.9	48441 ± 220.1	35290 ± 187.9	111406 ± 333.8
^{99m}Tc	89.00	140.80	6	4471 ± 66.7	12072 ± 109.9	8670 ± 93.1	32125 ± 179.2
^{99}Mo	6.140	181.32	66	369 ± 19.2	1654 ± 40.7	1678 ± 41.0	4704 ± 68.6
^{132}Te	88.00	228.64	76.8	2801 ± 52.9	13531 ± 116.3	4254 ± 65.2	32300 ± 179.7
^{141}Ce	48.00	145.98	780	2193 ± 46.8	0.00 ± 0.00	0.00 ± 0.00	0.00 ± 0.00
^{135}Xe	90.00	250.20	9.10	0.00 ± 0.00	4372 ± 66.1	2099 ± 45.8	4371 ± 66.1
^{149}Pm	87.20	285.70	53.1	0.00 ± 0.00	0.00 ± 0.00	1240 ± 35.2	6273 ± 79.2
^{97}Zr	2.09	355.72	16.75	1219 ± 34.9	0.00 ± 0.00	438 ± 20.9	0.00 ± 0.00
^{140}Ba	24.00	537.74	306	0.00 ± 0.00	0.00 ± 0.00	0.00 ± 0.00	991 ± 31.5
^{131}I	81.50	364.64	192.6	0.00 ± 0.00	0.00 ± 0.00	283 ± 16.8	0.00 ± 0.00
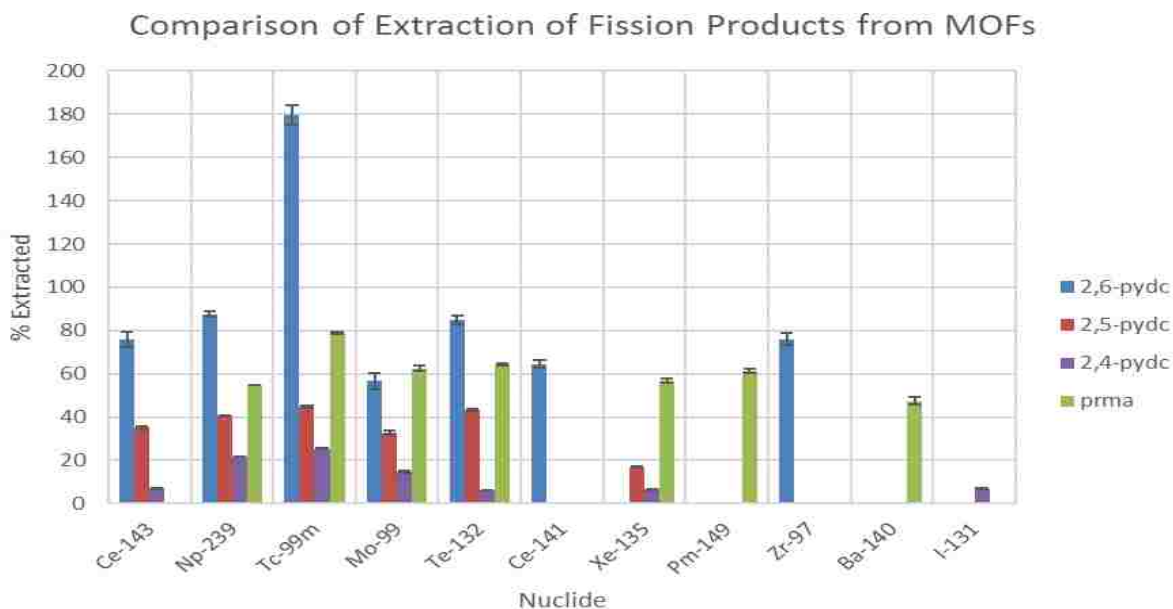
Figure 63. Comparison of the extraction percentages of fission products between the three MOF targets.

Several conclusions can be drawn from the data shown in Figure 63. Though few fission products were able to be analyzed for UO_2-2,6-pydc target, all of them were extracted in high yields. Several more fission products were extracted from the UO_2-2,5-pydc target, but in much lower yields; this could be due to a change in the pore size from 8 Å to 9 x 6.5 Å, causing retention of more fission products. The MOF with the lowest extraction yield, UO_2-2,4-pydc, also had the smallest pore size of 6 Å. The size of the pore decreases and becomes less symmetrical as the carboxylic acids move positions on the pyridine ring, which could explain the distinct difference in results between the three pydc targets. The final result was from a completely different framework; the most fission products were extracted in relatively good yields from the UO_2-prma target. The pore size of the prma target (8 Å) was not larger than the pydc targets (6.8 – 8 Å), though the pore shape and framework structure are completely different. This could indicate that the porous frameworks formed by the pyridinedicarboxylic acid molecules are not ideal for removing fission products well, but the framework shape of the UO_2-prma target it appears to allow for better separation.

93

Many fission products have low production yields from the fission process, and may have concentrations too low to be detected in a gamma spectrum, as exemplified by ^{140}Ba and ^{141}Ce. The targets were likely not placed in the same location during their respective runs, which may change the neutron flux on the target, and therefore impact the extraction data. It is also possible that fission products that can adopt a 4+ or 6+ oxidation state, such as ^{143}Ce, ^{97}Zr, ^{99}Mo, ^{99m}Tc, or ^{132}Te, could have fit chemically into the framework instead of being extracted. The structure of each framework was slightly different, and it could be possible that the fission products fit better within one framework type than the others. For example, ^{97}Zr was only extracted from the UO_2-2,6-pydc framework. Its predilection for adopting a 4+ oxidation state could allow it to bind within the tighter frameworks of the other MOFs. Discrepancies in the data can also be due to differences in specific activities and gamma yields between nuclides. A nuclide with a shorter half-life will have a higher specific activity, and more counts, than a longer-lived nuclide.

These data show that it is possible to extract fission products from a porous framework without completely dissolving it. The size and structure of the framework seems to have an effect on the type of fission products that are easily extracted. This result shows that frameworks like these could be used to selectively extract specific fission products efficiently.

Chapter 4: Irradiations of Other Materials

Metal organic frameworks (MOFs) are not the only porous structures that could show potential use as an irradiation target. Sol-gels, inorganic polymers transformed from a solution to a network structure,[90] are other examples of potentially porous, organic-based frameworks. Generally, these porous structures are formed from the hydrolysis of metal-alkoxides, forming cross-linking polymers. The formation of pores can be achieved using supercritical drying of the sample.[90] Ideally, if an irradiation target were formed from a sol-gel, the pores in the framework would allow for the escape of fission products in the same manner as the MOF targets. The gels may prove to be safer to work with than MOFs because they are a non-dispersible material. The gel could also act as a secondary matrix, much like the KBr salt discussed in Chapter 2, and increase the extraction of fission products simply by trapping the escaped fission products and dissolving in a solution. This could be advantageous because the polymer would not be activated in the neutron flux and form radioactive products that would interfere with the data in the gamma spectra.

4.1 Introduction

The majority of materials described in this work are synthesized in water, which can have negative effects on the neutron energy during the irradiation. Water contains two hydrogen atoms (protons) and one oxygen atom. The protons are each roughly the same size as the neutron, which leads to maximum energy transfer from the neutron if it interacts with a proton.[40] This process moderates the neutrons, reducing both their energy and the likelihood they will induce fission in a ^{238}U atom.[40] Removal of the water is necessary to prevent moderation of the neutrons; however, elimination of any solvent present in the channels of a framework by conventional drying techniques will cause the structure to collapse. Critical point drying of the sample allows water to be removed while leaving the structure intact.[91] The critical point of any material is the temperature and pressure at which the liquid and gaseous phases have the same physical characteristics.[91] Table 24 describes the critical point data for both H_2O and liquid carbon

dioxide (CO_2). Since the critical point of water cannot be feasibly reached in a laboratory setting CO_2 is used.

Table 24. The temperature and pressure at the critical point for different solvents.[91]

	Critical Point Temperature (°C)	Critical Point Pressure (psi)
H_2O	374	3322
CO_2	31	1073

However, CO_2 is not miscible with water. The water must be exchanged with another solvent, such as acetone or ethanol, in a pre-critical point drying step.[91] This chapter includes two other target materials that were not MOFs; however, all targets described in this chapter were synthesized using depleted uranium. The first target was a thin-sheet polymer made from the gelation of alginic acid with UO_2 microparticles suspended within the polymer. The second target material was made from a uranyl-oxalic acid framework and did not need to be dried prior to irradiation.

4.1.1   Critical Point Drying

Once a sample has been correctly prepared by exchanging water with another solvent, it can be dried. Figure 64 shows images of the dryer being assembled. The samples are placed in one of the six chambers of the mesh basket and the basket is placed in the pressure chamber. The chamber is sealed and filed with CO_2 from a gas cylinder until the meniscus is at the correct level, between the two red lines shown in Figure 64d. The temperature is increased to 36 °C, just above the critical point temperature, and the chamber is pressurized to approximately 1300 psi. In general, the chamber is held at these conditions for 5-10 minutes while the supercritical CO_2 is stirred through the mesh basket to fully exchange with the solvent.[92] The pressure and temperature are slowly brought back to ambient conditions to allow the CO_2 to escape the sample as a gas. This process is often repeated several times; in the case of these experiments, each sample was contacted with supercritical CO_2 three times for 5 minutes each.

Figure 64. This series of images shows a sample being prepared for critical point drying. A) The basket that holds up to six samples. B) The three parts of the basket compared to a pen cap. C) The fully assembled basket. D) The chamber where the basket sits during the drying. The window shows the level of the CO_2 in the chamber – the meniscus should be between the two red lines in order for the process to work. E) The benchtop critical point dryer. The chamber is located on the top left of the instrument.

The thin sheets of UO_2-alginate polymer were soaked in acetone for one week in order to exchange any water in the material prior to critical point drying. The acetone-soaked samples were placed in the benchtop critical point dryer, and the temperature and pressure in the sample chamber were increased to 36 °C and 1300 psi. The acetone in the samples was exchanged with liquid CO_2. As the temperature and pressure were brought back to atmospheric conditions over 10 minutes, the CO_2 became gaseous and evaporated from the gel, leaving behind pores.

4.2 Target Materials

4.2.1 Alginate Gel

Sodium-alginate was chosen as the metal-alkoxide for the Sol-gel because the mechanism of the gelation process is well understood,[93] the material is nontoxic, and the gelation is easy to produce.[94] Figure 65 shows the polymeric structure of the sodium salt of alginic acid.[94] Alginate was originally found in several varieties of seaweed, particularly those that grow in cold waters.[95] Major commercial sources of the compound are located off the coasts of California, Scotland, and Norway.[95] The chain is generally a co-polymer of L-guluronic acid and β-D-mannuronic acid, although the type of seaweed and growing conditions will affect the ratio of acids as well as the structure of the chains.[95] This structure can affect the gelation properties of the polymer; for example, guluronic acid binds calcium more efficiently, so a polymer with a higher guluronic acid concentration will form more rigid gels.[95]
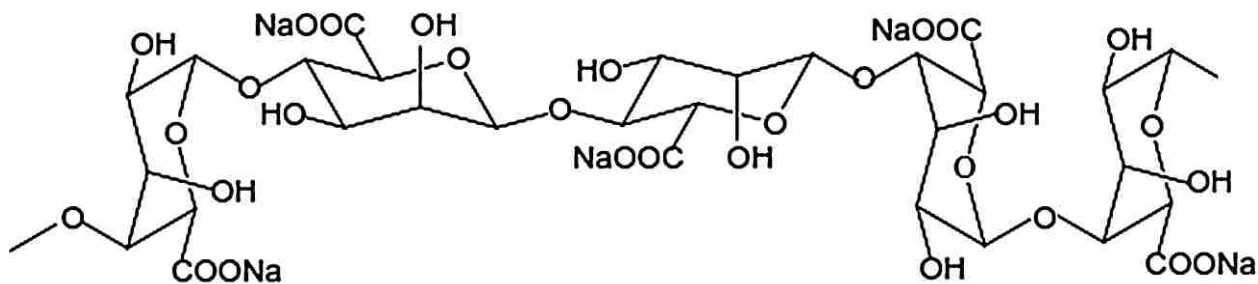
Figure 65. Chemical structure of sodium alginate polymer.[94]

The alginate target was created by suspending UO_2 microparticles (see Chapter 2) within the solution prior to gelation. The goal was to mimic the $KBr:UO_2$ targets described in Chapter 2 using the same UO_2 particles, but adding alginate polymer rather than KBr as the secondary matrix. The suspension of microparticle UO_2 in the gel was relatively simple; the UO_2 particles were suspended in DI H_2O by rapidly stirring the solution before the addition of alginic acid. The gel formed quickly, trapping and suspending the UO_2 particles in the clear gel (Figure 66).

Figure 66. UO_2 particles suspended in an alginate gel

The gel was allowed to dry in air for several days until it became a thin layer approximately 0.16 mm thick. This clear sheet of polymer no longer has the same characteristics of the original gel. The material is no longer tacky and gelatinous, but has become a thin, flexible sheet of polymer.

Part of the thin sheet was placed in 0.01 M HCl in order to examine its behavior in this solution. Within an hour the gel had dissolved in the acid, leaving behind the small UO_2 particles. This indicates that the fission products from the irradiated target would be easily separable from the UO_2 particles, much like the KBr matrix described in Chapter 2. Prior to irradiation, the polymer material was critically point dried using CO_2 and the techniques described above. This process was carried out to remove any residual solvent, and increase the porosity of the gel. The change in structure of the material due to the formation of pores and bubbles from the critical point drying process may allow for easier dissolution of the polymer post-irradiation.

Although it was not crucial to the irradiation experiments, the dispersion of the particles within the gel matrix was explored via autoradiography. Three gels with approximately 50 mg of UO_2 particles each were prepared by the method described above (Figure 67). As the intensity of the radiation in the sample

changes, so does the color in the image. The bottom image of Figure 67 shows the audioradiograph of the alginate samples (as compared to the sample on the left). Red indicates a higher concentration of radioactive material, yellow is indicative of moderate concentration, and blue indicates a lower concentration. Clearly the UO_2 particles are not evenly distributed throughout the sample, but for the purposes of this research, the homogeneity of the sample is not imperative because the entire sample will be in the neutron flux.
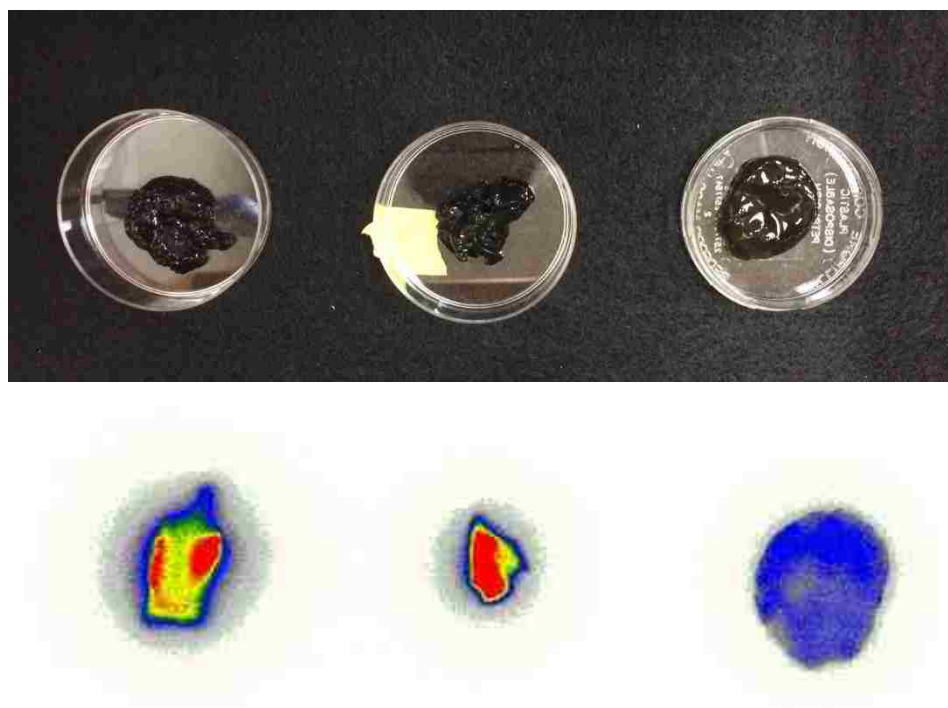
Figure 67. The three UO_2-alginate gels and their autoradiography results (bottom).

4.2.2 Irradiation

Approximately 20 mg of UO_2 microparticles were suspended in alginate gel, critically point dried to remove solvent and increase porosity of the material, and irradiated with fast neutrons. The thin sheets of the gel were cut to fit within the sample holder (approximately 1 cm^2), stacked four sheets high, wrapped in aluminum foil, and placed in the sample holder. The sample was irradiated in Flattop but the organic material sublimed and caused loss of the target. Unfortunately, it appears that the temperature

in the core of Flattop is high enough that the alginate gel decomposed and built up pressure within the sample holder. Temperatures in the core of Flattop can reach in excess of 220°C.[96] It was later determined that under laboratory conditions the alginate gel decomposes at approximately 180 °C, and so is better suited for the environment present in a research reactor. Research reactors are much smaller than typical power reactors: 100 megawatts (MW) and 3000 MW, respectively.[97] Because they are smaller and put out less power, research reactors run at lower temperatures than typical power reactors.[97] For example, the University of Missouri Research Reactor operates at 136 °C, significantly lower than the sublimation point of the alginate target.[98] Recent studies from the Korean Atomic Energy Research Institute have also shown that it is possible to irradiate materials in a research reactor below 100 °C.[99]

4.3 Oxalic Acid

Oxalic acid (Figure 68) has historically been used in uranium synthesis, including the formation of UO_2 fuel,[100] formation of clusters,[101] and frameworks.[102] It is most commonly used in precipitation of uranium during fuel production. The precipitation can form either uranium (IV) oxalate or uranyl oxalate;[103] this process is often studied by the nuclear forensics community for its effect on surface formation of the final UO_2 fuel.[100] The target discussed herein is uranium (VI) oxalate, which has a different chemical structure owing to the addition of two oxygen atoms to the uranium center. Though not technically a MOF, the UO_2-oxalate polymer forms stacks of 1-dimensional sheets that interact via Van der Waals interactions. The resulting framework includes channels between the polymer sheets, which could be advantageous for extracting fission products.
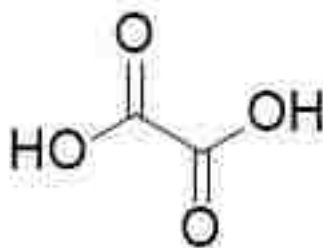
Figure 68. Oxalic acid linker molecule

4.3.1 Experimental

The UO_2-oxalate structure was synthesized hydrothermally via a reaction of $UO_2(NO_3)_2 \cdot 6H_2O$ (0.0978 mg, 0.1948 mmol), adipic acid (0.0301 g, 0.2060 mmol), and oxalic acid (0.0302 mg, 0.2395 mmol, 2 equiv.) in 2 mL of water at 180 °C for 18 hours. After cooling to room temperature over 4 hours, the yellow liquid was transferred to a scintillation vial and cooled to 4 °C. Small yellow crystals grew overnight and were shown by SCXRD analysis to be identical to the structure for $(UO_2)_2C_2O_4(OH)_2(H_2O)_2$, published by Giesting, et. al. in 2005.[104] The structure contains chains of uranyl moieties bound to oxalate groups, which are then linked together into layers by hydrogen bonding.[104] Though it is not a porous framework, there are channels that run between the chains.

The yellow crystalline material (25.4 mg) was pressed into a 6 mm pellet using 2 tons of force for 10 minutes. The resulting pellet was wrapped in aluminum foil and sealed in an aluminum sample holder identical to those used for previous samples (Figure 69). Upon return from irradiation, the target was contacted with 0.01 M HNO_3 following the standard procedure.

Figure 69. Image of UO$_2$-oxalate target prior to irradiation.

4.3.2 Results

The target did not remain intact through the irradiation process. The initial yellow pellet became a black

powder - likely losing oxalate ligands and reducing to UO$_2$ within the environment of Flattop. Typically the

decomposition of the oxalate species occurs between 300 and 400 °C in vacuum,[100] but it is possible that

the neutron bombardment on the framework facilitated the decomposition. The oxalate ligand is not

particularly complex, and the sheets of the polymer are held together via Van der Waals interactions

rather than by stronger bonds. The bombardment of neutrons against the simple framework may cause

destruction of the ligands or the MOF-like porosity. In the reducing atmosphere within Flattop, the uranyl

cation could be reduced to UO$_2$. The solid material and four liquid aliquots were counted on the BEGe

detector within 36 hours of irradiation. Figure 70 shows the percent extraction of fission products from

the target material when contacted with 0.01 M HNO$_3$. The full treatment details and explanation can be

found in Chapter 3 Section 3.4.

The size of the UO$_2$ particles formed from the oxalate target were not measured due to their activity, but

literature reports site diameters of irradiated UO$_2$ particles as ranging from 20 μm to 2 mm;[105] significantly

greater than the diameter of particles described in Chapter 2 (2.66 μm, on average). The data from the

UO$_2$-oxalate target (Figure 70) shows that fission products can be extracted from the target diameter UO$_2$

particles, although the yields were not high. The low yield may be due to a lack of secondary matrix onto which the products can embed (such as KBr), or due to the larger size of the particles. If the fission event occurs within a particle whose diameter is greater than 10 μm, the products from that event may not escape the particle. The extraction of certain products, such as ^{99m}Tc and ^{99}Mo, is promising; with optimization of the target, these results could lead to a better target material for the production of these and other medical isotopes. The only fission products that were extracted from this target material are those centered around the humps on the fission curve (Chapter 1 Section 1.6). This is not particularly surprising, as the fission products at the top of the humps have the highest fission yield due to their enhanced stability in the nucleus. However, these results indicate that this target was exposed to a low neutron flux. The activity calculated for each isotope extracted is listed in Table 25; calculations were done according to Equation 4 (see Section 3.4).
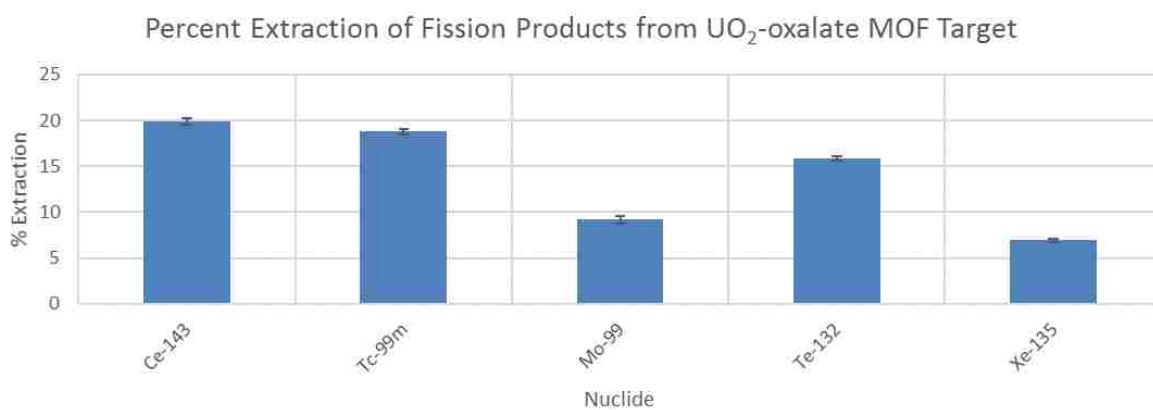
Figure 70. Bar graph depicting the percent extraction of fission products from the UO$_2$-oxalate MOF target. Error bars are present, but may be too small to see.

Table 25. Counts in the original target for each nuclide extracted from the UO_2-oxalate target.

Nuclide	Energy (keV)	Gamma Yield	Counts in Target
^{143}Ce	57.32	0.117	14003
^{99m}Tc	140.8	0.89	28690
^{99}Mo	181.32	0.0614	6079
^{132}Te	228.64	0.88	35761
^{135}Xe	250.2	0.90	22495

Table 25 lists the counts observed in the target material for the fission products extracted from the target. These values are reasonably similar to the targets described in Chapter 3; indicating that this target was located in a similar neutron flux environment as the UO_2-2,5-pydc MOF target, but in a lower flux than the UO_2-2,4-pydc target. Only those fission products with high fission yield were present, which is likely related to the neutron flux. The isotopes whose half-lives are on the order of days, ^{143}Ce and ^{99}Mo, have the highest activity present. Because of its 9.1 hour half-life, ^{135}Xe had significantly decayed before the completion of the experiment.

The material did not remain in a polymer configuration, and thus a direct comparison cannot be drawn between the extraction yield data and the extraction yields from the MOFs described in Chapter 3. However, a general comparison between this target and the microparticle UO_2 target that did not contain KBr (see Chapter 2 Section 2.5.3.6) can be made because both products are UO_2 particles of different size, and both were contacted with 0.01 M HNO_3. The comparison shows the extraction potential of the target can be correlated to the size of the UO_2 particles. For the purposes of this discussion, the particles synthesized as part of the earlier chapters of this thesis work are referred to as microparticles because they are less than 10 μm in diameter, and the particles formed from the UO_2-oxalate target irradiation are referred to as macroparticles. In this comparison, the microparticle UO_2 target showed significantly more fission products extracted at higher percentages than the target with macroparticle UO_2. Figure 71 depicts this difference; the microparticles are shown as red bars, and the oxalate macroparticles are shown as

blue bars. In most cases, the microparticulate UO_2 particles allow for better extraction of more fission products compared to the particles produced in the irradiation of the oxalate framework. The UO_2 target samples were not counted on a BEGe detector until 10 days after the irradiation, which limited the number of short-lived fission products still present in the sample, and the oxalate target samples were counted within 36 hours of irradiation. The oxalate target therefore shows extraction of more short-lived fission products, such as ^{99m}Tc and [135]Xe. However, even with the discrepancy in time between irradiation and measurement, the data still shows that the smaller particles have a higher extraction potential in 0.01 M HNO_3 than larger particles.
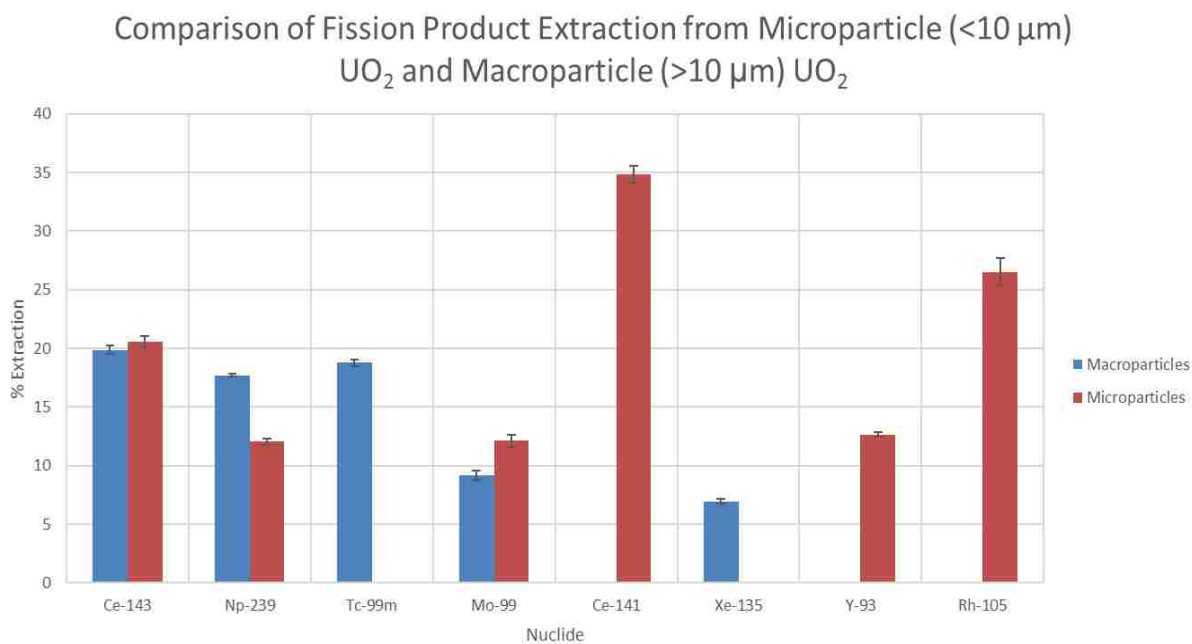
Figure 71. Comparison of extraction of fission products between two UO_2 particle sizes. Error bars are present, but may be too small to see.

Based on this limited amount of data, it appears that the smaller UO_2 particles do allow for a better extraction of fission products, even without the presence of a secondary matrix. Experiments using UO_2 particles with known diameters should be done to fully understand the difference in extraction potential of microparticles compared to macroparticles. The experiment with the UO_2 microparticles should also be

106

repeated and counted within 36 hours to obtain data for a better comparison, since some of the short-lived isotopes like ^{135}Xe aren't represented in the current data.

The use of organic-based polymers as a secondary matrix for a target may not be the best course of action due to the temperature and environment in Flattop. The high temperature within the core can cause the polymer to degrade, which increases the pressure within the sample holder. If the polymer degrades, the target could lose its secondary matrix. This is one disadvantage that the UO$_2$:KBr targets do not have. It may be beneficial to move the target father from the core to reduce the localized heat, or to increase the enrichment of the uranium particles and irradiate the material in a cooler environment, such as a research reactor.

Chapter 5: Organoactinide Synthesis – Chalcogenides

5.1   Background

The following three chapters describe synthetic efforts in organometallic actinide chemistry. Details of each project will be explained in an introduction section at the beginning of each chapter. Unless otherwise noted, all reactions and manipulations were performed at 25 °C in a recirculating Vacuum Atmospheres NEXUS model inert atmosphere (N_2) drybox equipped with a 40CFM Dual Purifier NI-Train. Glassware was dried overnight at 150 °C before use. All NMR spectra were obtained using a Bruker Avance 400 MHz spectrometer. Chemical shifts for ^{1}H NMR spectra were referenced to solvent impurities (δ = 7.16 for benzene-d_6, 3.58 for THF-d_8). Unless otherwise noted, reagents were purchased from commercial suppliers and were used without further purification. Benzene-d_6 and THF-d_8 (Cambridge Isotope Laboratories) were purified by storage over activated 4 Å molecular sieves for at least 48 hours prior to use. Celite and 4 Å molecular sieves (Aldrich) were dried under dynamic vacuum at 250 °C for 48 hours before use. All solvents (Aldrich) were purchased anhydrous and were dried over sodium for at least 24 hours, passed through a column of activated alumina, and were stored over activated 4 Å molecular sieves prior to use. Melting points were measured with a Barnstead Thermolyne MEL-TEMP capillary melting point apparatus using capillary tubes flame-sealed under vacuum; values are uncorrected. Elemental analyses were performed by Atlantic Microlab, Inc., in Norcross, GA. Several other characterization techniques were utilized in the course of these projects, including NMR, UV-Vis-NIR, and IR spectroscopies, electrochemistry, and X-Ray diffraction. These techniques are described in Chapter 1. The history and general chemistry of thorium and uranium are explained in Chapter 1, Section 1.3.1.

5.2 Actinide chalcogenide studies

5.2.1 Introduction

Actinide compounds are often studied for their unique chemical and structural properties which are made possible by the presence of the 5f electrons.[106-108] Actinide-chalcogenide systems have been previously studied to better understand the hypothesis that separation of the actinides and lanthanides from spent fuel, or from each other, could be facilitated by using soft-donor ligands (e.g. N, S).[107,109-111] The actinides have a greater tendency than the lanthanides to form covalent bonds with soft-donors, including sulfides, due to the radial extension of the 5f orbitals.[110,112] It is important to understand the fundamental structural, electronic, and bonding properties of actinide-chalcogenide compounds in order to learn to what extent the 5f-electrons impact the coordination chemistry of the actinides. There is also interest in how chalcogenide ligands bind with thorium,[113] which has no 5f-electrons. A comparison of how chalcogenides interact with thorium versus uranium may enhance actinide separations, including the target-based separations described in previous chapters. Recent publications show a growing interest in the reactivity of thorium with sulfur based ligands. Hayton in particular has studied the reactivity of thorium trisulfides,[114] and thorium-sulfide multiple bonds.[115] There are several examples in the literature of recent thorium-sulfide compounds,[108,111,113,114,116-121] including Evans and coworker's reaction of $[(C_5Me_5)_2ThH_2]_2$ with PhSSPh to give $(C_5Me_5)_2Th(SPh)_2$ (**1**),[111] and the bridging sulfide complex $[[\eta^5\text{-}1,3\text{-}(Me_3C)_2C_5H_3]_2Th](\mu\text{-}S)_2$ (**2**) published by Ren et.al. from the reaction of $[\eta^5\text{-}1,3\text{-}(Me_3C)_2C_5H_3]_2Th(bipy)$ with CS_2.[118] There are far fewer illustrations of sulfide insertion into thorium-X bonds (X = C,[122-124] N[125]); for example, Walter and coworkers published the insertion of PhNCS into $(C_5Me_5)_2Th(\eta^4\text{-}C_4Ph_2)$ to give $(C_5Me_5)_2Th[SC(=NPh)(C_4Ph_2)]$ (**3**).[123]Sattelberger published the original synthesis and the structural characterization of $(C_5Me_5)_2ThS_5$ (**4**) in 1986,[113] and it was recently reported by the Kiplinger group that **4** can be prepared using an actinide hydride route.[15]

5.3 Thorium

5.3.1 Experimental

The compounds $(C_5Me_5)_2ThCl_2$ (**5**),[126] $(C_5Me_5)_2ThMe_2$ (**6**),[127] $(C_5Me_5)_2ThPh_2$ (**7**),[128] $(C_5Me_5)_2Th(SPh)_2$ (**1**),[17] and K_2S_5 (**8**)[129] were prepared according to literature reports. NMR data can be found in Appendix B: NMR Data. Crystal structures for all the following compounds are described in Section 5.3.3.

Synthesis of $(C_5Me_5)_2ThS_5$ (4):

Route a: From $(C_5Me_5)_2ThCl_2$. A 20 mL scintillation vial equipped with a stir bar was charged with $(C_5Me_5)_2ThCl_2$ (**5**, 100.5 mg, 0.1748 mmol), K_2S_5 (**8**, 38.1 mg, 0.1728 mmol) and THF (2 mL). The reaction was stirred at ambient temperature for 18 h. The solvent was removed under reduced pressure and the product was extracted with toluene (5 mL), followed by filtration through Celite. The filtrate was collected and volatiles removed under reduced pressure to give **4** as a yellow-orange solid (106.3 mg, 0.1604 mmol, 92%). X-ray quality crystals were obtained by crystallization from a saturated toluene solution layered with hexane at −35 °C. The ^1H NMR spectrum and X-ray crystal structure data are in agreement with literature data for the compound.[113] ^1H NMR (C_6D_6, 298 K): δ 2.04 (s, 30H, C_5Me_5).

Route b: From $(C_5Me_5)_2ThMe_2$. A 20 mL scintillation vial equipped with a stir bar was charged with $(C_5Me_5)_2ThMe_2$ (**6**, 100.8 mg, 0.1893 mmol), S_8 (48.9 mg, 0.1906 mmol), and toluene (4 mL). The reaction was stirred at 70 °C for 18 h and filtered through Celite. The filtrate was collected and volatiles removed under reduced pressure to give **4** as a yellow solid (115.3 mg, 0.1739 mmol, 92%). X-ray quality crystals were obtained by crystallization from a saturated toluene solution layered with hexane at −35 °C. The ^1H NMR spectrum and X-ray crystal structure data are in agreement with literature data for the compound.

Route c: From $(C_5Me_5)_2ThPh_2$. A 20 mL scintillation vial equipped with a stir bar was charged with $(C_5Me_5)_2ThPh_2$ (**7**, 145.8 mg, 0.222 mmol), S_8 (57.0 mg, 0.222 mmol) and toluene (5 mL). The reaction was stirred at 70 °C for 6 h and the solvent removed under reduced pressure. The crude product was triturated

with $(Me_3Si)_2O$ (10 mL) and the solution passed through a Celite plug. The filtrate was discarded and the insoluble solid was redissolved in toluene (5 mL), passed through Celite and the volatiles removed under reduced pressure to give **4** as a yellow solid (98.7 mg, 0.149 mmol, 67%). The ^1H NMR spectrum is in agreement with literature data for the compound.

Route d: From $(C_5Me_5)_2Th(SMe)_2$. A 20 mL scintillation vial equipped with a stir bar was charged with $(C_5Me_5)_2Th(SMe)_2$ (**9**, 101.4 mg, 0.1695 mmol), S_8 (43.1 mg, 0.1680 mmol) and toluene (4 mL). The reaction was stirred at 70 °C for 18 h and filtered through Celite. The filtrate was collected and volatiles removed under reduced pressure to give **4** as a yellow solid (109.8 mg, 0.1695 mmol, 98%). X-ray quality crystals of **4** were obtained by crystallization from a saturated toluene solution layered with hexane at −35 °C. The ^1H NMR spectrum and X-ray crystal structure are in agreement with literature data for the compound.

Route e: From $(C_5Me_5)_2Th(SPh)_2$. A 20 mL scintillation vial equipped with a stir bar was charged with $(C_5Me_5)_2Th(SPh)_2$ (**1**, 100.0 mg, 0.139 mmol), S_8 (35.6 mg, 0.139 mmol) and toluene (5 mL). The reaction was stirred at 70 °C for 6 h and the solvent removed under reduced pressure. The crude product was triturated with $(Me_3Si)_2O$ (10 mL) and the solution passed through a Celite plug. The filtrate was discarded and the insoluble solid was redissolved in toluene (5 mL), passed through Celite, and the volatiles removed under reduced pressure to give **4** as a yellow solid (65.1 mg, 0.098 mmol, 71%). The ^1H NMR spectrum is in agreement with literature data for the compound.

Synthesis of $(C_5Me_5)_2Th(SMe)_2$ (9): A 20 mL scintillation vial equipped with a stir bar was charged with $(C_5Me_5)_2ThCl_2$ (**5**, 99.6 mg, 0.173 mmol, 1 equiv.), $NaSCH_3$ (25.3 mg, 0.361 mmol, 2 equiv.) and THF (5 mL) and the reaction was stirred at room temperature for 18 h. The solvent was removed under reduced pressure and the product extracted with toluene (5 mL), followed by filtration through Celite. The filtrate was collected and volatiles removed under reduced pressure to give **9** as a microcrystalline beige powder (91.1 mg, 0.152 mmol, 88%). X-ray quality crystals of **9** were obtained by recrystallization from a saturated

toluene solution layered with hexane at −35 °C. ^{1}H NMR (C$_6$D$_6$, 298 K): δ 2.11 (s, 30H, C$_5$*Me*$_5$), 2.51 (s, 6H, SC*H*$_3$). ^{13}C NMR (C$_6$D$_6$, 298 K): δ 11.52 (C$_5$*Me*$_5$), 12.06 ($v_{1/2}$ = 7 Hz, S-*Me*), 126.43 (*C*$_5$Me$_5$). NIR (29.59 mM, toluene, 298 K, cm^{-1} (M^{-1}cm^{-1}): 5886 (1.76), 5760 (3.31), 4610 (5.58), 4390 (15.21), 4297 (16.56). m.p. 242.1-244.0 °C. Anal. Calcd. for C$_{22}$H$_{36}$S$_2$Th (mol. wt. 596.69): C, 44.28; H, 6.08. Found: C, 44.42; H, 6.11.
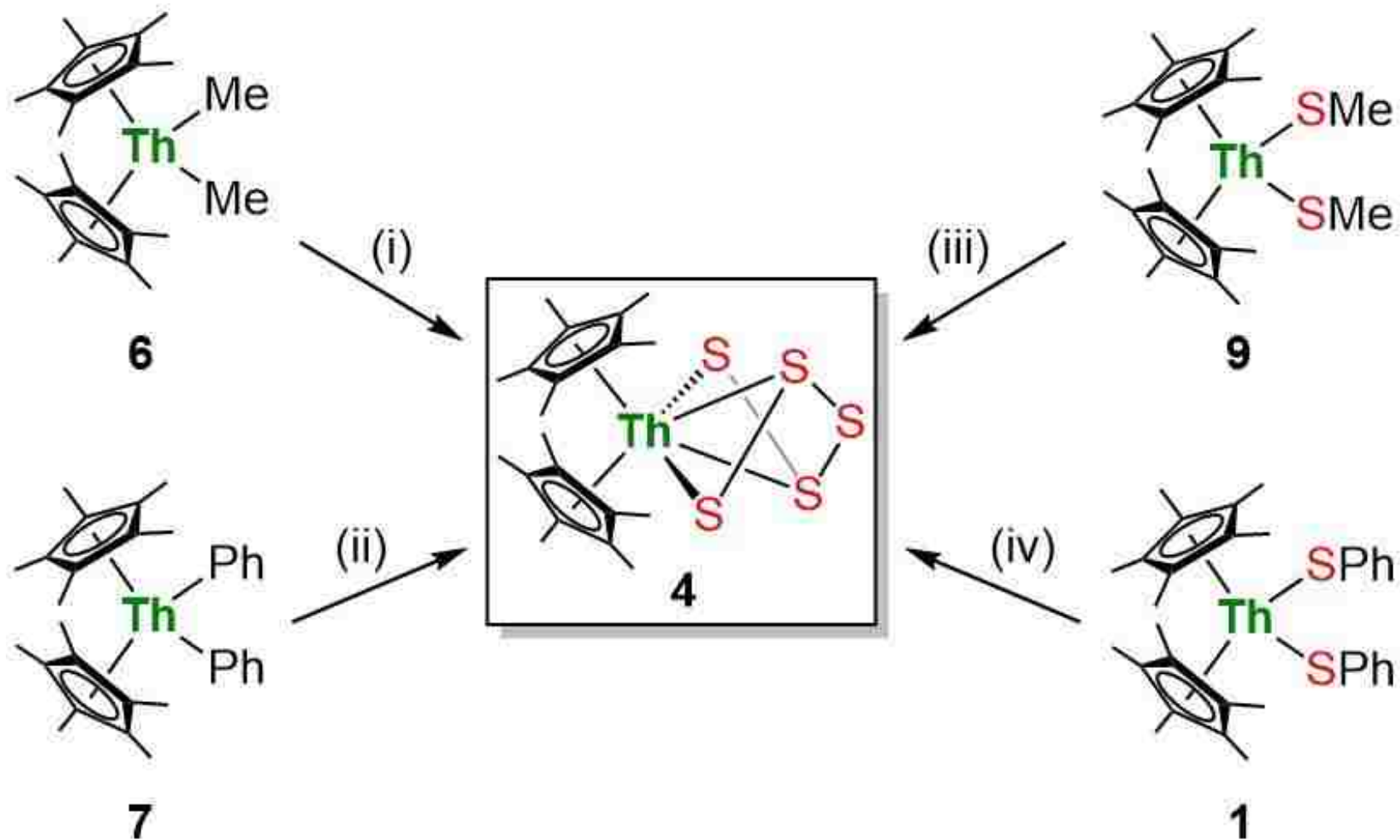
Scheme 2: Reagents and conditions: (i) 1 equiv. S8, toluene, 70 °C, 18 h, 92% yield, –Me2Sn, n=1-3; (ii) 1 equiv. S8, toluene, 70 °C, 6 h, 67% yield, –Ph2S2; (iii) 1 equiv. S8, toluene, 70 °C, 18 h, 98% yield, –Me2Sn, n=1,2; (iv) 1 equiv. S8, toluene, 70 °C, 18 h, 71% yield, –Ph2S2.

5.3.2 Results

The original preparation of **4** was carried out by reaction of $(C_5Me_5)_2ThCl_2$ (**5**) with one equivalent of Li_2S_5.[113] The most similar reaction in this research is that of **5** with K_2S_5 to yield **4** in 92% yield (Equation 7).

5 → **4**, 92% Yield
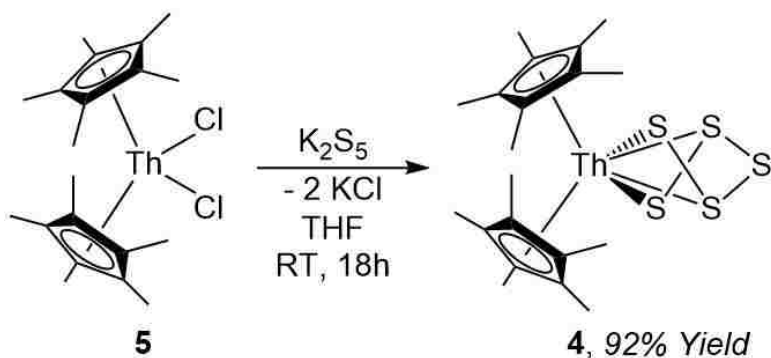
Equation 7. Synthesis of **4** using salt metathesis between $(C_5Me_5)_2ThCl_2$ and K_2S_5

The ^1H NMR spectroscopy (C_6D_6, δ = 2.04 ppm (s, 30H, C_5Me_5)) suggests that pure **4** was obtained. Single crystals of **4** suitable for X-ray diffractometry were obtained from toluene layered with hexane at −35 °C. Figure 72 shows the crystal structure of **4** from two different angles in order to draw attention to the η-4 bonding nature of the S_5 ring. Scheme 2 describes the variety of other ways that **4** can be synthesized, including the reaction of **1**, **6**, **7**, or **9** with elemental sulfur in toluene.

5 → **9**, 88% Yield
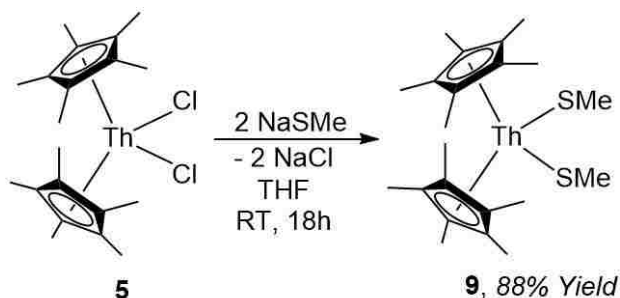
Equation 8. Synthesis of **9** using salt metathesis

Equation 8 shows the reaction of $(C_5Me_5)_2ThCl_2$ with NaSMe (2 equiv.) to form $(C_5Me_5)_2Th(SMe)_2$ (**9**). After recrystallization from toluene layered with hexane at −35 °C, large orange crystals of **5** (Figure 73) were obtained in 88% yield. The ^1H NMR spectrum in C_6D_6 of **9** exhibits two singlets at 2.11 ppm and 2.50 ppm corresponding to (C_5Me_5) and −SCH_3 respectively. A similar compound, $(C_5Me_5)_2Th(SCH_2CH_2CH_3)_2$, has a

similar ^{1}H NMR spectrum in C$_6$D$_6$. The C$_5$*Me$_5$* peaks appear at 2.12 ppm, and the propyl protons appear at

3.13, 1.78, and 1.06 ppm.[114] The ^{13}C NMR of **4** shows three peaks corresponding to the three distinct

carbons in the complex (*C$_5$*Me$_5$ = 126.43 ppm, C$_5$*Me$_5$* = 11.52 ppm; –S*Me* = 12.06 ($v_{1/2}$ = 7 Hz) ppm). Figure

73 shows the solid state structure of **9**, which is isostructural to the known uranium analogue

((C$_5$Me$_5$)$_2$U(SMe)$_2$, **10**).[107]

5.3.3 Crystal Structures

a)

b)
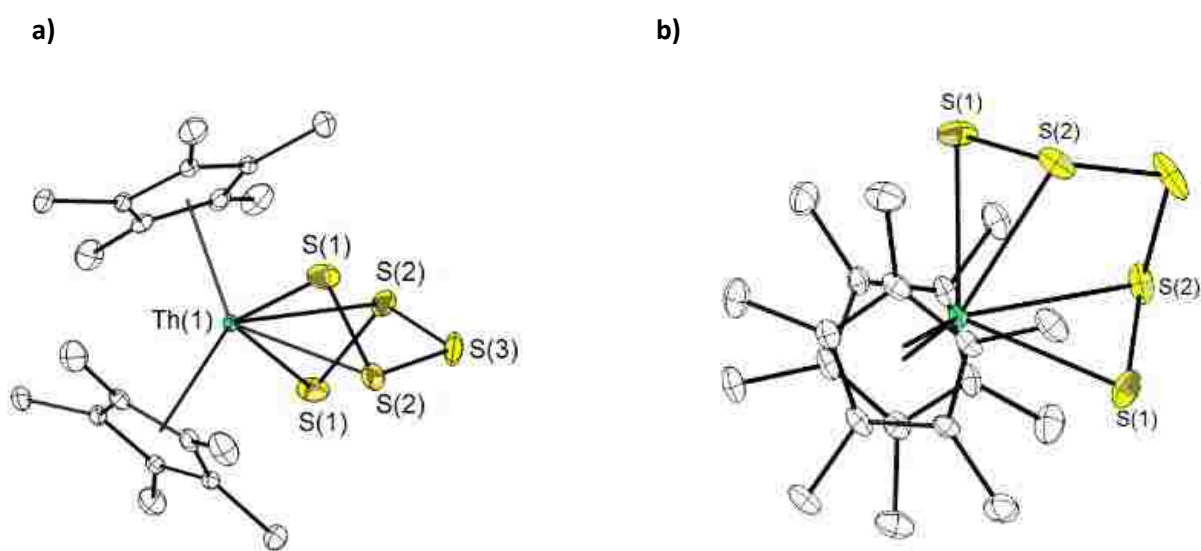
Figure 72. a) Side view and b) top-down view of complex **4** formed from the reactions detailed in Scheme 2, with 50% probability ellipsoids. Hydrogen atoms are omitted for clarity. Selected bond lengths (Å) and angles (deg): Th(1)–S(1) = 2.785(7), Th(1)–S(2) = 3.024, Cent–Th(1) = 2.537(2), S(1)–Th(1)–S(1) = 13

Compound **4** crystallizes in the tetragonal P$\bar{4}$n2 space group (Figure 72). The lattice parameters of this structure

are slightly shorter (*a* = 15.2456 Å and *c* = 10.1349 Å) than previously reported (*a* = 15.350(3) Å and *c* = 10.281(5)

Å), which is a direct result of the temperature difference between experiments (140 K vs 298 K). Complex **4** has a

distorted trigonal prism structure, with the ThS$_5$ ring adopting a twist boat conformation, in agreement with the

known structure. The Th–S and C$_{cent}$–Th (Cent = C$_5$Me$_5$ centroid) bond distances as well as C$_{cent}$–Th–C$_{cent}$' and S–

Th–S' bond angles for **4** are comparable to Sattelberger's compounds [(C$_5$Me$_5$)$_2$ThS$_5$] (Th–S = 2.768(4) Å, C$_{cent}$–Th

= 2.52 Å, C$_{cent}$–Th–C$_{cent}$' = 129.9 °, S–Th–S' = 113.3(1) °),[113] as well as other similar thorium-calcogenide compounds

[η^5-1,3-(Me$_3$C)$_2$C$_5$H$_3$]$_2$Th}(μ-CS$_3$)$_2$ (Th–S = 2.988(1) Å, C$_{cent}$–Th = 2.587(2) Å, C$_{cent}$–Th–C$_{cent}$′ = 117.5(1) °),[118]

[(C$_5$Me$_5$)$_2$Th(SCH$_2$CH$_2$CH$_3$)$_2$] (Th–S = 2.718(3) Å, C$_{cent}$–Th = 2.535 Å, C$_{cent}$–Th–C$_{cent}$′ = 134.9 °, S–Th–S′ = 102.5(2) °),[114]

[η^5-1,2,4-(Me$_3$C)$_3$C$_5$H$_2$]$_2$Th}$_2$-(μ-S)$_2$] (Th–S = 2.709(2) Å, C$_{cent}$–Th = 2.659(9) Å, C$_{cent}$–Th–C$_{cent}$′ = 119.4(1) °, S–Th–S′ = 76.8(1) °).[119]

Compound **9** crystallizes in the orthorhombic space group Pbcn (Figure 73). The molecular structure of **9** can best be described as a pseudo-tetrahedral bent metallocene. Crystallographic comparisons between compounds **4** and **9** show the Th–S bond distance in **4** (2.785(7) Å) is longer than in **9** (2.724(5) Å). Likewise, the C$_{cent}$–Th bond distance in **4** (2.537(2) Å) is slightly longer than in **9** (2.526(2) Å). The C$_{cent}$–Th–C$_{cent}$′ bond angle in **4** (130.11(6) °) is slightly more acute than in **9**, (136.42(5) °), and could be the result of the dative interactions of the β sulfurs with thorium in **4**. This last point is corroborated by comparing the thiolate–thorium–thiolate bond angles in **4** (113.85(3) °) and **9** (98.81(3) °), since the β dative interactions take place inside the S-Th-S′ bond angle in **4**. Thus compound **4** is more sterically encumbered than **9**.

Compound **9** can also be compared to the crystal structure of the uranium analogue, (C$_5$Me$_5$)$_2$U(SMe))$_2$ (**10**). The Th–S and C$_{cent}$–Th bond distances (2.724(5) and 2.526(2) Å, respectively) and the C$_{cent}$–Th–C$_{cent}$′, S–Th–S′, and Th–S–C bond angles (136.42(5) °, 98.81(3) °, and 106.22(7) °, respectively) are longer and more obtuse than those reported for (C$_5$Me$_5$)$_2$U(SMe)$_2$ (**10**) (U–S = 2.639(3) Å, C$_{cent}$–U = 2.47(2) Å, C$_{cent}$–U–C$_{cent}$′ = 137.6(4) °, S–U–S′ = 97.2(4) °, U–S–C = 108.1(5) °).[107] The elongated Th–S distances in **10** are longer than the 0.05 Å expected difference between the ionic radii of uranium(IV) and thorium(IV),[130] which may indicate greater covalency between uranium and the SMe$^-$ fragment.
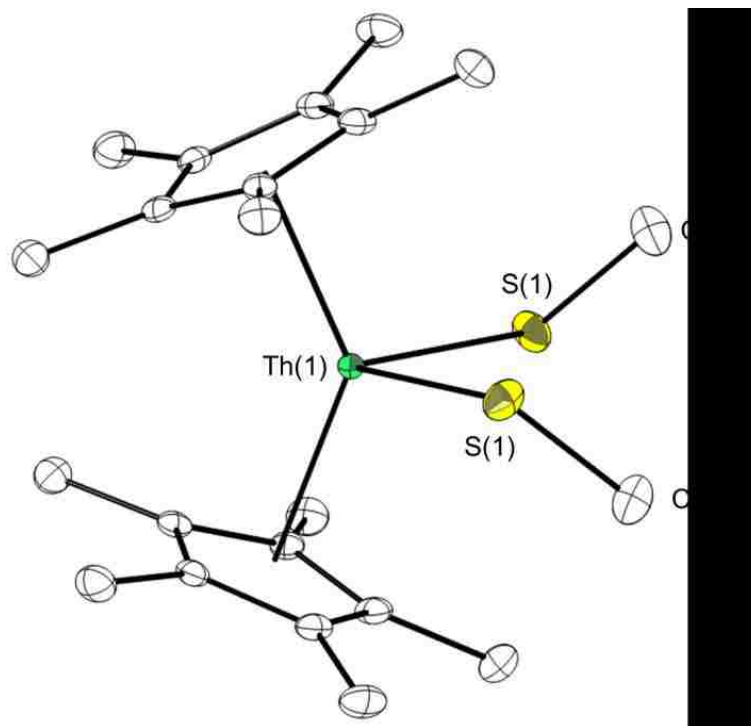
Figure 73. ORTEP structure of **9**. Hydrogens are removed for clarity and ellipsoids are at 50% probability.

Table 26. Crystal data for $(C_5Me_5)_2Th(SMe)_2$.

	$(C_5Me_5)_2Th(SMe)_2$
Empirical Formula	$C_{22}H_{36}S_2Th$
Formula Weight	596.67
Crystal System	Orthorhombic
a [Å]	14.360(5)
b [Å]	9.552(8)
c [Å]	16.540(1)
B [°]	90
V [Å^3]	2256.7(3)
Space Group	Pbcn
Z	4
ρ [g/cm^3]	1.756
μ [MoKα]	6.796
T [K]	140(1)
$2\Theta_{max}$ [°]	57.28
Min/max trans.	0.1935/0.3435
Total reflns	24625
Unique reflns	2820
Parameters	120
$R_1(wR_1)$ (all data)	0.0133 (0.0185)

117

5.3.4 Mechanism

During the investigation of the reaction of S_8 with $(C_5Me_5)_2ThMe_2$ (**5**), several volatile byproducts (Me_2S_n, n = 1–3) and $(C_5Me_5)_2Th(SMe)_2$ were discovered as potential intermediates, as identified by their ^{1}H NMR spectroscopic resonances (in C_6D_6, δ = 1.74 ppm, 1.97 ppm, and 2.15 ppm for n = 1–3 respectively as compared to authentic standards). Once the reaction goes to completion, no other thorium complexes are observed (Figure 74). This might suggest that **5** can undergo insertion of S_8 in the thorium-carbon bond to yield compound **4**. Compound **9** appears in the NMR spectrum at 2.11 ppm (C_5Me_5) and 2.51 ppm (CH_3), denoted by asterisks in Figure 74.
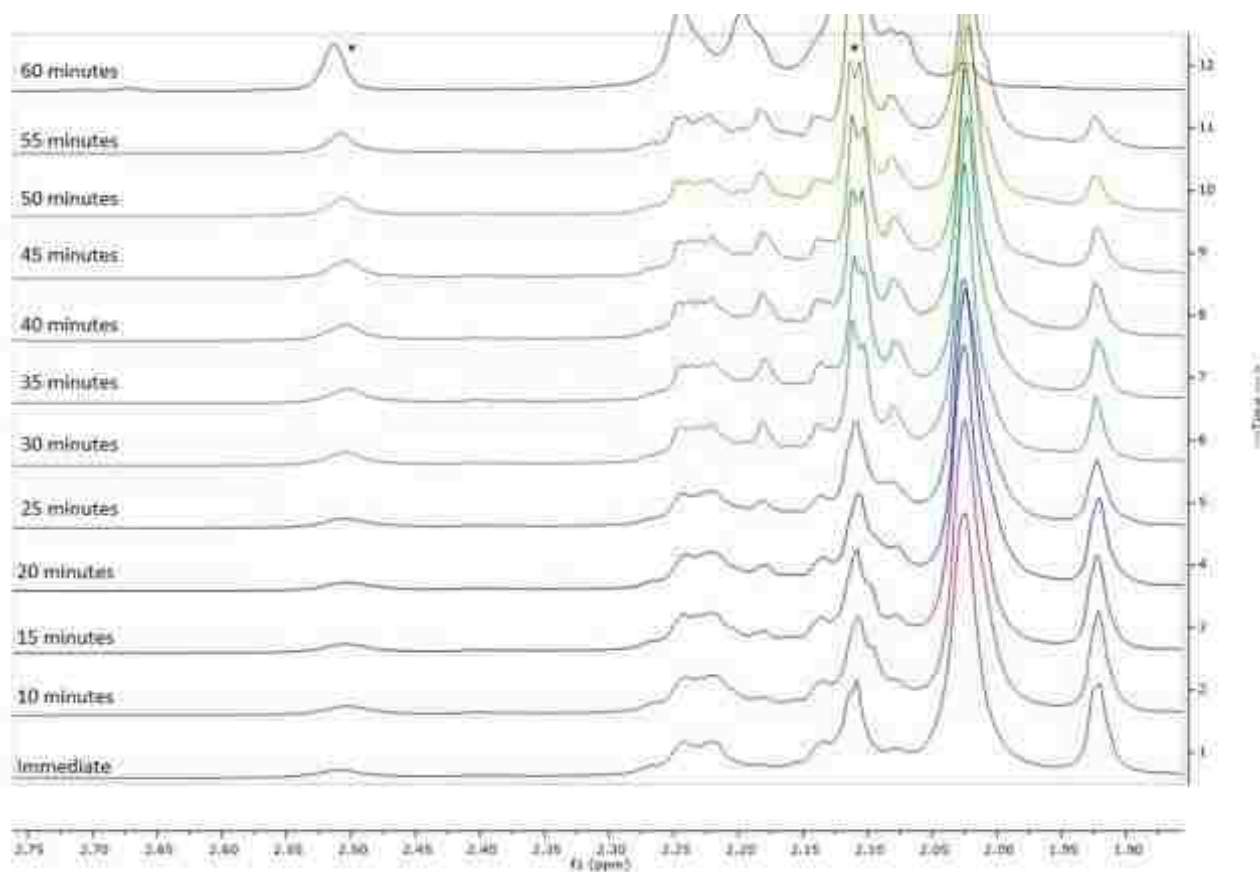
Figure 74. NMR data taken over the course of an hour shows the ingrowth of the intermediate $(C_5Me_5)_2Th(SMe)_2$ at 2.11 ppm and 2.51 ppm (indicated by asterisks).

It also appears that **9** will react with Me_2S_3 to form a second, unknown, intermediate at 2.07 ppm. In a separate experiment, $(C_5Me_5)_2Th(SMe)_2$ (2.11 ppm C_5Me_5, 2.51 ppm SMe) and Me_2S_3 (2.15 ppm) were reacted in an NMR tube at room temperature (Figure 75). In less than 30 minutes, Me_2S_2 is present in the NMR at 1.98 ppm. The

mechanism of the overall reaction to make $(C_5Me_5)_2ThS_5$ (2.02 ppm) is more complicated than initially thought, but seems to imply a sulfur insertion between the thorium-carbon bond in the first step.
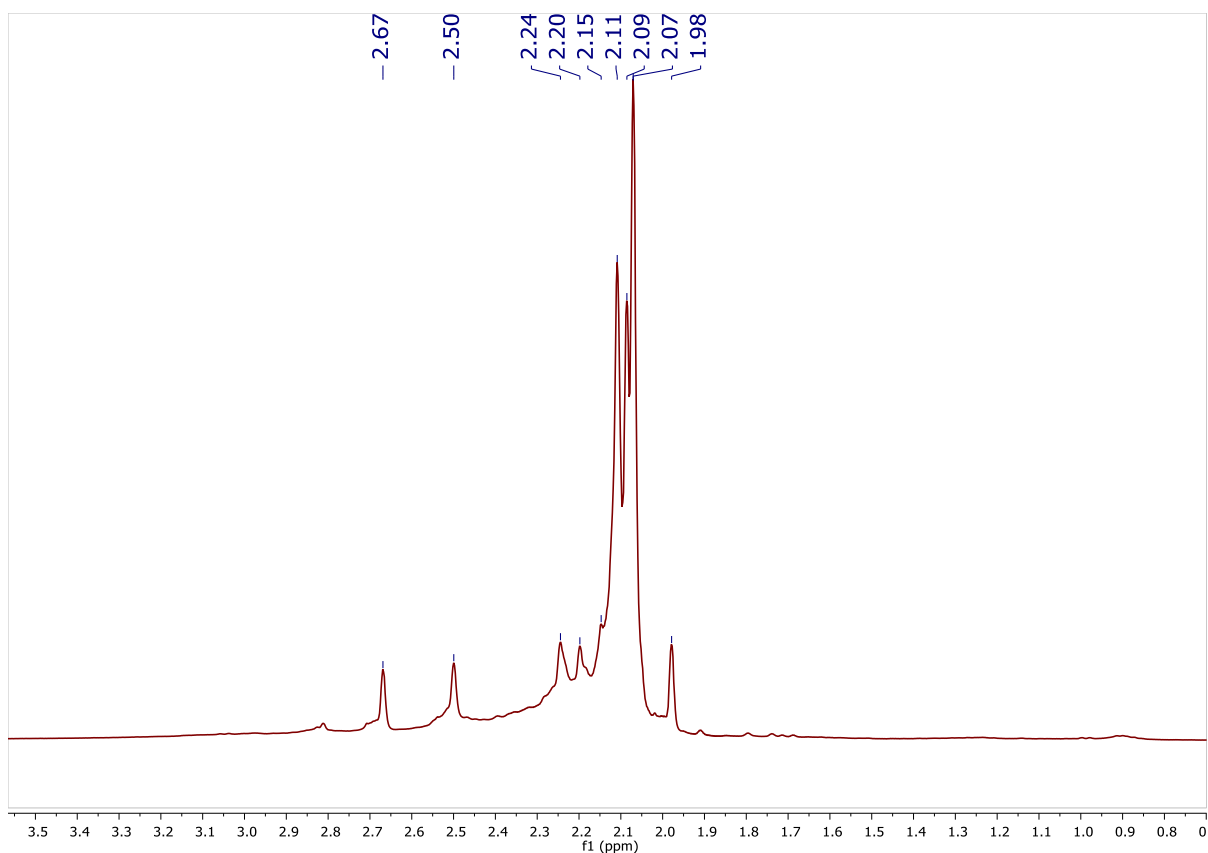
Figure 75. ^1H NMR (400 MHz, C_6D_6) of $(C_5Me_5)_2Th(SMe)_2$ + Me_2S_3

To further examine if $(C_5Me_5)_2Th(SR)_2$ was an intermediate, S_8 was reacted with both $(C_5Me_5)_2Th(SMe)_2$ (**9**) and $(C_5Me_5)_2Th(SPh)_2$ (**8**) in toluene at 70 °C. Both reactions yielded complex **4**, as well as Me_2S_n and Ph_2S_n, respectively (n =1-3, Scheme 2). While compound **4** can be obtained in 98% yield from **9**, **4** is only attainable from **8** in 71% yield, due to difficulties in removing nonvolatile Ph_2S_2.

5.4 Uranium

5.4.1 Experimental

Interest in comparisons between uranium and thorium chalcogenide complexes stems from the potential influence of 5f-electrons on the chemistries between these two actinides. The uranium analogue to **9** is known (**10**), and is described above. No known analogue to **4** exists and any attempts to synthesize it using the previous methods (Scheme 2) resulted in $(C_5Me_5)H$, $(C_5Me_5)_2$, and unidentified uranium-sulfide products. In the first 30 minutes of the reaction, peaks appear at 10.06 and 8.89 ppm in the ^{1}H NMR that were promising (Figure 76), but over time they disappear and an unidentified solid precipitates out. Also present in the NMR are $(C_5Me_5)_2$ (1.77, 1.69, and 1.15 ppm) and $(C_5Me_5)H$ (1.80, 1.75, 1.01, and 0.98 ppm); more evidence that the molecule is prone to decomposition as evidenced by the free (C_5Me_5) groups.
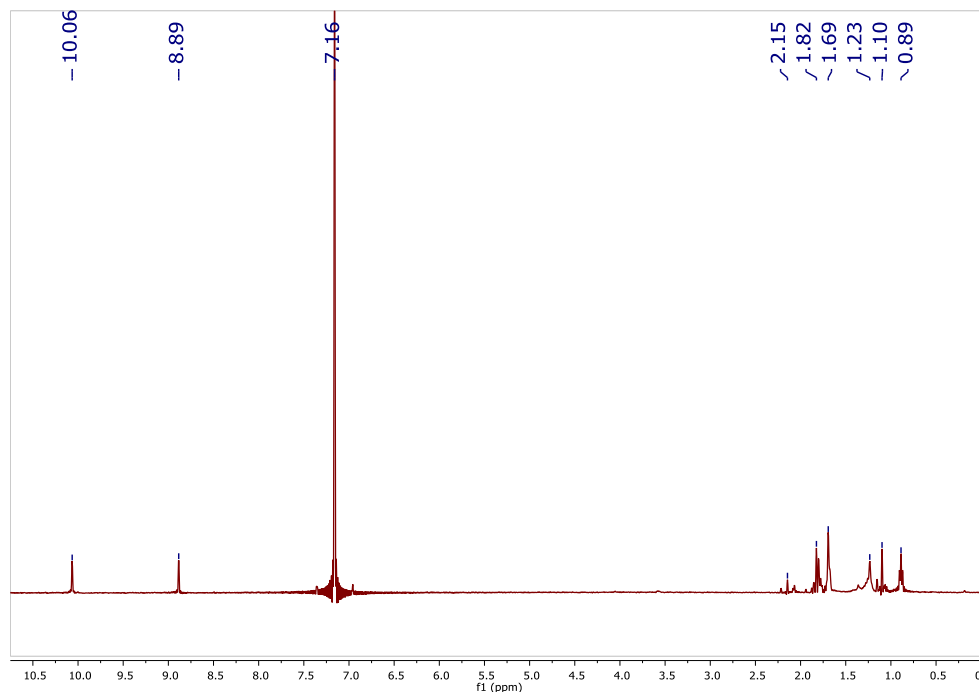
Figure 76. ^{1}H NMR spectrum (400 MHz, 295 K, C_6D_6) of the reaction between $(C_5Me_5)_2UMe_2$ and S_8.

5.4.2 Results

Comparisons between the structures of $(C_5Me_5)_2U(SMe)_2$ and $(C_5Me_5)_2Th(SMe)_2$ were previously mentioned, but the two compounds were also compared spectroscopically using UV-Vis-NIR data and cyclic voltammetry. Cyclic and square wave voltammetry were performed for both compounds as well as $(C_5Me_5)_2Th(SPh)_2$, in THF using $[NPr_4][B(C_6F_5)_4]$ as the supporting electrolyte and referenced to ferrocenium/ferrocene. However, the results were not reproducible and therefore were inconclusive.

UV-Vis-NIR spectroscopy was done for $(C_5Me_5)_2Th(SMe)_2$, $(C_5Me_5)_2Th(SPh)_2$, and $(C_5Me_5)_2U(SMe)_2$. Figure 77 details the Near-IR region for all three complexes. Both thorium complexes show very little absorption, but weak peaks can be seen for the uranium complex. These peaks correspond to Laport-forbidden transitions, which are consistent with a uranium(IV) center.[131] Figure 78 presents the UV-Visible spectra for all three complexes. Features in the UV-Visible region are generally indicative of electronic transitions between metal-based 5f orbitals and higher energy 6d metal-based orbitals, which explains why there are no apparent transitions for the thorium complexes.[131]
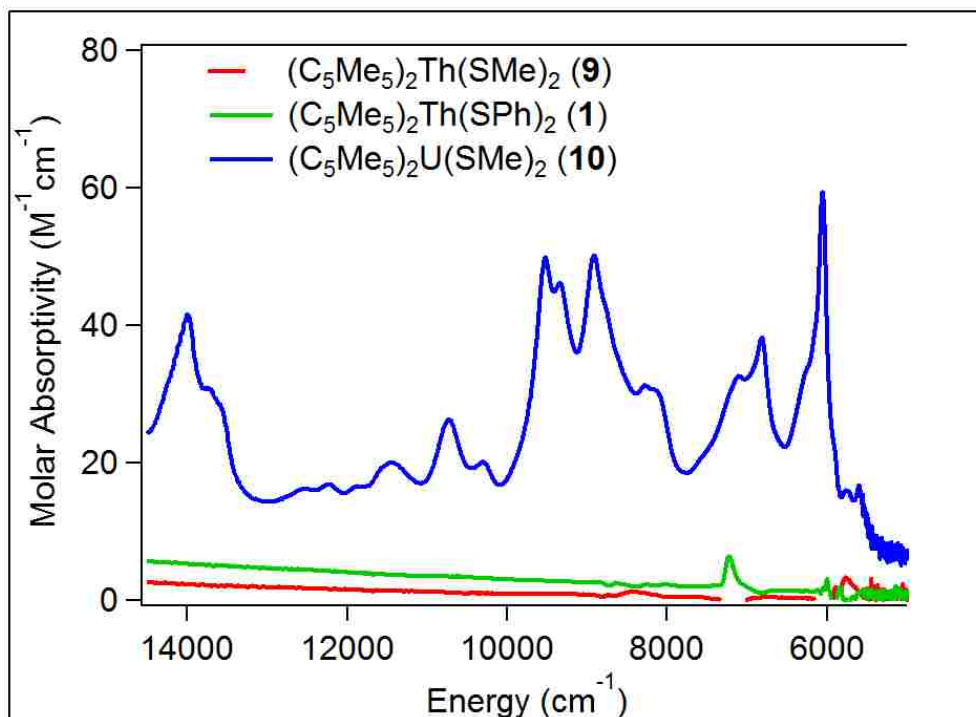
Figure 77. Near-IR absorption region for $(C_5Me_5)_2Th(SMe)_2$, $(C_5Me_5)_2Th(SPh)_2$, and $(C_5Me_5)_2U(SMe)_2$.
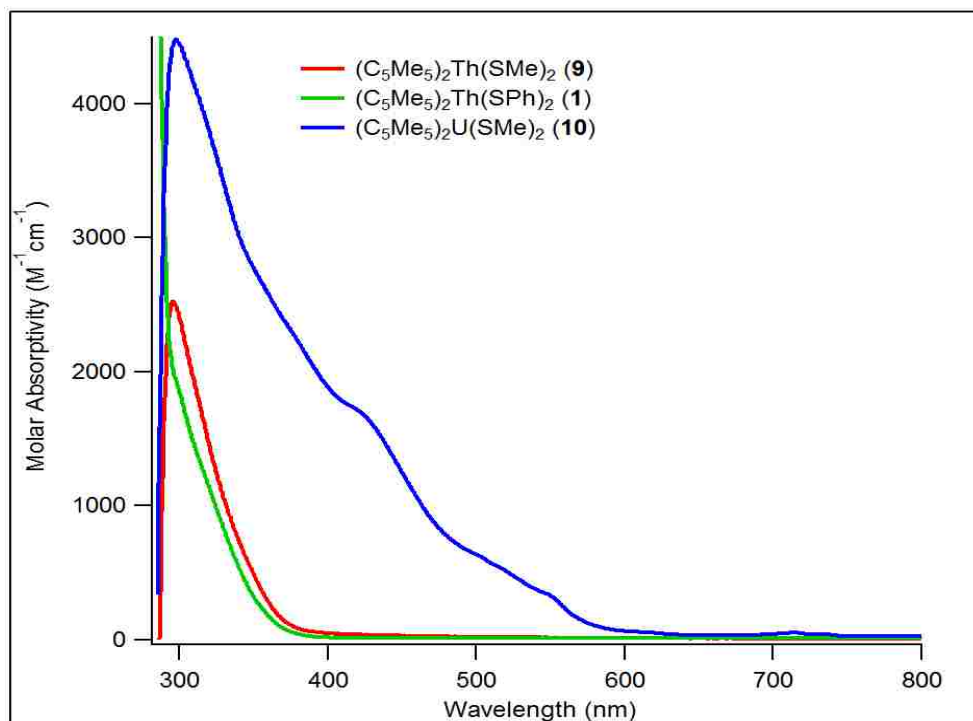
Figure 78. UV-Visible spectra for $(C_5Me_5)_2Th(SMe)_2$, $(C_5Me_5)_2Th(SPh)_2$, and $(C_5Me_5)_2U(SMe)_2$.

5.5   Conclusions

The data presented in this chapter show that $(C_5Me_5)_2ThS_5$ is a thermodynamic sink achievable through several synthetic routes. Evidence from NMR experiments suggests that the reaction of $(C_5Me_5)_2ThMe_2$ and S_8 first forms $(C_5Me_5)_2Th(SMe)_2$ as an intermediate, indicating the insertion of sulfur between the thorium-carbon bond as a step in the mechanism. The formation of Me_2S_x during the course of the reaction supports this hypothesis. The novel complex $(C_5Me_5)_2Th(SMe)_2$ was fully characterized by ^{1}H and ^{13}C NMR spectroscopy, elemental analysis, and X-ray diffractometry. Both ^{1}H NMR spectroscopy and X-ray crystallography were used to characterize $(C_5Me_5)_2ThS_5$, and the results were compared to literature values as well as to $(C_5Me_5)_2Th(SMe)_2$.

The NMR results from small-scale experiments show that uranium does not behave chemically similarly to the thorium analogue under the examined conditions. The reaction of $(C_5Me_5)_2UMe_2$ and S_8 may form the $(C_5Me_5)_2US_5$ analogue, but it quickly degrades into an insoluble uranium-sulfide product and $(C_5Me_5)_2$. The ability of uranium to adopt multiple oxidation states may interfere with the stability of the desired product. However, a longer distance between the sulfur atoms and the metal center of the novel complex $(C_5Me_5)_2Th(SMe)_2$ compared to its known uranium analogue show that there is greater covalency between the metal and the SMe^- fragment in the uranium complex. This could be due to the involvement of the 5f-electrons in bonding.   Differences in spectroscopic and electrochemical features between the thorium(IV) and uranium (IV) compounds have been shown, which could relate to additional f-electron bonding ability in uranium.

Chapter 6: C–X Activation Mediated by Uranium

6.1   Background

Transition metal mediated C–X (X = H, F, Cl, Br, or I) bond activations have been studied for decades as a way to improve synthetic routes to novel organometallic compounds.[132-142] Theoretical calculations have shown that C–X activation is important for the formation of C–C bonds;[133,134] because halides are generally good leaving groups, the activation barrier is lower thus promoting the formation of C–C bonds and the synthesis of organic (or organometallic) molecules.[133]   However, studies of actinide mediated C–X activation are lacking in the literature. Several organometallic U–F complexes have been studied,[143-160] but of those, very few were formed using C–X activation techniques.[153,160] Non-fluorinated uranium complexes have been used in studies of C–H activation,[161-163] but there is a distinct lack in the literature of uranium-based C–X activation exploration. The interest in the $(C_5Me_5)_2$U–bpy (bpy = 2,2'-bipyridyl) system stems from its low-valent synthetic equivalence and of the potential for radical formation with the redox-active bpy ligand.[151,164,165] The only other actinide example of addition of organics across a bpy ligand was reported in late 2016 by Garner et.al.[166] Their example shows C–N bond activation and addition of an alkyl at the *p*-carbon of 2,2'–bipyridine bound to a thorium metal center. A few publications show examples of transition metal C–X bond activations that include bpy ligands on the metal; [140-142] however, the alkyl group adds to the metal center rather than across the bpy ligand.

This chapter describes the reactivity of An-bpy compounds with a suite of benzyl halides to afford $(C_5Me_5)_2$U(X)(bpy)Bn (Bn = benzyl, X = F, Cl, Br, I). These are unusual examples of C–X activation using organouranium compounds and feature a rare example of a uranium-fluoride bond. Interestingly, there is evidence of the trans effect, a weakening and lengthening of a metal-halide bond when it is trans to a more strongly bonded ligand, in all of the examples. Typically, the opposite is seen with actinide metal–halide bonds.[167,168] The U–F complex is the only one of the series that shows radical character in the bipyridine ring. The exploration of the mechanism behind the formation of $(C_5Me_5)_2$U(X)(bpy)(Bn) is also

described, as well as evidence of potential f-electron participation in bonding. Understanding the chemistry of uranium in halide-containing environments is important for expanding the knowledge base of how the actinides may interact with fission products or in detonation environments that are rich in salts.

6.2 Experimental

The starting materials $(C_5Me_5)_2U$-bpy (**11**),[165] its precursors,[169] KC_8,[170] and $[Cp_2Co]F$[171] were prepared according to literature procedures. Benzyl chloride, benzyl bromide, and benzyl iodide were purchased from Aldrich and treated with a column of activated alumina before use to remove impurities or degradation products. All NMR data can be found in Appendix B and crystal structure parameters are located in Appendix C. Crystal structures are described in Section 6.3.1.

Synthesis of benzyl fluoride (12): A 20 mL scintillation vial was charged with a stir bar, $[Cp_2Co]F$ (0.1512 g, 0.7265 mmol, 1.5 equiv), benzyl bromide (0.0592 mL, 0.4984 mmol), and 3 mL of C_6D_6. The reaction stirred at room temperature for 3 h to give full halide exchange by NMR. The solution was filtered through Celite and a glass wool plug to remove $[Cp_2Co]Br$ and give a clear, pale-green-colored solution of benzyl fluoride in C_6D_6. The solution was then added directly to the reaction described below to make **3**. ^1H and ^{19}F NMR spectra collected in benzene-d_6 were consistent with data previously reported for benzyl fluoride.[171,172]

Synthesis of $(C_5Me_5)_2U(F)(bpy)(Bn)$ (13): a) A 20 mL scintillation vial was charged with a stir bar, $(C_5Me_5)_2U$-bpy (**11**, 0.1024g, 0.1542 mmol), benzyl fluoride (0.0250 mL, 0.2313 mmol, 1.5 equiv.) and 3 mL of toluene. The solution turned red-brown immediately, and the majority of the reaction had taken place within 10 minutes at room temperature. The reaction mixture was stirred at room temperature for 2 h. Volatiles were then removed under reduced pressure and the red-brown residue was re-dissolved in hexane, filtered through a Celite-padded frit, and washed with 20 mL of hexane. Volatiles were again

removed under reduced pressure and the tacky red-brown solid was re-dissolved in minimal hexane and cooled to −30 °C overnight to give red-brown crystalline $(C_5Me_5)_2U(bipy)$benzyl-fluoride (0.0923 g, 0.1191 mmol, 77.2 %). ^{1}H NMR (benzene-d_6, 298 K): δ 1.46 (d, 30H, C$_5$*Me*$_5$ isomer A), -2.51 (s, 40H, C$_5$*Me*$_5$ isomer B). ATR-IR (Neat, 296 K, cm^{-1}): ν 2898m, 2850m, 1977w, 1773s, 1734s, 1700s, 1558s, 1437s, 1365s, 1289s, 1127s, 1013s, 952s, 770s, 740s, 698s, 639s, 536s. UV/Vis (Toluene, 296 K, 1 mM, cm^{-1} (M^{-1}cm^{-1})): 33389 (5763), 22026 (1525). NIR (Toluene, 296 K, 30 mM, cm^{-1} (M^{-1}cm^{-1})): 9524 (260.9), 9200 (245.7), 8776 (226.3), 8313 (202.7), 7994 (178.9), 7648 (183.7), 6911 (125.8), 6494 (112.1), 6042 (78.7), 5700 (107.6), 4840 (39.3), 4337 (70.5). mp: 152.5-154.9 °C. Anal. Calcd. For $C_{37}H_{45}FN_2U$ (mol. wt. 774.79): C, 58.20; H, 6.39; N, 3.48. Found: C, 57.99; H, 6.41; N, 3.77.

b) A 5 mL dram vial was charged with a stir bar, $(C_5Me_5)_2U(Br)(bpy)Bn$ (**15**, 7.30 mg, 0.0087 mmol), [Cp$_2$Co]F (2.4 mg, 0.0115 mmol), and 0.5 mL C$_6$D$_6$. The reaction mixture was monitored at room temperature for 24 h. One isomer of the bromide converted to the fluoride in less than quantitative yields. After 24 h, $(C_5Me_5)_2$ had formed and bromide starting material was still present.

Synthesis of $(C_5Me_5)_2U(Cl)(bpy)(Bn)$ (14): A 20 mL scintillation vial was charged with a stir bar, $(C_5Me_5)_2U$-bpy (0.1019 g, 0.1534 mmol), benzyl chloride (0.0175 mL, 0.1521 mmol) and 3 mL of toluene. The reaction mixture was stirred at room temperature for 2 h, although the reaction changed color to dark brown immediately. Volatiles were then removed under reduced pressure and the brown residue was re-dissolved in hexane, filtered through a Celite-padded frit, and washed with 20 mL of hexane. Volatiles were again removed under reduced pressure and the tacky brown solid was re-dissolved in minimal hexane and cooled to −30 °C overnight to give brown crystalline $(C_5Me_5)_2U(Cl)(bpy)Bn$ (0.0635 g, 0.0803 mmol, 52.3%). ^{1}H NMR (benzene-d_6, 298 K): δ 13.15 (d, 30H, C$_5$*Me*$_5$ isomer A), 6.03 (s, 44H, C$_5$*Me*$_5$ isomer B). $(C_5Me_5)_2UCl_2$ is also present by NMR.[169] ATR-IR (Neat, 296 K, cm^{-1}): ν 2900m, 2850m, 1636s, 1600s, 1474s, 1440s, 1366s, 1290s, 1246s, 1162s, 1126s, 1010s, 885s, 743s, 699s, 610s, 558s. UV/Vis (Toluene, 296 K, 1 mM, cm^{-1} (M^{-1}cm^{-1})): 33223 (2772), 22883 (1018). NIR (Toluene, 296 K, 30 mM, cm^{-1} (M^{-1}cm^{-1})):

10560 (76.1), 9268 (141.5), 8503 (97.1), 8217 (110.1), 7339 (73.5), 7018 (67.8), 6361 (67.8), 6127 (79.3), 5736 (67.4), 4568 (60.4), 4207 (74.5). mp: 213.1 °C – 215.3 °C. Elemental analysis for $C_{37}H_{45}ClN_2U$ (mol. wt. 791.25) was not identified after three attempts.

Synthesis of $(C_5Me_5)_2U(Br)(bpy)(Bn)$ (15): A 20 mL scintillation vial was charged with a stir bar, $(C_5Me_5)_2U$-bpy (0.1999 g, 0.3010 mmol), benzyl bromide (0.0518 g, 0.3031 mmol) and 3 mL of toluene. The reaction mixture was stirred at room temperature for 2 h, although the reaction changed color to dark brown immediately. Volatiles were then removed under reduced pressure and the brown residue was re-dissolved in hexane, filtered through a Celite-padded frit, and washed with 30 mL of hexane. Volatiles were again removed under reduced pressure and the tacky brown solid was re-dissolved in minimal hexane and cooled to −30 °C overnight to give brown crystalline $(C_5Me_5)_2U(Br)(bpy)Bn$ (0.1001 g, 0.1156 mmol, 38.4 %). ^1H NMR (benzene-d_6, 298 K): δ 14.93 (s, 15H, C$_5$*Me*$_5$ isomer A), 14.60 (s, 15H, C$_5$*Me*$_5$ isomer A), 8.55 (d. 85H, C$_5$*Me*$_5$ isomer B). $(C_5Me_5)_2UBr_2$ is also present by NMR.[173] ATR-IR (Neat, 296 K, cm^{-1}): ν 2894m, 2850m, 1636s, 1600s, 1572s, 1440s, 1365s, 1290s, 1245s, 1162s, 1126s, 1009s, 883s, 742s, 699s, 620s, 537s. UV/Vis (Toluene, 296 K, 1 mM, cm^{-1} (M^{-1}cm^{-1})): 33278 (4616.6), 23202 (1682). NIR (Toluene, 296 K, 30 mM, cm^{-1} (M^{-1}cm^{-1})): 10515 (34.7), 9255 (107.7), 8889 (68.5), 8237 (81.7), 7396 (53.3), 7052 (55.3), 6402 (44.8), 6209 (52.4), 5767 (27.3), 4530 (24.7), 4094 (34.2). mp: 203.4-206.1 °C. Anal. Calcd. For $C_{37}H_{45}BrN_2U$ (mol. wt. 835.70): C, 53.18; H, 5.43; N, 3.35. Found: C, 53.04; H, 5.44; N, 3.32.

Synthesis of $(C_5Me_5)_2U(I)(bpy)(Bn)$ (16): a) A 20 mL scintillation vial was charged with a stir bar, $(C_5Me_5)_2U$-bpy (0.0993 g, 0.1495 mmol), benzyl iodide (0.0187 mL, 0.1500 mmol) and 5 mL of toluene. The reaction mixture was stirred at room temperature for 2 h, although the reaction changed color to dark brown immediately. Volatiles were then removed under reduced pressure and the dark brown residue was re-dissolved in hexane, filtered through a Celite-padded frit, and washed with 30 mL of hexane. Volatiles were again removed under reduced pressure and the tacky dark brown solid was re-dissolved in minimal hexane and cooled to −30 °C overnight to give dark brown crystalline $(C_5Me_5)_2U(I)(bpy)Bn$ (0.0852 g,

0.0965 mmol, 65 %). ^{1}H NMR (benzene-d_6, 298 K): δ 16.51 (s, 15H, C$_5Me_5$ isomer A), 15.66 (s, 15H, C$_5Me_5$ isomer A), 11.53 (d, 80H, C$_5Me_5$ isomer B). (C$_5$Me$_5$)$_2$UI$_2$ is also present by ^{1}H NMR.[169] ATR-IR (Neat, 296 K, cm^{-1}): ν 3853s, 3750s, 3744s, 3675m, 3629m, 2427m, 2159s, 2032s, 1653s, 1559s, 1540s, 1437s, 1325s, 1290s, 1126s, 1010s, 988s, 769s, 737s, 728s, 614s. UV/Vis (Toluene, 296 K, 0.50 mM, cm^{-1} (M^{-1}cm^{-1})): 22831 (4838) NIR (Toluene, 296 K, 30 mM, cm^{-1} (M^{-1}cm^{-1})): 10395 (37), 9461 (78), 9208 (94), 8846 (72), 8268 (80), 7424 (53), 7025 (48), 6433 (43), 6166 (51), 5999 (39), 5850 (36), 5571 (22), 4638 (21), 4590 (26), 4544 (32), 4480 (37). mp: 162.3-163.1 °C. Anal. Calcd. For C$_{37}$H$_{45}$IN$_2$U (mol. wt. 882.70): C, 50.35; H, 5.14; N, 3.17. Found: C, 50.95; H, 5.40; N, 3.06.

b) An NMR tube was charged with a stir bar, (C$_5$Me$_5$)$_2$U(Br)(bpy)Bn (0.0053 g, 0.0063 mmol), iodotrimethylsilane (0.9 µL, 0.0063 mmol) and 0.5 mL of C$_6$D$_6$. Within 40 minutes, the halide exchanged (in less than quantitative yields) to give one isomer of (C$_5$Me$_5$)$_2$U(I)(bpy)Bn.

Synthesis of (C$_5$Me$_5$)$_2$U(^{t}Bu$_2$bpy) (17): A 20 mL scintillation vial was charged with a stir bar, (C$_5$Me$_5$)$_2$UI(py) (0.1025 g, 0.1436 mmol), KC$_8$ (0.0299 g, 0.2212 mmol, 1.5 equiv.), 4,4'-^{t}Bu$_2$-2,2'-bipyridyl (^{t}Bu$_2$bpy, 0.0393 g, 0.1464 mmol) and 3 mL of toluene. The reaction mixture was stirred at room temperature for 24 h, and then was filtered through a Celite-padded frit and washed with 20 mL of toluene. Volatiles were then removed under reduced pressure and the dark-green residue was taken up in a minimum amount of hexane and toluene and cooled to −30 °C overnight to give black crystalline (C$_5$Me$_5$)$_2$U(^{t}Bu$_2$bpy) (0.0850 g, 0.1094 mmol, 76.2 %). ^{1}H NMR (benzene-d_6, 298 K): δ -1.89 (s, 30H, C$_5Me_5$), -5.53 (s, 18H, ^{t}Bu), -23.54 (s, 2H, o-bpy), -82.19 (s, 2H, m-bpy), -91.39 (s, 2H, m-bpy). ATR-IR (Neat, 296 K, cm^{-1}): 2950m, 2898m, 2853m, 1576m, 1427s, 1362s, 1321s, 1278s, 1197s, 1097m, 947s, 862s, 774s, 639m, 538s. UV/Vis (Toluene, 296 K, 0.5 mM, cm^{-1} (M^{-1}cm^{-1})): 33333 (1531), 27360 (1544), 20576 (575), 12763 (438). NIR (Toluene, 296 K, 5 mM, cm^{-1} (M^{-1}cm^{-1})): 9162 (137), 7704 (140), 5886 (80), 4394 (134). mp: 125.3-127.7 °C.

Electrochemical studies were performed using 10 mg of **17**, 390 mg of electrolyte ([NPr$_4$][BAr$^F_4$]) in either 2.6 g of THF or 3.6 g of trifluorotoluene. Both cases yielded the same result: there is no redox event between -2 volts and 3 volts.

Synthesis of (C$_5$Me$_5$)$_2$U(4,4'-Me$_2$bpy) (18): A 20 mL scintillation vial with stir bar was charged with (C$_5$Me$_5$)$_2$UI(py) (0.2529 g, 0.3542 mmol), KC$_8$ (0.0702 g, 0.5193 mmol, 1.5 equiv), 4,4'-bpy (0.0658 g, 0.3571 mmol), and 5 mL of toluene. The reaction stirred at room temperature for 24 hr, filtered through a Celite-padded medium porosity frit, and rinsed with toluene (25 mL). Volatiles were removed under reduced pressure at 50 °C to give a black oil. The oil was triturated in hexane and volatiles were again removed to give (C$_5$Me$_5$)$_2$U(4,4-Me$_2$bpy) as a black microcrystalline powder (0.2036 g, 0.2939 mmol, 83% yield). ^{1}H NMR (400 MHz, 298K, C$_6$D$_6$): δ 38.27 (s, 6H, *Me*), -2.45 (s, 30H, C$_5$*Me$_5$*), -27.98 (s, 2H, bpy), -76.09 (s, 2H, bpy), -98.22 (s, 2H, bpy). ATR-IR (Neat, 296 K, cm^{-1}): 2958w, 2891s, 2850s, 2721w, 2384w, 2159w, 1968b, 1569s, 1490s, 1431s, 1374s, 1322s, 1265s, 1173s, 1122w, 1014w, 944s, 865s, 848s, 761s, 725s. UV/Vis (Toluene, 296 K, 0.5 mM, cm^{-1} (M^{-1}cm^{-1})): 34843 (22842), 33670 (23712), 27473 (20974), 20877 (8925). NIR (Toluene, 296 K, 30 mM, cm^{-1} (M^{-1}cm^{-1})): 9533 (206), 8489 (206), 7107 (166), 5711 (169). mp: 228.5 – 230.6 °C.

Electrochemical studies were performed using 10 mg of **18**, 390 mg of electrolyte ([NPr$_4$][BAr$^F_4$]) in 2.6 g of THF. There was no redox event between -2 volts and 3 volts.

Synthesis of (C$_5$Me$_5$)$_2$U(Cl)(4,4'-^{t}Bu$_2$bpy)(Bn) (19): A 20 mL scintillation vial was charged with a stir bar, **17** (0.1021 mg, 0.1314 mmol), benzyl chloride (0.0148 mL, 0.1286 mmol), and toluene (3 mL). The reaction mixture was stirred at room temperature for 2 hr. Volatiles were removed under reduced pressure and the dark brown residue was taken up in hexane, filtered through a Celite-padded frit, and washed with 10 mL of hexane. Volatiles were again removed under reduced pressure and the dark brown tacky solid was dissolved in a mixture of toluene and hexane and cooled to -30 °C overnight to give brown needle-shaped

crystals (0.0891 mg, 0.0984 mmol, 75 %). ^{1}H NMR (benzene-d_6, 298 K): δ 13.31 (s, 15H, C$_5$*Me$_5$* isomer A),

12.56 (s, 15H, C$_5$*Me$_5$* isomer A), 6.96 (s, 30H, C$_5$*Me$_5$* isomer B). ATR-IR (Neat, 296 K, cm^{-1}): 3853b, 3801w,

3745s, 3676w, 3629w, 3055w, 2956w, 2893s, 2852s, 2721w, 1965w, 1701w, 1614s, 1558s, 1539s,

1429s, 1363w, 1336w, 1246s, 1205w, 1082s, 1011s, 962s, 867w, 814w, 733s, 696s, 615w. UV/Vis

(Toluene, 296 K, 5 mM, cm^{-1} (M^{-1}cm^{-1})): 26954 (31200), 22523 (21800), 16420 (4000). NIR (Toluene,

296 K, 10.5 mM, cm^{-1} (M^{-1}cm^{-1})): 9542 (427), 9328 (513), 8658 (703), 8123 (475), 7283 (342), 6807

(370), 6369 (655), 6143 (646), 5879 (228), 4312 (503). mp: 187.2 - 189.1 °C.

Synthesis of (C$_5$Me$_5$)$_2$U(6,6'-Me$_2$bpy) (20): A 20 mL scintillation vial was charged with a stir bar,

(C$_5$Me$_5$)$_2$UI(py) (0.1014 mg, 0.1420 mmol), KC$_8$ (0.0290 mg, 0.2145 mmol, 1.5 equiv.), 6,6'-Me$_2$bpy (0.0261

mg, 0.1417 mmol) and toluene (5 mL). The reaction mixture was stirred at room temperature for 24 hr,

filtered through a Celite-padded frit, and rinsed with ~20 mL of toluene. Volatiles were removed under

reduced pressure to give a dark brown-black residue. The dark oil was triturated with hexane, and volatiles

were again removed under reduced pressure. The dark brown tacky solid was dissolved in toluene and

cooled to -30 °C overnight to give brown crystals (0.0811 mg, 0.1171 mmol, 82 %). ^{1}H NMR: (benzene-d_6,

298 K): 2.61 (s, 30H, C$_5$*Me$_5$*), -8.88 (s, 6H, *Me*), -20.57 (s, 2H, bpy), -77.10 (s, 2H, bpy), -96.45 (s, 2H, bpy),

-126.42 (s, 2H, bpy).

6.3   Results and Discussion

The reaction of (C$_5$Me$_5$)$_2$U(bpy) (**11**) with benzyl halides in toluene forms a novel suite of compounds

(C$_5$Me$_5$)$_2$U(X)(bpy)Bn (Bn = benzyl, X = F (**13**), Cl (**14**), Br (**15**), I (**16**)). As illustrated in Equation 9, the

synthesis of these molecules is relatively simple, and occurs quite quickly. However, yields are not high

(<80%), even when conditions (e.g. temperature, reaction time, equivalents of benzyl–X) are changed.

Other products are present, including (C$_5$Me$_5$)$_2$UX$_2$ (X = Cl, Br, I).
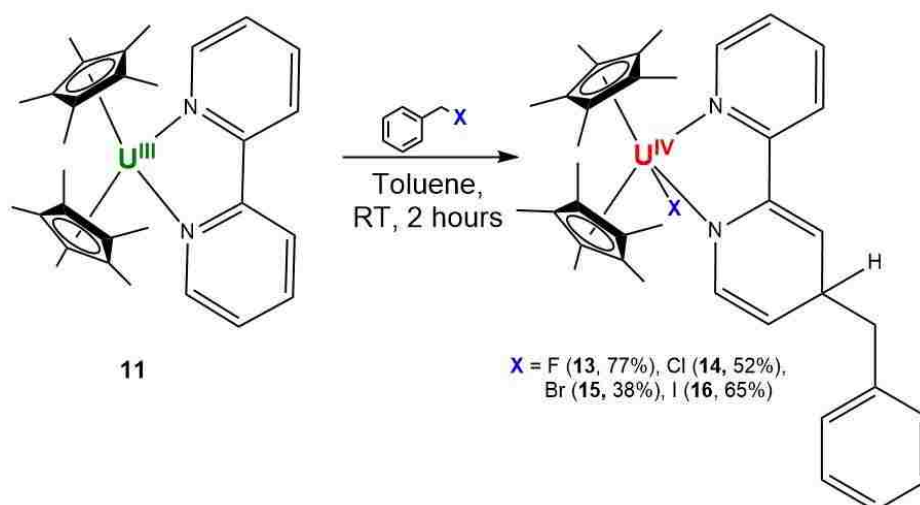
Equation 9. Reaction of $(C_5Me_5)_2$U-bpy with benzyl-X to form $(C_5Me_5)_2$U(X)(bpy)Bn

The majority of the benzyl-X (X = Cl, Br, I) starting materials were available commercially; however, it was

necessary to synthesize benzyl fluoride (**12**) on an as-needed basis given its propensity to degrade at room

temperature. This was done in quantitative yields by reacting benzyl–X (X = Cl, Br) with 1.5 equivalents of

$[Cp_2Co]F$ (Cp = C_5H_5) – a "naked", anhydrous fluoride source first used by Bennett et.al.[171] The insoluble

byproduct $[Cp_2Co]X$ can be easily removed by filtration, leaving benzyl fluoride in solution.
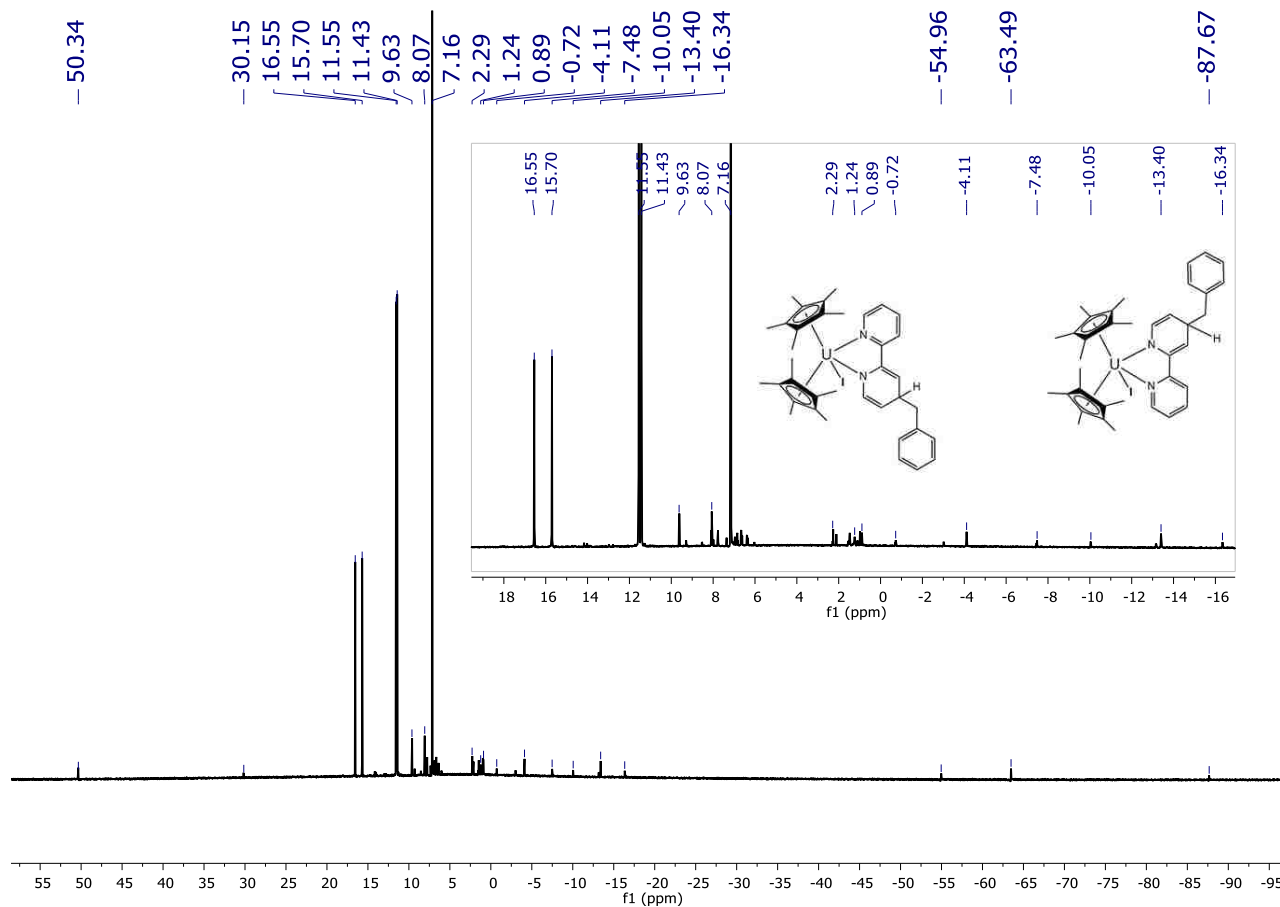
Figure 79. ^{1}H NMR spectrum showing both isomers of $(C_5Me_5)_2U(I)(bpy)$

Figure 79 shows the ^{1}H NMR spectrum for $(C_5Me_5)_2U(I)(bpy)Bn$, and the peak shifts and integrations suggest that there are two isomers present. Both isomer structures are also shown; in one case, the benzyl ring can add to the pyridine ring closest to the halide; in the other isomer, the benzyl ring adds to the pyridine ring farthest from the halide. The peak at 7.16 ppm is the C_6D_6 solvent peak, and both toluene and hexane are present in the spectrum at 2.11 and 1.26, 0.88 ppm respectively. Because these halide complexes are paramagenetic, due to the oxidation state of the uranium(IV) metal center, the spectrum covers a wide range of chemical shifts from 50 ppm to -64 ppm. It is difficult to tell to which isomer each peak belongs, but the peaks at either end of the spectrum likely belong to the protons on the pyridine rings. The two peaks at 16.51 and 15.66 ppm correspond to the methyl groups on the cyclopentadienyl rings for one of the isomers; the other isomer appears at 11.53 and 11.40 ppm. Based on the integrations

132

of these four peaks, the isomer at 11.53 and 11.40 ppm is roughly 3 times more likely to be formed. The results seen in this NMR spectrum are typical for all four halide complexes. Data for the remaining complexes can be found in Appendix B: NMR Data

Although it is difficult to distinguish which peaks belong to which isomer, it is evident that there are two isomers present for each halide compound. Figure 80 shows the ^{1}H NMR of all four halide complexes stacked together. The peak at 7.16 ppm represents C_6D_6 solvent, and the peak at 2.11 ppm is from toluene. The shifts representing the (C_5Me_5) ligands for each isomer are labeled in Figure 80; the smaller the halide, the more upfield the chemical shifts.
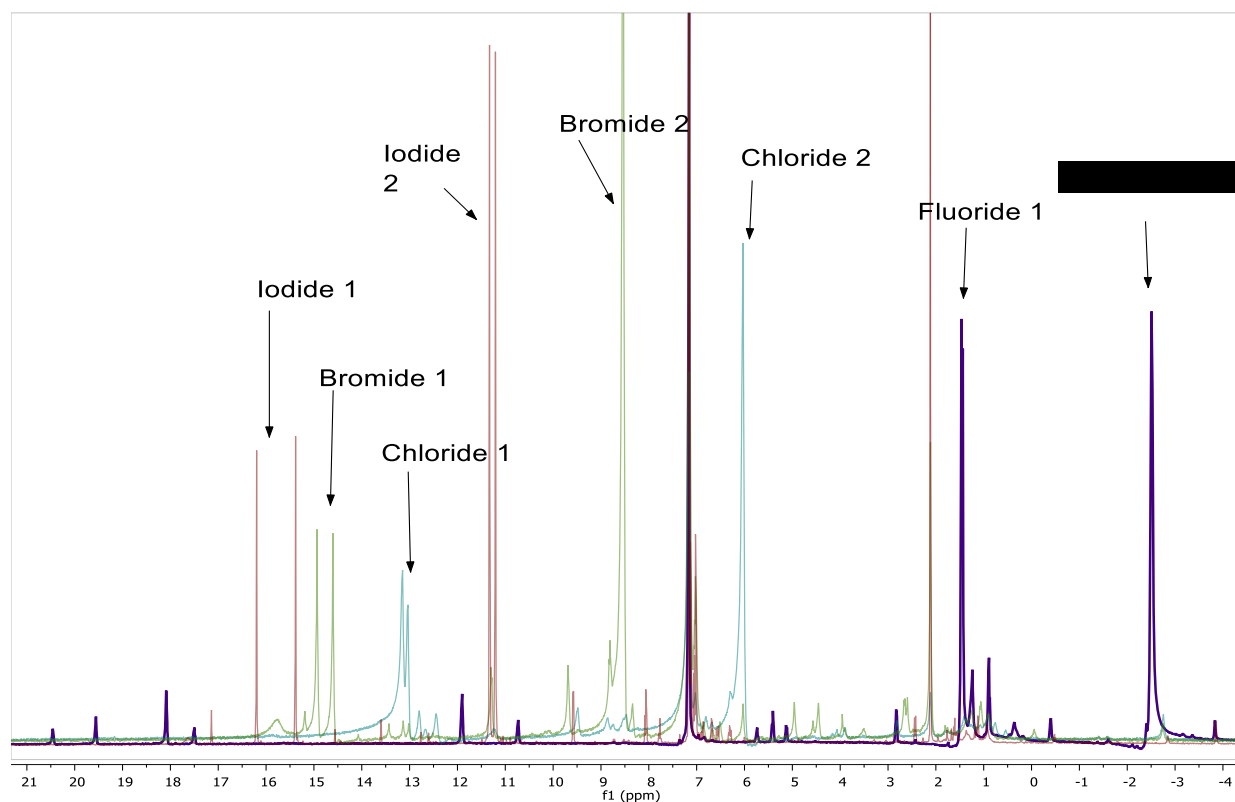
Figure 80. NMR of all four halide complexes showing the presence of two isomers of each complex.

In an attempt to avoid the extra steps necessary to obtain the benzyl fluoride, [Cp$_2$Co]F was reacted directly with **14** and **15**. However, halide exchange with **14** does not occur, possibly due to bulky sterics around the metal center. After 2 h at room temperature (C$_5$Me$_5$)$_2$ formation can be seen by NMR. When [Cp$_2$Co]F and **15** are reacted at room temperature (Equation 10), formation of one isomer of **13** can be seen by NMR. Not only is bromide a better leaving group than chloride,[174] the U–Br bond length (2.8650(13) Å) is longer than the U–Cl bond length (2.6793(13) Å), which may allow for easier halide exchange. Based on the appearance of only one fluorine isomer in the NMR, only one of the isomers is able to undergo halide exchange. After 24 h at room temperature, (C$_5$Me$_5$)$_2$ is seen in the NMR, but both

the bromide starting material and the fluoride product are still present. It is conceivable that the other fluoride isomer is falling apart because it is unable to exchange the halide.

It is also possible to exchange the bromide for iodide using iodotrimethylsilane (TMS–I, Equation 10). After 40 minutes at room temperature, peaks corresponding to $(C_5Me_5)_2U(I)(bpy)Bn$ appear in the ^{1}H NMR, though not in high relative yields.
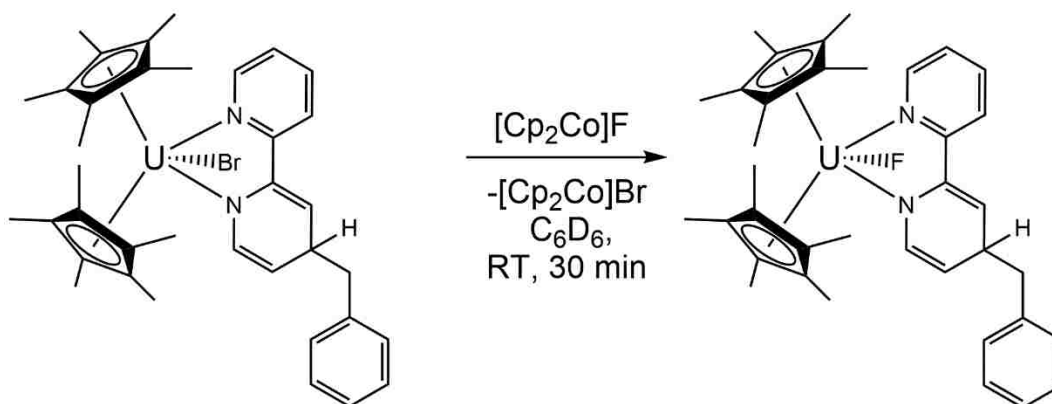
Equation 10. Exchange of bromine using $[Cp_2Co]F$

6.3.1 Crystal Structures

Crystals of **13-16** suitable for X–ray diffraction were grown from hexane solutions at -30 °C. Interestingly, the crystal structure of **13** shows the benzyl group adding to the bpy ring farthest from the halide, whereas in **14**-**16** the benzyl group adds to the bpy ring closest to the halide (see Figure 81). The evidence suggests that isomers of all four compounds exist, due to the appearance of two species in the NMR and crystal structure evidence that it is possible for the benzyl group to add to either bpy ring.

a)
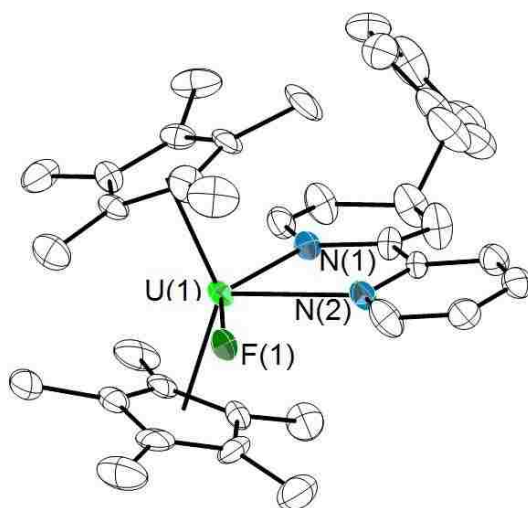
b)
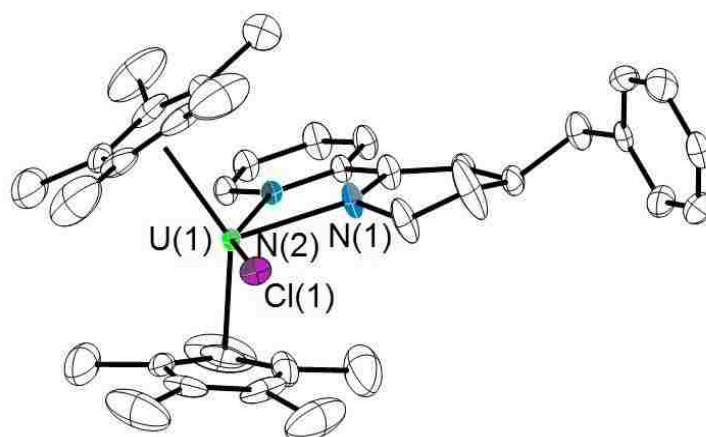
c)
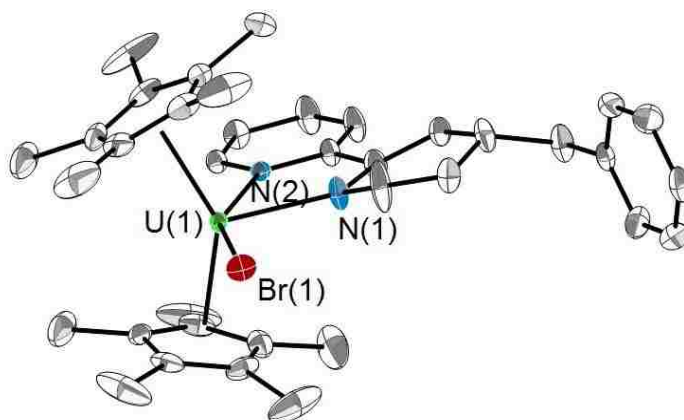
d)
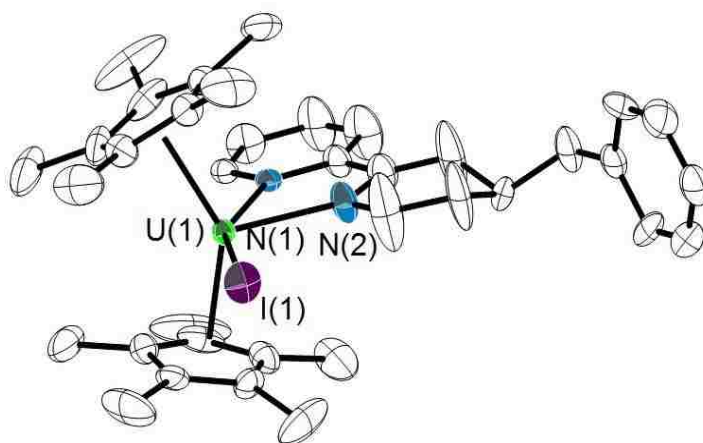
Figure 81. ORTEP drawings of the bpy benzyl halide series (ellipsoids at 50% probability, hydrogens excluded for clarity). A) $(C_5Me_5)_2U(F)(bpy)Bn$ has the benzyl group pointing away from the fluoride. B) $(C_5Me_5)_2U(Cl)(bpy)Bn$ has the benzyl group pointing in the same direction as the chloride C) $(C_5Me_5)_2U(Br)(bpy)Bn$ has the benzyl group pointing in the same direction as the bromide. D) $(C_5Me_5)_2U(I)(bpy)Bn$ also has the benzyl group pointing in the same direction as the halide.

Table 27. Select bond distances (Å) and angles (°) for the halide series 3-6. [a] denotes the centroid of the Cp* (Cp* = C_5Me_5) ring. Both isomers are reported for 3.

$(C_5Me_5)_2U(X)(bpy)Bn$	U – Cp*[a]	U – N(1)	U – N(2)	U – X	Cp*[a] – U – Cp*[a]	N(1) – U – N(2)
3 (X = F)	1) 2.50(1), 2.48(1) 2) 2.50(1), 2.48(1)	1) 2.335(10) 2) 2.326(9)	1) 2.519(10) 2) 2.577(9)	1) 2.144(6) 2) 2.123(6)	1) 140.1(4) 2) 137.5(4)	1) 64.7(3) 2) 64.0(3)
4 (X = Cl)	2.511(4)	2.309(4)	2.525(4)	2.6793(13)	141.1(1)	65.14(15)
5 (X = Br)	2.515(4)	2.313(4)	2.511(4)	2.8650(13)	140.9(1)	65.27(14)
6 (X = I)	2.526(8)	2.312(9)	2.522(8)	3.104(1)	139.7(2)	65.2(3)

Table 27 shows select bond distances and angles for compounds **13-16**. It is worth noting that the U–X bond distance in this series of compounds increases significantly as the size of the halide increases. This is most likely due to the increase in radius of the halide from fluorine to iodine. This increase in bond distance is consistent with literature trends among other uranium-halide compounds.[150,169,173,175,176]

Another important feature of these compounds to note is that the bipyridine-like structure is no longer reduced (as it is for $(C_5Me_5)_2U(2,2'-bpy)$[165]) in all but the fluorine compound. This can be seen through the bond length of the 2,2' bond between pyridine rings. In free (e.g. neutral) bipyridine, that bond length is 1.490(3) Å, whereas in reduced bipyridine rings, the length is shortened to between 1.409(13) Å and 1.45(2) Å.[165] The bond lengths of the 2,2'-bond in the pyridyl ligand for the chloride (1.479(7) Å), the bromide (1.476(7) Å), and the iodide (1.479(16) Å) are more similar to the neutral bipyridyl. However, for the fluoride (1.382(18) Å and 1.449(16) Å), both isomers could be within the range of a reduced bipyridyl system.

Very few similar compounds exist in the literature; listed in Table 28 are select bond distances and angles for $(C_5Me_5)_2UF_2(py)$,[150] $(C_5Me_5)_2UCl_2$,[176] $(C_5Me_5)_2UBr_2$,[173] and $(C_5Me_5)_2UI_2$.[175] The bond length between uranium and the halide is longer in most of the compounds prepared in this work compared to $(C_5Me_5)_2UX_2$. This may be explained by the trans effect whereby a strongly bound ligand (bpy) is trans to

the less electronegative halide, causing the U–X bond to be lengthened. Typically with actinides the inverse is seen, [167,168] but that does not appear to be the case in the majority of the examined molecular systems. However, for one of the fluorine isomers, the U–F bond length (2.123(6) Å) is shorter than the known U-F bond length in $(C_5Me_5)_2UF_2(py)$ (2.146(5) Å).[150] This could be an example of the inverse trans effect, given that fluorine is extremely electronegative.

Table 28. Comparison of select bond distances (Å) and angles (°) between this work and similar known compounds. [a] denotes the centroid of the (C_5Me_5) ring. [b] This work. [c]Reference[150] [d]Reference[176] [e]Reference[173] [f]Reference[175]. NR = Not Reported.

Compound	U − Cp*[a]	U − X	Cp*[a] − U − Cp*[a]
$(C_5Me_5)_2U(F)(bpy)Bn$[b]	1)2.50(1), 2.48(1) 2)2.50(1), 2.48(1)	1) 2.144(6) 2) 2.123(6)	1) 140.1(4) 2) 137.5(4)
$(C_5Me_5)_2UF_2(py)$[c]	2.482 2.485	2.146(5)	139.93
$(C_5Me_5)_2U(Cl)(bpy)Bn$[b]	2.511(4)	2.6793(13)	141.1(1)
$(C_5Me_5)_2UCl_2$[d]	2.47(3)	2.583(6)	132(1)
$(C_5Me_5)_2U(Br)(bpy)Bn$[b]	2.515(4)	2.865(13)	140.9(1)
$(C_5Me_5)_2UBr_2$[e]	2.438(4)	2.7578(5)	137.57(15)
$(C_5Me_5)_2U(I)(bpy)Bn$[b]	2.526(8)	3.104(1)	139.7(2)
$(C_5Me_5)_2UI_2$[f]	2.430 2.445	2.9807(9) 2.9868(9)	136.43

Mehdoui et.al. published $(C_5Me_5)_2U(bpy)I$ in 2005 and a comparison between that structure[164] and the corresponding iodine structure reported in this work are listed in Table 29. The greater difference between the U–N(1) and U–N(2) bond distances in the synthesized structures is most likely due to the addition of the benzyl group to one ring of the bpy ligand. The U–N(1) bond, corresponding to the pyridine ring without the benzyl group, is significantly shorter; the ligand has become skewed due to the presence of the benzyl ring. There is also a decrease in the bond angle between the (C_5Me_5) centroids and the uranium metal center; likely the (C_5Me_5) ligands were forced to move closer together to accommodate a bulky benzyl ligand into the system.

Table 29. Comparison of select bond distances (Å) and angles (°) between this work and similar known U-I compounds. [a] denotes the centroid of the (C_5Me_5) ring. [b] This work. [c] Reference[164]

Compound	$U\text{-}Cp^{*a}$	$U-N(1)$	$U-N(2)$	$U-X$	$Cp^{*a}-U-Cp^{*a}$	$N(1)-U-N(2)$
$(C_5Me_5)_2U(I)(bpy)Bn^b$	2.526(8)	2.312(9)	2.522(8)	3.104(1)	139.7(2)	65.2(3)
$(C_5Me_5)_2U(bpy)I^c$	2.82(3)	2.635(5)	2.561(4)	3.2135(4)	141.28	62.39(15)

6.3.2 Electrochemistry

Electrochemical analysis was performed on all of the complexes described in this chapter using ferrocene as an internal standard. For an explanation on the conditions, see Chapter 1 Section 1.13. Although $(C_5Me_5)_2Ubpy$ was published by Bart's group in 2012,[165] the cyclic voltammogram was never discussed. Figure 82 shows the cyclic voltammogram for $(C_5Me_5)_2Ubpy$. There are two reversible redox events at -3.09 and -3.64 V, likely corresponding to the U(III)/U(IV) couple and a ligand-based event, respectively.[131] The aromaticity of the bypyridyl rings on the $(C_5Me_5)_2U(X)(bpy)(Bn)$ has been disrupted, likely leading to a difference in electrochemical behavior, but the unsubstituted compound is a good place to start for comparisons. In all of the cyclic voltammograms shown below, the legend in the top left corner contains a number of variables defined during the experiment. The initial point (IP) describes the voltage at which the experiment started; V1 defines the most negative voltage reached during the experiment; V2 defines the most positive voltage reached; the final point (FP) describes where the experiment stopped; and the scan rate (SR) explains the velocity of the scan in millivolts per second.
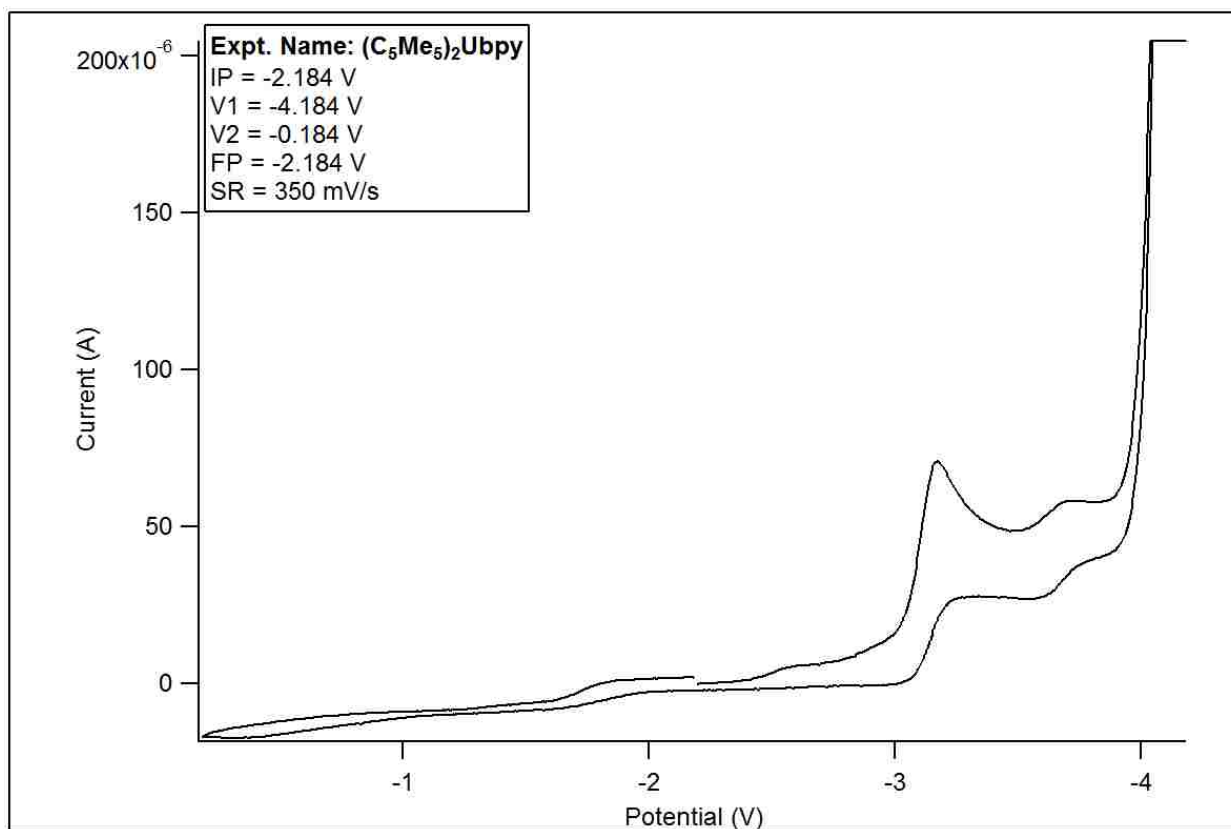
Figure 82. Cyclic voltammogram for $(C_5Me_5)_2Ubpy$
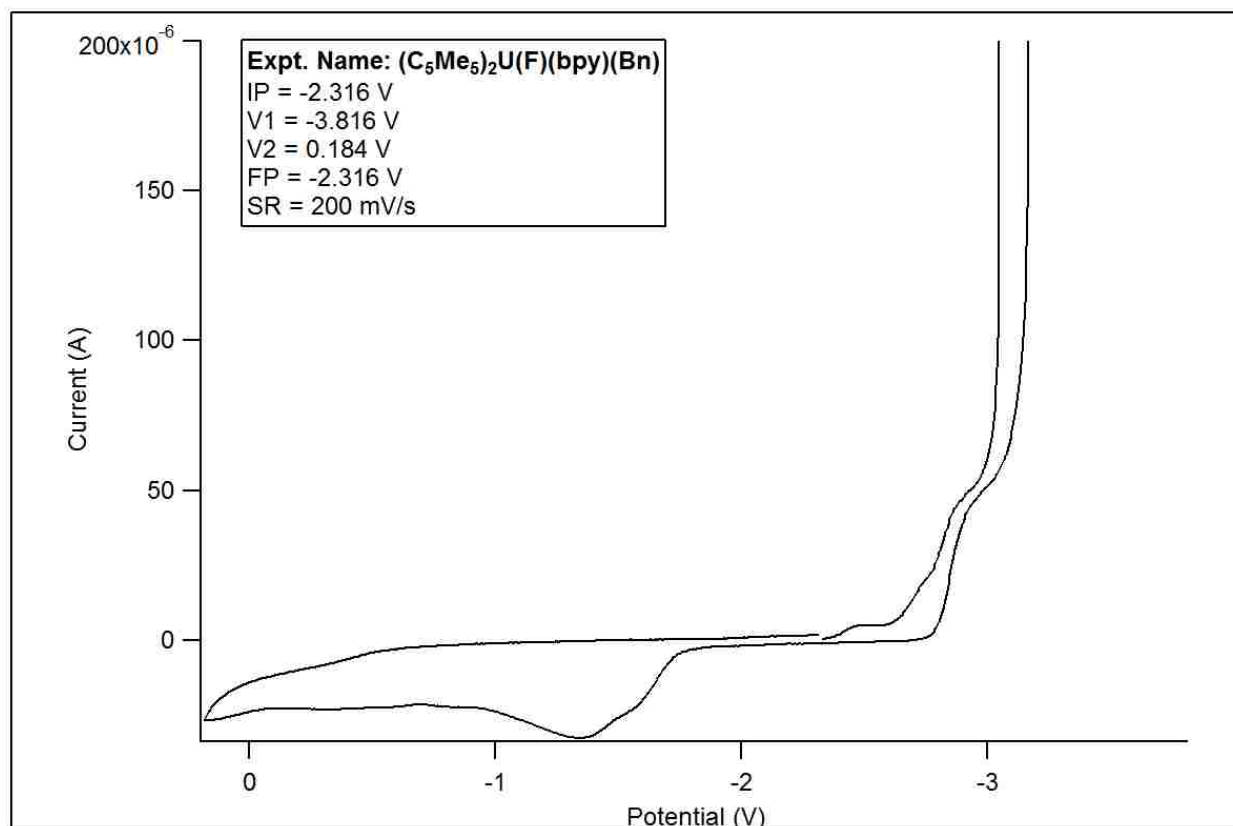
Figure 83. Cyclic voltammogram for $(C_5Me_5)_2U(F)(bpy)(Bn)$

Figure 83 shows the cyclic voltammogram for $(C_5Me_5)_2U(F)(bpy)(Bn)$. Fluorine is the most electronegative element on the periodic table, and as such, the electrochemistry of fluorinated species is distinct from its other halogen analogues. There are two irreversible and one quasi-reversible events in the fluorine voltammogram. The first is in the anodic region at -1.34 V. It is likely ligand based, perhaps due to oxidative events on the C_5Me_5 ligands.[131] The second irreversible event is in the cathodic region at -2.47 V, and is likely ligand based. What appears to be a quasi-reversible event is located at -2.816 V. Based on literature data, this could be due to the U(III)/U(IV) couple.[131]
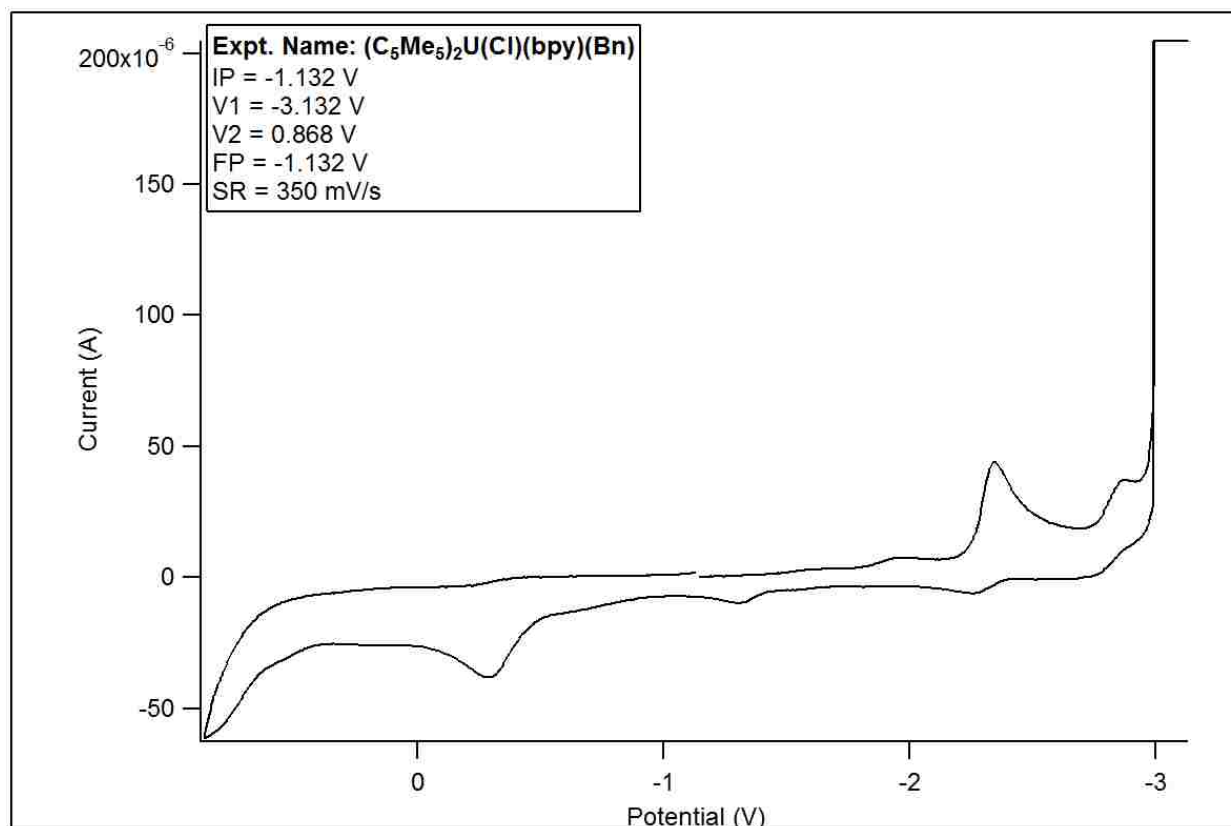
Figure 84. Cyclic voltammogram for (C$_5$Me$_5$)$_2$U(Cl)(bpy)(Bn)

The cyclic voltammogram for (C$_5$Me$_5$)$_2$U(Cl)(bpy)(Bn) is depicted in Figure 84. There is one irreversible event in the anodic region at -0.268 V, possibly due to the C$_5$Me$_5$ ligand oxidation. There is a quasi-reversible event in the cathodic region at -2.30 V, and a fully reversible redox event at -2.80 V. These are due to a ligand-based event and the U (III)/U(IV) couple, respectively.
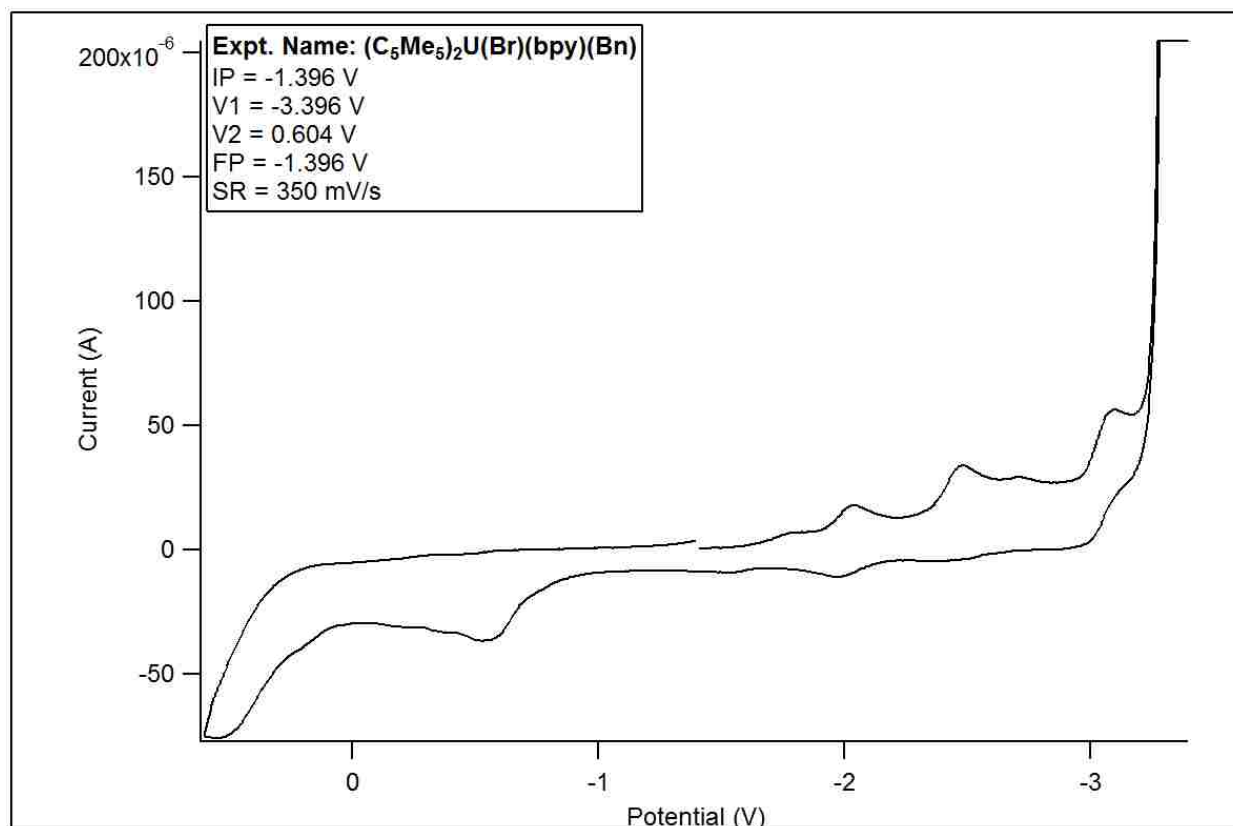
Figure 85. Cyclic voltammogram for (C₅Me₅)₂U(Br)(bpy)(Bn)

There are several similarities between the cyclic voltammograms for the chloride (Figure 84) and bromide (Figure 85) analogues. The ligand-based irreversible event is present at -0.524 V, as are the quasi-reversible and fully reversible events at -2.48 and -3.03 V, respectively. The reversible event at -2.48 V likely corresponds to the U(III)/U(IV) couple. There are additional events in the bromide voltammogram, including a small irreversible event at -2.71 V and a reversible event at -2.00 V. These may be ligand based.
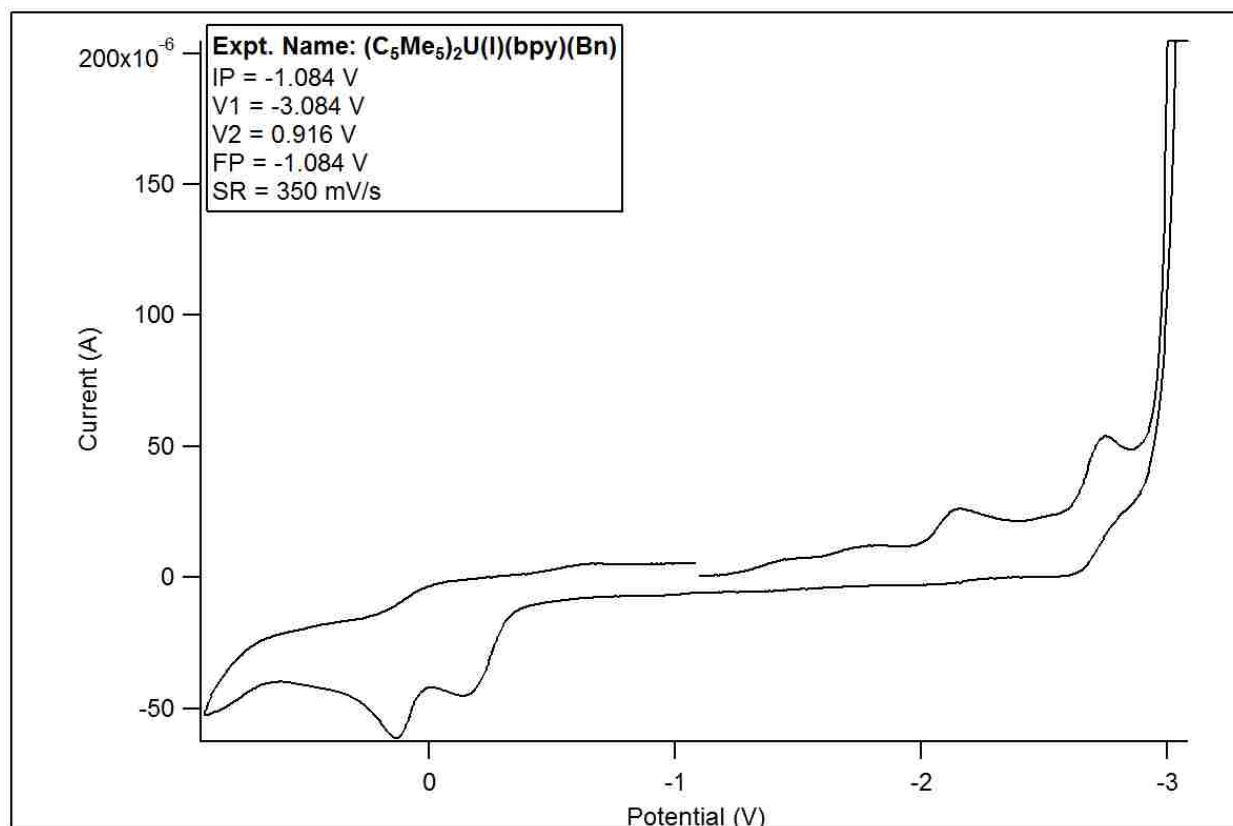
Figure 86. Cyclic voltammogram for (C₅Me₅)₂U(I)(bpy)(Bn)

The iodine analogue (Figure 86) is not extraordinarily different from the chloride and bromide compounds. There is an irreversible event in the anodic region at 0.14 V in addition to the expected irreversible event at -0.15 V. In the cathodic region, an irreversible event at -2.15 V is present, along with a reversible redox event at -2.69 V, corresponding to the U(III)/U(IV) couple.
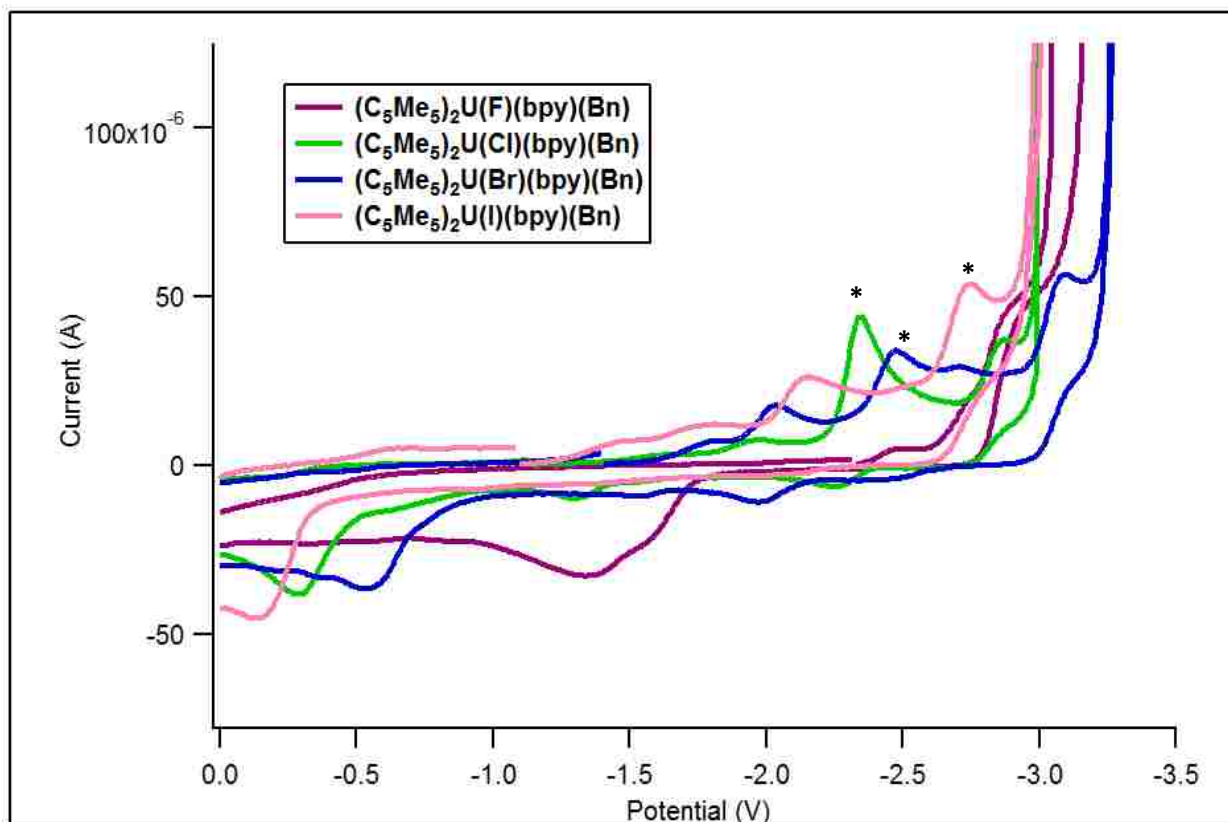
Figure 87. Comparison of cyclic voltammograms for the $(C_5Me_5)_2U(X)(bpy)(Bn)$ series.

A comparison of the cyclic voltammograms all four halide compounds is shown in Figure 87. While they are not identical, they do share similarities. An irreversible event in the anodic region representing oxidations on the C_5Me_5 ligand is evident in all four sets of data, as well as a reversible redox event between -2.69 and -3.03 V corresponding to the U(III)/U(IV) couple. There are several irreversible and quasi-reversible events in each voltammogram that likely are from events on the ligands. In general, as the size of the halide increases, the events in the voltammogram shift to become more positive. The asterisks in the voltammogram indicate an example of the peaks in this progression: from the pink line of the iodine spectrum to the blue line of the bromide spectrum to the green line of the chloride spectrum, the peaks corresponding to the U(III)/U(IV) couple shift to less negative values.

6.3.3 Mechanistic Studies

In all of these compounds, the benzyl group adds only to the para position of the ring. Computational studies performed within the group[*] show that the para position has an almost neutral electrostatic charge, which would facilitate the addition of the benzyl ring to that position. The ortho positions on the bpy rings have slightly positive electrostatic charges, although their orbital densities are not conducive to addition. Therefore the theory is that, rather than a direct oxidative addition to the para position, the benzyl group is actually adding to the electropositive ortho position and migrating to the para positions, which have higher orbital densities. To support this theory, preliminary studies using substituted bipyridyl complexes reacted with benzyl–X were done. The $(C_5Me_5)_2U(R_2bpy)$ (**17**, R = 4,4'-^tBu; bpy = 2,2'-bipyridyl; **18**, R = 4,4'-Me) complexes were synthesized as shown in Equation 11.

$$R = {}^tBu\ (\mathbf{17}),\ Me\ (\mathbf{18})$$
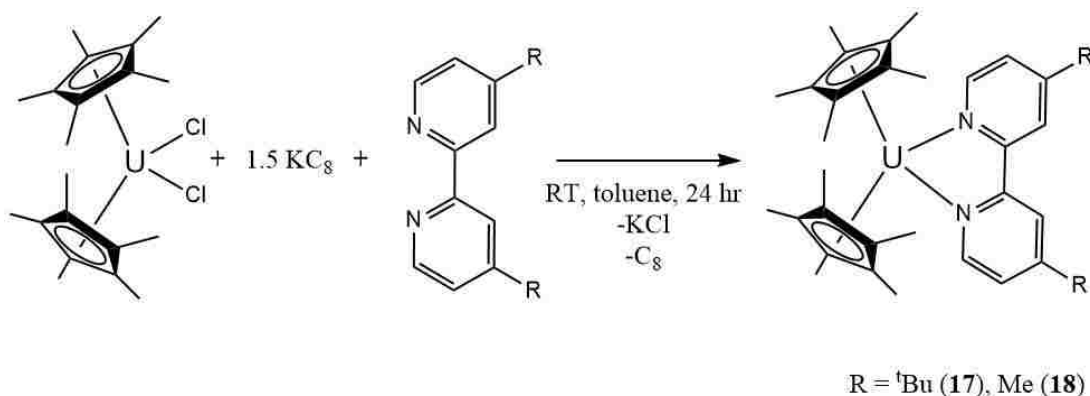
Equation 11. Formation of $(C_5Me_5)_2U(R_2bpy)$ (R = tBu. Me)

When reacted with benzyl chloride under analogous conditions to previous reactions, the benzyl group still added to the para position to make $(C_5Me_5)_2U(Cl)(tBu_2bpy)Bn$ (**19,** see Figure 88). The addition of bulky groups to the para position does not appear to be enough to prevent the addition of the benzyl. To test the hypothesis that the benzyl group first adds to the ortho position of the bipyridine ring, $(C_5Me_5)_2U(6,6'-Me_2bpy)$ (**20**) was synthesized as shown in Equation 12.
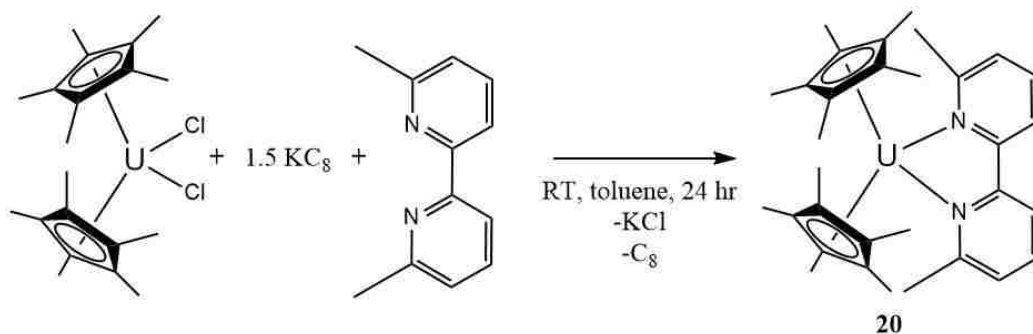
Equation 12. Synthesis of $(C_5Me_5)_2U(6,6'-Me_2bpy)$

When **20** was reacted with benzyl-chloride, the resulting products were $(C_5Me_5)_2UCl_2$, free 6,6'-Me$_2$bpy, and an unidentified solid. Because the ortho positions of the bipyridyl rings were blocked, the benzyl group was not able to add to the ring and then migrate to its final position. This is evidence to support the hypothesis that the mechanism of formation for the $(C_5Me_5)_2U(X)(bpy)(Bn)$ complexes begins with addition of the benzyl group to the ortho position of the bpy ring, followed by a migration of the group to its final place. However, these data are not enough to definitively argue that this is the only mechanism by which these complexes could be formed.

6.3.4 Crystal Structures

Crystal structure data for both $(C_5Me_5)_2U(^tBu_2bpy)$ (**17**) and $(C_5Me_5)_2U(4,4'-Me_2bpy)$ (**18**) were unable to be obtained in high quality, though the low-quality data confirms the structures match what is shown in Equation 11.
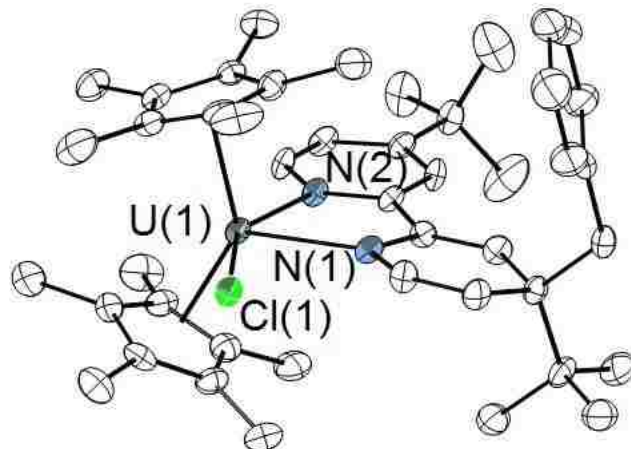
Figure 88. ORTEP view of **19**. Hydrogens omitted for clarity; ellipsoids at 50% probability.

The crystal structure of $(C_5Me_5)_2U(Cl)(^tBu_2bpy)Bn$ (**19**) is shown in Figure 88. As with most of the halide complexes, the benzyl group added to the pyridine ring closest to the halide, although, it has a different geometry relative to the pyridine groups. The *tert*-butyl group on the same ring is no longer in the plane of the bipyridine, but has shifted to be roughly 65 ° out of the plane. The bond lengths and angles for complex **19** are listed in Table 30, and are compared to those for $(C_5Me_5)_2U(Cl)(bpy)Bn$ (**14**). The bonds and angles are, for the most part, comparable between the two compounds. However, it is worth noting that in complex **19** the U–C$_{cent}$ distances are not identical, and the angle of and the C$_{cent}$1–U–C$_{cent}$2 bonds is significantly smaller, indicating a shift around the metal center to accommodate the extra bulk of the *tert*-butyl groups.

Table 30. Comparison of certain bond lengths and angles between complexes **19** and **14**.

Bond	Distance (Å) or Angle (°) for **19**	Distance (Å) or Angle (°) for **14**
U–N1	2.354(3)	2.309(4)
U–N2	2.523(3)	2.525(4)
U–C$_{cent}$1	2.530(4)	2.511(4)
U–C$_{cent}$2	2.493(4)	2.511(4)
U–Cl	2.6843(16)	2.6793(13)
N1–U–N2	65.29(11)	65.14(15)
C$_{cent}$1–U–C$_{cent}$2	135.8(1)	141.1(1)
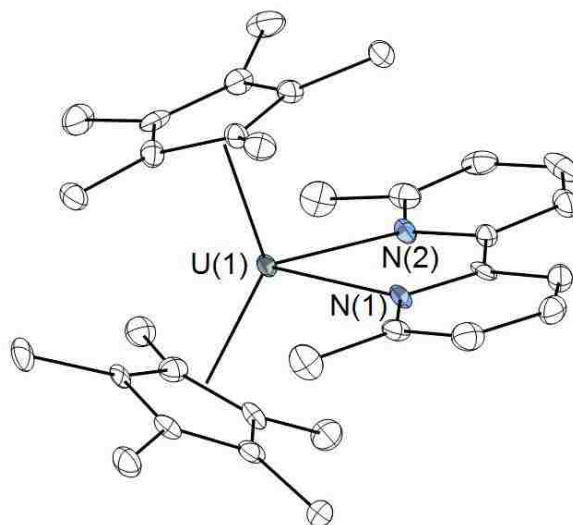
Figure 89. ORTEP image of (C$_5$Me$_5$)$_2$U(6,6'-Me$_2$bpy). Hydrogens omitted for clarity; ellipsoids at 50% probability.

Figure 89 shows the crystal structure of (C$_5$Me$_5$)$_2$U(6,6'-Me$_2$bpy) (**20**). Complex **20** crystallizes as a triclinic

P-1 space group. The crystal structure of (C$_5$Me$_5$)$_2$(4,4'-Me$_2$bpy) (**18**) was also solved; although the data is

not high quality, it does give an idea of the nature of the bonding within the molecule. Complex **18**

crystallizes as a monoclinic P2$_1$/c, which is slightly more symmetric than complex **20**. The anti-symmetry

of **20** is more apparent after analysis of certain bond lengths and angles (Table 31). The distances of the U–C$_{cent}$ bonds are not identical, which shows the molecule is not centered on an inversion plane.

Table 31. List of bond lengths and angles for complex **10**.

Bond	Distance (Å) or Angle (°) for **20**
U–N1	2.447(7)
U–N2	2.429(4)
U–C$_{cent}$1	2.495
U–C$_{cent}$2	2.552
N1–U–N2	66.02(15)
C$_{cent}$1–U–C$_{cent}$2	136.02

6.3.5 Electrochemistry

Electrochemical studies were performed on $(C_5Me_5)_2U(R_2bpy)$ (R = ^tBu, Me) and $(C_5Me_5)_2U(Cl)(tBu_2bpy)(Bn)$. Neither $(C_5Me_5)_2U(R_2bpy)$ molecule gave redox events in either THF or trifluorotoluene, but the cyclic voltammogram for $(C_5Me_5)_2U(Cl)(tBu_2bpy)(Bn)$ is shown in Figure 90. There is an irreversible event in the anodic region at -0.34 V, likely related to oxidation events on the C_5Me_5 ligand, and a reversible redox event at -2.51 V corresponding to the U(III)/U(IV) couple. This value for the U(III)/U(IV) couple is fairly consistent with literature values: $(C_5Me_5)_2U[\eta^2-(N,N')\text{-tetrazolate}]_2$, -1.88 V;[131] $(C_5Me_5)_2UCl_2$, -1.85 V;[177] $(C_5Me_5)_2UMe_2$, -2.41 V;[177] $(C_5Me_5)_2U(CH_2Ph)_2$, -1.95 V.[177]
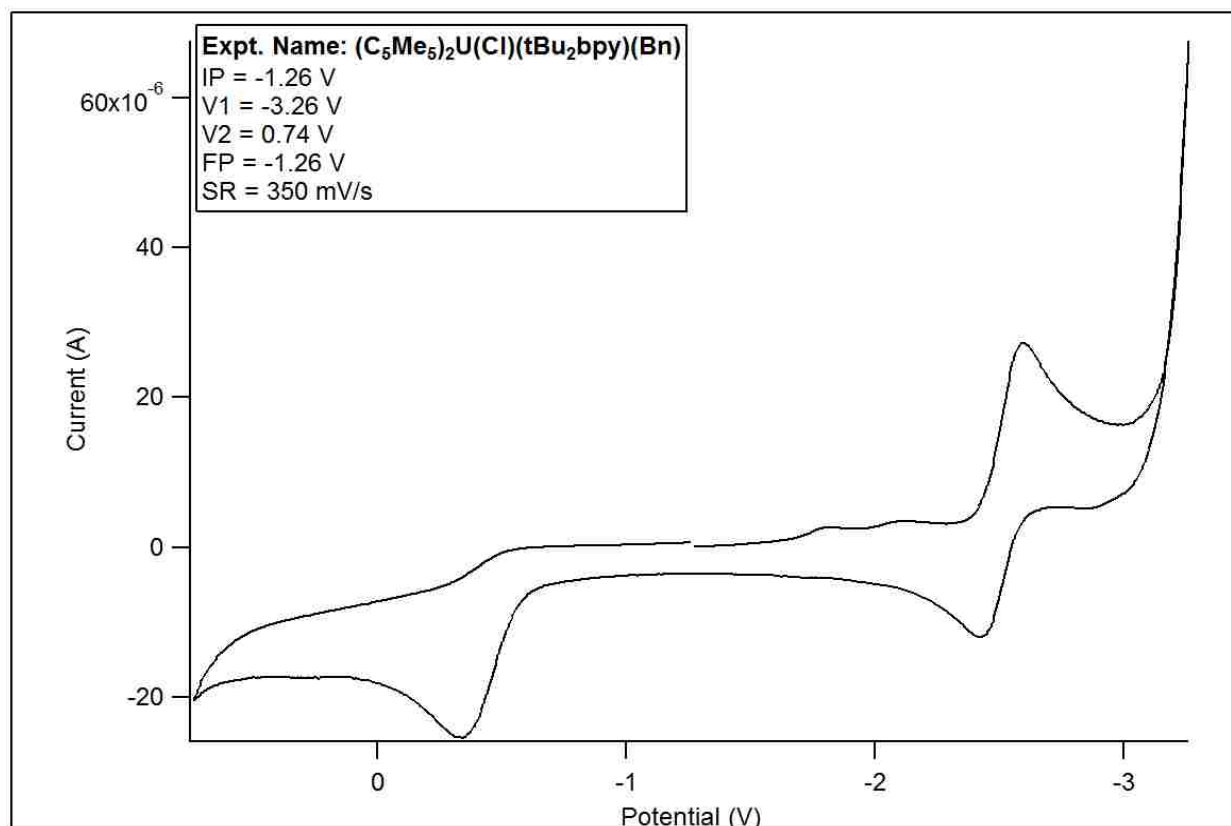
Figure 90. Cyclic voltammogram for $(C_5Me_5)_2U(Cl)(tBu_2bpy)(Bn)$

Though the mechanism of formation may be better understood, the extent of the participation of f-electrons in the binding of the ligands to the metal center is still uncertain.

6.4   C–X activation attempts using thorium

6.4.1   Experimental

One of the experimental ways to test for f-electron participation in actinide mediated C–X activation is to use thorium as the metal center and compare the results to the other actinides. Thorium is similar in size to uranium, (1.05 and 1.00 Å,[88] respectively) but it does not have any f-electrons to use in bonding.[11] Thus, discrepancies in results could potentially be due to f-electron involvement in the mechanism.

152

The compound $(C_5Me_5)_2$Th-bpy was synthesized as described in a 2016 manuscript by Walter et.al.[121] The dark purple powder was reacted analogously to the uranium species; however, when $(C_5Me_5)_2$Th-bpy reacts with benzyl-X (X = Cl, Br), the analogous reaction does not occur. Instead, formation of the major product, $(C_5Me_5)_2$ThX$_2$, is seen, along with several other unidentified decomposition products. These reactions were tested at room temperature as well as at 50 °C for up to 24 h with no change in the product (Equation 13). No further attempts were made during the course of this project to synthesize $(C_5Me_5)_2$Th(X)(bpy)Bn.

X = Cl, Br
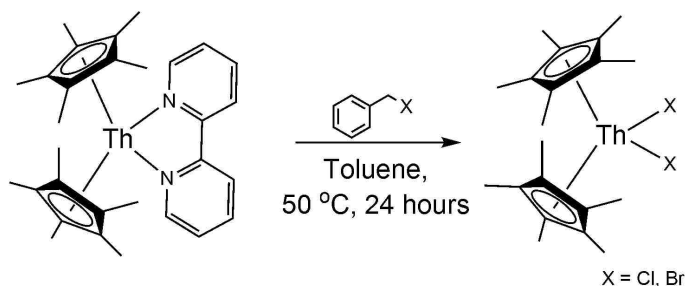
Equation 13. Reaction of $(C_5Me_5)_2$Th-bpy with benzyl-halides results in the formation of $(C_5Me_5)_2$ThX$_2$.

6.4.2 Results

Clearly, there is a difference in reactivity between the thorium and uranium metal centers, which may be due to the influence of the 5f electrons. However, it is more likely the ability of uranium to adopt multiple oxidation states that allows this chemistry to occur. The oxidation state changes from U(III) in the $(C_5Me_5)_2$U-bpy starting material to U(IV) in all of the $(C_5Me_5)_2$U(X)(bpy)Bn complexes; however, thorium will likely only adopt a Th(IV) oxidation state and cannot be oxidized further. Figure 91 shows the ^{1}H NMR data from the reaction of $(C_5Me_5)_2$Th-bpy with benzyl bromide to give $(C_5Me_5)_2$ThBr$_2$ at 2.06 ppm. The peak at 7.16 ppm is C_6D_6, the solvent in which the NMR was performed. Other peaks are present in the system, but are not identified as a specific decomposition product. A dark powder precipitates from the solution, giving more evidence that the reaction does not proceed as expected.
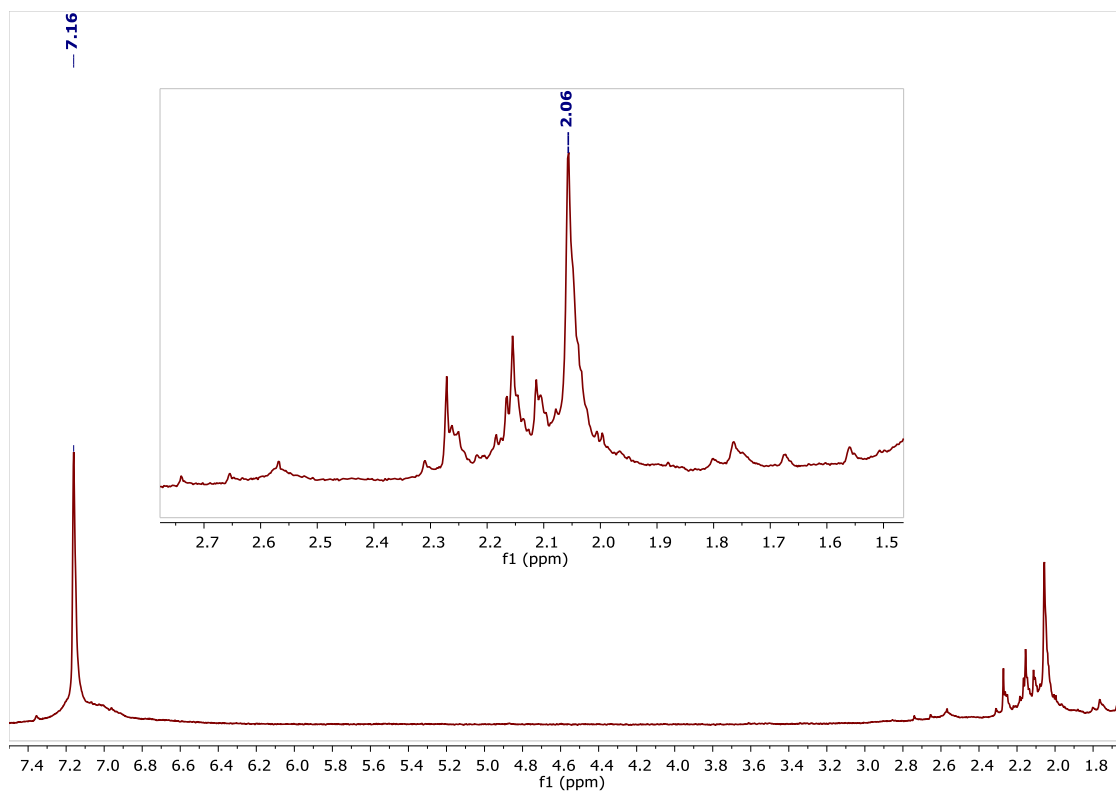
Figure 91. ^{1}H NMR (400 MHz, 295 K, C_6D_6) data shows the formation of $(C_5Me_5)_2ThBr_2$ at 2.06 ppm.

6.5   Conclusions

Examples of actinide mediated C–X activation are rare, and this work has shown examples for the majority

of the halide group. An unusual example of a U–F bond was also described. Aspects of the mechanism

have been explained, including the theory that the benzyl group adds to a different position on the

pyridine ring and migrates to its final position, and the potential for f-electron involvement has been

shown based on the results from the analogous thorium reactions. The divergence in results between

thorium and uranium could also be due to the size of the metal atom, or the ability for uranium to change

oxidation states. The covalent radius of thorium is approximately 0.1 Å larger than that of uranium,[11]

which may influence the bond distances within the structures. The level of influence of the oxidation state

of the metal center on the mechanism of formation for the uranium complexes is not well understood;

however, if there is an influence, the lack of redox capabilities with thorium may help explain why those

analogues are not stable via this synthetic method. Theoretical studies of the mechanism may yield a better understanding of the bonding, including the redox behavior or the influences of f-electrons within the structure.

Chapter 7: Transfer of High-Nitrogen Ligands

7.1 Introduction

Tetrazoles have a long history of being used in multiple disciplines from medicine[178] to explosives.[179] In some cases, 5-monosubstituted tetrazoles are used as intermediates to other organic heterocycles, particularly in drug design.[180] They have also seen use in coordination polymers[181,182] and metal organic frameworks.[183,184] Transition metals have been used in the literature to form metal-tetrazolate complexes, or as catalysts in tetrazole synthesis,[185-190] but gold-tetrazolates are rare, with only a few examples reported.[186,187,189,190] There is a particular interest in using gold-tetrazolates as precursors for f-element-tetrazolate synthesis; only one previously published organoactinide-tetrazolate complex exists in the literature,[131] and more exploration in this field is necessary to understand high-nitrogen f-element chemistry.

Nitrogen is a relatively soft donor atom, and its interactions with the hard donor f-elements may give insight into the bonding properties of the actinides. The simultaneous interactions of f-elements with multiple nitrogen atoms are also of interest. However, high-nitrogen complexes are known for their sensitivity to shock, which can complicate synthetic procedures. The use of a benign transfer agent can facilitate the addition of high-nitrogen ligands to metal centers in a safe way. Lanthanide-tetrazolate complexes have also become more of interest in the literature recently,[191-201] with most of the research focusing on luminescent properties of the 4f tetrazolates.[191-194,197-199] They have also been studied for their ability to behave as single-molecule magnets, due to their strong spin-orbit coupling ability.[196] Very few organometallic lanthanide-tetrazolate complexes have been published,[200,201] and there are no current examples of cerium-tetrazolates. This chapter describes the synthesis and characterization of a novel gold-tetrazolate compound, and gives brief insight into its use as a precursor for actinide-tetrazolate synthesis.

7.2 Experimental

All compounds described in this chapter were evaluated for shock sensitivity using a hammer prior to continuation of analysis. Each compound was struck repeatedly with a hammer at varying intensities to test for shock sensitivity. All complexes were tested for friction sensitivity by rubbing a hammer against the material with some pressure. If no reaction or detonation occurred in either scenario, the material was deemed to be mechanically stable. While none of the compounds reported herein were found to be mechanically unstable, tetrazolate ligands are nitrogen-rich and have the potential to form unstable compounds. The starting compound $(C_5Me_5)_2UI(thf)$ was prepared as described in the literature,[169] and $(C_5Me_5)_2UO(2,6\text{-di-}tert\text{-butylbenzene})$ was synthesized by a former colleague. The starting tetrazolate ligand, potassium methyltetrazolate (**21**), was prepared by addition of $KN(TMS)_2$ (0.2384 g, 1.195 mmol) to a solution of 5-methyltetrazole (0.1020 g, 1.213 mmol) in THF (15 mL). The reaction mixture was stirred at room temperature for 48 hours. White precipitate formed and was collected by filtration. The white solid was washed with THF (10 mL) and hexane (10 mL) and dried under reduced pressure. Yield: 0.1452 g (1.188 mmol, 98 %). Characterizations are described in the literature.[202] All NMR data can be found in Appendix B: NMR Data, and crystal structure parameters are located in Appendix C: Crystal Structure Data. Crystal structures are discussed in Section 7.3.2.

(Ph₃P)Au-methyltetrazolate (22)†: To a solution of $(Ph_3P)AuCl$ (0.2061 g, 0.4141 mmol) in toluene (25 mL), **21** (0.0553 g, 0.4525 mmol, 1.1 equiv.) was added. The reaction mixture was stirred at room temperature for 18 hours, after which time a white precipitate had formed. The solution was filtered through a Celite-padded fritted filter and rinsed with hot (85 °C) toluene. Volatiles were removed under reduced pressure to give an off-white powder of $(Ph_3P)Au$-methyltetrazolate (0.1800 g, 0.3319 mmol, 80 %). Single crystals suitable for X-ray crystallography were grown from toluene at -30 °C. MP: 197.5 °C, decomp. at 200 °C. ¹H

---

† Synthesis and crystal structure originally done by Dr. Kevin Browne. Other analyses and subsequent reactions were done as part of this work.

NMR (400 MHz, benzene-d_6, 298 K): δ 2.58 (s, 3H), 6.87 (t, 6H), 6.96 (t, 3H), 7.06 (m, 6H); ^{13}C NMR (400 MHz, benzene-d_6, 298 K): δ 129.46 (d, J = 12.4 Hz), 134.27 (d, 13.5 Hz); ^{31}P NMR (400 MHz, benzene-d_6, 298 K): δ 30.70. ATR-IR (Neat, 296 K, cm^{-1}): v 3902s, 3853s, 3744s, 3675s, 3628s, 3567m, 2919m, 2851m, 2160w, 1734m, 1700s, 1653s, 1559s, 1436s, 1387m, 1100s, 997w, 756s, 697s. Anal. Cald. For $C_{20}H_{18}AuN_4P$ (mol. wt. 542.30): C, 44.29; H, 3.35; N, 10.33. Found: C, 44.81; H, 3.58; N, 9.99.

Electrochemistry: Approximately 10 mg of **22** were mixed with approximately 390 mg of [NPr4][BAr$^f_4$] and 2.6 g of THF. A series of scans were done with a potential between -2 and 0 volts. The results are shown below.

(C₅Me₅)₂U[η^2-(N,N')-tetrazolate]₂ (23): To a solution of (C₅Me₅)₂UI(thf) (26.40 mg, 0.0373 mmol) in benzene-d_6 (<1 mL), **22** (39.90 mg, 0.0736 mmol, 2 equiv.) was added. A color change from olive green to dark red was seen immediately. The reaction mixture was monitored by ^{1}H NMR for several hours at room temperature to give a quantitative yield of (C₅Me₅)₂U[η^2-(N,N')-tetrazolate]₂. ^{1}H NMR (400 MHz, benzene-d_6, 296 K): δ 10.31 (s, 30H, C₅Me_5), -18.72 (s, 6H, tetrazole-CH_3). Further characterizations of this compound have been previously reported.[131]

(C₅Me₅)₂U(OAr)methyltetrazolate (24): To a solution of (C₅Me₅)₂UO(2,6-di-tert-butylbenzene) (0.0996 g, 0.1395 mmol) in toluene (3 ml), **22** (0.0758 g, 0.1398 mmol) was added. A color change from dark brown to dark red was seen almost immediately. The reaction was stirred at room temperature for 2 hours to give (C₅Me₅)₂U(OAr)methyltetrazolate (0.0646 g, 0.0809 mmol, 58 %). MP: 89.2 – 92.1 °C. ^{1}H NMR (400 MHz, benzene-d_6, 298 K): δ 21.61 (d, 1H, OAr), 19.52 (d, 1H, OAr), 14.93 (t, 1H, OAr), 9.46 (s, 9H, tBu), 7.77 (s, 30H, C₅Me_5), -4.44 (s, 9H, tBu), -26.46 (s, 3H, Metz). ATR-IR (Neat, 296 K, cm^{-1}): v 2953m, 2900m, 2866m, 2543b, 2181m, 2157m, 2047w, 1867w, 1653w, 1559w, 1435s, 1399s, 1181s, 1118w, 1019w, 855s, 818s, 744s, 691s. UV-Vis (toluene, 296 K, 5 mM cm^{-1} (M^{-1}cm^{-1}): 18657 (744), 14695 (141); NIR (toluene,

296 K, 30 mM cm^{-1} (M^{-1}cm^{-1}): 9718 (63), 8733 (50), 8450 (64), 8237 (57), 7616 (42), 7364 (43), 7087 (34), 6464 (30), 6297 (30), 5966 (29), 5863 (24), 4651 (36), 4596 (38), 4552 (36), 4482 (35).

Electrochemistry: Approximately 10 mg of **24** were mixed with approximately 390 mg of [NPr4][BAr^f$_4$] and 2.6 g of THF. A series of scans (rates varied from 50 to 5000) were done with a potential between -1 and 0 volts. The results are shown below.

(C_5Me_5)$_2$CeO(2,6-di-*tert*-butylbenzene) (25): To a solution of (C_5Me_5)$_2$CeCl(py) (0.1055 g, 0.2009 mmol) in THF (3 mL), K(OAr) (0.0489 g, 0.2001 mmol) was added. An immediate color change from yellow to red-orange was observed. The solution stirred at room temperature for 1 hour before the THF was removed under reduced pressure. The orange oil was picked up in toluene, which resulted in an immediate color change to magenta. The magenta solution was filtered through a Celite-padded frit and rinsed with 20 mL of toluene. Volatiles were removed under reduced pressure to give a magenta-colored powdered (C_5Me_5)$_2$Ce(OAr) (0.1103 g, 0.1785 mmol, 89% yield). ^{1}H NMR (400 MHz, benzene-d_6, 296 K): δ 8.00 (d, 2H, *Ar*), 7.36 (d, 1H, *Ar*), 2.80 (s, 30H, C$_5$*Me$_5$*), -7.48 (s, 18 H, ^{t}*Bu*). NMR data is consistent with literature values.[203]

(Ph$_3$P)Au-(C$_5$Me$_5$) (26): a) To a solution of (C_5Me_5)$_2$CeCl(py) (0.0987 g, 0.1880 mmol) in toluene (5 mL), **22** (0.1037 g, 0.1912 mmol) was added. The orange solution slowly turned yellow over the course of 10 minutes at room temperature. After 24 hours, the solution is olive green in color. It was filtered through a Celite-padded frit and rinsed with toluene (20 mL). Volatiles were removed to give a dark yellow-green oil, which was taken up in hexane, filtered through a Celite-padded frit, and volatiles were once again removed under reduced pressure. A light yellow powder (**26**, 0.0382 g, 0.0643 mmol, 34% yield) remained. X-ray quality crystals of **26** were grown in toluene at -30 °C overnight. ^{1}H NMR (400 MHz, benzene-d_6, 296 K): δ 7.35 (m, 6H, *Ph*), 6.91 (d, 9H, *Ph*), 2.41 (s, 15H, C$_5$*Me$_5$*). ^{31}P NMR (400 MHz, benzene-d_6, 296 K): δ 36.28. Data is consistent with literature values.[204]

b) Complex **25** (0.0251 g, 0.0406 mmol), **22** (0.0212 g, 0.0391 mmol) and benzene-d_6 (0.5 mL) were added to an NMR tube. A color change from magenta to orange, and finally dark yellow occurred almost immediately. The solution reacted for 1 hour at room temperature, after which time, ^{1}H and ^{31}P NMR data show the production of **26**, and no other phosphorus containing compounds.

7.3 Results

7.3.1 Exploratory Chemistry of Compound 22

The formation of (Ph$_3$P)Au-methyltetrazolate (**22**) is achieved through the salt metathesis reaction of potassium methyltetrazolate (**21**) and (Ph$_3$P)Au-Cl in toluene (Equation 14). The reaction proceeds at room temperature and is complete in under 24 hours. Once the KCl byproduct is filtered off, the toluene solution can be dried down to give **22** as an off-white powder.
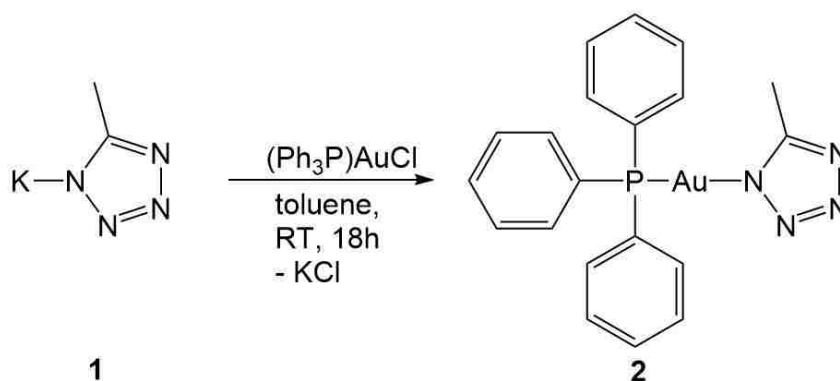
Equation 14. Formation of (Ph$_3$P)Au-methyltetrazolate

Complex **22** is not only a novel compound, but it has some interesting chemical properties that have been explored using the f-elements. It can be used as a transfer agent for the tetrazolate ligand on to uranium metal centers in a very facile, safe way. When two equivalents of **22** are reacted with a uranium (III)-halide complex, such as (C$_5$Me$_5$)$_2$UI(thf), the metal oxidizes to U(IV) and two tetrazolates are bound, each in an η^2 conformation to give the known complex,[131] **23** (Equation 15).
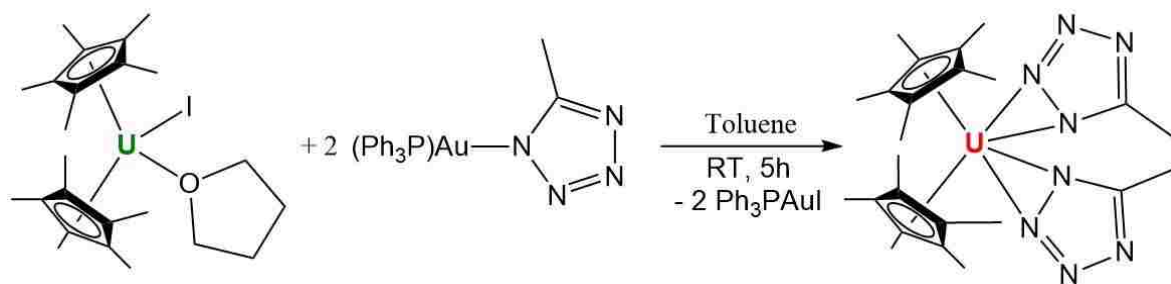
Equation 15. Synthesis of (C$_5$Me$_5$)$_2$U[η^2-(N,N')-tetrazole]$_2$ using 22.

When **22** is reacted with a non-halide uranium (III) complex, such as (C$_5$Me$_5$)$_2$U-OAr, the uranium is again oxidized to U(IV), but only one tetrazolate ligand is bound, to give (C$_5$Me$_5$)$_2$U(OAr)methyltetrazolate (Equation 16).
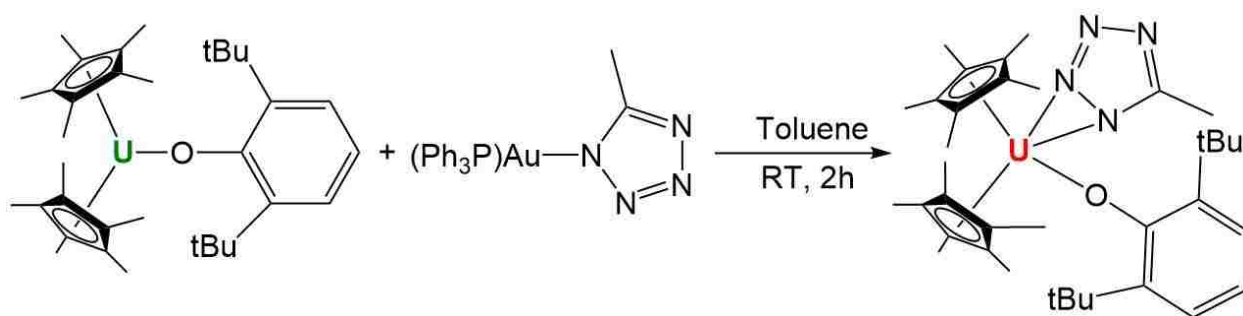
Equation 16. Synthesis of 24 from (C$_5$Me$_5$)$_2$U-OAr and Ph$_3$PAu-Metz.

Complex **22** was also reacted with the cerium complexes (C$_5$Me$_5$)$_2$CeCl(py) and (C$_5$Me$_5$)$_2$CeO(2,6-di-*tert*-butylbenzene) in an attempt to create the first organometallic cerium tetrazolate. However, the reaction with cerium produces several byproducts and decomposition products, including (C$_5$Me$_5$)$_2$. A major byproduct of the cerium reaction is the known complex (Ph$_3$P)Au-(C$_5$Me$_5$), which was originally published in 1984 by Werner et.al (Scheme 2).[204] This byproduct occurs in roughly 35% yield. During the course of the reaction, a purple-brown solid, likely containing a cerium product, precipitated out of the toluene solution. The solid was dissolved in pyridine to give a purple-brown solution, but no crystals could be grown from the mother liquor.
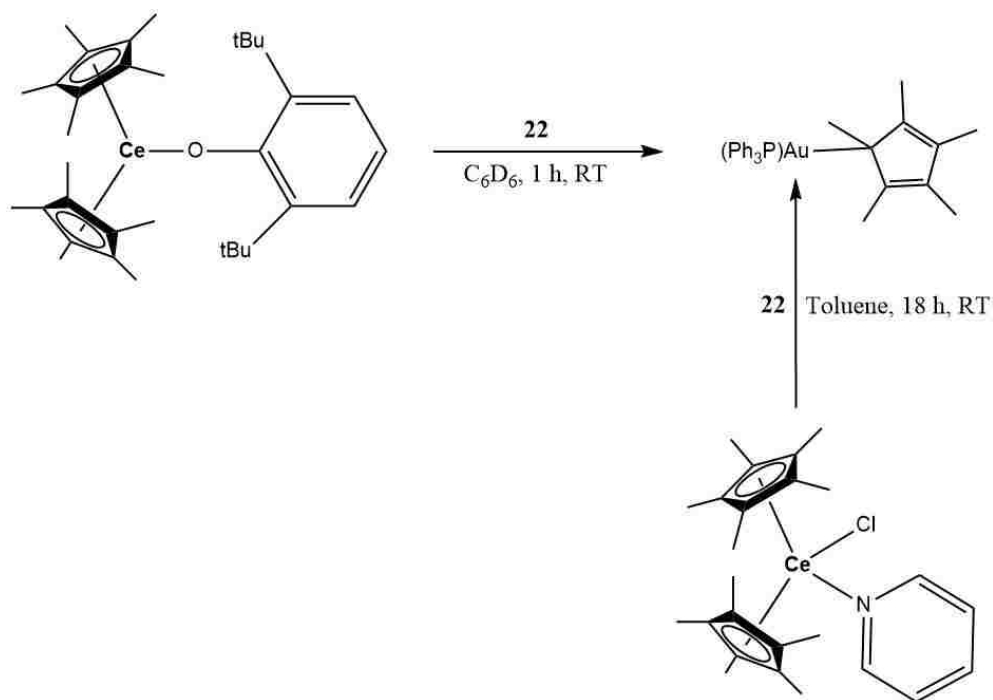
Scheme 2. Synthesis of $(Ph_3P)Au\text{-}(C_5Me_5)$ from two different routes.

7.3.2   Crystallography

The ORTEP view of **22** is shown in Figure 92. Selected bond lengths and angles for **22** are reported in Table 32. The geometry around the gold atom is nearly linear, with a P – Au – N bond angle of 177.89(6) °. As with similar complexes, only one of the nitrogen atoms on the tetrazolate ligand participates in coordination to the gold metal center.[186,190]
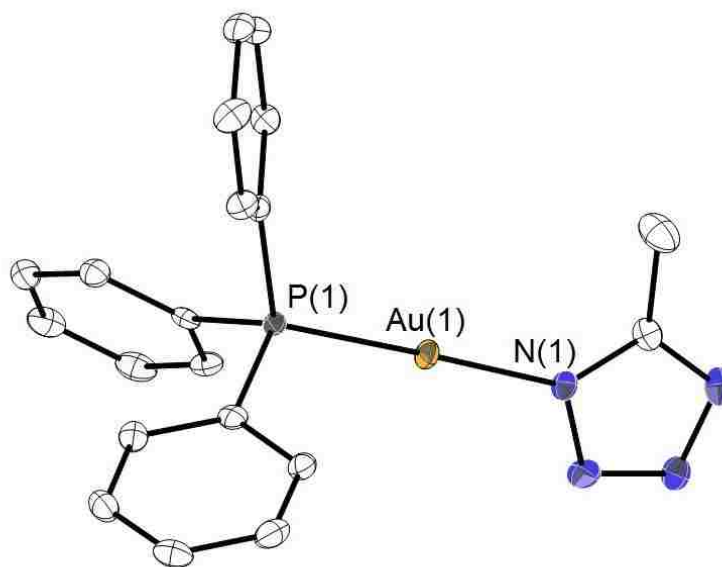
Figure 92. ORTEP view of **22**. Hydrogens are omitted for clarity, ellipsoids are drawn at the 50% probability level.

Table 32. Selected bond lengths (Å) and angles (°) of complex **22**.

Au – N	2.054(2)
Au – P	2.2450(7)
P – C(1)	1.810(2)
P – C(7)	1.813(2)
P – C(13)	1.821(2)
P – Au – N	177.89(6)
C – N – Au	132.05(17)
C(7) – P – Au	111.71(8)
C(1) – P – C(13)	104.64(10)

A very similar complex, $(Ph_3P)Au$-tetrazolate, was published in 2000 by Nomiya et.al.[186] Table 33 compares the bond lengths and angles between that complex and **22**. The values are very similar, particularly for Au – P, Au – N, and P – C bond lengths and the P – Au – N bond angle. There is a noticeable difference between the two complexes for the Au – N – C bond angle, most likely due to the addition of the methyl group on the tetrazolate ring of **22**.

Table 33. A comparison of bond lengths (Å) and angles (°) between complex **22** and previously reported work. [a]This work.

	(Ph₃P)Au-tet[186]	(Ph₃P)Au-Metz (**22**)[a]
Au − P	2.239(2)	2.2450(7)
Au − N	2.043(5)	2.054(2)
P − C	1.811 – 1.815	1.810 – 1.821
P − Au − N	178.4(1)	177.89(6)
Au − N − C	129.0(5)	132.05(17)

The Au − P (2.2450(7) Å) and Au − N bond distances (2.054(2) Å) of **22** are in agreement with the Au − P (2.239 – 2.250 Å) and Au − N (2.060 – 2.067 Å) bond length ranges from series of similar gold-tetrazolate compounds, published by Gaydou et.al. in 2013.[190] The Au − N − C bond angle of **22** (132.05(17) °) matches well with the range from Gaydou (131.63 – 132.01 °); however, the P − Au − N bond angle of **22** (177.89(6) °) is slightly larger (P − Au − N range = 174.57 – 176.82 °).[190] This could be due to the presence of different R groups on the phosphorus atom in **22**.

7.3.3   Electrochemistry

Electrochemical studies were performed with **22** and **24** using the electrolyte [NPr₄][BArᶠ₄] in THF. Potential was applied to the solution between -2 and 2 volts and the current was measured. Any reversible events in the current are indicative of a reversible oxidation-reduction reaction, likely occurring at the metal center. No oxidation/reduction occurred with **22** (Figure 93), which is unsurprising given the nature of gold. Electrochemical studies of **24** show a reversible U(III)/U(IV) couple, which is expected for uranium (Figure 94).
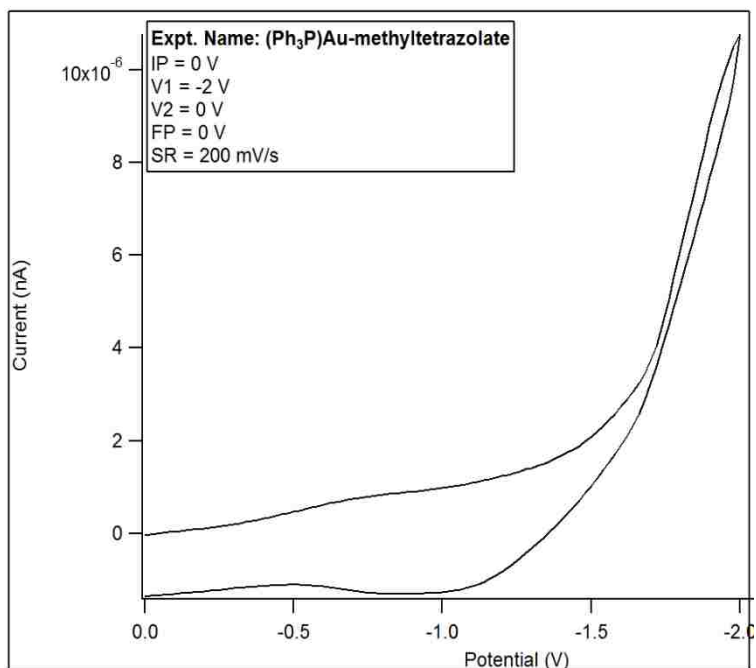
Figure 93. Electrochemistry data showing no redox potential of compound **22**.
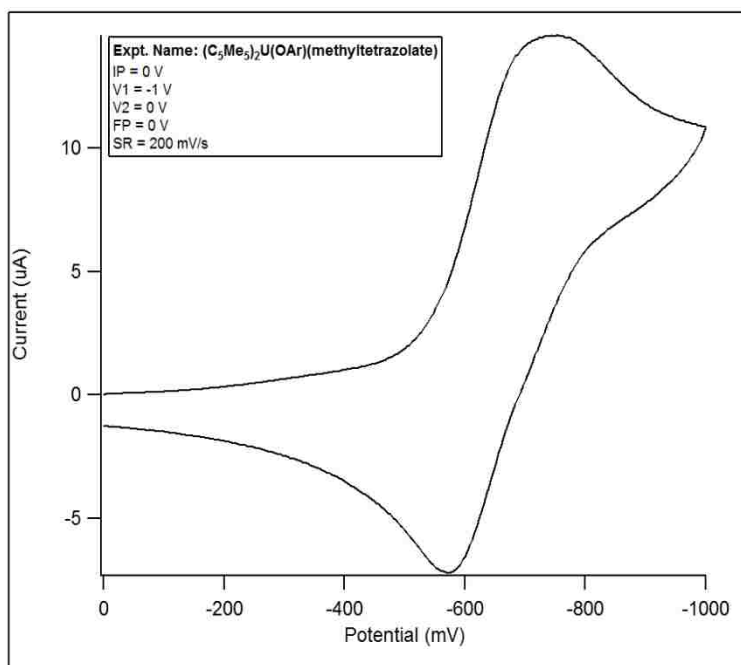
Figure 94. Electrochemical data for **24** showing a reversible couple

7.4 Conclusion

This work shows an example of a previously uncharacterized gold-tetrazolate compound and its use as a tetrazolate transfer agent in reactions with uranium. These reactions show an example of a novel organouranium-tetrazolate complex, of which there was previously only one in the literature.[131] The same chemistry was attempted using a cerium metal center with distinctly different results. The formation of $(Ph_3P)Au-(C_5Me_5)$ is rare, but not unheard of, in f-element synthetic chemistry. However, no crystal structure of a cerium tetrazolate complex was obtained. These results are important for the development of the chemistry of high-nitrogen containing actinide and lanthanide complexes because they show a novel, facile route to adding high-nitrogen ligands to the f-elements. Future efforts will focus heavily on obtaining crystal structure data for a cerium tetrazolate complex in order to determine its structure, as well as attempting the same chemistry with thorium.

Chapter 8: Conclusion

The previous seven chapters have described in detail the data and analysis of two different research projects; both irradiation of uranium-based materials and organometallic synthesis of thorium and uranium. This chapter sums up the conclusions of the two major projects by chapter, and then discusses future plans for each project based on the results shown in this document. The contributions of this work will be detailed in each summary.

8.1.   Summary of Irradiations

The main objective of this research was to create an actinide target from which fission products could be extracted in a simple, rapid way. Two types of targets were created: a microporous UO_2 material combined with KBr, and uranium-based metal organic frameworks. Each target was irradiated with neutrons of sufficient energy to induce fission in ^{238}U, contacted with a dilute acid, and analyzed via gamma spectroscopy for separation potential. Experiments with both the UO_2 targets and the UO_2-MOF targets showed that it is possible to extract fission products from an actinide target in good yields without dissolving the target material. A wide range of fission and activation products were extracted into acid solutions in less than 24 hours.

Chapter 2 described the synthesis and irradiation experiments of several UO_2 targets. These targets comprised microparticles of UO_2, often combined with the secondary matrix KBr. A secondary matrix was used to aid in the separation of the fission products from the target material by capturing the products and easily dissolving in aqueous solutions. Though KBr is inexpensive, readily soluble, and readily available, it does have downsides. The material needed to be fully dried before use to prevent the moderation of the neutron energies. It was also activated by the neutrons to give ^{82}Br, which has several gamma lines that can overshadow fission products in the sample.

However, the data shows that a matrix material, even one as simple as KBr, greatly enhanced the ability to remove fission products from the target. Fewer fission products were extracted from a target comprised solely of UO_2 microparticles, and those that were extracted were removed in much lower percentages. For example, only 26.52 ± 1.17 % of the fission product ^{105}Rh was extracted from the UO_2 particle target, compared to 58.62 ± 0.97 % extraction from a UO_2:3KBr pellet contacted with 0.01 M HNO_3. Four different types of acid (0.1 M HCl, 0.01 M HCl, 0.1 M HNO_3, and 0.01 M HNO_3) were analyzed for their extraction potential. The study confirmed that HNO_3 is a better extractant than HCl, but a more concentrated acid will dissolve the entire target. For example, the increase in separation yields for the target contacted with 0.1 M HNO_3 was due to the dissolution of the uranium target; this outcome was not desirable. Therefore, 0.01 M HNO_3 was chosen as an extractant for the remaining targets. This information shows that the targets can be further optimized for the extraction of fission products.

The data also show that irradiation of the target in a neutron flux formed from a dense plasma pinch is not as efficient at creating fission products as a neutron flux from the critical assembly device Flattop. This is likely due to the continuous flux formed from the critical assembly device versus the short, high intensity pulses from the plasma. Future applications of this research should explore other ways to use a continuous flux of neutrons to achieve the highest rates of fission events, or create a target more suited to short, high intensity pulses. For example, increasing the amount of fissionable material may lead to more fission events; enriching the sample slightly to increase the probability of a neutron inducing fission could have the same effect.

Chapter 3 described the synthesis, irradiation, and extraction of fission products from uranium based metal-organic frameworks (MOFs). Four MOFs were irradiated using Flattop over the course of these studies, and the results show that it is possible to extract fission products from the frameworks by contacting them with dilute acid. Based on the structure of the framework, different amounts and types of fission products were extracted. For example, fission products that can adopt either 4+ or 6+ oxidation

states were less likely to be extracted from smaller frameworks. These fission products may have the ability to chemically interact with the framework before they can escape.

As the pore sizes in the framework decrease, the extraction yield appears to decrease as well. The MOF targets using the linker molecules 2,6-pyridinedicarboxylic acid (2,6-pydc), 2,5-pydc, and 2,4-pydc were compared for their extraction efficiency. As the pore sizes of the frameworks decrease (2,6-pydc > 2,5-pydc > 2,4-pydc), the extraction efficiency also decreases. Size exclusion of larger isotopes, such as ^{140}Ba, may be a factor as the frameworks get smaller; chemical interactions of products that can adopt higher oxidation states also become more likely. The MOF material made of pyromellitic acid has pore sizes similar in size to the 2,5-pydc framework, but they are elongated rather than circular. More data is needed to make a firm conclusion, but the current data set indicates that less symmetrical pore sizes allow for better extraction of a wider variety of fission products. The nearly symmetrical pores formed by the pyridinedicarboxylic acid linkers do not appear to be as efficient at allowing for extraction as those formed by pyromellitic acid. It would be interesting to study other MOFs with significantly different structures for their extraction potential. The pore sizes in this study ranged from roughly 6 Å to approximately 9 Å, which is a fairly narrow window. Typical ionic radii values for fission products are on the order of 0.5–2 Å,[88] so a study of smaller pore sizes may be useful to determine if the products are getting trapped in the framework. Though more studies should be done, the knowledge that the potential exists to design a target to allow for extraction of specific fission products could greatly benefit the production of medical isotopes.

Chapter 4 summarized other attempts at creating porous target materials using depleted uranium. Alginate polymer based targets could potentially be useful, but the organic nature of the material caused the alginate material to sublime in the heat of the core of the critical assembly device, which can often attain temperatures in excess of 220 °C.[96] Targets of this type are likely to perform better in a temperature-moderated scenario, such as the core of a reactor. A UO$_2$-oxalate polymer was also

irradiated using the critical assembly device. Though the target holder did not pop open, the organic material changed and reduced the uranium to black UO_2. This UO_2 material was likely larger in diameter than the UO_2 studied in Chapter 2, and so a comparison was made between the extraction potentials of varying particle sizes. Based on the limited amount of data, it appears that more fission products were extracted at higher percentages from the smaller diameter (<10 μm) particles than the larger diameter (>10 μm) particles when contacted with the same acid.

Chapters 2-4 of this thesis work show positive results from the proof-of-principle concept that fission products can be extracted easily and rapidly from uranium target materials using dilute (< 0.1 M) acids while avoiding the unnecessary step of dissolving the entire target. This concept could lead the advancement of the library of fission product ratios based on the original actinide material, which could prove beneficial to the field of nuclear forensics. This work could also benefit nuclear medicine as a means to quickly produce medical isotopes from the fission of depleted uranium; or lead to the advancement in production of ^{238}Pu for fuel fabrication of space exploration vehicles (See Section 8.3.1.1)

8.2.   Summary of Organometallic Work

The main objective of this set of projects was to understand more about the basic chemistry of thorium and uranium, including the involvement of f-electrons in bonding, the interactions of "hard' actinides with "soft" chalcogenide ligands, the examination of uranium-mediated C–X activation, and the facilitation of adding high-nitrogen ligands to actinide materials. The understanding of these chemical interactions could lead to the next generation of actinide targets; materials composed of compounds that are not easily destroyed or activated in a neutron flux are ideal for next generation targets.

Chapter 5 details the synthesis and characterization studies of thorium-chalcogenide complexes, including the novel compound $(C_5Me_5)_2Th(SMe)_2$, and the many routes that lead to $(C_5Me_5)_2ThS_5$. Understanding the nature of bonding between the actinides and soft donors such as sulfur may aid in using chalcogenides

in the separation of actinides and lanthanides in large scale processes.[110] Studies have been done over the past few years that show there is a tendency for chalcogenides to preferentially bind to lanthanides, which could lead to advancements in separating the later actinides from the lanthanides in spent fuel.[110] However, the chemistry differences between 4f- and 5f-electron compounds must first be better understood. The examination of thorium interactions with the chalcogenides, particularly sulfur, show a lesser degree of covalent tendencies than its uranium analogues. These results has the potential to be exploited in the separation of lower valent actinides from lanthanides. This work also demonstrates a rare example of sulfide insertion into an actinide-carbon bond. While similar routes to create $(C_5Me_5)_2US_5$ proved ineffective, comparisons between $(C_5Me_5)_2Th(SMe)_2$ to $(C_5Me_5)_2U(SMe)_2$ indicate that there is more covalency in bonds between the chalcogenides and uranium than with thorium. This may be suggestive of f-electron interactions within the molecule.

Chapter 6 describes the studies of $(C_5Me_5)_2U(bpy)$, a low-valent uranium synthetic equivalent, with benzyl halides (F, Cl, Br, and I) as examples of actinide-mediated C–X activation. A series of $(C_5Me_5)_2U(X)(bpy)(Bn)$ (X = F, Cl, Br, I) complexes were synthesized and characterized. Attempts at understanding the mechanism of addition were also made; including the synthesis of the novel compound $(C_5Me_5)_2U(4,4'-tBu_2bpy)$ and its subsequent reaction with benzyl chloride to form $(C_5Me_5)_2U(Cl)(tBu_2bpy)(Bn)$. In both the substituted and unsubstituted bpy ring cases, the benzyl group adds to the 4 position of one ring, even if the position had been "blocked" by the *tert*-butyl groups. This leads to the conclusion that the benzyl group is adding to a different position (most probably the 6 or 6') and migrating around the bpy ring to the 4 (or 4') position. The reaction of $(C_5Me_5)_2U(6,6'Me_2-bpy)$ with benzyl chloride leads to the formation of $(C_5Me_5)_2UCl_2$ and free bipyridine, indicating an inability of the benzyl ring to add to the blocked 6 (or 6') position. Similar attempts to create thorium analogues did not result in C–X activation, but rather $(C_5Me_5)_2ThX_2$ and free bipyridine. This is perhaps a result of the ability of uranium to inhabit several oxidation states.

Chapter 7 summarizes the synthesis and characterizations of (Ph$_3$P)Au-methyltetrazolate and its uses in transfer of the methyltetrazolate to actinide compounds. Because tetrazoles are known for their potential for sensitivity to shock, it was essential that a pacified complex be created that could safely and easily transfer the high-nitrogen ligand to metal centers. Results from this chapter show that it can be used as a transfer reagent in a safe environment. For example, reaction of two equivalents of (Ph$_3$P)Au-methyltetrazolate with (C$_5$Me$_5$)$_2$UI(thf) gives the known compound (C$_5$Me$_5$)$_2$U(Metz)$_2$ (Metz = methyltetrazolate). The reaction of one equivalent of (Ph$_3$P)Au-methyltetrazolate with a non-halide U(III) complex, such as (C$_5$Me$_5$)$_2$U(OAr) will give (C$_5$Me$_5$)$_2$U(OAr)(methyltetrazolate). Preliminary research also shows that the transfer of tetrazolates to lanthanides such as cerium may also be completed, although more studies and characterizations are needed. The attempts at transferring methyltetrazolate to (C$_5$Me$_5$)$_2$Ce(OAr) gave (Ph$_3$P)Au-Cp* rather than the expected compound (C$_5$Me$_5$)$_2$Ce(OAr)(methyltetrazolate). Similar results were seen with other types of cerium starting materials.

8.3. Future Work

Based on the developments made during the course of these projects, there are myriad future directions for this research. Listed below are examples from each project that could utilize the conclusions drawn from this dissertation to further develop the fields of nuclear forensics and organoactinide synthetic chemistry.

8.3.1 Irradiations

8.3.1.1 UO$_2$

The results detailed in this thesis document are only the beginning of a promising exploration into the use of actinide target materials to quickly separate fission products for the purpose of building a library of fission products. This library can be used to compare fission products their ratios for a given fissionable material, or combination of materials, to a detonated device in order to determine its origin. While KBr

is proof that a matrix material is useful in increasing the separation, the neutron activation of bromine can make data analysis difficult. Future studies may want to use a different matrix in order to avoid complications in the gamma spectrum. For example, a simple salt such as potassium iodide (KI) could be used. Though very similar to its KBr counterpart, KI is activated in the neutron flux to give the short-lived isotope ^{128}I ($t_{1/2}$ = 25 min).[38] This isotope decays to stable ^{128}Xe, and would not appear in the gamma spectroscopy data. Though salts are conveniently removed by dilute acid solutions, they are not the only type of secondary matrix worth exploring. The gel targets described in Chapter 4 Section 4.2.1 easily dissolved in dilute HCl, and could be used as a removable secondary matrix in experiments with thermally cooler conditions.

A second experiment of interest could be comparing the extraction potential of various sizes of known macroparticulate UO_2 to the microparticulate version. Comparison of "macroparticle" (i.e. > 10 µm diameter) UO_2 using a secondary matrix will give insight into the design of the particles for future, larger-scale experiments. Different methods of analyzing the fission products can also be used: ICP-MS or ICP-AES will allow one to see fission products that are not gamma emitters, as well as the stable daughters from fission products that are too short-lived to see otherwise. Along these lines, imaging and analysis of the UO_2 particles post-irradiation could also be done to determine if any significant quantity of the particles had been dissolved, or otherwise deformed.

Another possibility to gather data would be to use an enriched sample and irradiate it using thermal neutrons from a reactor, rather than fast neutrons from a criticality device. This would allow the organic-based samples to be irradiated without being heated above their sublimation point. It would also allow for the studies of actinide materials with different concentrations of certain actinide isotopes.

Ideally, the targets presented here can be a proof of principle for studies involving other actinides, such as plutonium, and their fission product libraries. It could also be possible to utilize this methodology to

create and separate activation products. For example, because it has been shown that ^{239}Np can easily be extracted, the creation and separation of ^{238}Pu could be simplified by irradiating a target consisting of microparticles of ^{237}NpO$_2$ and a secondary matrix, and using the kinetic energy of the neutron activation recoil as the main means of separation.

8.3.1.2   MOFs

Future work with MOFs includes diversifying the types of organic linker materials used (i.e. using nitrogen based ligands instead of carboxylic acids), choosing a material that forms a different framework type, repeating experiments with current frameworks to gather more data points, and changing the actinide metal in the framework. The pore sizes of the frameworks can also be varied depending on the isotopes of interest. As stated previously, the range in this work was roughly 6 to 9 Å; MOFs have the capability to contain pore sizes in excess of 30 Å,[24] so more studies with a variety of pore sizes should be done to expand the data set. Though there do not seem to be thermal problems with the organic components, these materials could also be enriched and irradiated using neutrons from a reactor. Analysis of the material post-irradiation to determine the extent of irradiation damage to the framework should also been done. This could include powder X-ray diffraction or optical or SEM imaging.

8.3.1.3   Gels

Though the alginate gel targets did not provide irradiation data due to their decomposition, they may still prove useful using other methods. The experimental data show that the gel is soluble in dilute HCl, indicating that the gel could be treated as a secondary matrix, much like the KBr discussed in Chapter 2. Comparisons between the UO$_2$:KBr targets and future gel targets may show a correlation between type of secondary matrix and efficacy of the separation method described in this document. The gel targets would need to be irradiated under different conditions; particularly lower than their decomposition temperature, which is roughly 180 °C. Previous chapters have explained that this is possible using a research reactor and a target enriched to approximately 3-5% ^{235}U. Explorations into the need for

homogenous distribution of UO_2 particles within the gel should also be performed; improving the special distribution of the particles within the target may benefit the extraction yields. Though the entire target would be situated within the neutron flux, targets with large clusters of UO_2 particles in one area may not give separation yields as high as a target with equal dispersion of particles throughout the gel. The fission products escaping from a particle located within the cluster could embed themselves on neighboring particles rather than in the gel.

8.3.2 Organometallics

8.3.2.1   Thorium chalcogenides

The lack of 5f-electrons on thorium may contribute to chemical differences between thorium chalcogenides and other actinide chalcogenides. Preliminary comparisons between uranium and thorium sulfides have been completed, but there are still studies to be done. There have also been attempts to synthesize $(C_5Me_5)_2US_5$ in order to investigate the differences between it and the thorium analogue, but none have been successful. Should the compound be successfully characterized, comparisons can be made between its f-electrons involvement in chalcogenide bonding to the thorium analogue, which has no f-electrons.

8.3.2.2   C-X activation

A series of novel uranium-halide complexes have been synthesized and characterized. Rare examples of actinide-mediated C-X activation, particularly with fluorides, have been presented, although the mechanism of the benzyl addition to the bipyridine rings is not fully understood. Theoretical calculations and comparisons to experimental data can be done to elucidate the mechanism, as well as the electron density around the non-aromatic bipyridine ligand. Comparisons between results from uranium and thorium studies can also be drawn. If the chemistry is dependent upon the size of the metal, or if the 5f-electrons are actively involved in the bonding, it could explain why the reaction does not appear to work

with a thorium metal center. Studies with other alkyl-X groups could also be done to see if the chemistry is similar when the bulk of the alkyl group is changed.

8.3.2.3 Methyltetrazolate transfer

Several examples of the use of (Ph$_3$P)Au-methyltetrazolate as a transfer agent to actinides have been presented. Future work on this project involves using the gold transfer agent to add other tetrazoles to actinides, thus opening a world of safely synthesized high-nitrogen actinide complexes. The gold transfer agent could also be used to add other ligands - such as alkoxides - to metal centers. Studies are on-going to use this method of transfer to attach high-nitrogen ligands to other f-elements, such as cerium. The potential contributions from this work include opening the possibility for the synthesis of safe, stable high-nitrogen actinide complexes for the study of soft-donor nitrogen interactions with the hard-donor actinides.

Appendix A: Raw data for extraction experiments

Table 34. Raw data for Figure 19

Time (min)	[U] (mmol/L)
10	1.66
20	0.93
30	1.85
40	1.74
50	1.76
90	4.74
120	3.86
150	4.19
210	5.27
270	4.93
330	4.92
390	6.32
1440	8.19

Table 35. Raw data for Figure 20

Time (min)	[U] (mmol/L)
10	3.50
20	0.75
30	1.12
40	0.80
50	0.44
60	0.47
90	0.62
120	0.59
150	1.36
210	1.37
270	1.32
330	2.33
390	2.22
1440	6.19
7200	5.57
8640	6.53

Table 36. Raw data for Figure 21

Time (min)	[U] (mmol/L)
10	2.00
20	2.34
30	2.69
40	2.52
50	2.74
60	3.12
90	2.80
120	3.00
150	3.71
210	4.88
270	3.18
330	3.91
390	3.94
1440	6.83
7200	7.00
8640	6.47

Table 37. Raw data for Figure 34

Nuclide	Energy	% Extracted over 1 hour
Ce-143	293.8	25.87 ± 0.59
Np-239	99.63	27.26 ± 0.23
	104	26.75 ± 0.18
	106.27	2.86 ± 0.05
	117.29	19.42 ± 0.29
	228.64	3.11 ± 0.07
	316.17	15.62 ± 0.52
Nd-147	91.04	52.69 ± 1.00
Tc-99m	140.8	23.39 ± 0.26
Te-132	228.64	3.11 ± 0.07
Zr-97	743.42	36.47 ± 0.89
Pm-149	285.7	65.86 ± 1.70
I-133	530.12	10.84 ± 0.30
Rh-105	319.57	92.01 ± 1.86
I-131	364.63	30.64 ± 0.85

Table 38. Raw data for Figure 35

Nuclide	Energy	0.01 M HCl	Error
Ce-143	57.32	0.00	0.00
	231.72	4.75	0.48
	293.8	53.58	0.74
	350.85	9.73	0.87
	721.64	9.20	1.42
	664.48	7.45	1.15
Np-239	61.36	0.00	0.00
	99.63	16.30	0.18
	104	13.56	0.13
	106.27	12.92	0.12
	117.29	25.51	0.33
	210.01	35.45	0.46
	228.64		0.18
	277.92	72.35	0.22
	316.17	3.91	0.27
	334.65	3.62	0.24
Nd-147	91.04	54.25	0.74
Tc-99m	140.8	31.95	0.34
Mo-99	181.32	0.00	0.00
	739.53	0.00	0.00
Ce-141	145.98	65.88	1.06
Te-132	49.38	0.00	0.00
	228.64	18.53	0.18
Xe-135	250.2	19.82	0.24
Zr-97	743.42	31.45	0.54
Y-93	267.22	77.20	1.26
I-135	1131.44	3.72	0.77
	1259.65	54.64	2.33
Pm-149	285.7	5.94	0.44
I-133	530.12	43.06	0.50
Rh-105	306.61	7.34	0.66
	319.57	66.96	1.03
Pm-151	340.64	9.28	0.81
I-131	364.63	73.76	1.16
Ru-103	497.38	11.32	1.02
Ba-140	537.74	10.35	1.29

Table 39. Raw data for Figure 36

Nuclide	Energy	0.1 M HNO3	Error
Ce-143	57.32	68.30	1.25
	231.72	0.00	0.00
	293.8	76.63	1.18
	350.85	0.00	0.00
	721.64	0.00	0.00
	664.48	0.00	0.00
Np-239	61.36	0.00	0.41
	99.63	29.52	0.32
	104	27.14	0.25
	106.27	26.70	0.23
	117.29	43.53	0.58
	210.01	54.58	0.80
	228.64		0.38
	277.92	36.00	0.42
	316.17	12.32	0.81
	334.65	11.89	0.64
Nd-147	91.04	60.82	0.88
Tc-99m	140.8	48.75	0.59
Mo-99	181.32	0.00	1.35
	739.53	0.00	0.00
Ce-141	145.98	81.06	1.52
Te-132	49.38	0.00	0.00
	228.64	34.29	0.38
Xe-135	250.2	31.51	0.47
Zr-97	743.42	47.72	0.94
Y-93	267.22	85.61	1.66
I-135	1131.44	72.16	5.13
	1259.65	62.77	5.75
Pm-149	285.7	11.39	0.98
I-133	530.12	59.35	0.83
Rh-105	306.61	0.00	0.00
	319.57	82.35	1.52
Pm-151	340.64	18.01	0.00
I-131	364.63	87.62	1.63
Ru-103	497.38	0.00	0.00
Ba-140	537.74	0.00	0.00

Table 40. Raw data for Figure 37

Nuclide	Energy	0.1 M HCl	Error
Ce-143	57.32	43.92	0.63
	231.72	0.00	0.00
	293.8	48.31	0.56
	350.85	0.00	0.00
	721.64	0.00	0.00
	664.48	0.00	0.00
Np-239	61.36	6.46	0.23
	99.63	14.36	0.12
	104	13.40	0.09
	106.27	12.65	0.08
	117.29	21.59	0.23
	210.01	27.69	0.32
	228.64	17.81	0.15
	277.92	17.41	0.17
	316.17	4.92	0.25
	334.65	6.10	0.27
Nd-147	91.04	41.46	0.46
Tc-99m	140.8	22.11	0.20
Mo-99	181.32	2.27	0.19
	739.53	1.54	0.32
Ce-141	145.98	0.00	0.00
Te-132	49.38	2.54	0.19
	228.64	17.81	0.15
Xe-135	250.2	15.92	0.18
Zr-97	743.42	24.92	0.40
Y-93	267.22	7.09	0.52
I-135	1131.44	0.00	0.00
	1259.65	0.00	0.00
Pm-149	285.7	7.24	0.41
I-133	530.12	36.10	0.39
Rh-105	306.61	1.61	0.27
	319.57	57.45	0.86
Pm-151	340.64	0.00	0.00
I-131	364.63	68.21	0.99
Ru-103	497.38	0.00	0.00
Ba-140	537.74	0.00	0.00

Table 41. Raw data for Figure 38

Nuclide	Energy	0.01 M HNO3	Error
Ce-143	57.32	0.00	0.00
	231.72	0.00	0.00
	293.8	49.29	0.68
	350.85	2.63	0.34
	721.64	0.00	0.00
	664.48	0.00	0.00
Np-239	61.36	0.00	0.00
	99.63	19.22	0.21
	104	16.33	0.15
	106.27	15.83	0.14
	117.29	30.93	0.39
	210.01	12.26	0.30
	228.64	20.99	0.20
	277.92	21.40	0.24
	316.17	16.16	0.56
	334.65	17.09	0.55
Nd-147	91.04	56.25	0.77
Tc-99m	140.8	29.87	0.31
Mo-99	181.32	10.89	0.48
	739.53	0.00	0.00
Ce-141	145.98	3.51	0.28
Te-132	49.38	0.00	0.00
	228.64	20.99	0.20
Xe-135	250.2	17.86	0.21
Zr-97	743.42	30.81	0.56
Y-93	267.22	6.20	0.46
I-135	1131.44	0.00	0.00
	1259.65	0.00	0.00
Pm-149	285.7	25.93	0.90
I-133	530.12	39.99	0.49
Rh-105	306.61	0.00	0.00
	319.57	58.62	0.97
Pm-151	340.64	2.42	0.32
I-131	364.63	69.04	1.08
Ru-103	497.38	5.00	0.56
Ba-140	537.74	0.00	0.00

Table 42. Raw data for Figure 40

Nuclide	Energy	%Branch	% Extracted
Ce-143	57.32	11.7	20.59 ± 0.48
	350.85	3.23	24.51 ± 0.57
Mo-99	181.32	6.14	12.11 ± 0.52
	739.53	12.26	4.43 ± 0.26
Ce-141	145.98	48	34.85 ± 0.69
Y-93	267.22	7.4	12.65 ± 0.21
Rh-105	306.61	5.1	7.14 ± 0.38
	319.57	19.1	26.52 ± 1.17

Table 43. Extraction data for the UO$_2$ foam sample in Figure 42

Nuclide	Energy	% Extracted	Error	
Ce-143	57.32	0.00	0.00	
	231.72	0.00	0.00	
	293.8	9.53	0.17	
	350.85	5.92	0.30	
	664.48	0.00	0.00	
	721.64	0.00	0.00	
Np-239	61.36	0.00	0.00	
	99.63	1.07	0.03	
	104	0.96	0.02	
	106.27	0.86	0.02	
	117.29	1.66	0.06	
	210.01	2.25	0.07	
	228.64	0.82	0.02	
	277.92	0.84	0.03	
	316.17	0.73	0.06	
	334.65	0.70	0.06	
Nd-147	91.04	3.80	0.13	
Tc-99m	140.8	5.04	0.08	
Mo-99	181.32	0.00	0.00	
	739.53	0.00	0.00	
Ce-141	145.98	5.72	0.21	
Te-132	49.38	0.00	0.00	
	228.64	0.82	0.02	
Xe-135	250.2	1.31	0.03	
Zr-97	254.58	0.00	0.00	
	355.72	0.00	0.00	
	507.75	0.00	0.00	
	743.42	0.26	0.03	
Y-93	267.22	6.36	0.25	
I-135	1131.44	0.00	0.00	
	1259.65	7.58	0.53	
Pm-149	285.7	0.00	0.00	
I-133	530.12	8.39	0.12	
Rh-105	306.61	4.51	0.23	
	319.57	4.82	0.17	
Pm-151	340.64	6.21	0.29	
I-131	364.63	6.43	0.22	
Ru-103	497.38	4.88	0.29	
Ba-140	537.74	6.45	0.38	

Table 44. Raw data for Figure 58

Nuclide	Energy	Branching Ratio %	% Extracted Target 1 PYDC
Ce-143	57.32	11.7	95.52±1.97
	231.72	2.05	0.00
	293.8	42.8	92.54±1.65
	350.85	3.23	83.12±3.91
	721.64	53.1	0.00
	664.48	5.69	70.02±5.28
Np-239	61.36	1.3	97.45±1.91
	99.63	12.9	95.89±0.69
	104	20.5	96.01±0.57
	106.27	25.34	96.13±0.53
	117.29	4.87	96.55±1.10
	210.01	3.36	96.98±1.49
	228.64	10.73	96.38±0.77
	277.92	14.51	96.55±0.91
	316.17	1.6	94.06±2.41
	334.65	2.06	94.10±2.20
Nd-147	91.04	28.1	97.05±1.61
Tc-99m	140.8	89	108.65±1.06
Mo-99	181.32	6.14	94.45±2.64
	739.53	12.26	95.38±5.11
Ce-141	145.98	48	95.95±2.61
Te-132	49.38	15	97.69±2.49
	228.64	88	96.38±0.77
Xe-135	250.2	90	99.05±2.45
Zr-97	254.58	1.15	83.04±3.40
	355.72	2.09	68.75±3.77
	507.75	5.03	68.36±3.73
	743.42	93.09	84.50±1.49
Y-93	267.22	7.4	67.54±2.69
I-135	1131.44	22	0.00
	1259.65	29	0.00
Pm-149	285.7	87.2	93.54±2.96
I-133	530.12	87	84.53±1.16
Rh-105	306.61	5.1	87.86±3.68
	319.57	19.1	88.30±2.38
Pm-151	340.64	22.5	89.21±4.13
I-131	364.63	81.5	97.96±3.00
Ru-103	497.38	91	98.55±4.36

Ba-140	537.74	24	94.08±5.48
Zr-95	724.29	44	62.28±4.67
Sr-91	749.74	23.7	81.13±5.09
	1023.98	33.5	76.37±4.87

Table 45. Raw data for Figure 59

Nuclide	% Extracted
Ce-143	75.80 ± 3.43
Np-239	87.57 ± 2.18
Mo-99	56.68 ± 3.69
Ce-141	64.50 ± 1.77
Zr-97	76.04 ± 2.89

Table 46. Raw data for Figure 60

Nuclide	Energy (keV)	% Extracted
Ce-143	57.32	35.15 ± 0.69
	721.64	8.22 ± 0.53
Np-239	104.00	37.24 ± 0.28
	106.27	40.57 ± 0.22
	117.29	36.10 ± 0.37
	210.01	37.46 ± 0.65
	228.64	43.47 ± 0.45
	277.92	16.45 ± 0.30
	316.17	32.72 ± 0.98
Tc-99m	140.80	44.90 ± 0.49
Mo-99	181.32	32.82 ± 0.93
Te-132	228.64	43.47 ± 0.45
Xe-135	250.20	16.83 ± 0.28

Table 47. Raw data for Figure 61

Nuclide	Energy (keV)	% Extracted UO_2-2,4-pydc
Ce-143	57.32	7.04 ± 0.20
	721.64	0.00 ± 0.00
Np-239	104.00	0 .00± 0.00
	106.27	21.68 ± 0.13
	117.29	18.06 ± 0.21
	210.01	5.70 ± 0.19
	228.64	6.20 ± 0.13
	277.92	6.23 ± 0.16
Tc-99m	140.80	25.38 ± 0.31
Mo-99	181.32	14.70 ± 0.46
Te-132	228.64	6.20 ± 0.13
Ce-141	145.98	0.00 ± 0.00
Xe-135	250.20	6.44 ± 0.14
Pm-149	285.70	0.00 ± 0.00
Zr-97	355.72	0.00 ± 0.00
Ba-140	537.74	0.00 ± 0.00
I-131	364.63	6.88 ± 0.42

Table 48. Raw data for Figure 62

Nuclide	Energy	% Extracted
Ce-143	721.64	47.74 ± 1.19
Np-239	104.00	68.41 ± 0.38
	106.27	54.80 ± 0.20
	117.29	51.91 ± 0.37
	210.01	55.39 ± 0.67
	228.64	64.24 ± 0.46
	277.92	35.27 ± 0.37
Tc-99m	140.80	78.84 ± 0.59
Mo-99	181.32	62.45 ± 1.16
Te-132	228.64	64.24 ± 0.46
Xe-135	250.20	56.94 ± 1.08
Pm-149	285.70	61.48 ± 0.99
Ba-140	537.74	47.48 ± 1.83

Table 49. Raw data for Figure 63

Nuclide	Energy (keV)	% Extracted UO_2-2,6-pydc	% Extracted UO_2-2,5-pydc	% Extracted UO_2-2,4-pydc	% Extracted UO_2-prma
Ce-143	57.32	75.80 ± 3.43	35.15 ± 0.69	7.04 ± 0.20	0.00 ± 0.00
	721.64	0.00 ± 0.00	0.00 ± 0.00	0.00 ± 0.00	47.74 ± 1.19
Np-239	104.00	0.00 ± 0.00	37.24 ± 0.28	0 .00± 0.00	68.41 ± 0.38
	106.27	87.57 ± 1.12	40.57 ± 0.22	21.68 ± 0.13	54.80 ± 0.20
	117.29	0.00 ± 0.00	36.10 ± 0.37	18.06 ± 0.21	51.91 ± 0.37
	210.01	0.00 ± 0.00	37.46 ± 0.65	5.70 ± 0.19	55.39 ± 0.67
	228.64	84.85 ± 2.18	43.47 ± 0.45	6.20 ± 0.13	64.24 ± 0.46
	277.92	0.00 ± 0.00	16.45 ± 0.30	6.23 ± 0.16	35.27 ± 0.37
Tc-99m	140.80	0.00 ± 0.00	44.90 ± 0.49	25.38 ± 0.31	78.84 ± 0.59
Mo-99	181.32	56. 68 ±3.69	32.82 ± 0.93	14.70 ± 0.46	62.45 ± 1.16
Te-132	228.64	84.85 ± 2.18	43.47 ± 0.45	6.20 ± 0.13	64.24 ± 0.46
Ce-141	145.98	64.50 ± 1.77	0.00 ± 0.00	0.00 ± 0.00	0.00 ± 0.00
Xe-135	250.20	0.00 ± 0.00	16.83 ± 0.28	6.44 ± 0.14	56.94 ± 1.08
Pm-149	285.70	0.00 ± 0.00	0.00 ± 0.00	0.00 ± 0.00	61.48 ± 0.99
Zr-97	355.72	76.04 ± 2.89	0.00 ± 0.00	0.00 ± 0.00	0.00 ± 0.00
Ba-140	537.74	0.00 ± 0.00	0.00 ± 0.00	0.00 ± 0.00	47.48 ± 1.83
I-131	364.63	0.00 ± 0.00	0.00 ± 0.00	6.88 ± 0.42	0.00 ± 0.00

Table 50. Raw data for UO2-oxalate extraction Figure 70

Nuclide	Energy (keV)	% Extracted UO_2- Oxalate
Ce-143	57.32	19.88 ± 0.39
	350.85	0.00 ± 0.00
Np-239	99.63	9.01 ± 0.11
	104	0.00 ± 0.00
	106	17.69 ± 0.12
	117	16.81 ± 0.22
	228	15.82 ± 0.22
Tc-99m	140.8	18.77 ± 0.27
Mo-99	181.32	9.20 ± 0.41
	739.53	0.00 ± 0.00
Ce-141	145.98	0.00 ± 0.00
Xe-135	250.2	6.96 ± 0.18
Y-93	267.22	0.00 ± 0.00
Rh-105	306.61	0.00 ± 0.00
	319.57	0.00 ± 0.00

Appendix B: NMR Data
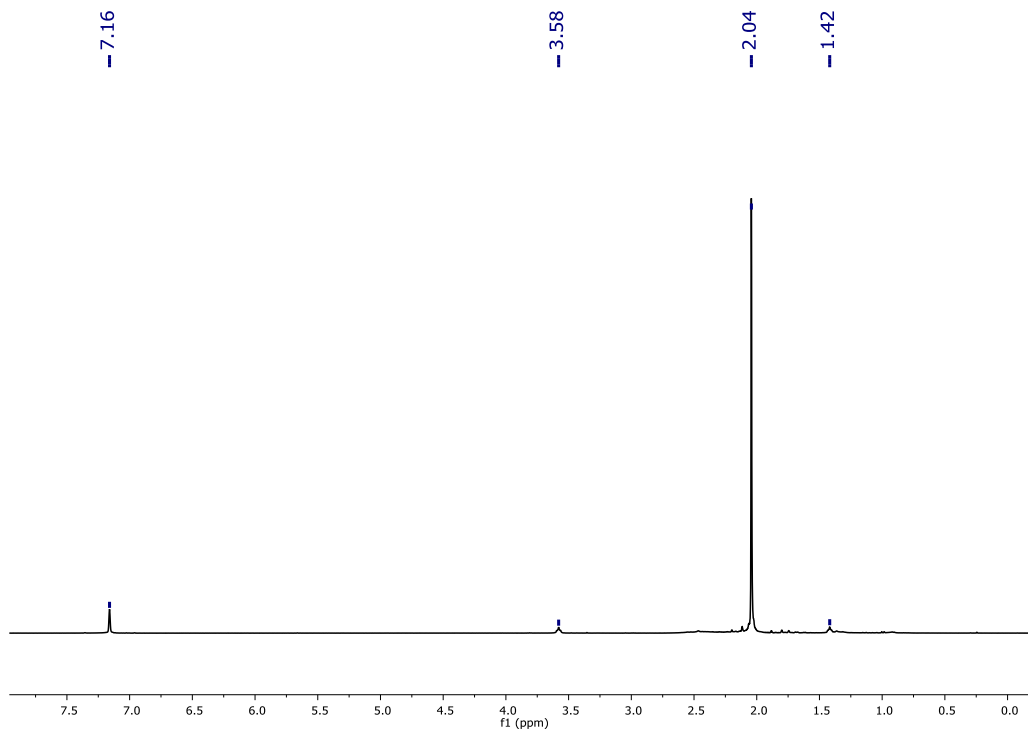
Figure 95. ^{1}H NMR (400 MHz, 295 K, C$_6$D$_6$) spectrum showing (C$_5$Me$_5$)$_2$ThS$_5$ at 2.04 ppm; THF solvent is present at 3.58 and 1.42 ppm.
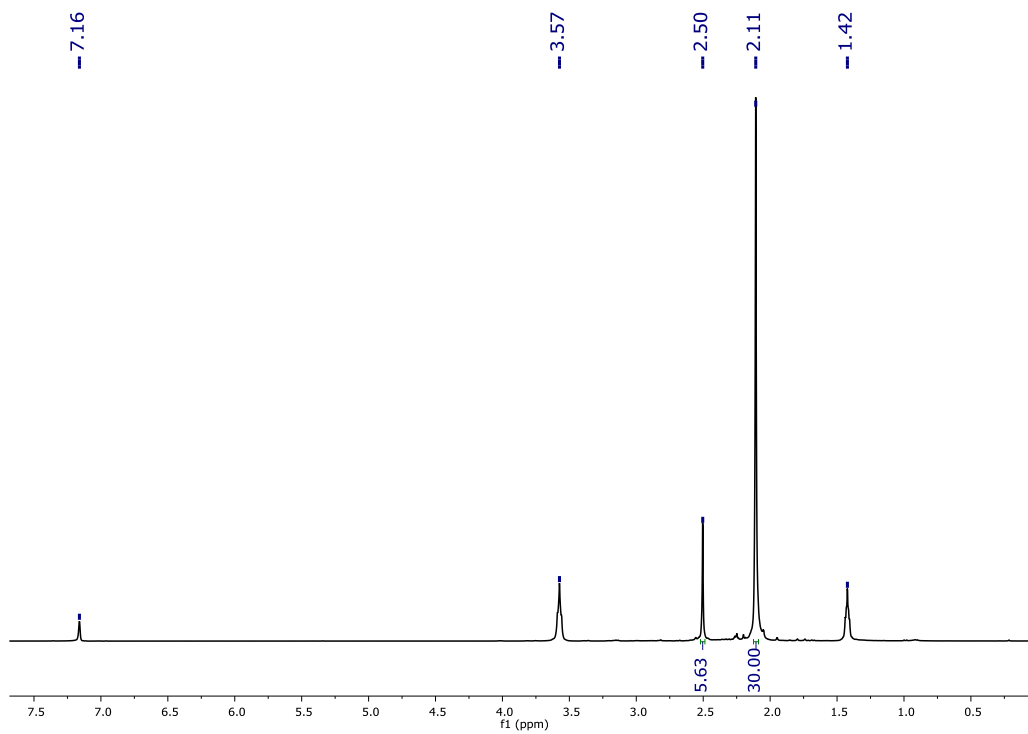
Figure 96. ^{1}H NMR (400 MHz, 295 K, C$_6$D$_6$) spectrum of (C$_5$Me$_5$)$_2$Th(SMe)$_2$: 2.50 ppm (S*Me*), 2.11 ppm (C$_5$*Me$_5$*); THF solvent is present at 3.58 and 1.42 ppm.
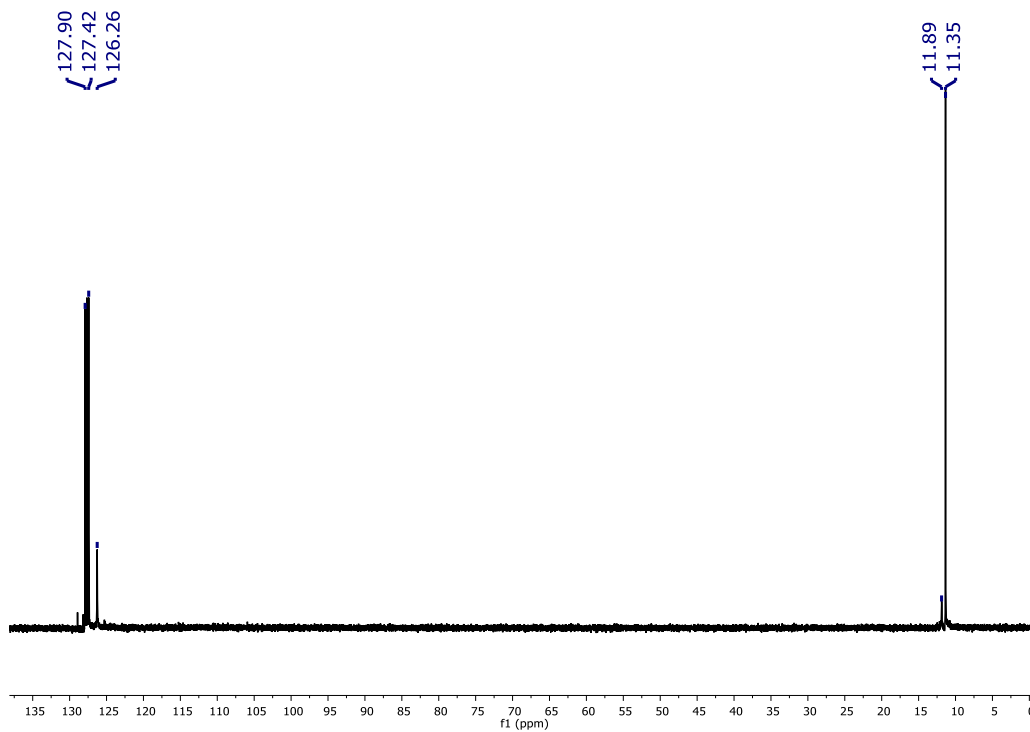
Figure 97. ^{13}C NMR (400 MHz, 295 K, C$_6$D$_6$) spectrum of (C$_5$Me$_5$)$_2$Th(SMe)$_2$: 126.25 ppm (*C*$_5$Me$_5$), 11.89 ppm (S*Me*), 11.35 ppm (C$_5$*Me$_5$*). The solvent C$_6$D$_6$ is present at 127 ppm.
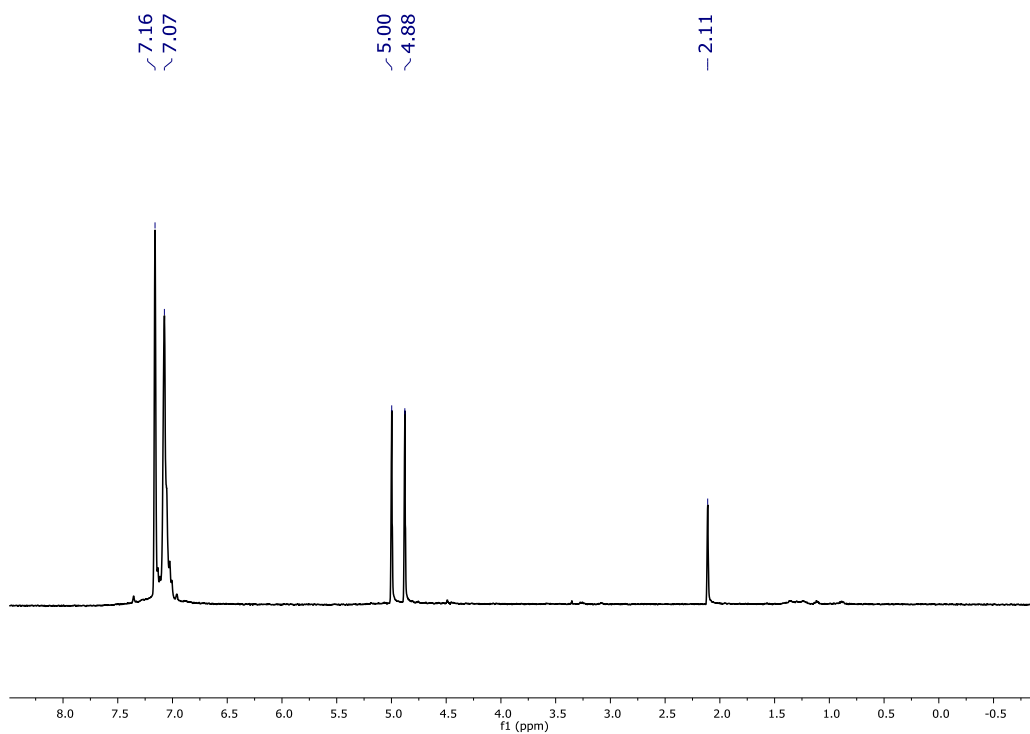
Figure 98. ^{1}H NMR (400 MHz, 295 K, C$_6$D$_6$) spectrum of benzyl fluoride ((C$_6$H$_5$)CH$_2$-F) from the synthesis of benzyl bromide and [Cp$_2$Co]F: 7.07 ppm (C$_6$*H$_5$*), 5.00 and 4.88 ppm (C*H$_2$*). Toluene is present at 2.11 ppm.
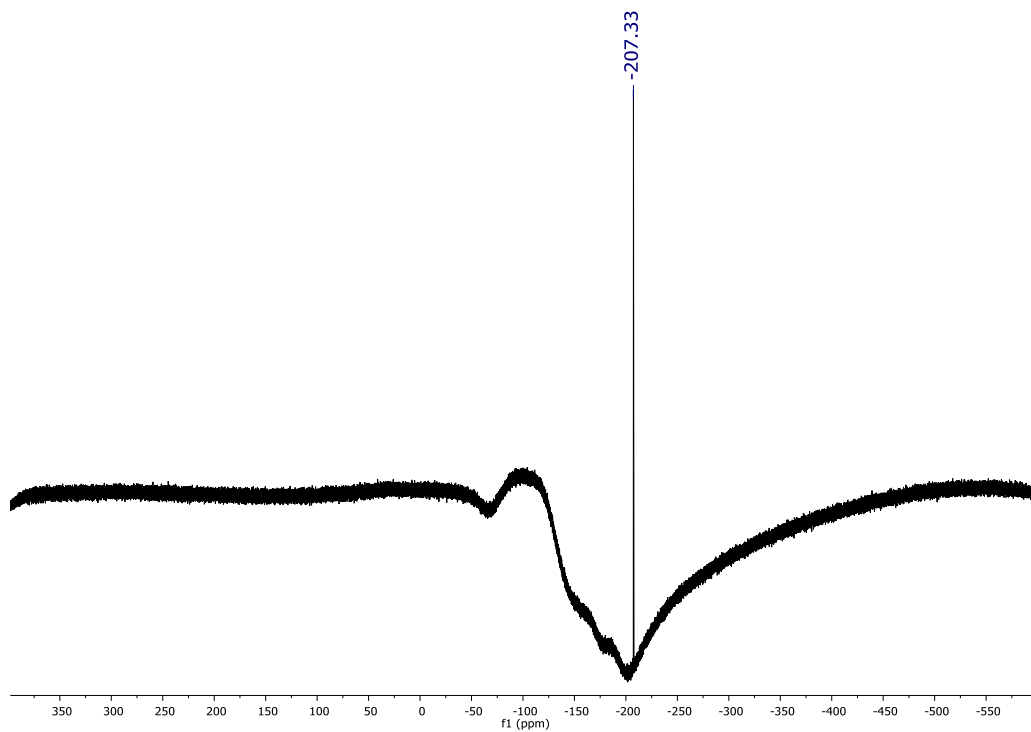
Figure 99. ^{19}F NMR (400 MHz, 295 K, C_6D_6) spectrum of benzyl fluoride.
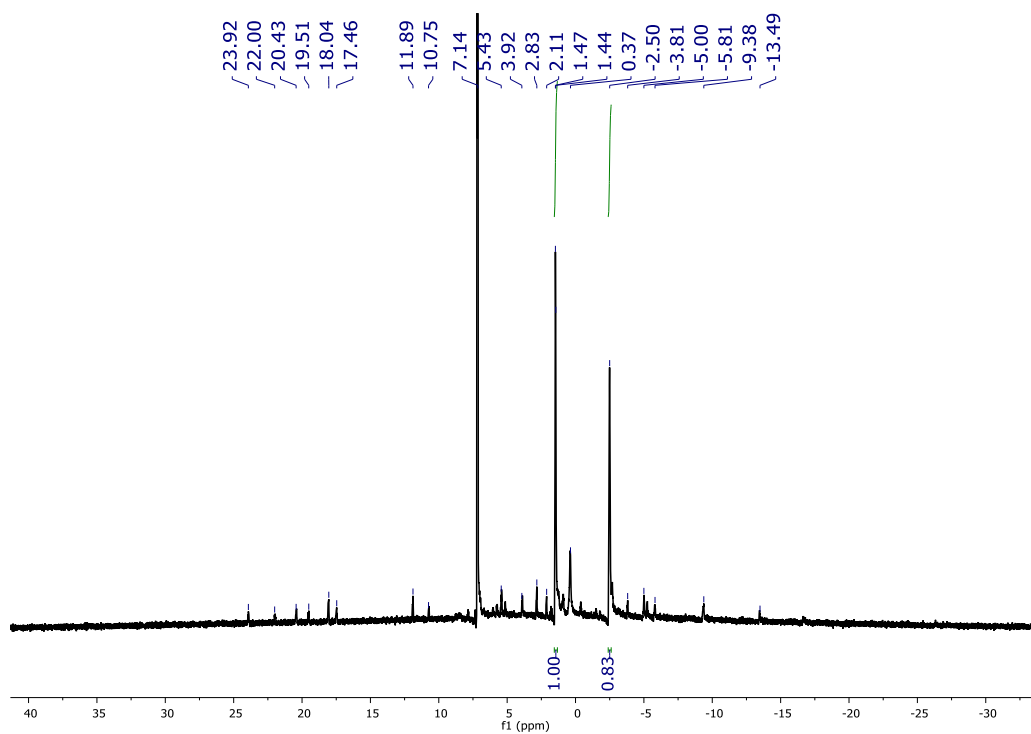
Figure 100. ^{1}H NMR (400 MHz, 295 K, C_6D_6) spectrum of $(C_5Me_5)_2U(F)(bpy)(Bn)$. The C5*Me*5 peaks for both isomers are present at 1.47 and -2.50 ppm. The ratio of formation between the isomers is 1:0.83.
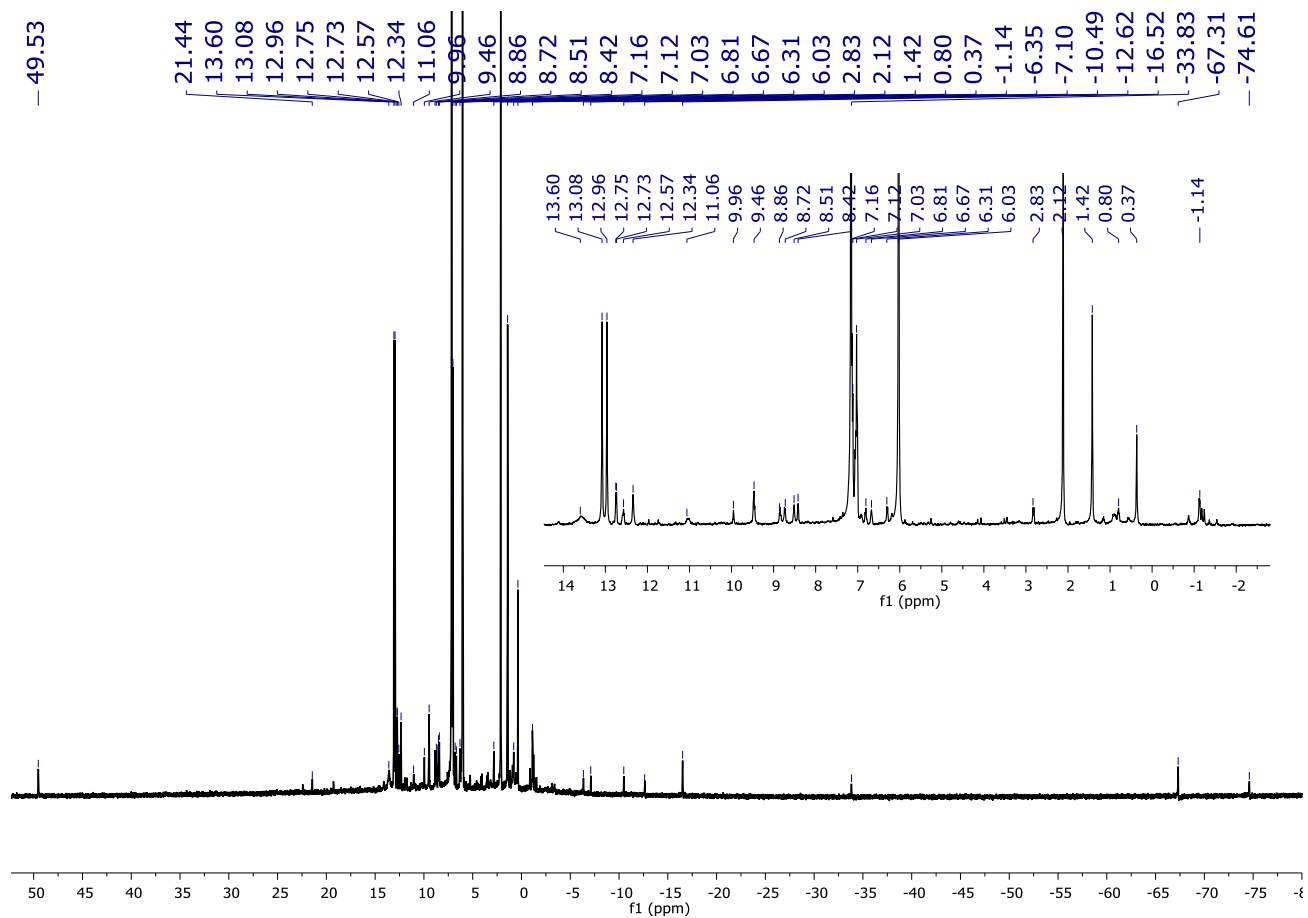
Figure 101. ^{1}H NMR (400 MHz, 295 K, C_6D_6) spectrum of $(C_5Me_5)_2U(Cl)(bpy)(Bn)$. The C$_5$*Me*$_5$ peak for one isomer occurs as a doublet at 13.08 ppm, and the other isomer appears as a singlet at 6.03 ppm. A small amount of $(C_5Me_5)_2UCl_2$ is seen at 13.60 ppm. The paramagnetism of the uranium(IV) metal center leads to extreme shifts in the bipyridine ligand as exemplified by the peaks at 49.53 ppm and -74.61 ppm, for example.
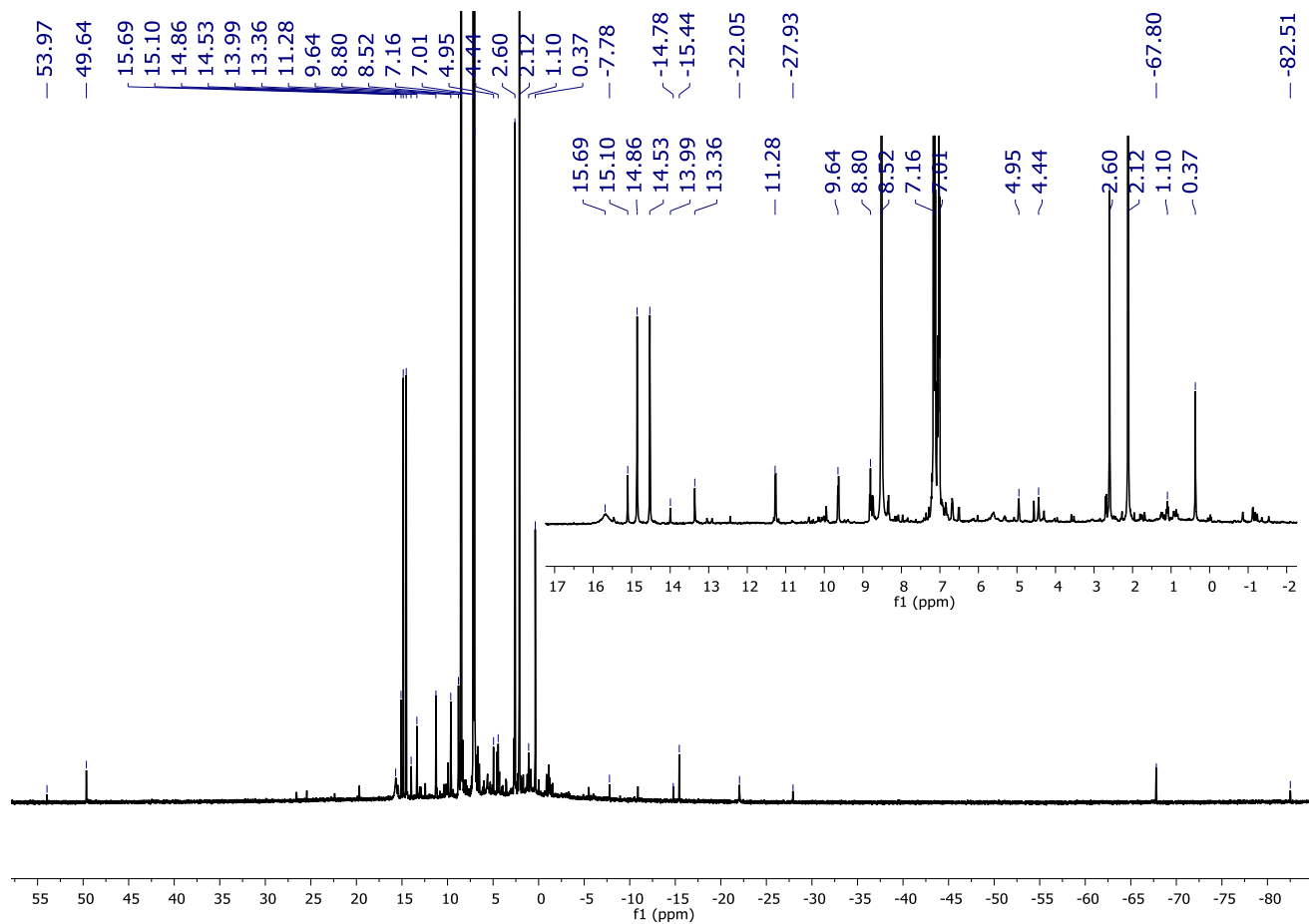
Figure 102. ^{1}H NMR (400 MHz, 295 K, C$_6$D$_6$) spectrum of (C$_5$Me$_5$)$_2$U(Br)(bpy)(Bn). As with the two previous compounds, there are two isomers present: one C$_5$*Me$_5$* peak occurs as a doublet at 14.86 and 14.53 ppm, the other as a singlet at 8.52 ppm. There is toluene present in the spectrum at 2.12 ppm. At 15.69 ppm, a broad peak indicates the presence of a small amount of (C$_5$Me$_5$)$_2$UBr$_2$. As with the chloride analogue, the paramagnetism of the uranium metal center causes shifts of the bipyridine ligand signals.
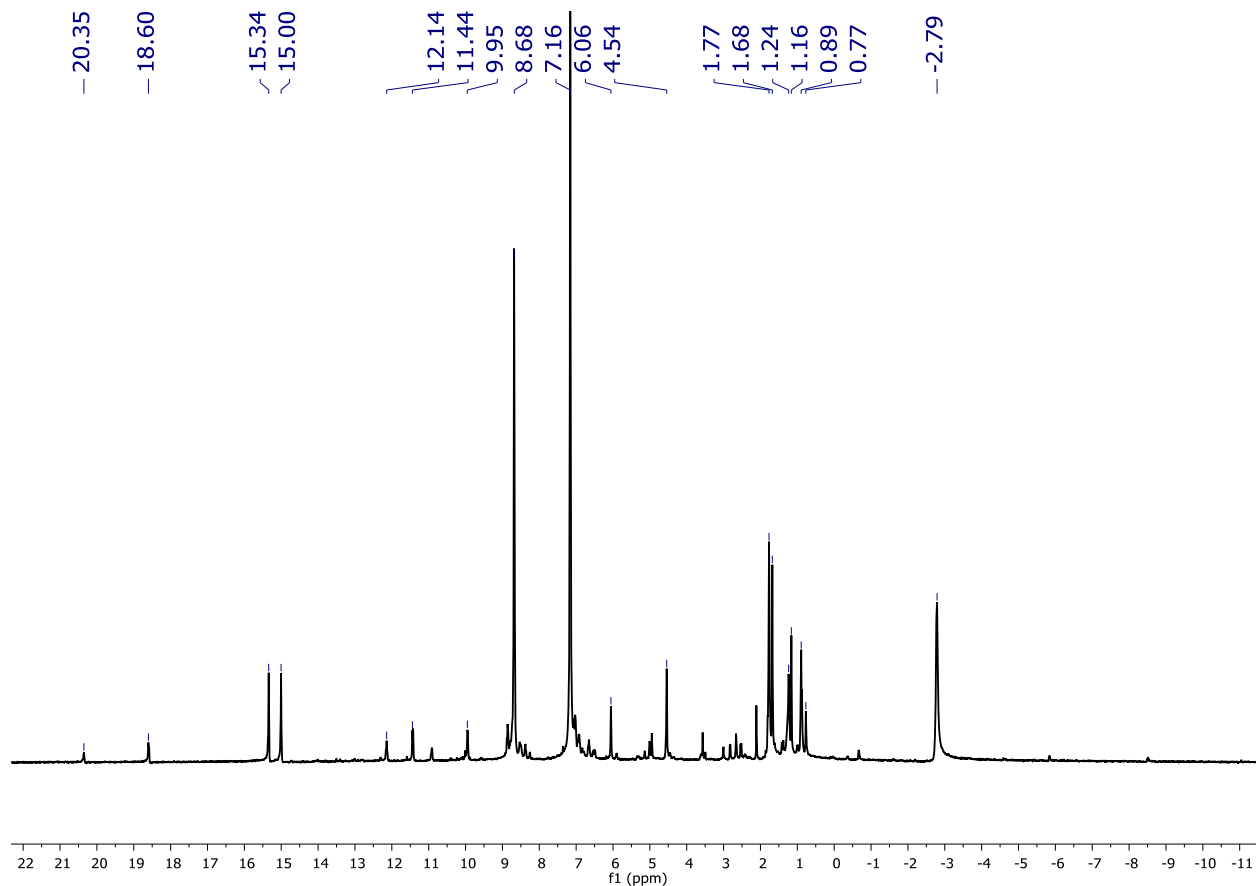
Figure 103. ^{1}H NMR (400 MHz, 295 K, C$_6$D$_6$) spectrum of the product from the reaction of (C$_5$Me$_5$)$_2$U(Br)(bpy)(Bn) with one equivalent of [Cp$_2$Co]F after 24 h. The ingrowth of a singlet peak at -2.79 ppm is indicative of one isomer of (C$_5$Me$_5$)$_2$U(I)(bpy)(Bn). The other isomer is not seen, and likely does not undergo halide exchange. One isomer of the bromide starting material is still present, and (C$_5$Me$_5$)$_2$ has grown in (1.77, 1.68, and 1.16 ppm), indicating the occurrence of decomposition of one or more of the (C$_5$Me$_5$)$_2$ containing materials.
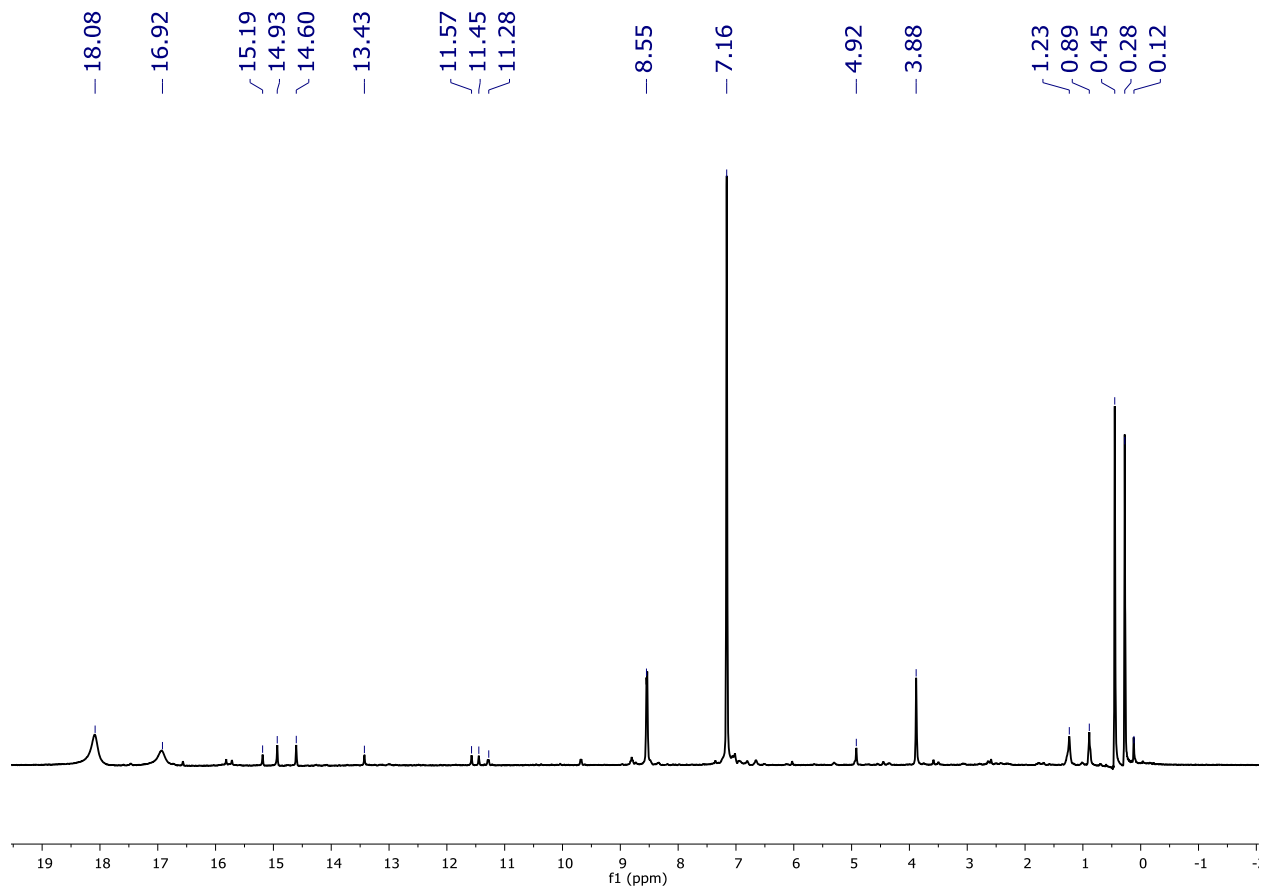
Figure 104. A small section of the ^1H NMR (400 MHz, 295 K, C_6D_6) spectrum of the product from the reaction of $(C_5Me_5)_2U(Br)(bpy)(Bn)$ with one equivalent of trimethylsilyl-iodide (TMS-I). Unreacted TMS-I is located at 0.45 ppm and 0.12 ppm, and ingrowth of TMS-Br occurs at 0.28 ppm, indicating an exchange of the halides. Formation of $(C_5Me_5)_2UI_2$ is seen as a broad peak at 18.08 ppm. Ingrowth of peaks corresponding to one isomer of the $(C_5Me_5)_2U(I)(bpy)(Bn)$ occur at 11.57 and 11.45 ppm. Both isomers of $(C_5Me_5)_2U(Br)(bpy)(Bn)$ are still present in the reaction after 5 h (14.93 ppm, 14.60 ppm, and 8.55 ppm), when the reaction appears to stop.

195
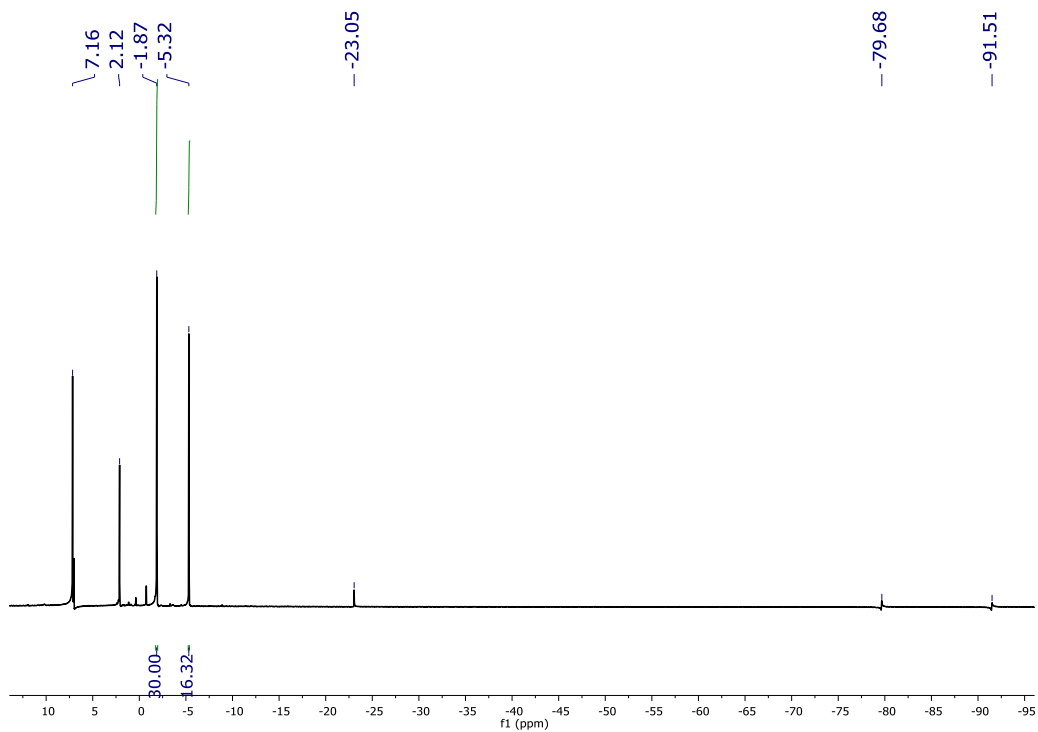
Figure 105. ^{1}H NMR (400 MHz, 295 K, C_6D_6) spectrum of $(C_5Me_5)_2U(4,4'-^tBu_2bpy)$: -1.87 ppm ($C_5Me_5$), -5.32 ppm ($^tBu$), -23.05 ppm (*bpy*), -79.68 (*bpy*), -91.51 (*bpy*). Toluene is present at 2.12 ppm.
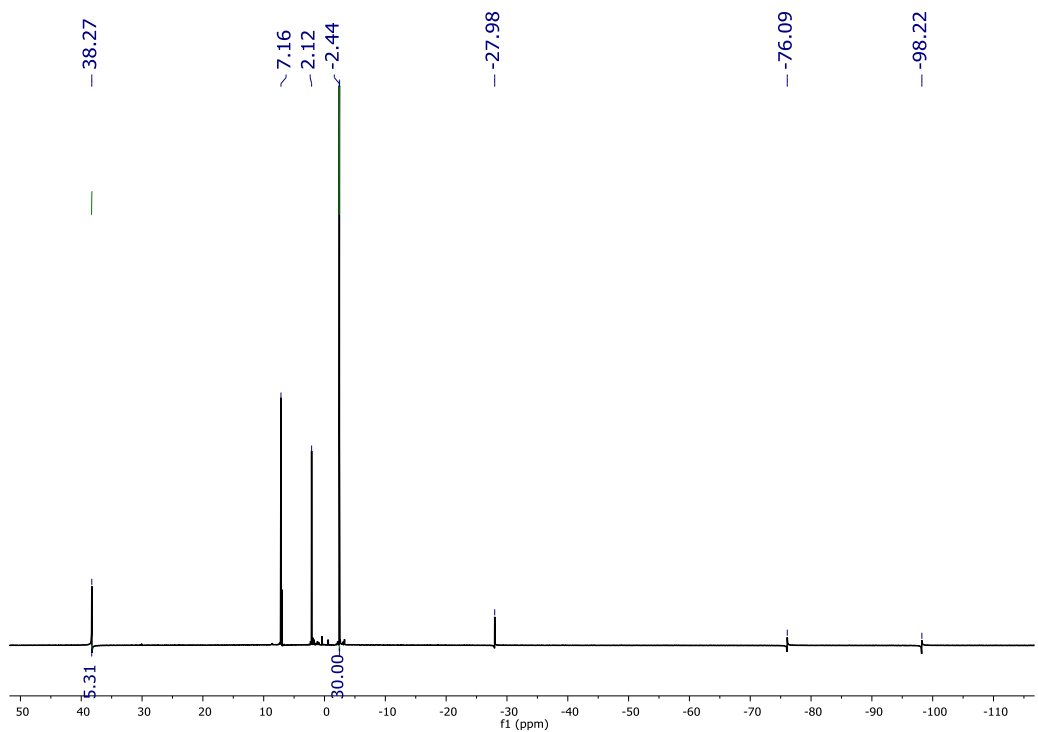
Figure 106. ^{1}H NMR (400 MHz, 295 K, C_6D_6) spectrum of $(C_5Me_5)_2U(4,4'-Me_2bpy)$: 38.27 ppm (*Me*), -2.44 ppm (C_5Me_5), -27.98 ppm (*bpy*), -76.09 ppm (*bpy*), -98.22 ppm (*bpy*). Toluene is present at 2.12 ppm.

196
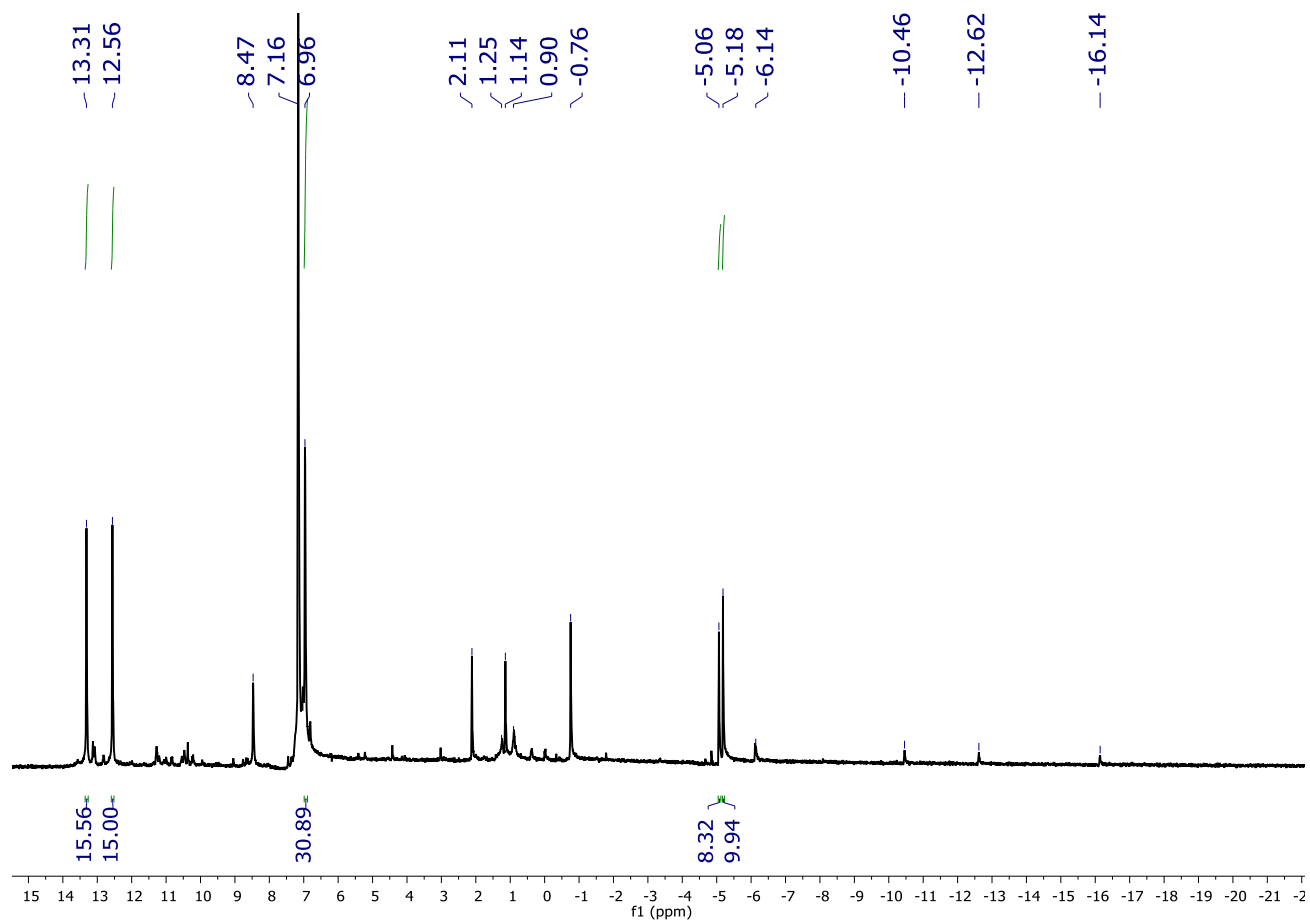
Figure 107. ^{1}H NMR (400 MHz, 295 K, C$_6$D$_6$) spectrum of (C$_5$Me$_5$)$_2$U(Cl)(4,4'-^{t}Bu$_2$bpy)(Bn). As with previous compounds, there are two isomers present: one C$_5$*Me*$_5$ peak occurs as a doublet at 13.31 and 12.56 ppm, the other as a singlet at 6.96 ppm. The ^{t}Bu groups for each isomer occur at -5.06 and -5.18 ppm, respectively. There is toluene present in the spectrum at 2.11 ppm.
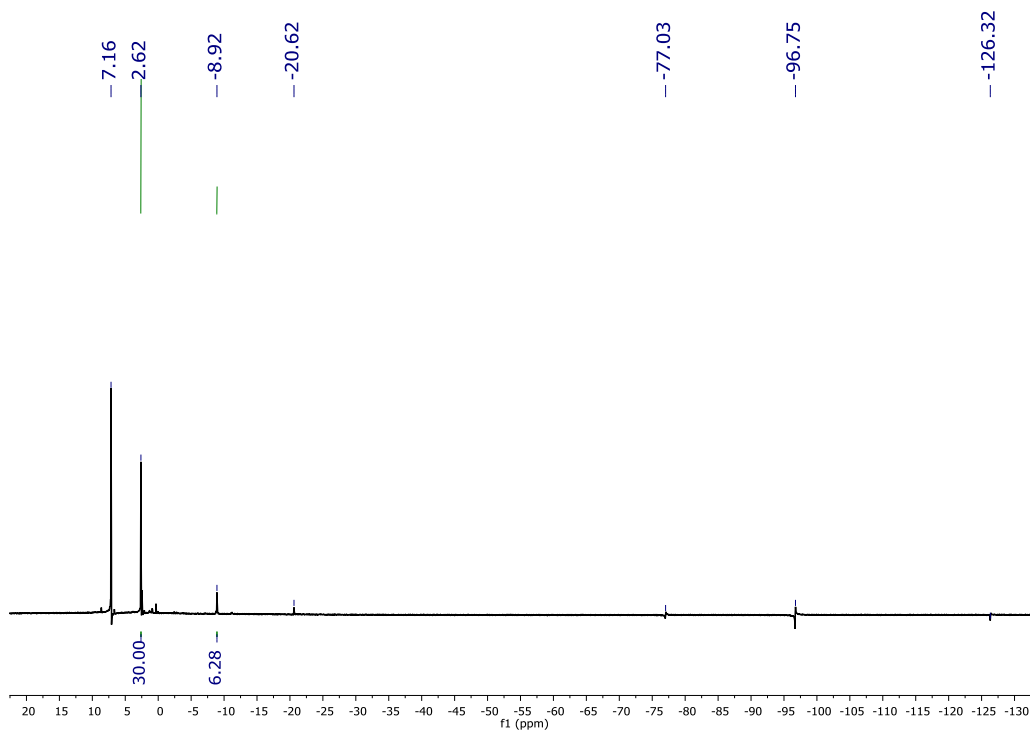
Figure 108. ^{1}H NMR (400 MHz, 295 K, C$_6$D$_6$) spectrum of (C$_5$Me$_5$)$_2$U(6,6'-Me$_2$bpy): 2.62 ppm (C$_5$*Me*$_5$), -8.92 ppm (*Me*$_2$bpy), -77.03 ppm (*bpy*), -96.75 ppm (*bpy*), -126.32 ppm (*bpy*).
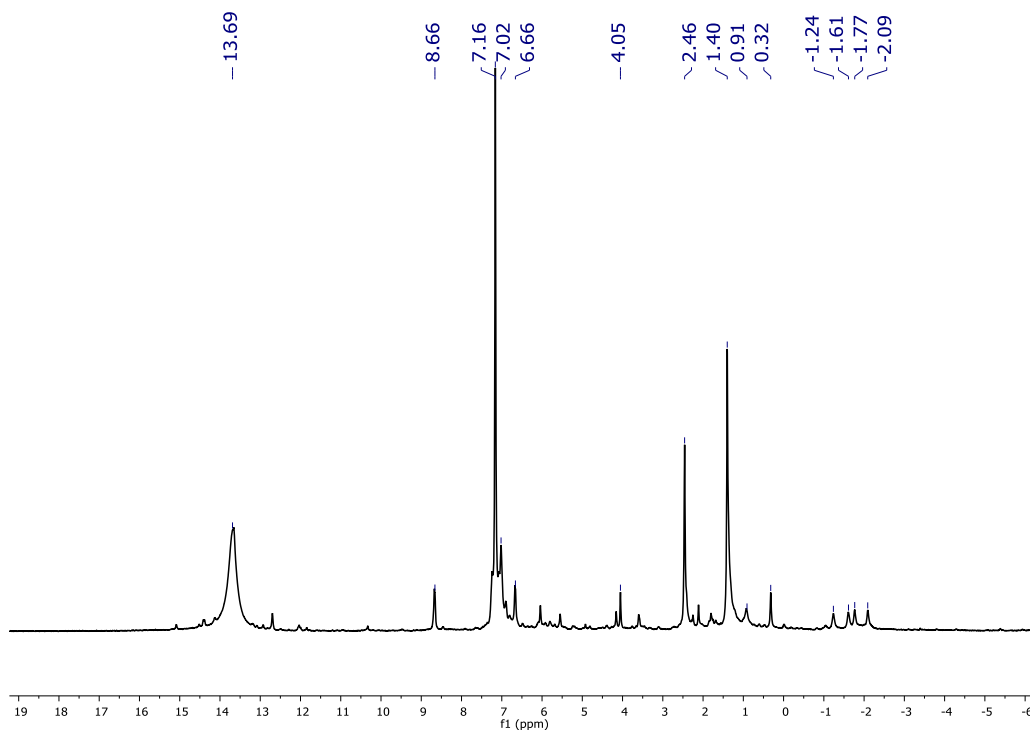
Figure 109. ^{1}H NMR (400 MHz, 295 K, C$_6$D$_6$) spectrum from the reaction of (C$_5$Me$_5$)$_2$U(6,6'-Me$_2$bpy) and benzyl chloride. The major products are (C$_5$Me$_5$)$_2$UCl$_2$ (13.69 ppm), and free 6,6'-Me$_2$bpy ligand (8.66, 7.24, 6.68, and 2.46 ppm), which shows that the reaction did not proceed.

198
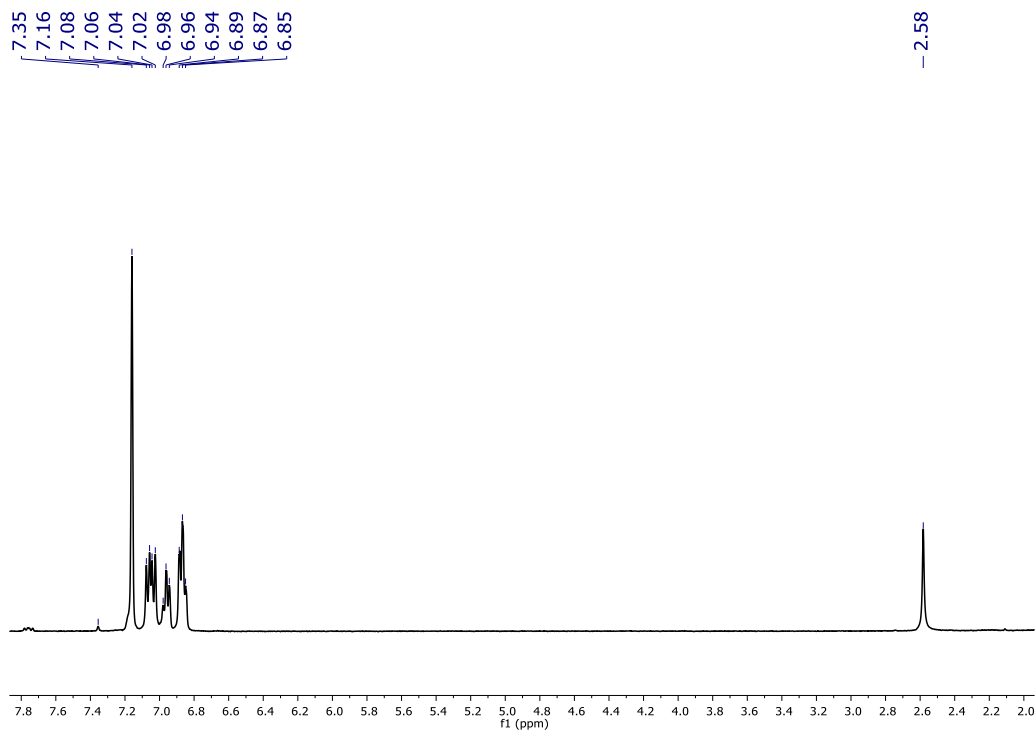
Figure 110. ^{1}H NMR (400 MHz, 295 K, C$_6$D$_6$) spectrum of (Ph$_3$P)Au-methyltetrazolate: 7.06 ppm (multiplet, *Ph*), 6.96 ppm (multiplet, *Ph*), 6.87 (multiplet, *Ph*), 2.58 (*Me*).
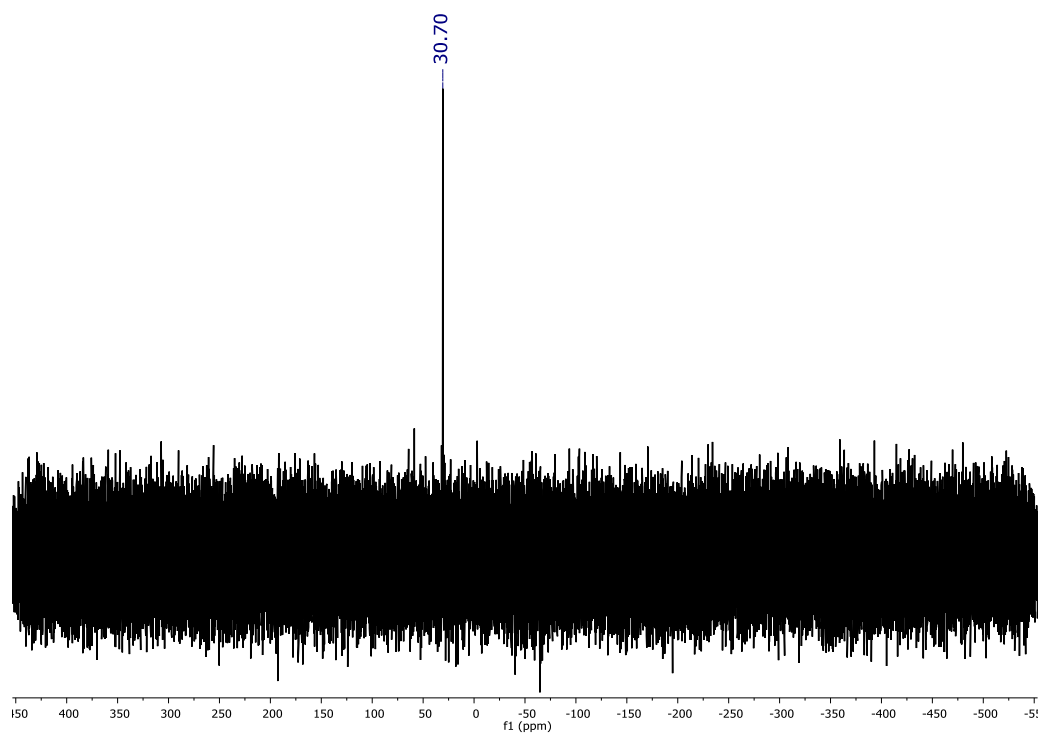
Figure 111. ^{31}P NMR (400 MHz, 295 K, C$_6$D$_6$) spectrum of (PH$_3$P)Au-methyltetrazolate. There is one peak in the spectrum at 30.70 ppm, corresponding to the phosphorus in the complex.
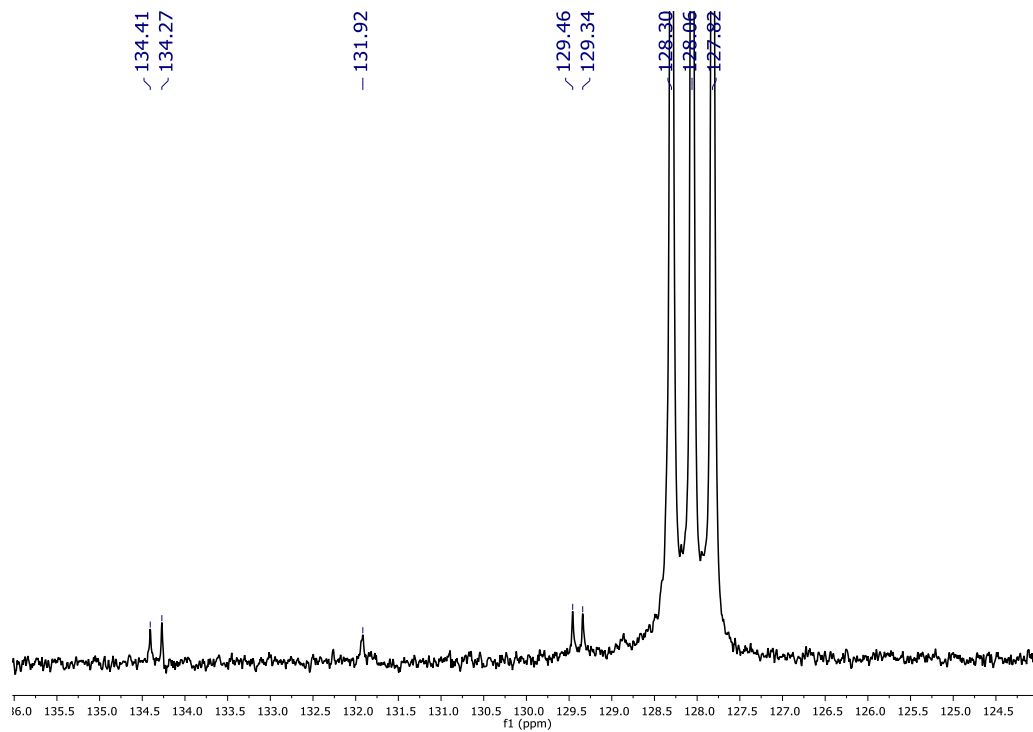
Figure 112. ^{13}C NMR (400 MHz, 295 K, C_6D_6) spectrum of (PH_3P)Au-methyltetrazolate: 134.41 and 134.27 pm (C-N), 131.92 ppm (*Me*), 129.46 and 129.34 ppm (*Ph₃P*).
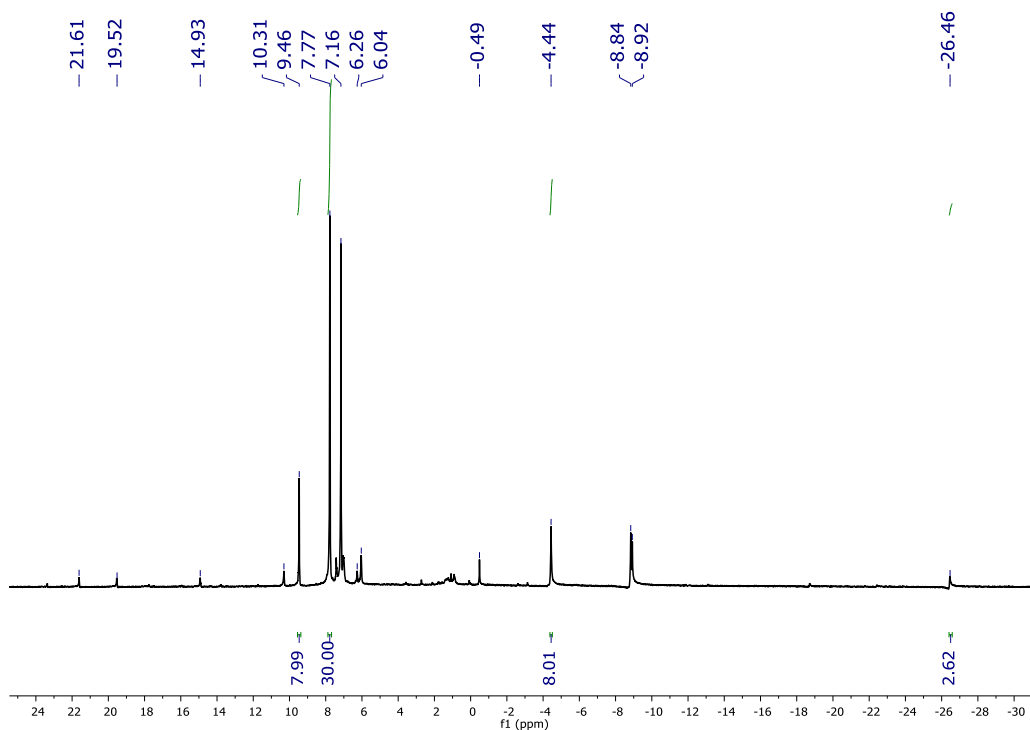
Figure 113. ^{1}H NMR (400 MHz, 295 K, C_6D_6) spectrum of (C_5Me_5)$_2$U(O-2,6-di-*tert*-butylbenzene)(methyltetrazolate): 9.46 ppm (*ᵗBu*), 7.77 ppm (C₅*Me₅*), -4.44 ppm (*ᵗBu*), -26.46 ppm (*Me*).

200

Appendix C: Crystal Structure Data

Table 51. Crystal Structure Parameters for $(C_5Me_5)_2Th(SMe)_2$

	$(C_5Me_5)_2Th(SMe)_2$
Empirical Formula	$C_{22}H_{36}S_2Th$
Formula Weight	596.67
Crystal System	Orthorhombic
a [Å]	14.360(5)
b [Å]	9.552(8)
c [Å]	16.540(1)
B [°]	90
V [Å^3]	2256.7(3)
Space Group	Pbcn
Z	4
ρ [g/cm^3]	1.756
μ [MoKα]	6.796
T [K]	140(1)
$2\Theta_{max}$ [°]	57.28
Min/max trans.	0.1935/0.3435
Total reflns	24625
Unique reflns	2820
Parameters	120
$R_1(wR_1)$ (all data)	0.0133 (0.0185)

Table 52. Crystal parameters for $(C_5Me_5)_2U(F)(bpy)Bn$

	$(C_5Me_5)_2U(F)(bpy)Bn$
Empirical Formula	$C_{37}H_{45}FN_2U$
Formula Weight	774.78
Crystal System	Triclinic
a [Å]	13.718(12)
b [Å]	15.396(13)
c [Å]	16.494(14)
B [°]	92.465(10)
γ [°]	94.153(10)
V [Å^3]	3188(5)
Space Group	P-1
Z	4
ρ [g/cm^3]	1.614
μ [MoKα]	5.124
T [K]	100(1)
$2\Theta_{max}$ [°]	51.99
Min/max trans.	0.607/0.821
Total reflns	31611
Unique reflns	7761
Parameters	759
$R_1(wR_1)$ (all data)	0.0651 (0.1137)

Table 53. Crystal parameters for $(C_5Me_5)_2U(Cl)(bpy)Bn$

	$(C_5Me_5)_2U(Cl)(bpy)Bn$
Empirical Formula	$C_{37}H_{45}ClN_2U$
Formula Weight	791.23
Crystal System	Orthorhombic
a [Å]	16.748(3)
b [Å]	13.217(2)
c [Å]	14.430(3)
B [°]	90
V [Å^3]	3194.3(10)
Space Group	Pnma
Z	4
ρ [g/cm^3]	1.645
μ [MoKα]	5.193
T [K]	140(1)
$2\Theta_{max}$ [°]	53.76
Min/max trans.	0.369/0.681
Total reflns	33530
Unique reflns	3127
Parameters	228
$R_1(wR_1)$ (all data)	0.0250 (0.0324)

Table 54. Crystal parameters for $(C_5Me_5)_2U(Br)(bpy)Bn$

	$(C_5Me_5)_2U(Br)(bpy)Bn$
Empirical Formula	$C_{37}H_{45}FN_2U$
Formula Weight	835.69
Crystal System	Orthorhombic
a [Å]	16.993(8)
b [Å]	13.146(7)
c [Å]	14.428(7)
B [°]	90
V [Å^3]	3223(3)
Space Group	Pnma
Z	4
ρ [g/cm^3]	1.722
μ [MoKα]	6.304
T [K]	140(1)
$2\Theta_{max}$ [°]	54.74
Min/max trans.	0.560/0.704
Total reflns	35492
Unique reflns	7597
Parameters	228
$R_1(wR_1)$ (all data)	0.0285 (0.0388)

Table 55. Crystal parameter data for $(C_5Me_5)_2U(I)(bpy)Bn$

	$(C_5Me_5)_2U(I)(bpy)Bn$
Empirical Formula	$C_{37}H_{45}IN_2U$
Formula Weight	882.68
Crystal System	Orthorhombic
a [Å]	17.580(5)
b [Å]	13.040(4)
c [Å]	14.431(4)
B [°]	90
V [Å^3]	3308.3(16)
Space Group	Pnma
Z	4
ρ [g/cm^3]	1.772
μ [MoKα]	5.867
T [K]	100(1)
$2\Theta_{max}$ [°]	57.24
Min/max trans.	0.231/0625
Total reflns	37324
Unique reflns	4278
Parameters	219
$R_1(wR_1)$ (all data)	0.0502 (0.0568)

Table 56. Crystal parameters for $(C_5Me_5)_2U(Cl)(^tBu_2bpy)Bn$

	$(C_5Me_5)_2U(Cl)(tBu_2bpy)Bn$
Empirical Formula	$C_{30}H_{32}ClN_2U$
Formula Weight	694.05
Crystal System	Monoclinic
a [Å]	26.371(15)
b [Å]	17.109(10)
c [Å]	22.412(13)
B [°]	101.493(7)
γ [°]	90
V [Å^3]	9909(10)
Space Group	C2/c
Z	16
ρ [g/cm^3]	1.861
μ [MoKα]	6.682
T [K]	100(1)
$2\Theta_{max}$ [°]	51.586
Min/max trans.	0.263/0.479
Total reflns	48672
Unique reflns	9374
Parameters	446
$R_1(wR_1)$ (all data)	0.0315 (0.0498)

Table 57. Crystal parameters for $(C_5Me_5)_2U(6,6'-Me_2bpy)$

	$(C_5Me_5)_2U(6,6'-Me_2bpy)$
Empirical Formula	$C_{32}H_{42}N_2U$
Formula Weight	692.70
Crystal System	Triclinic
a [Å]	8.839(4)
b [Å]	9.856(4)
c [Å]	16.603(7)
α [°]	78.048(5)
B [°]	81.815(5)
γ [°]	70.826(5)
V [Å^3]	1332.3(10)
Space Group	P-1
Z	2
ρ [g/cm^3]	1.727
μ [MoKα]	6.115
T [K]	100(2)
$2\Theta_{max}$ [°]	52.26
Min/max trans.	0.225/0.486
Total reflns	13750
Unique reflns	5229
Parameters	316
R$_1$(wR$_1$) (all data)	0.0875 (0.0847)

Table 58. Crystal structure parameters for Ph$_3$PAu-methyltetrazolate

	Ph$_3$PAu-Metz
Empirical Formula	$C_{20}H_{18}AuN_4P$
Formula Weight	542.32
Crystal System	Monoclinic
a [Å]	9.0154(17)
b [Å]	15.158(3)
c [Å]	13.614(3)
B [°]	90
γ [°]	91.065(2)
V [Å^3]	1860.0(6)
Space Group	P21/n
Z	4
ρ [g/cm^3]	1.937
μ [MoKα]	8.006
T [K]	100(1)
$2\Theta_{max}$ [°]	57.28
Min/max trans.	0.213/0.533
Total reflns	20867
Unique reflns	4481
Parameters	120
R$_1$(wR$_1$) (all data)	0.0216 (0.0181)

References

(1)   Auxier, J. P.; Auxier II, J. D.; Hall, H. L. *Journal of Environmental Radiochemistry* **2017**, *171*, 246-252.

(2)   Bush, G. W. *The National Security Strategy of the United States of America*, The White House, 2002.

(3)   Aggarwal, S. K. *Curr. Sci.* **2016**, *110*, 782-791.

(4)   Srinivasan, B.; A., L. R.; S., A.; F., V. G.; A., M.; A., R.; H., L.; A., H.; S., A.; Y., N. Paris, France; Vol. 53, p 160-160.

(5)   Sun, S. L. G. L. Q. L. B. 1986.

(6)   Fact Sheet: Encouraging Reliable Supplies of Molybdenum-99 Produced without HEU.

(7)   Emsley, J.; Oxford University Press: Oxford, 2001.

(8)   Whapham, A. D.; Makin, M. J. *Philos. Mag.* **1962**, *7*, 1441-1441.

(9)   Krane, K. S. *Introductory Nuclear Physics*; John Wiley & Sons, 1987.

(10)   *The Chemistry of the Actinide and Transactinide Elements*; Springer, 2006.

(11)   Wickleder, M. S.; Fourest, B.; Dorhout, P. K. In *The Chemistry of the Actinide and Transactinide Elements*; Morss, L. R., Edelstein, N. M., Fuger, J., Eds.; Springer: The Netherlands, 2006; Vol. 1.

(12)   Marks, T. J.; Wachter, W. A. *J. Am. Chem. Soc.* **1976**, *98*, 703-710.

(13)   Grenthe, I.; Drozdzynski, J.; Fujino, T.; Buck, E. C.; Albrecht-Schmitt, T. E.; Wolf, S. F. In *The Chemistry of the Actinide and Transactinide Elements*; Morss, L. R., Edelstein, N. M., Fuger, J., Eds.; Springer: The Netherlands, 2006; Vol. 1.

(14)   Cotton, S. *Lanthanide and Actinide Chemistry*; John Wiley & Sons Inc.: West Sussex, 2006.

(15)   World Nuclear Association: Supply of Uranium.

(16)   National Institute of Advanced Industrial Science and Technology: 2005.

(17)   Hughes, K.-A.; Burns, P. C. *Acta Crystallogr., Sect. C.* **2003**, *59*, i7-i8.

(18)   Cahill, C. L.; Borkowski, L. A. *Structural Chemistry of Inorganic Actinide Compounds* **2007**.

(19)   Umreiko, D. S. *Journal of Applied Spectroscopy* **1965**, *2*, 302-304.

(20)   MacGillivray, L. R. *Metal Organic Frameworks: Design and Application*; John Wiley & Sons Inc.: Hoboken, 2010.

(21)   *Metal Organic Frameworks: Applications from Catalysis to Gas Storage*; Wiley-VCH: Weinheim, 2011.

(22)   Roth, W. J.; Nachtigall, P.; Morris, R. E.; Wheatley, P. S.; Seymour, V. R.; Ashbrook, S. E.; Chlubná, P.; Grajciar, L.; Položij, M.; Zukal, A.; Shvets, O.; Čejka, J. *Nat Chem* **2013**, *5*, 628-633.

(23)   Kim, J.; Chen, B.; Reineke, T. M.; Li, H.; Eddaoudi, M.; Moler, D. B.; O'Keeffe, M.; Yaghi, O. M. *Journal of the American Chemical Society* **2001**, *123*, 8239-8247.

(24)   Ye, J.; League, A.; Truhlar, D.; Cramer, C.; Gagliardi, L.; Bernales, V.; Farha, O.; Hupp, J.; Li, Z.; Platero Prats, A. E.; Chapman, K.; Camaioni, D.; Fulton, J.; Lercher, J. In *254th ACS National Meeting & Exposition* Washington, D.C., 2017.

(25)   Thuéry, P. *CrystEngComm* **2009**, *11*, 1081-1088.

(26)   Thuéry, P. *Cryst. Growth Des.* **2012**, 499-507.

(27)   Thuéry, P. *CrystEngComm* **2012**, *14*, 131-137.

(28)   Borkowski, L. a.; Cahill, C. L. *Crystal Growth and Design* **2006**, *6*, 2248-2259.

(29)   Kerr, A. T.; Cahill, C. L. *Crystal Growth {&} Design* **2011**, *11*, 5634-5641.

(30)   Thuéry, P. **2009**, 1081-1088.

(31)   Thuéry, P. *Cryst. Growth Des.* **2011**, *11*, 347-355.

(32)   Thuéry, P. *Cryst. Growth Des.* **2011**, *11*, 2606-2620.

(33)   Andrews, M. B.; Cahill, C. L. *Chem. Rev.* **2013**, *113*, 1121-1136.

(34)   Cantos, P. M.; Frisch, M.; Cahill, C. L. *Inorg. Chem. Commun.* **2010**, *13*, 1036-1039.

(35)   Frisch, M.; Cahill, C. L. *Dalton Trans.* **2006**, 4679-4690.

(36)   Blakemore, P.; Oregon State University: Corvallis, Oregon, 2017; Vol. 2017, p image of parr bomb.

(37)   Kaw, P. K.; Bandyopadhyay, I. In *Fusion Physics*; Kikuchi, M., Lackner, K., Tran, M. Q., Eds.; International Atomic Energy Agency: Vienna, 2012.

(38)   Baum, E. M.; Ernesti, M. C.; Knox, H. D.; Miller, T. R.; Watson, A. M.; Travis, S. D. *Nuclides and Isotopes Chart of the Nuclides*; Seventeenth ed.; Bechtel Marine Propulsion Corporation, 2009.

(39)   Woodbank Communications Ltd: United Kingdom, 2005; Vol. 2017.

(40)   Krane, K. S. *Introductory Nuclear Physics*; John Wiley & Son, Inc.: United States of America, 1988.

(41)   Jacobs, D. G.; Comission, U. S. A. E. A., Ed. 1968.

(42)   Prelas, M. A.; Weaver, C. L.; Watermann, M. L.; Lukosi, E. D.; Schott, R. J.; Wisniewski, D. A. *Prog. Nucl. Energy* **2014**, *75*, 117-148.

(43)   Krishnan, M. *IEEE Transactions on Plasma Science* **2012**, *40*, 3189-3221.

(44)   Haines, M. G. *Plasma Phys. Controlled Fusion* **2011**, *53*, 093001 - 093168.

(45)   Bernard, A.; Cloth, P.; Conrads, H.; Coudeville, A.; Gourlan, G.; Jolas, A.; Maisonnier, C.; Rager, J. P. *Nuclear Instruments and Methods* **1977**, *145*, 191-218.

(46)   Malenfant, R. E. *Los Alamos Critical Assemblies Facility*, Los Alamos Scientific Laboratory, 1981.

(47)   Energy, U. S. D. o.; Administration, N. N. S., Ed. Nevada, 2013.

(48)   Hayes, D. K.; Meyers, W. L. In *Institute of Nuclear Materials Management 53rd Annual Meeting* Orlando, Florida, 2012.

(49)   Brewer, R. W.; McLaughlin, T. P.; Dean, V. *Uranium-235 Sphere Reflected by Normal Uranium Using Flattop*, Nuclear Energy Agency, 1999.

(50)   Knoll, G. F. In *Radiation Detection and Measurement*; 4th ed.; John Wiley & Sons, Inc.: Hoboken, NJ, 2010.

(51)   In *Nuclear Power for Everybody*; WodPress: 2016; Vol. 2017.

(52)   Badawi, M. S.; Gouda, M. M.; Nafee, S. S.; El-Khatib, A. M.; El-Mallah, E. A. *Nuclear Instruments and Methods in Physics Research Section A: Accelerators, Spectrometers, Detectors and Associated Equipment* **2012**, *696*, 164-170.

(53)   Canberra; Mirion Technologies, Inc.: 2014.

(54)   Canberra; Canberra, Ed.; Mirion Technologies Inc.: 2016.

(55)   Canberra; Canberra: 2008.

(56)   Skoog, D. A.; Holler, F. J.; Crouch, S. R. In *Principles of Instrumental Analysis*; Sixth ed.; Brooks/Cole, Cengage Learning: California, USA, 2007, p 303-332.

(57)   Pollanen, R.; Kansanaho, A.; Toivonen, H. *Detection and analysis of radioactive particles using autoradiography*, Finnish Centre for Radiation and Nuclear Safety, 1996.

(58)   Lewis, L. A.; Knight, K. B.; Matzel, J. E.; Prussin, S. G.; Zimmer, M. M.; Kinman, W. S.; Ryerson, F. J.; Hutcheon, I. D. *Journal of Environmental Radiochemistry* **2015**, *148*, 183-195.

(59)   Wallner, A. S.; Anna, L. J.; Soulsby, D. In *NMR Spectroscopy in the Undergraduate Curriculum*; American Chemical Society: 2013; Vol. 1128, p 1-6.

(60)   Wade, L. G., Jr. In *Organic Chemistry*; Sixth ed.; Pearson Education, Inc.: United States of America, 2006, p 559-614.

(61)   Skoog, D. A.; Holler, F. J.; Crouch, S. R. In *Principles of Instrumental Analysis*; Sixth ed.; Brooks/Cole, Cengage Learning: California, USA, 2007, p 336-398, 430-480, 498-549.

(62)   Wade, L. G., Jr. In *Organic Chemistry*; Sixth ed.; Pearson Education, Inc.: United States of America, 2006, p 692 - 698.

(63)   Wade, L. G., Jr. In *Organic Chemistry*; Sixth ed.; Pearson Education, Inc.: United States of America, 2006, p 508 - 530.

(64)   Skoog, D. A.; Holler, F. J.; Crouch, S. R. In *Principles of Instrumental Analysis*; Sixth ed.; Brooks/Cole, Cengage Learning: California, USA, 2007, p 627-761.

(65)   Bruker Analytical X-Ray Systems, Inc.: Madison, WI, 2004.

(66)   Bruker Analytical X-Ray Systems, Inc.: Madison, WI, 2003.

(67)   Sheldrick, G. M.; University of Gottingen: Gottingen, Germany, 2001.

(68)   Bruker Analytical X-Ray Systems, Inc.: Madison, WI, 1997.

(69)   Johnson, L.; Günther-Leopold, I.; Kobler Waldis, J.; Linder, H. P.; Low, J.; Cui, D.; Ekeroth, E.; Spahiu, K.; Evins, L. Z. *J. Nucl. Mater.* **2012**, *420*, 54-62.

(70)   Perriot, R.; Liu, X. Y.; Stanek, C. R.; Andersson, D. A. *J. Nucl. Mater.* **2015**, *459*, 90-96.

(71)   Barrachin, M.; Dubourg, R.; Kissane, M. P.; Ozrin, V. *J. Nucl. Mater.* **2009**, *385*, 372-386.

(72)   Minato, K.; Ogawa, T.; Fukuda, K.; Shimizu, M.; Tayama, Y.; Takahashi, I. *J. Nucl. Mater.* **1994**, *208*, 266-281.

(73)   Whapham, A. D.; Sheldon, B. E. *Philos. Mag.* **1965**, *12*, 1179-1192.

(74)   Tuli, J. K. *Nuclear Data Sheets* **2003**, *98*, 209.

(75)   Aldrich, S.; 4.10 ed.; Sigma Aldrich: 2015.

(76)   Immirzi, A.; Bombieri, G.; Degetto, S.; Marangoni, G. *Acta Crystallographica Section B* **1975**, *31*, 1023-1028.

(77)   Loiseau, T.; Mihalcea, I.; Henry, N.; Volkringer, C. *Coord. Chem. Rev.* **2014**, *266–267*, 69-109.

(78)   Mihalcea, I.; Henry, N.; Volkringer, C.; Loiseau, T. *Cryst. Growth Des.* **2012**, *12*, 526-535.

(79)   Wang, Y.; Li, Y.; Bai, Z.; Xiao, C.; Liu, Z.; Liu, W.; Chen, L.; He, W.; Diwu, J.; Chai, Z.; Albrecht-Schmitt, T. E.; Wang, S. *Dalton Trans.* **2015**, *44*, 18810-18814.

(80)   Liu, B.; Yang, T.-Y.; Feng, H.-J.; Zhang, Z.-H.; Xu, L. *J. Solid State Chem.* **2015**, *230*, 90-94.

(81)   Wang, G.; Liu, Y.; Huang, B.; Qin, X.; Zhang, X.; Dai, Y. *Dalton Trans.* **2015**, *44*, 16238-16241.

(82)   Xue, X.; Zhang, M.; Xie, S.; Yuan, L. *Acta Chromatographica* **2015**, *27*, 15-26.

(83)   Mihalcea, I.; Henry, N.; Volkringer, C.; Loiseau, T. *Crystal Growth & Design* **2012**, *12*, 526-535.

(84)   Mihalcea, I.; Henry, N.; Loiseau, T. *European Journal of Inorganic Chemistry* **2014**, 1322-1332.

(85)   Zhang, Y.; Bhadbhade, M.; Karatchevtseva, I.; Price, J. R.; Liu, H.; Zhang, Z.; Kong, L.; Cejka, J.; Lu, K.; Lumpkin, G. R. *Journal of Solid State Chemistry* **2015**, *226*, 42-49.

(86)   Technologies, M.; Canberra: 2016.

(87)   Nichols, A. L.; Aldama, D. L.; Verpelli, M.; Agency, I. A. E., Ed.; International Atomic Energy Agency: Vienna, Austria, 2008.

(88)   Shannon, R. D. *Acta Crystallographica Section A* **1976**, *A32*, 751-767.

(89)   Sonzogni, A.; Brookhaven National Laboratory: Brookhaven, NY; Vol. 2017.

(90)   Danks, A. E.; Hall, S. R.; Schnepp, Z. *Materials Horizons* **2016**, *3*, 91-112.

(91)   Pandithage, R.; Leica Microsystems: 2012; Vol. 2017.

(92)   Abdelrasoul, A.; Zhang, H.; Cheng, C.-H.; Doan, H. *Microporous Mesoporous Mater.* **2017**, *242*, 294-348.

(93)   Ching, S. H.; Bansal, N.; Bahandari, B. *Critical Reviews in Food Science and Nutrition* **2017**, *57*, 1133-1152.

(94)   Sellimi, S.; Younes, I.; Ayed, H. B.; Maalej, H.; Montero, V.; Rinaudo, M.; Dahia, M.; Mechichi, T.; Hajji, M.; Nasri, M. *Int. J. Biol. Macromol.* **2015**, *72*, 1358-1367.

(95)   *Introduction to Alginate*, CyberColloids.

(96)   Sanchez, R. G.; Hayes, D. K.; Goda, J. M.; Grove, T. J.; Myers, W. L.; Bounds, J. A. In *Annual Meeting American Nuclear Society* Atlanta, Georgia, USA, 2013.

(97)   Association, W. N.; World Nuclear Association 2017; Vol. 2017.

(98)   MURR: Columbia, MO, 2017; Vol. 2017.

(99)   Kim, B. G.; Oh, J. M.; Park, S. J.; Yang, S. W.; Hwan, M.; Lee, B.-C.; Kim, T. K. In *5th ISMTR*; Korea Atomic Energy Research Institute: Columbia, MO, USA, 2012.

(100)   Martinez, J.; Clavier, N.; Ducasse, T.; Mesbah, A.; Audubert, F.; Corso, B.; Vigier, N.; Dacheux, N. *J. Eur. Ceram. Soc.* **2015**, *35*, 4535-4546.

(101)   Ling, J.; Wallace, C. M.; Szymanowski, J. E. S.; Burns, P. C. *Angew. Chem., Int. Ed.* **2010**, *49*, 7271-7273.

(102)   Clavier, N.; Hingant, N.; Rivenet, M.; Obbade, S.; Dacheux, N.; Barré, N.; Abraham, F. *Inorg. Chem.* **2010**, *49*, 1921-1931.

(103)   Bulbul, M.; Eral, M.; Tel, H.; Ozes, F.; Can, S. *Kim. Kim. Muhendisligi Semp.* **1992**, *3*, 201-205.

(104)   Giesting Paul, A.; Porter Nathan, J.; Burns Peter, C. In *Zeitschrift für Kristallographie - Crystalline Materials* 2006; Vol. 221, p 252.

(105)   Davis Jr., W.; West, G. A.; Stacy, R. G.; Safeguards, U. S. N. R. C. O. o. N. M. S. a., Ed. Washington, D.C., 1979.

(106)   Grenthe, I.; Drozdzynski, J.; Fujino, T.; Buck, E. C.; Albrecht-Schmitt, T. E.; Wolf, S. F. In *The Chemistry of the Actinide and Transactinide Elements*; 3 ed.; Morss, L. R., Edelstein, N. M., Fuger, J., Eds.; Springer: The Netherlands, 2006; Vol. 1, p 253-639.

(107)   Lescop, C.; Arliguie, T.; Lance, M.; Nierlich, M.; Ephritikhine, M. *J. Organomet. Chem.* **1999**, *580*, 137-144.

(108)   Wickleder, M. S.; Fourest, B.; Dorhout, P. K. In *The Chemistry of the Actinide and Transactinide Elements*; 3 ed.; Morss, L. R., Edelstein, N. M., Fuger, J., Eds.; Springer: The Netherlands, 2006; Vol. 1, p 52-160.

(109)   Brown, J. L.; Fortier, S.; Lewis, R. A.; Wu, G.; Hayton, T. W. *J. Am. Chem. Soc.* **2012**, *134*, 15468-15475.

(110)   Daly, S. R.; Keith, J. M.; Batista, E. R.; Boland, K. S.; Clark, D. L.; Kozimor, S. A.; Martin, R. L. *J. Am. Chem. Soc.* **2012**, *134*, 14408-14422.

(111)   Evans, W. J.; Miller, K. A.; Ziller, J. W.; DiPasquale, A. G.; Heroux, K. J.; Rheingold, A. L. *Organometallics* **2007**, *26*, 4287-4293.

(112)   Behrle, A. C.; Barnes, C. L.; Kaltsoyannis, N.; Walensky, J. R. *Inorg. Chem.* **2013**, *52*, 10623-10631.

(113)   Wrobleski, D. A.; Cromer, D. T.; Ortiz, J. V.; Rauchfuss, T. B.; Ryan, R. R.; Sattelberger, A. P. *J. Am. Chem. Soc.* **1986**, *108*, 174-175.

(114)   Lin, Z.; Brock, C. P.; Marks, T. J. *Inorg. Chim. Acta* **1988**, *141*, 145-149.

(115)   Smiles, D. E.; Wu, G.; Kaltsoyannis, N.; Hayton, T. W. *Chem. Sci.* **2016**, *6*, 3891-3899.

(116)   Casellato, U.; Sitran, S.; Tamburini, S.; Vigato, P. A.; Graziani, R. *Inorg. Chim. Acta* **1984**, *95*, 37-42.

(117)   Das, R. K.; Barnea, E.; Andrea, T.; Kapon, M.; Fridman, N.; Botoshansky, M.; Eisen, M. S. *Organometallics* **2015**, *34*, 742-752.

(118)   Ren, W.; Song, H.; Zi, G.; Walter, M. D. *Dalton Trans.* **2012**, *41*, 5965-5973.

(119)   Ren, W.; Zi, G.; Fang, D.-C.; Walter, M. D. *J. Am. Chem. Soc.* **2011**, *133*, 13183-13196.

208

(120)   Wang, X.; Andrews, L.; Thanthiriwatte, K. S.; Dixon, D. A. *Inorg. Chem.* **2013**, *52*, 10275-10285.

(121)   Yang, P.; Zhou, E.; Fang, B.; Hou, G.; Zi, G.; Walter, M. D. *Organometallics* **2016**, *35*, 2129-2139.

(122)   Fang, B.; Ren, W.; Hou, G.; Zi, G.; Fang, D.-C.; Maron, L.; Walter, M. D. *J. Am. Chem. Soc.* **2014**, *136*, 17249-17261.

(123)   Fang, B.; Zhang, L.; Hou, G.; Zi, G.; Fang, D.-C.; Walter, M. D. *Organometallics* **2015**, *34*, 5669-5681.

(124)   Settineri, N. S.; Garner, M. E.; Arnold, J. *J. Am. Chem. Soc.* **2017**, *139*, 6261-6269.

(125)   Ren, W.; Zi, G.; Fang, D.-C.; Walter, M. D. *Chem. Eur. J.* **2011**, *17*, 12669-12682.

(126)   Fagan, P. J.; Manriquez, J. M.; Maatta, E. A.; Seyam, A. M.; Marks, T. J. *J. Am. Chem. Soc.* **1981**, *103*, 6650-6667.

(127)   Jantunen, K. C.; Burns, C. J.; Castro-Rodriguez, I.; Da Re, R. E.; Golden, J. T.; Morris, D. E.; Scott, B. L.; Taw, F. L.; Kiplinger, J. L. *Organometallics* **2004**, *23*, 4682-4692.

(128)   England, A. F.; Burns, C. J.; Buchwald, S. L. *Organometallics* **1994**, *13*, 3491-3495.

(129)   Liao, J. H.; Kanatzidis, M. G. *Inorg. Chem.* **1992**, *31*, 431-439.

(130)   Shannon, R. D. *Acta Crystallographica Section A* **1976**, *32*, 751-767.

(131)   Browne, K. P.; Maerzke, K. A.; Travia, N. E.; Morris, D. E.; Scott, B. L.; Henson, N. J.; Yang, P.; Kiplinger, J. L.; Veauthier, J. M. *Inorg. Chem.* **2016**, *55*, 4941-4950.

(132)   Braun, T.; Perutz, R. N. *Chem. Comm.* **2002**, 2749-2757.

(133)   Sadhukhan, T.; Samanta, B.; Ansari, S. A.; Pal, S. *Theor. Chem. Acc.* **2016**, *135*, 1-10.

(134)   Huang, Z.; Yuan, Y.; Sun, L.; Wang, X.; Li, Y. *RSC Advances* **2016**, *6*, 84016-84024.

(135)   Jones, W. D. *Dalton Trans.* **2003**, 3991-3995.

(136)   Reinhold, M.; McGrady, J. E.; Perutz, R. N. *J. Am. Chem. Soc.* **2004**, *126*, 5268-5276.

(137)   Richmond, T. G.; Osterberg, C. E.; Arif, A. M. *J. Am. Chem. Soc.* **1987**, *109*, 8091-8092.

(138)   Stille, J. K.; Lau, K. S. Y. *Acc. Chem. Res.* **1977**, *10*, 434-442.

(139)   Kiplinger, J. L.; Richmond, T. G.; Osterberg, C. E. *Chem. Rev.* **1994**, *94*, 373-431.

(140)   Crespo, M.; Martínez, M.; Nabavizadeh, S. M.; Rashidi, M. *Coord. Chem. Rev.* **2014**, *279*, 115-140.

(141)   Nabavizadeh, S. M.; Hoseini, S. J.; Momeni, B. Z.; Shahabadi, N.; Rashidi, M.; Pakiari, A. H.; Eskandari, K. *Dalton Trans.* **2008**, 2414-2421.

(142)   Rashidi, M.; Momeni, B. Z. *J. Organomet. Chem.* **1999**, *574*, 286-293.

(143)   Blake, P. C.; Lappert, M. F.; Taylor, R. G.; Atwood, J. L.; Hunter, W. E.; Zhang, H. *J. Chem. Soc., Chem. Commun.* **1986**, 1394-1395.

(144)   Fischer, R. D.; Ammon, R. V.; Kanellakopulos, B. *J. Organomet. Chem.* **1970**, *25*, 123-137.

(145)   Graves, C. R.; Yang, P.; Kozimor, S. A.; Vaughn, A. E.; Clark, D. L.; Conradson, S. D.; Schelter, E. J.; Scott, B. L.; Thompson, J. D.; Hay, P. J.; Morris, D. E.; Kiplinger, J. L. *J. Am. Chem. Soc.* **2008**, *130*, 5272-5285.

(146)   Lukens, W. W.; Allen, P. G.; Bucher, J. J.; Edelstein, N. M.; Hudson, E. A.; Shuh, D. K.; Reich, T.; Andersen, R. A. *Organometallics* **1999**, *18*, 1253-1258.

(147)   Lukens, W. W.; Beshouri, S. M.; Stuart, A. L.; Andersen, R. A. *Organometallics* **1999**, *18*, 1247-1252.

(148)   Ryan, R. R.; Penneman, R. A.; BKanellakopulos, B. *J. Am. Chem. Soc.* **1975**, *97*, 4258.

(149)   Thomson, R. K.; Graves, C. R.; Scott, B. L.; Kiplinger, J. L. *Eur. J. Inorg. Chem.* **2009**, *2009*, 1451-1455.

(150)   Thomson, R. K.; Graves, C. R.; Scott, B. L.; Kiplinger, J. L. *Dalton Trans.* **2010**, *39*, 6826-6831.

(151)   Zi, G.; Jia, L.; Werkema, E. L.; Walter, M. D.; Gottfriedsen, J. P.; Andersen, R. A. *Organometallics* **2005**, *24*, 4251-4264.

(152)   Lukens, W. W.; Beshouri, S. M.; Blosch, L. L.; Stuart, A. L.; Andersen, R. A. *Organometallics* **1999**, *18*, 1235-1246.

(153)   Weydert, M.; Andersen, R. A. In *Inorganic Fluorine Chemistry*; American Chemical Society: 1994; Vol. 555, p 383-391.

(154)   Kanellakopulos, B.; Dornberger, E.; von Ammon, R.; Fischer, R. D. *Angewandte Chemie International Edition in English* **1970**, *9*, 957-958.

(155)   Hitchcock, P. B.; Lappert, M. F.; Taylor, R. G. *J. Chem. Soc., Chem. Commun.* **1984**, 1082-1084.

(156)   Weydert, M.; Andersen, R. A.; Bergman, R. G. *J. Am. Chem. Soc.* **1993**, *115*, 8837-8838.

(157)   Evans, W. J.; Nyce, G. W.; Johnston, M. A.; Ziller, J. W. *J. Am. Chem. Soc.* **2000**, *122*, 12019-12020.

(158)   Lyon, J. T.; Andrews, L.; Hu, H.-S.; Li, J. *Inorganic Chemistry* **2008**, *47*, 1435-1442.

(159)   Li, J.; Hu, H.-S.; Lyon, J. T.; Andrews, L. *Angewandte Chemie International Edition* **2007**, *46*, 9045-9049.

(160)   Clark, C. L.; Lockhart, J. J.; Fanwick, P. E.; Bart, S. C. *Chem. Comm.* **2015**, *51*, 14084-14087.

(161)   Thomson, R. K.; Cantat, T.; Scott, B. L.; Morris, D. E.; Batista, E. R.; Kiplinger, J. L. *Nat Chem* **2010**, *2*, 723-729.

(162)   Dietrich, H. M.; Ziller, J. W.; Anwander, R.; Evans, W. J. *Organometallics* **2009**, *28*, 1173-1179.

(163)   Yahia, A.; Castro, L.; Maron, L. *Chem. Eur. J.* **2010**, *16*, 5564-5567.

(164)   Mehdoui, T.; Berthet, J.-C.; Thuéry, P.; Salmon, L.; Rivière, E.; Ephritikhine, M. *Chem. Eur. J.* **2005**, *11*, 6994-7006.

(165)   Mohammad, A.; Cladis, D. P.; Forrest, W. P.; Fanwick, P. E.; Bart, S. C. *Chem. Comm.* **2012**, *48*, 1671-1673.

(166)   Garner, M. E.; Hohloch, S.; Maron, L.; Arnold, J. *Angewandte Chemie International Edition* **2016**, *128*, 13993-13996.

(167)   Chermette, H.; Rachedi, K.; Volatron, F. *Journal of Molecular Structure: THEOCHEM* **2006**, *762*, 109-121.

(168)   O'Grady, E.; Kaltsoyannis, N. *J. Chem. Soc., Dalton Trans.* **2002**, 1233-1239.

(169)   Monreal, M. J.; Thomson, R. K.; Cantat, T.; Travia, N. E.; Scott, B. L.; Kiplinger, J. L. *Organometallics* **2011**, *30*, 2031-2038.

(170)   Chakraborty, S.; Chattopadhyay, J.; Guo, W.; Billups, W. E. *Angewandte Chemie International Edition* **2007**, *46*, 4486-4488.

(171)   Bennett Brian, K.; Harrison, R. G.; Richmond, T. G. *J. Am. Chem. Soc.* **1994**, *116*, 11165-11166.

(172)   Bennett Brian, K., University of Utah, 1997.

(173)   Lichtscheidl, A.; Pagano, J.; Scott, B.; Nelson, A.; Kiplinger, J. *Inorganics* **2016**, *4*, 1.

(174)   Smith, M. B.; March, J. *March's Advanced Organic Chemistry*; 6th ed.; Wiley-Interscience 2007.

(175)   Graves, C. R.; Schelter, E. J.; Cantat, T.; Scott, B. L.; Kiplinger, J. L. *Organometallics* **2008**, *27*, 5371-5378.

(176)   Spirlet, M. R.; Rebizant, J.; Apostolidis, C.; Kanellakopulos, B. *Acta Crystallogr., Sect. C.* **1992**, *48*, 2135-2137.

(177)   Morris, D. E.; Da Re, R. E.; Jantunen, K. C.; Castro-Rodriguez, I.; Kiplinger, J. L. *Organometallics* **2004**, *23*, 5142-5153.

(178)   Zhao, T.; Boltjes, A.; Herdtweck, E.; Dömling, A. *Organic Letters* **2013**, *15*, 639-641.

(179)   Himo, F.; Demko, Z. P.; Noodleman, L.; Sharpless, K. B. *Journal of the American Chemical Society* **2002**, *124*, 12210-12216.

(180)   Roh, J.; Vávrová, K.; Hrabálek, A. *European Journal of Organic Chemistry* **2012**, *2012*, 6101-6118.

(181)   Zhang, J.-Y.; Cheng, A.-L.; Sun, Q.; Yue, Q.; Gao, E.-Q. *Crystal Growth & Design* **2010**, *10*, 2908-2915.

(182)   Wang, X.-S.; Tang, Y.-Z.; Huang, X.-F.; Qu, Z.-R.; Che, C.-M.; Chan, P. W. H.; Xiong, R.-G. *Inorganic Chemistry* **2005**, *44*, 5278-5285.

(183)   Tseng, T.-W.; Luo, T.-T.; Chen, S.-Y.; Su, C.-C.; Chi, K.-M.; Lu, K.-L. *Crystal Growth & Design* **2013**, *13*, 510-517.

(184)   Cui, P.; Chen, Z.; Gao, D.; Zhao, B.; Shi, W.; Cheng, P. *Crystal Growth & Design* **2010**, *10*, 4370-4378.

(185)   Himo, F.; Demko, Z. P.; Noodleman, L.; Sharpless, K. B. *Journal of the American Chemical Society* **2003**, *125*, 9983-9987.

(186)   Nomiya, K.; Noguchi, R.; Oda, M. *Inorganica Chimica Acta* **2000**, *298*, 24-32.

(187)   Wehlan, M.; Thiel, R.; Fuchs, J.; Beck, W.; Fehlhammer, W. P. *Journal of Organometallic Chemistry* **2000**, *613*, 159-169.

(188)   Silvester, D. S.; Uprety, S.; Wright, P. J.; Massi, M.; Stagni, S.; Muzzioli, S. *The Journal of Physical Chemistry C* **2012**, *116*, 7327-7333.

(189)   Fehlhammer, W. P.; Dahl, L. F. *Journal of the American Chemical Society* **1971**, *94*, 3370 - 3377.

(190)   Gaydou, M.; Echavarren, A. M. *Angewandte Chemie International Edition* **2013**, *52*, 13468-13471.

(191)   Andreiadis, E. S.; Imbert, D.; Pecaut, J.; Demadrille, R.; Mazzanti, M. *Dalton Transactions* **2012**, *41*, 1268-1277.

(192)   Chen, W.-B.; Li, Z.-X.; Ouyang, Z.-J.; Lin, W.-N.; Yang, L.; Dong, W. *RSC Advances* **2014**, *4*, 61104-61113.

(193)   Di Pietro, S.; Gautier, N.; Imbert, D.; Pecaut, J.; Mazzanti, M. *Dalton Transactions* **2016**, *45*, 3429-3442.

(194)   Giraud, M.; Andreiadis, E. S.; Fisyuk, A. S.; Demadrille, R.; Pécaut, J.; Imbert, D.; Mazzanti, M. *Inorganic Chemistry* **2008**, *47*, 3952-3954.

(195)   Gulevich, A. V.; Dudnik, A. S.; Chernyak, N.; Gevorgyan, V. *Chemical Reviews* **2013**, *113*, 3084-3213.

(196)   Jiménez, J.-R.; Díaz-Ortega, I. F.; Ruiz, E.; Aravena, D.; Pope, S. J. A.; Colacio, E.; Herrera, J. M. *Chemistry – A European Journal* **2016**, *22*, 14548-14559.

(197)   Wartenberg, N.; Raccurt, O.; Bourgeat-Lami, E.; Imbert, D.; Mazzanti, M. *Chemistry – A European Journal* **2013**, *19*, 3477-3482.

(198)   Wu, M.-F.; Wang, M.-S.; Guo, S.-P.; Zheng, F.-K.; Chen, H.-F.; Jiang, X.-M.; Liu, G.-N.; Guo, G.-C.; Huang, J.-S. *Crystal Growth & Design* **2011**, *11*, 372-381.

(199)   Xiao, Y.; Wang, S.-H.; Zheng, F.-K.; Wu, M.-F.; Xu, J.; Liu, Z.-F.; Chen, J.; Li, R.; Guo, G.-C. *CrystEngComm* **2016**, *18*, 721-727.

(200)   Zhou, X.-G.; Huang, Z.-E.; Cai, R.-F.; Zhang, L.-X.; Hou, X.-F.; Feng, X.-J.; Huang, X.-Y. *Journal of Organometallic Chemistry* **1998**, *563*, 101-112.

(201)   Zhou, X.-G.; Zhang, L.-X.; Huang, Z.-E.; Cai, R.-F.; Huang, X.-Y. *Synthesis and Reactivity in Inorganic and Metal-Organic Chemistry* **2000**, *30*, 965-978.

(202)   Poturovic, S.; Lu, D.; Heeg, M. J.; Winter, C. H. *Polyhedron* **2008**, *27*, 3280-3286.

(203)   Heeres, H. J.; Teuben, J. H.; Rogers, R. D. *J. Organomet. Chem.* **1989**, *364*, 87-96.

(204)   Werner, H.; Otto, H.; Ngo-Khac, T.; Burschka, C. *J. Organomet. Chem.* **1984**, *262*, 123-136.

Curriculum Vitae

Jacquelyn M. Dorhout, Ph.D.

E-mail: dorhoutj@lanl.gov

Education	**PhD, Radiochemistry** (December 2017 expected; GPA = 4.0/4.0)
	"Synthesis of Actinide Materials for the Study of Basic Actinide Science and Rapid Separation of Fission Products" Department of Chemistry University of Nevada -Las Vegas
	Las Vegas, Nevada
	Bachelor of Science, Chemistry (May 2012; GPA = 3.806/4.0) Commonwealth Honors College – Honors Student
	Summa cum Laude and Departmental Honors
	University of Massachusetts-Amherst
	Amherst, Massachusetts
Research Summary	• Operations with radioactive material (Th, U, fission products) • Experience with glove-box manipulations, air-sensitive materials • Completed course work in nuclear physics, radiation instrumentation
Research Experience	**Graduate Research Assistant (2012 – 2017)**
	Professor Ken Czerwinski
	Department of Chemistry (MSM 313)
	4505 Maryland Parkway, Box 454003 Las Vegas, NV 89154-4003

- Synthesized and characterized solid-state uranium compounds via hydrothermal methods, FT-IR analysis, SCXRD analysis
- Analyzed neutron-irradiated UO_2 target material via gamma spectroscopy for nuclear forensic purposes
- Worked with radioactive materials (Rad Worker I and II); manipulations with irradiated uranium material

Graduate Research Assistant (2014 – October 2017)

Dr. Jaqueline Kiplinger

Los Alamos National Laboratory C-IIAC

P.O. Box 1663, Mailstop J514

Los Alamos, NM 87545

- Completed summer internships 2014, 2015
- Full-time graduate research April 2016 – October 2017
- Rad Worker II trained
- Synthesized and characterized air-sensitive radioactive organoactinide compounds using dry-box manipulations, NMR spectroscopy, FT-IR, UV-Vis-NIR analysis
- Active Q-level security clearance

Undergraduate Research Assistant (2009-2012)

Professor Michael J. Knapp
512 LGRT, 710 N Pleasant Street
Amherst, MA 01003

- Synthesized and characterized complex organic molecules using Schlenk techniques, NMR spectroscopy

Nuclear Chemistry Summer School – Research Assistant (Summer, 2011)

Professor Louis Pena
Brookhaven National Lab Medical Department
Upton, NY 11973

- Completed the course on Nuclear Chemistry, Radiochemistry, and Nuclear Physics
- Worked with radioisotopes such as ^{3}H, ^{18}F, ^{59}Fe, ^{113}Sn, ^{113m}In

Radiochemistry Fuel Cycle Summer School - Research Assistant (Summer, 2010)

Professor Ken Czerwinski
Department Of Chemistry
4505 Maryland Pkwy-Box 454003
Las Vegas, NV 89154-4003

- Synthesized and characterized uranium (III) complexes using Schlenk techniques, dry-box manipulations
- Trained in handling radioactive materials (Pu, U)

Undergraduate Research Assistant (2008)

Professor Julian Thompson
710 N Pleasant Street
Amherst, MA 01003

- Collected and analyzed soil samples for arsenic
- Digested samples in preparation for ICP analysis

Honors & Awards	- Invited speaker for Radioanalytical Nuclear Chemistry Session, ACS Rocky Mountain Regional Meeting 2017 - Invited to present at Symposium in Honor of Jaqueline L. Kiplinger 249th ACS National Meeting March 2015 - Awarded Nuclear Forensics Graduate Fellowship April 2013 – Dec 2017 - Continuously recognized on the Dean's list Fall 2008 – Spring 2012 - Outstanding Chemistry Major on the Dean's list, 2009-2012 - William F. Field Alumni Scholar, 2011 - ACS Undergraduate Award for Inorganic Chemistry, 2011 - National Society of Leadership and Success member - Golden Key Honor Society member
Accomplishments	- Los Alamos County Science Fair judge 2017 - Summer internships (2014, 2015) and full-time research (2016-Fall 2017) at LANL through the Seaborg Institute - Continuous graduate research with the University of Nevada-Las Vegas since 2012 - Continuous undergraduate research at the University of Massachusetts-Amherst from 2008 to 2012 - Selected for and successfully completed the Department of Energy Nuclear Chemistry Summer School at Brookhaven National Laboratory

- Selected for and successfully completed the Department of Energy Radiochemistry Fuel Cycle Summer School at the University of Nevada-Las Vegas
- ACS member since 2009

Publications

Dorhout, J.M., Czerwinski, K.R. "Irradiation and Separation of Fission Products from Uranium MOFs" In Preparation.

Dorhout, J.M., Czerwinski, K.R. "A UO_2 Target for Rapid Separation of Fission Products" In Preparation.

Dorhout, J.M.; Browne, K.P.; Scott, B.L.; Veauthier, J.M.; Kiplinger, J.L. "Ph_3PAu-methyltetrazolate as a tetrazolate transfer agent to f-elements" In Preparation.

Dorhout, J.M.; Monreal, M.J.; Scott, B.L.; Kiplinger, J.L. "Actinide Mediated C-X Activation" In Preparation.

Dorhout, J.M. et.al. "All Roads Lead to $(C_5Me_5)_2ThS_5$: Insertion of Elemental Sulfur (S_8) into Thorium–Carbon and Thorium–Sulfur Bonds in Metallocene Complexes", In Preparation.

Erickson, K.A.; Pagano, J.K.; Dorhout, J.M. et.al. "Revisiting the Fagan-Nugent Reaction with Actinides: P-C Bond Forming Reactions with Thorium and Uranium Metallacyclopentadienes and Phosphine Chlorides", In Preparation

Pagano, J.K.; Dorhout, J.M.; Czerwinski, K.R.; Morris, D.; Scott, B.; Waterman, R.; Kiplinger, J.L. "Tuning the Oxidation State and Chemistry of Uranium Hydrides with Phenylsilane and Temperature: the Case of the Classic Uranium(III) Hydride Complex, $[(C_5Me_5)_2U(\mu\text{-}H)]_2$" *Organometallics,* **2016**, *35* (5), 617-620.

Pagano, J.K.; Dorhout, J.M., Waterman, R.; Czerwinski, K.R.; Kiplinger, J.L. "Phenylsilane as a safe, versatile alternative to hydrogen for the synthesis of organometallic actinide hydrides" *Chem Comm*. **2015**, *51*, 17379-17381.

Presentations

Dorhout, J.M.; Czerwinski, K.R. "Rapid Separations of Fission Products from Uranium-Based Target Materials", invited speaker; Radioanalytical Nuclear Chemistry Session, ACS Rocky Mountain Regional Meeting, October 2017.

Dorhout, J.M. "Explorations into Organouranium Synthetic Chemistry" Annual Student Symposium, Los Alamos National Laboratory, Los Alamos, New Mexico, August 2017.

Dorhout, J.M. "Rapid Separations of Fission Products from Uranium-Based Target Materials" Interagency Technical Nuclear Forensics Program Review, Oak Ridge National Laboratory, Oak Ridge, Tennessee, July 2017.

Dorhout, J.M., et.al. "Actinide mediated C-X activation chemistry" Poster INOR #971, ACS National Meeting, April 2017 (Division of Inorganic Chemistry; Session Lanthanide & Actinide Chemistry).

Dorhout, J.M. "Nuclear and radiochemistry summer school: (Almost) six years later" Publication NUCL #55 ACS National Meeting, April 2017 (Division of Nuclear Chemistry and Technology; Session Nuclear & Radiochemistry Summer School: Past, Present, & Future).

Dorhout, J.M. "Rapid Separation of Fission Products from UO2 Target Materials" Academic Laboratory Collaboration Meeting, Lawrence Livermore National Laboratory, Livermore California, August 2015

Dorhout, J.M. et.al. "New synthetic pathways to $(C_5Me_5)_2ThS_5$" Poster #689, ACS National Meeting, March 2015 (Division of Inorganic Chemistry; Session Organometallic Chemistry Synthesis and Characterization)

Dorhout, J.M.; Czerwinski, K. "Synthesis of rapid separation targets by hydrothermal methods", Publication #24, ACS National Meeting, March 2015 (Division of Nuclear Chemistry and Technology; Session Nuclear Forensics)

Dorhout, J.M.; Czerwinski, K. "Synthesis of rapid separation targets by hydrothermal methods" Poster #47, American Nuclear Society Student Conference, April 2013

Dorhout, J. M, Taabazuing, C.Y., Knapp, M. J. "Synthesis of potential inhibitors of FIH Fe^{2+} active site", abstract #19556, ACS National Meeting, August, 2011 (Division of Inorganic Chemistry; Session Bioinorganic Chemistry and SciMIx)